Georadar for small-scale high-resolution dielectric property and water content determination of soils

vorgelegt von
Diplom Geophysiker
Jürgen Schmalholz
aus Kempten (Allgäu)/Bayern

von der Fakultät VI – Planen Bauen Umwelt
der Technischen Universität Berlin
zur Erlangung des akademischen Grades
Doktor der Naturwissenschaften
Dr. rer. nat.
genehmigte Dissertation

Promotionsausschuss:

Vorsitzender: Prof. Dr. Gerd Wessolek
Berichter: Prof. Dr. Ugur Yaramanci
Berichter: Dr. Andreas Kemna

Tag der wissenschaftlichen Aussprache: 10.7.2007

Berlin 2007

D 83

ABSTRACT

Georadar for small-scale high-resolution dielectric property and water content determination of soils

Jürgen Schmalholz, PhD thesis, Technical University of Berlin, 2007

To understand processes and dynamics linked to the volumetric water content of soils thorough knowledge of the water distribution inside soils is required. The applicability of the georadar technique for small-scale soil heterogeneity mapping and monitoring is investigated using four different methods. Since the uppermost meter of the soil lacks a sufficient amount of spacious reflectors no standard georadar methods can supply adequate coverage of the investigated area under field conditions. Therefore four methods were evaluated to present an assortment of the most promising methods for different case-specific problems. Owing to the averaging nature of the georadar technique the introduced methods needed to be adapted to small-scale investigations. Based on numerical simulations and concise measurements new processing procedures are applied to achieve the required spatial resolution of less than 0.3 m. All four methods were successfully applied during realistic field measurement conditions.

The transmission method is applied to a soil column experiment filled with undisturbed natural soil. In the course of an irrigation experiment the infiltration of the water front as well as the water dynamics afterwards were reproduced. The application of georadar transmission tomography provided spatial-allocatable water content distributions over the time of the water seepage with spatial accuracies of approximately 0.1 m and a temporal resolution of approximately 30 min.

The acquisition of georadar ground wave data was optimized in order to record denser sampled datasets than generally used. Applying a travel time inversion algorithm enabled the localization and the determination of true volumetric water contents of otherwise masked anomalies. Due to the travel time inversion a reduction of the corresponding allocated soil region by a factor of approximately eight was achieved. Furthermore, data accuracy is greatly enhanced compared to standard ground wave measurements with similar spatial accuracy.

The local vertical distribution of the volumetric water content is determined with the radar based time domain reflectometry (RB-TDR) method. Even though this method cannot be assumed non-invasive, minimal disturbance of the soil is registered. Similar to common TDR methods travel times of guided electromagnetic waves are analyzed. The RB-TDR layout consists of a metallic rod inserted vertically into the soil next to a georadar antenna. Gradually inserting the rod into the soil a vertical distribution of the adjacent volumetric water content is recorded. Smooth as well as distinct changes of the volumetric water content can be mapped with vertical accuracies of approximately 0.1 m.

Standard constant offset reflection measurements can contain valuable information even when lacking significant reflection events. Diffracting objects can provide information of the overlaying soil's volumetric water content. A two-dimensional volumetric water content distribution can be deduced by utilizing the diffraction velocity analysis. With the application of a two-dimensional migration algorithm the validity of the volumetric water content distribution can be checked and additional diffracting objects can be identified, further enhancing the spatial accuracy.

ZUSAMMENFASSUNG

Georadar for small-scale high-resolution dielectric property and water content determination of soils

Jürgen Schmalholz, Dissertation, Technische Universität Berlin, 2007

Um zeitliche und andere Prozesse, die durch den volumetrischen Wassergehalt im Boden verursacht werden zu verstehen wird eine genaue Kenntnis der Wasserverteilung im Boden benötigt. Die Anwendbarkeit des Georadar Verfahrens für die Abbildung und zeitliche Überwachung kleinräumiger Bodenheterogenitäten wird untersucht. Standard Georadar Methoden können wegen der im obersten Meter des Bodens ungenügend vorhandenen Reflektoren mit ausreichender Größe keine adäquate Überdeckung des Untersuchungsgebietes unter Feldbedingungen liefern. Es wurden deshalb die vier vielversprechendsten Methoden evaluiert um eine Auswahl für verschiedene fallspezifische Problemstellungen anzubieten. Auf Grund des mittelnden Charakters des Georadar Verfahrens mussten die vorgestellten Methoden für die Fragestellung zur kleinräumigen Untersuchung angepasst werden. Basierend auf numerischen Simulationen und prägnanten Messungen wurden neue Bearbeitungsschritte verwendet um eine räumliche Auflösung von weniger als 0.3 m zu erreichen. Alle vier Methoden konnten unter realistischen Bedingungen im Feld erfolgreich durchgeführt werden.

An einer Säule, welche mit ungestörtem natürlichem Boden gefüllt war, wurden Transmissionsmessungen durchgeführt. Im Zuge eines Beregnungsversuches konnte sowohl die Wasserinfiltration als auch die Wasserversickerung nach Abschluss der eigentlichen Bewässerung verfolgt werden. Mittels Georadar Transmissionstomography konnte zusätzlich die Wassergehaltsverteilung während der Versickerungsphase mit einer räumlichen Genauigkeit von 0.1 m und einer zeitlichen Auflösung von etwa 30 min bestimmt werden.

Gegenüber der herkömmlichen Vorgehensweise wurde die Aufzeichnung von Georadar Bodenwellen Daten dahingehend optimiert, dass räumlich dichtere Daten zur Verfügung standen. Nach Anwendung eines Laufzeit Inversionsalgorithmus konnten nicht nur Anomalien, welche mit herkömmlichen Methoden nicht detektierbar sind, genau lokalisiert werden sondern auch deren wahrer volumetrischer Wassergehalt bestimmt werden. Durch die Anwendung des Laufzeit Inversionsalgorithmus konnte eine Verbesserung der räumlichen Zuordnung um etwa das Achtfache erzielt werden. Des Weiteren liefert die hier durchgeführte Methode verlässlichere Daten als herkömmliche Standard Bodenwellenmessungen mit vergleichbarer räumlicher Auflösung.

Die lokale vertikale Verteilung des volumetrischen Wassergehaltes wurde mit der radar-basierten Zeitbereichs Reflektometrie (RB-TDR) bestimmt. Wenngleich diese Methode nicht als zerstörungsfrei bezeichnet werden kann wird dennoch nur eine minimale Störung des Bodens verursacht. Ähnlich der Zeitbereichs Reflektometrie (TDR) werden Laufzeiten geführter elektromagnetischer Wellen ausgewertet. Der Aufbau der RB-TDR Methode besteht aus einem Metallrohr, das direkt neben einer Georadarantenne senkrecht in den Boden gesteckt wird. Bringt man das Rohr nun kontinuierlich weiter in den Boden ein, so kann die Verteilung des Wassergehaltes der Umgebung ermittelt werden. Wassergehalte können mit einer vertikalen Genauigkeit von etwa 0.1 m sowohl für scharfe Grenzen als auch für graduelle Übergänge erzielt werden.

Standard Reflexionsmessungen mit festem Antennenabstand können wertvolle Informationen beinhalten selbst wenn keine aussagekräftigen Reflexionsereignisse vorhanden sind. Diffraktionenerzeugende Objekte können Informationen über den darüberliegenden volumetrischen Wassergehalt des Bodens liefern. Wenn die Diffraktions Geschwindigkeitsanalyse (DVA) durchgeführt wird können zwei dimensionale Wassergehaltsverteilungen abgeleitet werden. Wird zusätzlich ein zwei dimensionaler Migrationsalgorithmus angewendet, so kann die Gültigkeit der Wassergehaltsverteilung überprüft und zusätzliche Diffraktoren aufgespürt werden, was die räumliche Auflösung weiter verbessert.

CONTENTS

1 Introduction

Mapping heterogeneous physical parameter distributions in soils is of great interest for a variety of applications. This may be agriculture to assure crop and food quality or engineering to ensure security and stability of e.g. dams or dikes. Although physical properties are generally not the requested parameter for the application, the physical properties can be transformed into e.g. petrophysical parameter using an appropriate relationship. Particularly the knowledge of the distribution of the volumetric water content in the unsaturated zone is important for a variety of investigations such as climate research, flood prevention, matter transport into the subsurface or decomposition and transformation processes in the soil. Geophysical methods can provide an interesting alternative to conventional water content estimations like time domain reflectometry (TDR) (Robinson et al., 2003), radio-active methods (Bachmann, 1997) or soil sampling. Advantages of the geophysical methods are their generally non-invasive character and the large sampling volume compared to the used probes or devices. E.g. the investigated area of a geoelectrical section measurement (Kemna et al., 2002) exceeds by several orders of magnitude the area disturbed by the inserted electrodes. Other methods such as magnetic resonance sounding (MRS) (Yaramanci and Hertrich, 2006), georadar (Greaves et al., 1996) or electromagnetic induction methods (Tabaggh, 1986) provide information without the insertion of probes into the subsurface.

The georadar (also referred to as ground-penetrating radar, ground probing radar, GPR, electromagnetic reflection technique, EMR) is a geophysical technique that emits electromagnetic (EM) waves and records the EM response of the close environment. A typical georadar instrument consists of a control unit, a transmitter and a receiver antenna. With the transmitter antenna a known signal is generated. The transmitter emits an EM wave, which travels through the media and is reflected or diffracted at interfaces with different electrical properties. The receiver antenna receives the EM signals and records the time series of the EM response. A georadar antenna is called monostatic if one antenna is used to transmit as well as to record the signal, otherwise the antenna is called bistatic. Most common georadar systems are bistatic systems with separate transmitter and receiver antennas (e.g. Daniels, 2004). The utilized EM signals range from 10 MHz to few GHz. Depending on the georadar system different signal types are common for georadar measurements. The most common signal type systems are pulse radar, stepped frequency radar, and impulse radar systems (e.g. Daniels, 2004). Pulse radar systems emit an almost mono-frequent pulse with a pulse of finite length much smaller than the expected recording time. Stepped frequency radar systems generate several mono-frequent signals and change successively the frequency over a broad spectra range. The whole broadband dataset is then transformed into a time-section using Fourier transformation. Impulse radar systems generate a short EM impulse of broad frequency range. The term “georadar” will be used for georadar systems with the impulse signal type from now on.

Georadar appears to be a promising geophysical technique for the determination of volumetric water content distributions in soils. Water is the dominant permittivity constituent of soil caused by the high contrast between the relative permittivity of water (approximately 80) compared to air (1) and the soil matrix (in the range of 4 to 10 (Schön, 1996)). Since both TDR and georadar utilize EM wave propagation, georadar can build on the broad interdisciplinary acceptance of the well-established TDR method (Fellner-Feldegg, 1969). Due to its design the georadar is a flexible geophysical device. The georadar antennas do not require much space since they are commonly realized in the form of electrical dipoles. Other geophysical methods, e.g. transient electromagnetics (TEM) (Nabighian and Macnae, 1991) or MRS (Yaramanci and Hertrich, 2006), require comparably larger areas to layout the

specific source and receiver loop geometries. Although most georadar measurements are performed at the surface, georadar antennas are also used in boreholes (e.g. Binley et al., 2001).

With the knowledge of the emission time and the initial intensity of the impulse, the travel time of the EM wave and information regarding the attenuation can be gathered (e.g. el Hagrey and Müller, 2000, Holliger et al., 2001). Commercial high-frequency (500 MHz to 1600 MHz) georadar antennas are, with few exceptions, shielded devices with transmitter and receiver antennas in the same housing. Most applications for water content determination such as common midpoint (CMP) measurements (Fisher et al., 1992), georadar tomography (Vasco et al., 1997), ground wave measurements (Huisman et al., 2001) or vertical radar profiling (VRP) (Tronicke and Knoll, 2005) require separated transmitter and receiver antennas.

Already utilized in a wide variety of different applications like prospection, stratigraphic interpretation, road and railway inspection or safety assessment (e.g. Thierbach, 1974, Young and Sun, 1999, Grote et al., 2002, Hugenschmidt, 2000, Orlando, 2003) georadar is gaining more importance for water content determination. Taking advantage of the flexible configuration of the georadar method, various scenarios can be realized. The applications, to name a few, range from borehole to surface profiling (vertical radar profiling, VRP) (Tronicke and Knoll, 2005), borehole to borehole tomography (Binley et al., 2001), tomography in small field scale (Hanafy and el Hagrey, 2006) and laboratory scale (Schmalholz et al., 2004b), multi offset measurements for deep (Turesson, 2006) and shallow (Huisman et al., 2001) investigations or constant offset measurements for deep (Loeffler and Bano, 2004) and shallow (Grote et al., 2003) investigations. All these examples provide convincing water content estimations for different spatial ranges and problems.

On the other hand, small-scale soil water content determination in the range of few decimeters remains a challenge. This is caused by the generally averaging character of the georadar technique. Depending on the investigated problem, spatial resolutions of a few meters may be justifiable (e.g. van Overmeeren et al., 1997). Although integral information of few-meter accuracy is mostly sufficient, some problems require higher spatial accuracy. Those could be the determination of preferential flow paths (Täumer et al., 2006) or the detection and monitoring of water-repellent areas (Bauters et al., 2000). Georadar may not be able to investigate the regulating processes directly, but is capable of providing essential information of secondary effects, i.e. changes in soil water content. To successfully provide information for such small scale problems a spatial resolution of less then approximately 0.3 m is necessary (e.g. Täumer et al., 2006). Considering heterogeneous soils or local water dynamics, mapping of two or three dimensional areas may be mandatory. In order to trace some specific water dynamics in the soil such as infiltration after an irrigation event, data acquisition of one time step must not exceed one hour (e.g. Schmalholz et al., 2004b).

Whereas a temporal resolution of less than one hour can be achieved in most cases, not all of the aforementioned georadar applications are suited for small-scale physical parameter determination. CMP measurements have the disadvantage of being an averaging method and require the presence of distinct plane reflectors (Sheriff, 1997). Resorting CMP measurements to a set of multi-offset measurements (e.g. Greaves et al., 1996) enables the interpretation of a two-dimensional subsurface model. The lateral resolution is, however, still relatively poor (Turesson, 2006) and the vertical resolution is predetermined by the position of the reflectors. Such reflectors are scarce in the uppermost soil, and the groundwater table mostly cannot be detected with high-frequency antennas (Harari, 1996). This is caused by the gradual increase of the water content down to the water table (Loeffler and Bano, 2004). Additionally, the deduced petrophysical parameters are too inaccurate when confronted with a heterogeneous site (Becht et al., 2006). VRP presents a capable method, but has the drawback that a borehole

has to be present and large enough to accommodate a georadar antenna. Since borehole antennas are generally of lower frequency (25 MHz to 200 MHz), the resolution is too low to detect heterogeneities in the desired range. Another problem is the signal interference caused by refracted EM waves (Tronicke and Knoll, 2005), which leads to interpretation problems for the uppermost soil regions and regions in the vicinity of the borehole.

In this work methods for georadar applications are evaluated, enabling spatial resolutions of approximately 0.3 m and better. Four methods with different but complementary spatial validity are discussed and each will be optimized to achieve the spatial as well as the temporal requirements. Depending on the method, new layouts, reorganized data acquisition and/or adapted data analysis are necessary. All methods are evaluated on their accuracy, and their applicability is checked with a typical application example.

In chapter 2 a short summary of the physical principles of EM wave propagation is presented. After the initial description of electromagnetics the decisive physical properties for georadar measurements are deduced. Additionally a concise definition of the term reflector and diffractor will be formulated. The different occurrences of water inside the soil are classified depending on its frequency and importance for georadar applications. The relative permittivity behavior of water is discussed and a general formulation is presented. An introduction of the most common mixing models for the transformation of relative permittivity data to volumetric water content is given. Eventual a summary of several empirical, structure-dependent, and volume-dependent mixing models is given.

In chapter 3 transmission methods are described. Beginning with the parallel transmission measurement, a description of the method is presented. In the course of a laboratory measurement the strategy to determine the relevant physical properties from the recorded time series is shown. A quantitative evaluation is conducted and an application example is discussed. This application example is performed at a small soil column during a controlled sector irrigation. With the tomographical transmission measurement a more sophisticated procedure is presented. The common layout of the tomographical transmission measurement is described and its application on small objects is evaluated. A sensible restriction and general strategy to accurately trace dynamical water content changes is formulated and checked during the aforementioned irrigation experiment.

In chapter 4 the principles and applicability of the ground wave of the georadar is discussed. After a short summary of different ground wave models a new procedure is introduced to determine accurate and reliable volumetric water content distributions with a common ground wave measurement. This new procedure is compared to commonly applied routines. Based on simple propagation time modeling and finite difference time domain (FDTD) modeling of the EM wave propagation this new procedure is evaluated. The general accuracy as well as the detectability of small relative permittivity anomalies will be checked. In order to identify anomalies an easy case-specific threshold criterion is formulated. The procedure is applied on a field data set and compared to on-site TDR measurements.

In chapter 5 a new method for vertical volumetric water content determination is introduced. Here a common georadar antenna is placed next to a metallic rod and the propagation time of the guided wave along the rod is recorded. The radar based time domain reflectometry (RB-TDR) is described and a short summary of previous work is given. To estimate the soil region affecting the RB-TDR measurement some basic tests are performed. A zone is defined in which the propagation characteristics of the guided wave are similar. A new antenna combination is presented to optimize data quality and accuracy for travel time determination. Furthermore, necessary data processing steps are discussed to enhance data quality. Based on two calibration measurements under controlled conditions the accuracy of the RB-TDR is determined. An irrigation experiment in the field is then used to check the applicability as well as the temporal resolution of the RB-TDR.

In chapter 6 a new approach for the determination of volumetric water content distribution is formulated and termed diffraction velocity analysis (DVA). The effect of lateral and vertical variability of the relative permittivity on the shape of diffraction hyperbolas is investigated. Using FDTD modeling a synthetic radar section is derived, and based on several determined hyperbola shapes a two dimensional relative permittivity distribution is deduced. A method to check the validity of the DVA result is introduced, making the knowledge of the initial site condition not imperative. The DVA is applied at a field site and checked with the formulated method. Moreover, a new approach is introduced to uncouple the DVA from visible diffraction hyperbolas.

2 Electromagnetic wave propagation principles

2.1 General physical principles

2.1.1 Fundamental equations

All electromagnetic phenomena can be described by eight fundamental equations. Of those eight equations the four Maxwell equations build the fundament (Jackson, 1975).

$$\vec{\nabla} \times \vec{H}(\vec{r},t) = \vec{J}(\vec{r},t) + \frac{\partial \vec{D}(\vec{r},t)}{\partial t} \tag{2.1}$$

$$\vec{\nabla} \times \vec{E}(\vec{r},t) = -\frac{\partial \vec{B}(\vec{r},t)}{\partial t} \tag{2.2}$$

$$\vec{\nabla} \cdot \vec{D}(\vec{r},t) = \rho_e(\vec{r}) \tag{2.3}$$

$$\vec{\nabla} \cdot \vec{B}(\vec{r},t) = 0 \tag{2.4}$$

With the following parameters:

$\vec{H}$: magnetic field vector [A/m]

$\vec{J}$: current density vector [A/m^2]

$\vec{D}$: electric displacement vector [C/m^2]

$\vec{E}$: electric field vector [V/m]

$\vec{B}$: magnetic induction vector [T]

$\vec{\nabla}$: vector differential operator

ρ_e : charge density [C/m^3]

$\vec{r}$: position vector [m]

t : time [s]

In those four Maxwell equations only the vectors $\vec{E}$ and $\vec{B}$ as well as $\vec{D}$ and $\vec{H}$ respectively are linked. Assuming isotropic media and field vectors with not too high intensities all four aforementioned vectors can be related. Therefore three constitutive equations can be introduced.

$$\vec{D}(\vec{r},\omega) = \varepsilon_0 \varepsilon_r(\vec{r},\omega)\vec{E}(\vec{r},\omega) \tag{2.5}$$

$$\vec{B}(\vec{r},\omega) = \mu_0 \mu_r(\vec{r},\omega)\vec{H}(\vec{r},\omega) \tag{2.6}$$

with the following parameters:

ε_0 : dielectric permittivity of vacuum [C/(Vm)]

ε_r : relative permittivity [-]

μ_0 : magnetic permeability of vacuum [(Vs)/(Am)]

μ_r : relative magnetic permeability [-]

ω : angular frequency [2π/s]

The angular frequency ω is not to be confused with the frequency υ. The relation between these two frequencies is given by:

$$\upsilon = \frac{\omega}{2\pi} \tag{2.7}$$

To supplement the two previous constitutive equations Ohm's law in its general form is included.

$$\vec{J}(\vec{r},\omega) = \sigma(\vec{r},\omega)\vec{E}(\vec{r},\omega) \tag{2.8}$$

with σ the electrical conductivity. Although a relationship between $\vec{B}$ and $\vec{H}$ or $\vec{E}$ and $\vec{D}$ respectively is established, a direct transformation cannot be performed. If anisotropy is present, the three electrical properties ε_r, μ_r and σ become tensors. Generally the four Maxwell equations (2.1) through (2.4) are valid in the time domain, whereas the constitutive equations (2.5), (2.6) and (2.8) are valid in the frequency domain. Only by assuming non-dispersive media, i.e. the relative permittivity, relative magnetic permeability and electric conductivity are not frequency dependent, the equations can be substituted. Such a case cannot be assumed for general georadar applications (see 2.2). To allow the application of the three constitutive equations to the four Maxwell equations, the four Maxwell equations have to be transformed into the frequency domain. This can be achieved by applying the Fourier transformation on the Maxwell equations. Assuming any vector $\vec{A}(\vec{r},t)$ in the time domain, the Fourier transformation can be described as follows (Bronstein and Semendjajew, 1991):

$$\vec{A}(\vec{r},t) = \frac{1}{2\pi}\int_{-\infty}^{\infty}\vec{A}(\vec{r},\omega)e^{i\omega t}d\omega \tag{2.9}$$

and

$$\vec{A}(\vec{r},\omega) = \int_{-\infty}^{\infty}\vec{A}(\vec{r},t)e^{-i\omega t}dt \tag{2.10}$$

Assuming a space free of electrical charges and applying the transformation rules (2.9) and (2.10) on the four Maxwell equations, (2.1) to (2.4) with respect to (2.5), (2.6) and (2.8) can be written as follows.

$$\vec{\nabla}\times\vec{B}(\vec{r},\omega) = \mu_0\mu_r(\vec{r},\omega)\left(\sigma(\vec{r},\omega)\vec{E}(\vec{r},\omega) + i\omega\varepsilon_0\varepsilon_r(\vec{r},\omega)\vec{E}(\vec{r},\omega)\right) \tag{2.11}$$

$$\vec{\nabla}\times\vec{E}(\vec{r},\omega) = -i\omega\vec{B}(\vec{r},\omega) \tag{2.12}$$

$$\vec{\nabla} \cdot \left(\varepsilon_0 \varepsilon_r (\vec{r}, \omega) \vec{E}(\vec{r}, \omega) \right) = 0 \tag{2.13}$$

$$\vec{\nabla} \cdot \vec{B}(\vec{r}, \omega) = 0 \tag{2.14}$$

The assumption of a space absent of electrical charges is valid for georadar applications since generally no free charges are present in the field.
If free charges are present, (2.13) has to be written as

$$\begin{aligned} &\vec{\nabla} \cdot \left(\varepsilon_0 \varepsilon_r (\vec{r}, \omega) \vec{E}(\vec{r}, \omega) \right) = \delta(\omega) \rho_e (\vec{r}, \omega), \\ &\delta(\omega) = \begin{cases} \infty, & \omega = 0 \\ 0, & \omega \neq 0 \end{cases} \end{aligned} \tag{2.15}$$

with $\delta(\omega)$ Dirac's delta function.

To complement all fundamental equations to describe all phenomena in electromagnetics the Lorentz force has to be mentioned. The Lorentz force will be neglected, since it describes effects of moving charges.

2.1.2 Dispersion relation

For the following derivations some additional assumptions are necessary. The investigated region is homogeneous, i.e. the relative permittivity, the relative magnetic permeability and the electrical conductivity do not show dependence on the position. With these assumptions equation (2.13) can be written as

$$\vec{\nabla} \cdot \left(\varepsilon_0 \varepsilon_r (\omega) \vec{E}(\vec{r}, \omega) \right) = \vec{\nabla} \cdot \vec{E}(\vec{r}, \omega) = 0 \tag{2.16}$$

By applying a rotation on equation (2.12) and obeying the mathematical rule of

$$\vec{\nabla} \times \vec{\nabla} \times \vec{A}(\vec{r}, \omega) = \vec{\nabla} \left(\vec{\nabla} \cdot \vec{A}(\vec{r}, \omega) \right) - \vec{\nabla} \cdot \left(\vec{\nabla} \vec{A}(\vec{r}, \omega) \right)$$

equation (2.16) can be used resulting in:

$$\vec{\nabla} \cdot \vec{\nabla} \vec{E}(\vec{r}, \omega) = i\omega \vec{\nabla} \times \vec{B}(\vec{r}, \omega) \tag{2.17}$$

Using the Fourier transformed Maxwell equation (2.11) the dispersion relation can be derived by:

$$\vec{\nabla} \cdot \vec{\nabla} \vec{E}(\vec{r}, \omega) = -\omega^2 \mu_0 \mu_r (\omega) \varepsilon_0 \left(\varepsilon_r (\omega) - i \frac{\sigma(\omega)}{\varepsilon_0 \omega} \right) \vec{E}(\vec{r}, \omega) \tag{2.18}$$

Generally all three parameters, i.e. relative magnetic permeability, relative permittivity and electrical conductivity, are complex parameters. Considering georadar measurements, a few constrictions can be assumed. In most soils the relative magnetic permeability is equal to the value of one (Schön, 1996) and will hereby be neglected in the following details. In the

frequency range of typical georadar applications of 10 MHz to few GHz the imaginary part of the electrical conductivity can be neglected (Du, 1995). Therefore, the expression inside the bracket in equation (2.18) is often merged into one parameter, called the effective relative permittivity $\varepsilon_{eff}(\omega)$, or

$$\varepsilon_{eff}(\omega) = \varepsilon'_{eff}(\omega) - i\varepsilon''_{eff}(\omega) = \varepsilon'_r(\omega) - i\left(\varepsilon''_r(\omega) + \frac{\sigma'(\omega)}{\varepsilon_0 \omega}\right) \tag{2.19}$$

with ε'_{eff} and ε''_{eff} the real and imaginary part of the effective relative permittivity.

Equation (2.18) can be solved by assuming a plane wave.

$$\vec{\nabla} \cdot \vec{\nabla} \vec{E}_0 \, e^{i\left(\vec{k}\cdot\vec{r} - \omega t\right)} = -\omega^2 \mu_0 \mu_r(\omega) \varepsilon_0 \left(\varepsilon_r(\omega) - i\frac{\sigma(\omega)}{\varepsilon_0 \omega}\right) \vec{E}_0 \, e^{i\left(\vec{k}\cdot\vec{r} - \omega t\right)} \tag{2.20}$$

with $\vec{k}$ the wave vector. This differential equation can be solved using

$$k^2(\omega) = \omega^2 \mu_0 \varepsilon_0 \varepsilon_{eff}(\omega) \tag{2.21}$$

k can be a complex parameter depending on the effective relative permittivity. By dividing the complex wave number *k* into its real part β and imaginary part α, and solving equation (2.20) for a plane wave, the following relationships can be derived:

$$\beta = \sqrt{\frac{\omega^2 \mu_0 \varepsilon_0 \varepsilon'_{eff}(\omega)}{2}\left(\sqrt{1 + \tan^2(\delta)} + 1\right)} \tag{2.22}$$

$$\begin{aligned} \alpha &= \sqrt{\frac{\omega^2 \mu_0 \varepsilon_0 \varepsilon'_{eff}(\omega)}{2}\left(\sqrt{1 + \tan^2(\delta)} - 1\right)} \\ \tan\delta &= \tan\left(\frac{\varepsilon''_{eff}(\omega)}{\varepsilon'_{eff}(\omega)}\right) \end{aligned} \tag{2.23}$$

The expression tan δ is often referred to as the loss tangent (e.g. Greaves et al., 1996) and can be interpreted as the ratio between the conduction current density to the displacement current density. Equation (2.22) defines the phase constant of the EM wave and (2.23) is the attenuation constant of the EM wave. The phase velocity *v* for the general case can be determined by:

$$\begin{aligned} v(\omega) &= \frac{\omega}{\beta} = \frac{c_0}{\sqrt{\frac{\varepsilon'_{eff}(\omega)}{2}\left(\sqrt{1 + \tan^2(\delta)} + 1\right)}} \\ c_0 &= \frac{1}{\sqrt{\varepsilon_0 \mu_0}} \end{aligned} \tag{2.24}$$

with c_0 the speed of light in vacuum. Assuming a low loss medium with $\varepsilon''_{eff} << \varepsilon'_{eff}$, the phase velocity v of an EM wave can be simplified to

$$v(\omega) = \frac{c_0}{\sqrt{\varepsilon'_{eff}(\omega)}} \tag{2.25}$$

For most georadar applications equation (2.25) is sufficiently correct since media with significant loss tangents also feature inferior data quality caused by the higher attenuation (eq. (2.23)). For media with insignificant dispersion, i.e. $\varepsilon_{eff}(\omega) \approx \varepsilon_{eff}(\omega + \delta\omega)$, the EM phase velocity v is equal to the EM propagation velocity v.

2.1.3 Transmission, reflection and diffraction of EM waves

In 2.1.2 the various phenomena of EM wave propagation through a homogeneous medium, i.e. attenuation and propagation velocity, were described. For typical georadar applications on the surface such conditions are not present. Assuming a plane EM wave approaching an interface from medium A with a relative permittivity $\varepsilon_{eff\_A}(\omega) = \varepsilon'_{eff\_A}(\omega)$ to medium B with a relative permittivity $\varepsilon_{eff\_B}(\omega) = \varepsilon'_{eff\_B}(\omega) - i\,\varepsilon''_{eff\_B}(\omega)$ and $\tan(\delta) << 1$ (Fließbach, 1997), the following two equations can be determined (Figure 2.1).

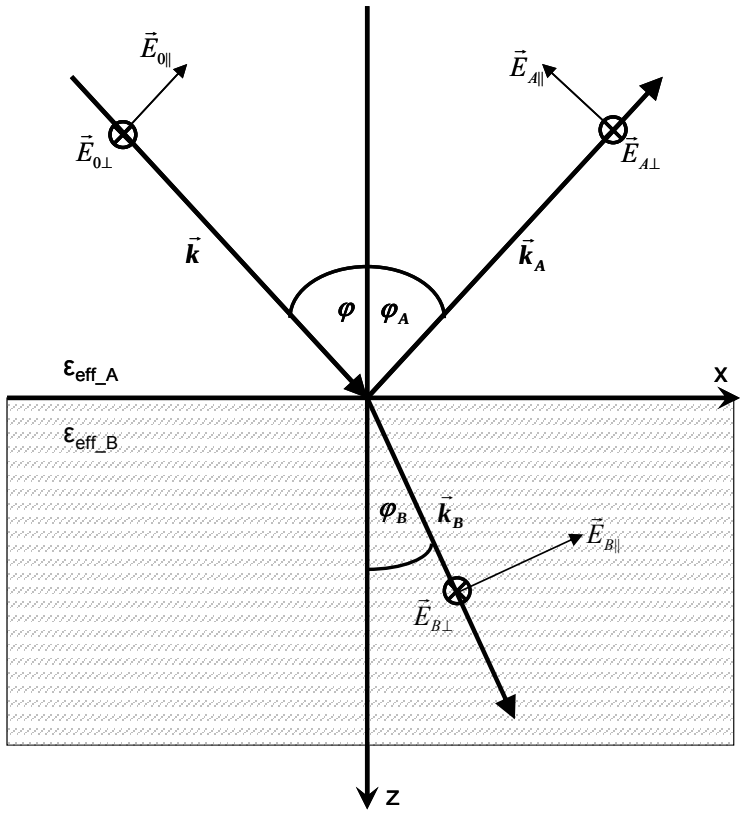

Figure 2.1: Reflection and transmission of a plane wave at an interface.

$$\begin{aligned}\vec{E}(\vec{r},\omega) &= \vec{E}_0\, e^{i\left(\vec{k}\cdot\vec{r}-\omega t\right)} \\ \vec{B}(\vec{r},\omega) &= \frac{1}{\omega}\vec{k}\times\vec{E}(\vec{r},\omega) \\ \text{with } \vec{k} &= \vec{e}\,\frac{\omega\sqrt{\varepsilon_{eff}(\omega)}}{c_0}\end{aligned} \tag{2.26}$$

Considering a Cartesian coordinate system with $\vec{e}_i$ the unit vector in direction *i*, some continuity constraints for the interface boundary can be deduced from the Maxwell equations.

$$\begin{aligned}\vec{e}_z\cdot\vec{D}_A(\vec{r},\omega) &= \vec{e}_z\cdot\vec{D}_B(\vec{r},\omega) \\ \vec{e}_z\cdot\vec{B}_A(\vec{r},\omega) &= \vec{e}_z\cdot\vec{B}_B(\vec{r},\omega) \\ \vec{e}_z\times\vec{E}_A(\vec{r},\omega) &= \vec{e}_z\times\vec{E}_B(\vec{r},\omega) \\ \vec{e}_z\times\vec{H}_A(\vec{r},\omega) &= \vec{e}_z\times\vec{H}_B(\vec{r},\omega)\end{aligned} \tag{2.27}$$

The resulting reflected and transmitted components have to meet specific requirements to ensure these constraints. With the interface at $z = 0$ and rotating the coordinate system until the modulus of the y-component of the incident EM wave is zero (Fließbach, 1997),

$$\begin{aligned}\left|\vec{k}_y\right| &= \left|\vec{k}_{y\_A}\right| = \left|\vec{k}_{y\_B}\right| = 0 \\ \left|\vec{k}_x\right| &= \left|\vec{k}_{x\_A}\right| = \left|\vec{k}_{x\_B}\right|\end{aligned} \tag{2.28}$$

and defining an angle φ with

$$\left|\vec{k}_x\right| = \left|\vec{k}\right|\sin\varphi(\omega) \tag{2.29}$$

the following relationships can be deduced (Figure 2.1).

$$\begin{aligned}\left|\vec{k}\right|\sin\varphi &= \left|\vec{k}_A\right|\sin\varphi_A \Rightarrow \varphi = \varphi_A \\ \left|\vec{k}\right|\sin\varphi &= \left|\vec{k}_B\right|\sin\varphi_B(\omega) \Rightarrow \frac{\sin\varphi}{\sin\varphi_B(\omega)} = \frac{\sqrt{\varepsilon_{eff\_B}(\omega)}}{\sqrt{\varepsilon_{eff}(\omega)}}\end{aligned} \tag{2.30}$$

Equation (2.30) is better known as Snell's law. If the relative permittivity is of complex value, the resulting angles are also complex. To describe the whole behavior of EM waves at an interface the vector $\vec{E}_0$ has to be divided in a component parallel and one perpendicular to the plane of incident (Figure 2.1) (Nolting, 1993).

$$\begin{aligned}\frac{\vec{E}_{B\perp}(\omega)}{\vec{E}_{0\perp}(\omega)} &= \frac{2\varepsilon_A^2\cos(\varphi)}{\varepsilon_A^2\cos(\varphi)+\varepsilon_B^2(\omega)\cos(\varphi_B(\omega))} = \frac{\sin(\varphi_B(\omega)-\varphi)}{\sin(\varphi_B(\omega)+\varphi)} \\ \frac{\vec{E}_{A\perp}(\omega)}{\vec{E}_{0\perp}(\omega)} &= \frac{\varepsilon_A^2\cos(\varphi)-\varepsilon_B^2(\omega)\cos(\varphi_B(\omega))}{\varepsilon_A^2\cos(\varphi)+\varepsilon_B^2(\omega)\cos(\varphi_B(\omega))} = \frac{2\sin(\varphi_B(\omega))\cos(\varphi)}{\sin(\varphi+\varphi_B(\omega))}\end{aligned} \tag{2.31}$$

$$\begin{aligned}\frac{\vec{E}_{B\|}(\omega)}{\vec{E}_{0\|}(\omega)} &= \frac{2\varepsilon_A^2\cos(\varphi)}{\varepsilon_A^2\cos(\varphi_B(\omega))+\varepsilon_B^2(\omega)\cos(\varphi_A)} = \frac{\sin(2\varphi)-\sin(2\varphi_B(\omega))}{\sin(2\varphi)+\sin(2\varphi_B(\omega))} \\ \frac{\vec{E}_{A\|}(\omega)}{\vec{E}_{0\|}(\omega)} &= \frac{\varepsilon_B^2(\omega)\cos(\varphi_A)-\varepsilon_A^2\cos(\varphi_B(\omega))}{\varepsilon_A^2\cos(\varphi_B(\omega))+\varepsilon_B^2(\omega)\cos(\varphi_A)} = \frac{2\sin(\varphi_B(\omega))\cos(\varphi)}{\sin(\varphi+\varphi_B(\omega))\cos(\varphi-\varphi_B(\omega))}\end{aligned} \tag{2.32}$$

Equations (2.31) and (2.32) are also known as the Fresnel equations and describe the behavior of a plane EM wave when reaching an interface under a specific angle of incident. A plane wave assumption is of course only assured for sufficient distance between EM source and interface. Generally the wave vector $\vec{k}$ is a variable of space. To investigate small shallow objects or interfaces the plane wave assumption can only be used for preliminary analysis. On the other hand, the equations (2.31) and (2.32) are necessary for the description of the reflected and transmitted absolute amplitudes of the EM wave. Since it will be necessary to clarify the difference between reflectors and diffractors, a definition will be formulated for the following chapters.

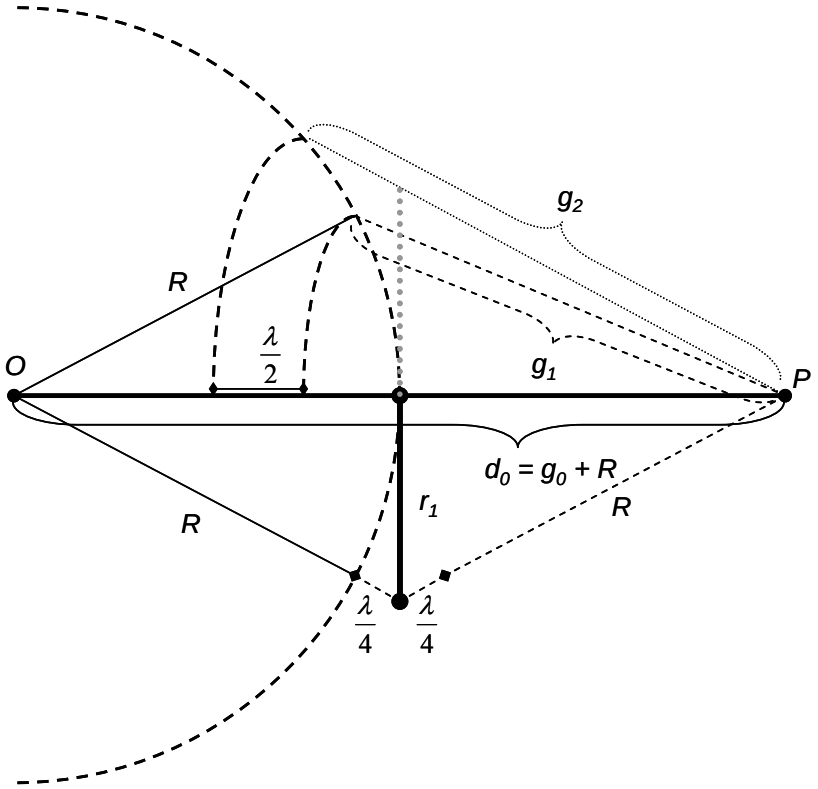

Figure 2.2: Schematic deduction of the Fresnel zone for the transmission case, i.e. wave propagation from *O* to *P*, and the reflection case, i.e. point *O* resembles transmission and receiving point.

Christiaan Hyugens formulated a principle in 1690 AD which states that each point of an EM wave front is the origin of a new EM source. Using this principle, a differentiation between two phenomena will be formulated to classify recorded events in the radar sections. Generally a reflection occurs when the object causing the reflection is at least of the order of the first Fresnel region. Assuming a spherical EM wave in a homogeneous space, the amplitude and the phase are constant for a spherical plane with distance *R* to the origin *O* (Figure 2.2).

$$\left|\vec{E}(R,\omega)\right| = \frac{\left|\vec{E}_0(O,\omega)\right|}{R} e^{i(kR-\omega t)} \tag{2.33}$$

By analyzing sectors of this spherical plane from a point P with distance d_0 greater R from O, one can find circular sectors on the spherical plane with the following ray paths d_n:

$$d_n = g_n + R = d_{n-1} + \frac{\lambda(\omega)}{2} = d_{n-1} + \frac{c_0 \pi}{\omega\sqrt{\varepsilon_{eff}(\omega)}} \tag{2.34}$$

with λ the wavelength of the EM wave and g the distance from P to the spherical wave plane (Figure 2.2). Using equation (2.34) the resulting electrical field in P can be derived by (Demtröder, 1995):

$$\begin{aligned} E(P,\omega) &= \sum_{m=1}^{N} E_m(P,\omega) = \left|E_1(P,\omega)\right| - \left|E_2(P,\omega)\right| + \left|E_3(P,\omega)\right| - \ldots \pm \left|E_N(P,\omega)\right| \approx \\ &\approx \frac{1}{2}\left(\left|E_1(P,\omega)\right| + \left|E_N(P,\omega)\right|\right) \end{aligned} \tag{2.35}$$

Since the contribution of the N-th element can be neglected, the electrical field in P can be written as follows.

$$E(P,\omega) = \frac{E_0(O,\omega)}{d_0} e^{-i(kd-\omega t)} \tag{2.36}$$

Using those relationships, the radius of the first Fresnel region can be derived to

$$r_1(\omega) = \sqrt{\left(d_0 - R + \frac{c_0 \pi}{2\omega\sqrt{\varepsilon_{eff}(\omega)}}\right)^2 - (d-R)^2} \tag{2.37}$$

or being more specific

$$\begin{aligned} F_{ref}(d_0 = 2R,\omega) &= \pi r_1^2(\omega) = \frac{c_0 \pi^2}{\omega\sqrt{\varepsilon_{eff}(\omega)}}\left(R + \frac{c_0 \pi}{4\omega\sqrt{\varepsilon_{eff}(\omega)}}\right) \\ &\text{or} \\ F_{ref}(d = 2R,\upsilon) &= \frac{c_0 \pi}{2\upsilon\sqrt{\varepsilon_{eff}(\upsilon)}}\left(R + \frac{c_0}{8\upsilon\sqrt{\varepsilon_{eff}(\upsilon)}}\right) \end{aligned} \tag{2.38}$$

F_{ref} in equation (2.37) can be interpreted as the minimum spherical plane required to be considered as a reflector for a monostatic georadar measurement. Assuming a relative permittivity of 9 and a distance of 0.5 m for a frequency of 800 MHz, the required plane to be considered a reflector can be derived from $F_{ref}(0.5\,\mathrm{m}, 800\,\mathrm{MHz}) \approx 0.1021\,\mathrm{m}^2$ or a circular

plane with a diameter of approximately 0.180 m. When confronted with layered stratigraphy, such spacious layering requirements are easily fulfilled. For shallow investigations such distinct and spacious reflectors are scarce. On the other hand a lot of events can be registered in common radar sections which are not originated by objects large enough to be considered reflectors by equation (2.38). Because of the Huygens principle such objects can still be an origin of an EM wave recorded by georadar. Such objects will be referred to as diffractors from now on.

2.2 Effect of water in soils

Water stands out from other soil constituents by its particular electrical behaviour in the frequency range of georadar. Compared to the relative permittivity of soil minerals, between approx. 4 to 10 (e.g. Schön, 1996), the relative permittivity of water is in the range of ten times larger, approx. 80. This high relative permittivity is caused by the dipole character of the water molecule and its tendency to build clusters (von Hippel, 1988). The electron and atom polarisation effects only contribute small shares to this high relative permittivity (Kupfer, 1997).

2.2.1 Electrical behaviour of water

The relative permittivity of water features a significant dependency on temperature and frequency. Water can be found in many states in the soil different from bulk (free) water.

- It can be chemically combined water in the mineral structure of the soil minerals, e.g. ettringit. Due to the inclusion in the soil mineral, such water fractions are typically not investigated for volumetric water content measurements.
- Water can be physically-chemically bound at the surface of the minerals. This physically-chemically bound water, or adsorption water, can be several molecular layers thick and features a relative permittivity lower than that of bulk water (Or and Wraith, 1999). Depending on the publication this relative permittivity is in the range of 3 – 50 and estimated to be approximately three molecular layers thick.
- The next layers of water following the adsorption water are the adhesion water. Adhesion water is bound due to molecular forces and withstands the gravitational force. Although not considered free water, adhesion water is available for plants and the relative permittivity of adhesion water is comparable to free water.
- The water in cells or capillaries can be considered of the same relative permittivity as free water.

Considering a natural soil with low clay contents, the main fraction of occurring water molecules can be accredited to being free water or of relative permittivity properties of free water. Therefore the volumetric fractions of adhesion water, cell water, capillary water and free water are combined and will be referred to as bulk water from now on. Although the adsorption water content can be determined by different water content analysis methods, e.g. thermo-gravimetric analysis, the adsorption water content is of less interest for most of the investigated problems, e.g. agricultural. The focus on the following investigations of the volumetric water content will be placed on the determination of the bulk water content Θ. Therefore, when speaking of water and its effects, only bulk water is discussed.

The electrical behaviour of bulk water in the frequency of georadar can be described by a modified Debye equation (Hübner, 1999).

$$\varepsilon_{eff\_w}(\omega,T)=\varepsilon_{w\infty}(T)+\frac{\varepsilon_{w0}(T)-\varepsilon_{w\infty}(T)}{1+i\omega\tau_w(T)}-i\frac{\sigma(T)}{\varepsilon_0\omega} \tag{2.39}$$

with $\varepsilon_{w\infty}$ the relative permittivity of water for infinite frequency, ε_{w0} the relative permittivity of water for the static case, τ_w the relaxation time of the water molecule and T the temperature. The relaxation time τ_w is the time a displaced water molecule takes to get back into 1/e of its adjusted value (Kupfer, 1997). τ_w can be understood as a measure of the mobility of the water molecule. For pure water with no electrical conductivity the temperature-dependent parameter can be derived by the following equations according to Kaatze (1989).

$$\begin{aligned} \varepsilon_{w0}(T) &= 10^{\left(1.94404-1.991\cdot10^{-3}\zeta\right)} \\ \varepsilon_{w\infty}(T) &= 5.77-2.74\cdot10^{-2}\zeta \\ \tau_w(T) &= 3.745\cdot10^{-15}\left(1+7\cdot10^{-5}(\zeta-27.5)^2\right)e^{\left(\frac{2295.7}{\zeta+273.15}\right)} \\ \zeta &= \frac{T}{1°C} \end{aligned} \tag{2.40}$$

with ζ the normalized temperature to establish a dimensionless quantity. The relaxation time τ_w can be transformed into the relaxation frequency υ_w by the following equation.

$$\upsilon_w(T) = \frac{1}{2\pi\tau_w(T)} \tag{2.41}$$

Looking at equation (2.39) one can see that for no electrical conductivity the imaginary part of the relative permittivity has a maximum for the same frequency as the relaxation frequency. Combining equation (2.41) and the third relationship in (2.40), a temperature-dependent relaxation frequency of pure water can be derived. (Figure 2.3) For 5 °C a relaxation frequency of approximately 10.7 GHz is registered, whereas a temperature of 20 °C results in a relaxation frequency of 16.8 GHz. This effect can also be seen when deriving the complex relative permittivity for those two temperatures (Figure 2.4). For lower temperatures the imaginary part is gaining more significance for lower frequencies. For 5 °C and a frequency of 1 GHz the imaginary part of the relative permittivity is approximately 10 percent of the real part.

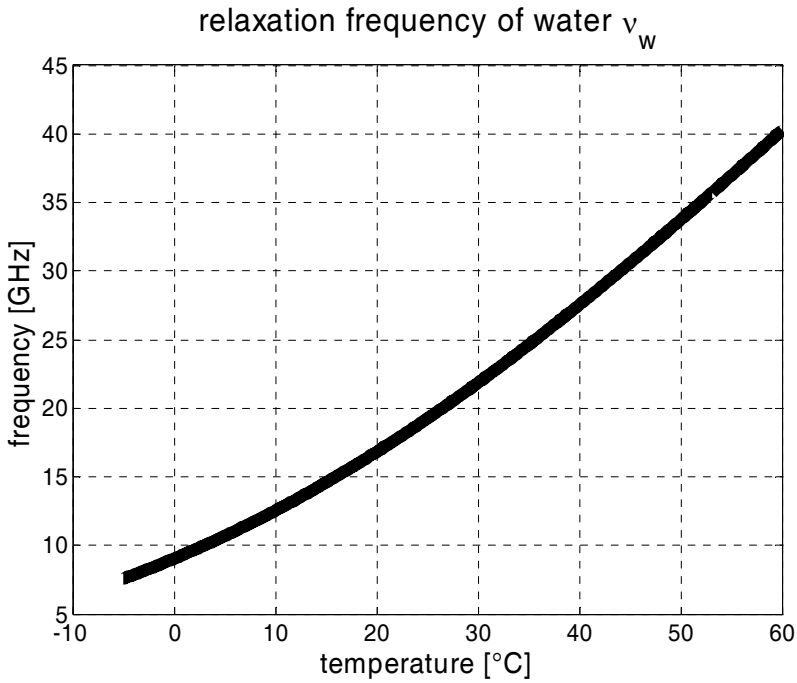

Figure 2.3: Temperature-dependent relaxation frequency of the water molecule.

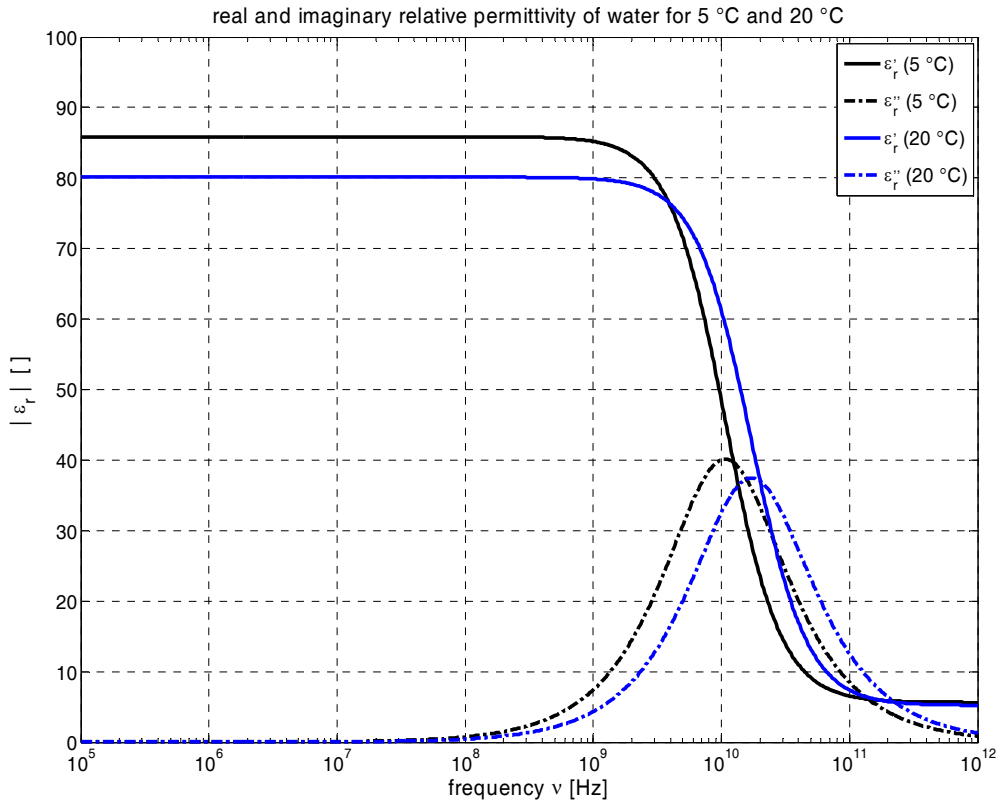

Figure 2.4: Temperature effect on the real (solid line) and imaginary (dash-dotted line) part of the relative permittivity of pure water.

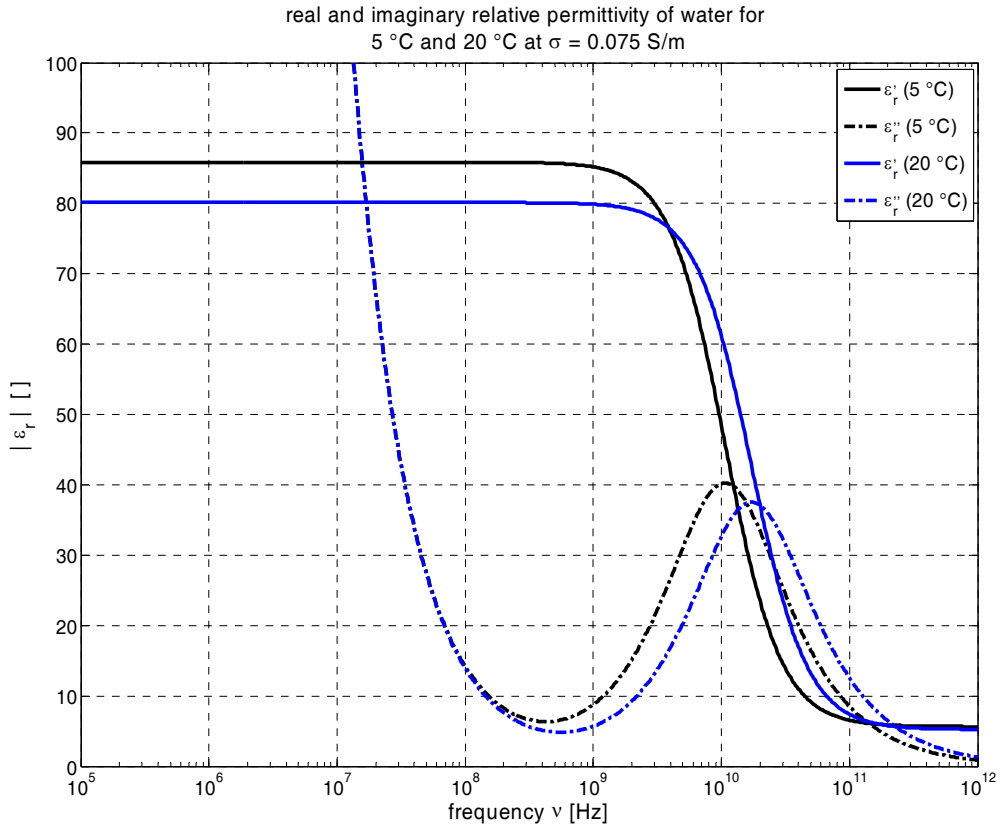

Figure 2.5: Temperature effect on the real (solid line) and imaginary (dash-dotted line) part of the relative permittivity of electrical conducting water.

Including an electrical conductivity unequal zero in equation (2.39), only the imaginary part of the relative permittivity is affected (Figure 2.5). By assuming an electrical conductivity of 0.075 S/m, which corresponds to the electrical conductivity of tap water in the Berlin area, a significant change in the imaginary part can be registered. Depending on the temperature, a local minimum of the imaginary part of the relative permittivity can be spotted in the range of 0.3 to 0.7 GHz (Figure 2.5).

2.2.2 Effect of water on EM wave propagation

The georadar records time series of the EM wave field at the location of the receiver. To deduce the relative permittivity and the electrical conductivity, the measured signal amplitudes and arrival times have to be analyzed. According to the dispersion relation (2.18) and its solution (2.23) and (2.24) equation (2.39) has to be transformed. The conjugated complex solution of (2.39) is written as

$$\begin{aligned}\varepsilon'_{eff\_w}(\omega,T) &= \varepsilon_{w\infty}(T)+\frac{\varepsilon_{w0}(T)-\varepsilon_{w\infty}(T)}{1+\omega^2\tau_w^2(T)} = \varepsilon'_w(\omega,T)\\ \varepsilon''_{eff\_w}(\omega,T) &= \omega\tau_w(T)\frac{\varepsilon_{w0}(T)-\varepsilon_{w\infty}(T)}{1+\omega^2\tau_w^2(T)}+\frac{\sigma(T)}{\varepsilon_0\omega} = \varepsilon''_w(\omega,T)+\frac{\sigma(T)}{\varepsilon_0\omega}\end{aligned} \tag{2.42}$$

With the two equations in (2.42) the attenuation constant in (2.23) and the EM propagation velocity (2.24) can be derived. On the other hand, the real and imaginary part of the medium's relative permittivity can be derived with the knowledge of the initial amplitude as well as the

propagation time and distance. For a plain wave and the propagation distance d the EM wave is given by

$$\vec{E}(r=d,t)=E_0\,e^{-\alpha d}\,e^{i(\beta d-\omega t)} \tag{2.43}$$

With the aforementioned known quantities and equation (2.23) the imaginary part of the effective relative permittivity can be written as

$$\begin{aligned}\varepsilon''_{eff\_w}(\omega,T)&=\varepsilon'_{eff\_w}(\omega,T)\arctan\sqrt{\left(1+\left(\frac{\alpha\,c_0}{\omega}\sqrt{\frac{2}{\varepsilon'_{eff}(\omega,T)}}\right)^2\right)^2-1}\;=\\&=\varepsilon''_{w}(\omega,T)+\frac{\sigma(T)}{\varepsilon_0\omega}\end{aligned} \tag{2.44}$$

Using equation (2.42) and the parameters of (2.40) the electrical conductivity can be derived.

$$\sigma(T)=\left[\left(\varepsilon'_{eff\_w}(\omega,T)\arctan\sqrt{\left(1+\left(\frac{\alpha\,c_0}{\omega}\sqrt{\frac{2}{\varepsilon'_{eff}(\omega,T)}}\right)^2\right)^2-1}\right)-\varepsilon''_{w}(\omega,T)\right]\varepsilon_0\omega \tag{2.45}$$

The coefficient of attenuation α can be determined experimentally. This can be achieved with various techniques.

- The most obvious, but also the least likely to perform, is by knowledge of the two electrical fields $\vec{E}(r=d,t)$ and E_0. The initial electric field intensity is difficult to determine since it is strongly dependent on a variety of parameters, e.g. antenna design, relative permittivity of the medium in the nearest vicinity of the antenna, antenna orientation, or angle of radiation (Radzevicius et al., 2003, van der Kruk, 2004, Lampe et al., 2003).
- A more realistic method is measuring a reference $\vec{E}(r,t)$ with a known relative permittivity of the reference medium
- or with the same unknown relative permittivity but a different propagation distance.

In both cases, the coefficient of attenuation can be determined by comparing the two registered electrical fields. Looking at the difference between the resulting relative permittivities (Figure 2.5) it is obvious that the effect of the electrical conductivity is the dominating constituent for frequencies below approximately 500 MHz. Examining high frequency georadar measurements of antenna frequencies above 500 MHz, the complex relative permittivity of the water's Debye relaxation has to be considered.

2.2.3 Mixing models

Although water is the dominant relative permittivity constituent of soils, other frequency- or temperature-dependent effects can additionally occur. Most soil minerals show no significant variation in the georadar frequency under natural conditions (Schön, 1996), but clay minerals can possess a high electrical conductivity or even relaxation frequencies in the georadar range (Oswald et al., 2006). This high electrical conductivity is even stronger related to the adsorption water (Schön, 1996). Since such additional relaxation events are difficult to distinguish by common impulse georadar measurements, those effects are solely accredited as

electrical conductivities. In the following soils will be described as a three-phase constituent. The single phases are water, air and structural soil constituents. Investigating natural soils the structural soil constituents can be divided into mineral constituents, biological constituents without free cell water and adhesion water. Including adsorption water in the class of structural soil constituents may be problematic, but since its relative permittivity is more in the range of soil minerals than of free water (Or and Wraith, 1999) it will appear as part of the structural soil constituents in most georadar measurements.

Mixing models are used to obtain the volumetric water content from the measured relative permittivities. Here, a relationship between the measured relative permittivity of a medium to its volumetric water content is deduced by various ways. Such a relationship can be determined by calibration measurements (e.g. Topp et al., 1980, Wensink, 1993), empirical considerations (e.g. Topp et al., 1980 Wensink, 1993), semi-physical considerations (Shen et al., 1985, Roth et al., 1990) or physical models (e.g. Shen et al., 1985, Sihvola and Alanen, 1991). In the following discussion of different mixing models all relative permittivities are frequency dependent also not explicitly denoted.

Calibration measurements

The easiest and most often the best option to obtain a valid relationship between the volumetric water content and the relative permittivity of a soil is a calibration measurement. Here, several data pairs of volumetric water content Θ to relative permittivity of soil ε_s are acquired and a fitting relationship $\Theta(\varepsilon_s)$ is derived. This ensures the correct consideration of the specific properties of the investigated soil. Every soil is different with varying mineral constituents, soil organic matter content, corn fraction size distribution, porosities or electrical conductivities, to name a few. First a soil sample is extracted from the investigation site. Then several volumetric water contents are realized by gradually saturating or drying the sample. The resulting relative permittivity is measured with an applicable device. Such are e.g. sample holders controlled by frequency domain network analyzers (e.g. Hübner, 1999, Wensink, 1993, Oswald et al., 2006), sample holders controlled by time domain cable testers (e.g. Topp et al., 1980, Or and Wraith, 1999) or utilizing TDR probes (e.g. Roth et al., 1990, Robinson and Friedman, 2003).

When conducting calibration measurements the resulting $\Theta(\varepsilon_s)$ relationship is the best alternative. Since the used sample is representative for the investigation site, all site-specific properties are considered. On the other hand calibration measurements are the most time consuming and labor intensive. Dealing with measurements on sites with strongly heterogeneous soils, numerous samples have to be used to obtain a representative dataset (e.g. Mosey and Knight, 2004). Those site-specific calibration functions would have to be considered individually for the extraction location and would require an areal interpretation for georadar measurements.

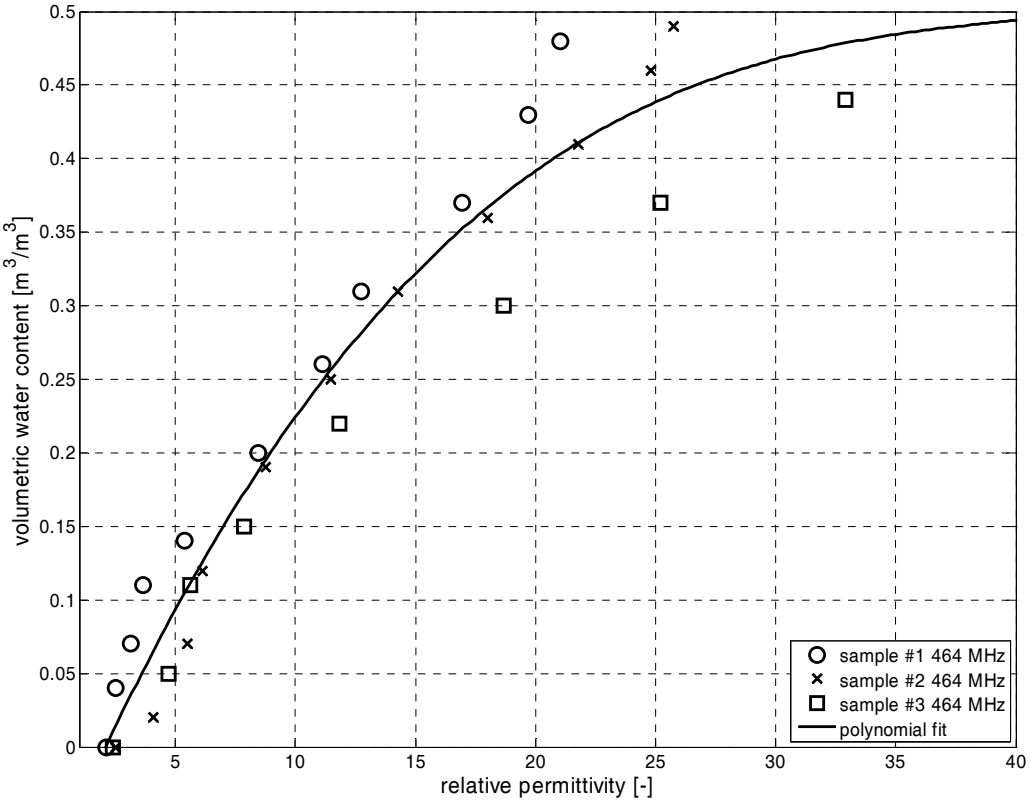

Figure 2.6: Measured relative permittivities and determined relationship using a polynomial of the third order.

By acquiring a site specific calibration function additional general parameters are not considered. Those may be e.g. temperature effects or soil densities, which can vary strongly from the situation on-site due to sample extraction or preparation. Depending on the used device for the calibration measurements other problems may occur such as inhomogeneous volumetric water content distribution over the whole sample for all realized volumetric water contents. Therefore it is advisable to perform several measurements to ensure statistical significance. Looking at Figure 2.6 one can see that the three datasets acquired from the same soil sample differ quite strongly. The shown data were generated from samples extracted at the INTERURBAN site Buch (Müller et al., 2003, Täumer et al., 2006), northwest of Berlin, Germany. The relationship between the relative permittivity and the volumetric water content was determined by the device described in Fechner et al. (2004) and Pelster (1995). The samples were inserted into the sample holder manually and cannot be considered undisturbed. The sample holder had a cylindrical shape with a diameter of 12 mm and a height of 2.05 mm. Such dimensions can hardly be described representative for relative permittivity determination of soils, but are here to be considered as exemplary data. The temperature was held constant (22 °C) over the course of the measurements. In this case a polynomial of the third order can be fitted with a coefficient of correlation of $R^2 = 0.95$.

$$\Theta(\varepsilon_s) = -0.0760 + 0.0381\varepsilon_s - 8.74 \cdot 10^{-4}\varepsilon_s^2 + 6.95 \cdot 10^{-6}\varepsilon_s^3 \qquad (2.46)$$

Depending on the dataset, other fits may be better suited such as polynomials of higher or lower degree (e.g. Wensink, 1993).

Empirical model

A general problem of the calibration measurement is the site-specific nature of the $\Theta(\varepsilon_s)$ relationship. It is quite difficult to apply this relationship to another site with a different soil. Therefore new calibration measurements would be required to obtain a valid mixing model. One way to avoid such a labor-intensive and time-consuming routine is the deduction of a general calibration model. For example Topp et al. (1980) used a set of 18 different $\Theta(\varepsilon_s)$ relationships ranging from glass beads to organic soils with different electrical conductivities of the water. They noticed the similarity of the derived calibration functions for their mineral soils and used those datasets to derive a universal $\Theta(\varepsilon_s)$ function often known as "Topp's equation".

$$\Theta(\varepsilon_s) = -0.053 + 0.0292\varepsilon_s - 5.5 \cdot 10^{-4}\varepsilon_s^2 + 4.3 \cdot 10^{-6}\varepsilon_s^3 \qquad (2.47)$$

Although equation (2.47) has still wide acceptance in the TDR and georadar community until today (e.g. Turesson, 2006) it should be used as a first estimate rather than a final mixing model. Since additional polynomial fits are included for the 18 different cases, the best matching polynomial in terms of mineral composition should be used for interpretation. Misinterpretations of several percent in volumetric water content can be registered depending on the soil's properties (Topp et al., 1980). The deduced equation (2.47) does not consider temperature variations or frequency dependences. The frequency dependence was not investigated because of the used device and the temperature effect was deemed irrelevant due to the higher experimental errors.

Another example of empirical models is given by Wensink (1993). Here a set of different soils including clay, peat and silt were investigated on their properties. The frequency dependence was regarded. Concluding the investigation, a set of empirical mixing models for 1000 MHz, 50 MHz and 5 MHz is given. Since most georadar applications are in the frequency range covered by the two relationships for 1000 MHz and 50 MHz in equation (2.48), the relationship for 5 MHz will not be considered for further discussion.

$$\begin{aligned} \Theta_{1000\_MHz}(\varepsilon_s) &= -0.0625 + 0.0225\varepsilon_s - 8 \cdot 10^{-5}\varepsilon_s^2 \\ \Theta_{50\_MHz}(\varepsilon_s) &= -0.0075 + 0.0102\varepsilon_s + 6 \cdot 10^{-5}\varepsilon_s^2 \end{aligned} \qquad (2.48)$$

The two functions given in equation (2.48) were deduced from the investigated soils for the two frequencies, similar to equation (2.47). A temperature effect was not investigated, but significant frequency dependence is registered. The relationship for 50 MHz will be left out in further consideration, since spatially high resolving measurements are investigated.

Using determined relative permittivity data for different volumetric water contents collected on two sites with sandy soils (see Müller et al., 2003, Täumer et al., 2006, Huraß and Schaumann, 2006), a similar empirical model can be derived exemplarily. In the presented case 10 datasets of four different samples were combined to derive the empirical model. The data was generated with the device described in Fechner et al. (2004) and Pelster (1995).

$$\Theta_{464\_MHz}(\varepsilon_s) = -0.0588 + 0.0359\varepsilon_s - 8.37 \cdot 10^{-4}\varepsilon_s^2 + 6.72 \cdot 10^{-6}\varepsilon_s^3 \qquad (2.49)$$

The correlation for equation (2.49) with $R^2 = 0.93$ is satisfactory considering the different soils.

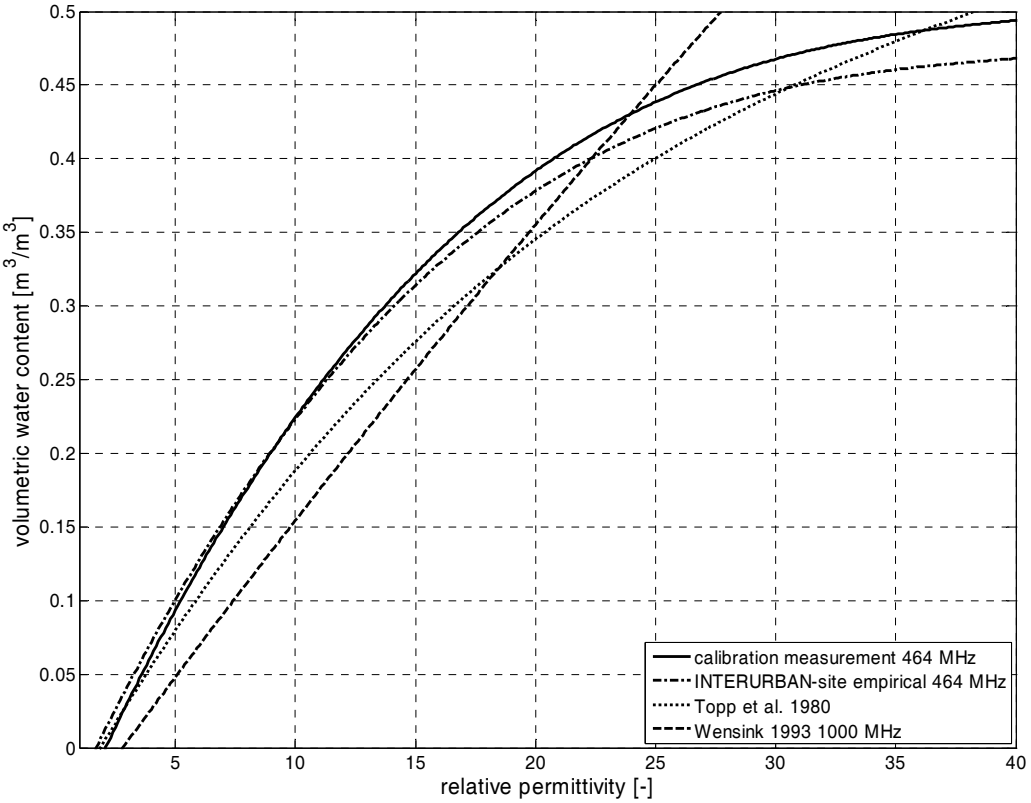

Figure 2.7: Comparison of the empirical mixing models of the equations (2.47) (dotted), (2.48) (dashed), (2.49) (dash dotted), and the calibration measurement (2.46) (solid).

Comparing all empirical models presented here, including equation (2.46), one can see quite different forms of the resulting functions (Figure 2.7). The two relations (2.46) and (2.49), introduced here, feature a steeper increase of the volumetric water content for lower relative permittivity values than (2.47) or the 1000 MHz function of (2.48). This can be explained by the comparably low silt and clay content of the investigated soil in the INTERURBAN project. Whereas the mineral soils in Topp et al. (1980) feature silt contents between 26 and 42 weight percent and clay contents between 9 and 66 weight contents, the INTERURBAN soils feature silt contents of only 5 to 10 weight percent and only 0 to 4 weight percent for the clay fraction (Huraß and Schaumann, 2006, Täumer et al., 2006). The volumetric water content Θ_{vtg} was determined by thermo-gravimetric measurements in the form:

$$\Theta_{vtg} = \rho_b \frac{m_w}{m_b} \tag{2.50}$$

with ρ_b the bulk density of the soil and m_w and m_b the mass of water and the dry mass of the soil. As described earlier the thermo-gravimetric water content includes the adsorption water, which features a lower relative permittivity (Or and Wraith, 1999). With higher clay and silt contents, the amount of water in the form of adsorption water is larger than for sandy soils. By increasing the volumetric water content, first adsorption water will be registered with lower relative permittivity and hence a lower resulting soil relative permittivity. This effect could be even interpreted for the two functions (2.46) and (2.49). Function (2.46) is deduced based on a dataset of a soil with approximately 94 % sand, 5 % silt and 0 % for the clay fraction. (2.49) additionally features soils with approximately 85 % sand, 11 % silt and 4 % clay. The higher relative permittivity of the function (2.48) given by Wensink (1993) can be

explained by the examined clays, which feature generally higher particle relative permittivities than sands or sandy loams (Robinson and Friedman, 2003). It requires mentioning that both (2.47) and (2.48) were derived from a larger data basis.

Although the interpreted volumetric water contents can vary relatively strongly from the chosen model, their shape is quite similar.

Table 2.1: Derived volumetric water contents from different empirical models.

model	$\varepsilon_s = 10$	$\varepsilon_s = 15$	$\Delta\Theta$
calibration measurement (2.46)	0.225 m^3/m^3	0.322m^3/m^3	0.097m^3/m^3
empirical INTERURBAN model (2.49)	0.223m^3/m^3	0.314m^3/m^3	0.091m^3/m^3
Topp et al., 1980 (2.47)	0.188m^3/m^3	0.276m^3/m^3	0.088m^3/m^3
Wensink, 1993 1000 MHz (2.48)	0.155m^3/m^3	0.257m^3/m^3	0.102m^3/m^3

In Table 2.1 the similarity between the empirical models is fairly obvious. The resulting volumetric water content variations of the INTERURBAN model and the Topp et al. (1980) model differ only by 0.003 m^3/m^3. Although the choice of the empirical mixing model has an influence on the interpreted absolute volumetric water content, relative changes are quite similar. Including the two other models for extreme cases, sandy soil and clayey soil, the maximum variation caused by the choice of the model is only 0.014 m^3/m^3.

Empirical models still do not take into account soil variations or other environmental variations, e.g. temperature. Since the relative permittivity of the soil minerals (e.g. Robinson and Friedman, 2003) as well as the temperature (see 2.2.1) have an effect on the relative permittivity of the soil, general empirical models cannot be used for accurate absolute volumetric water content determinations.

Structure-dependent model

Structure-dependent models (Sihvola and Alanen, 1991) take the geometrical form of the medium's constituents into account. A general example is given by Sihvola and Kong (1988). In this model a background constituent with relative permittivity ε_1 is furnished with spherical inclusions of relative permittivity ε_2. Those spherical inclusions occupy the volumetric fraction V_2 of the whole volume V.

$$\frac{\varepsilon_s - \varepsilon_1}{\varepsilon_s + 2\varepsilon_1 + \xi(\varepsilon_s - \varepsilon_1)} = (1 - V_2)\frac{\varepsilon_2 - \varepsilon_1}{\varepsilon_2 + 2\varepsilon_1 + \xi(\varepsilon_s - \varepsilon_1)} \qquad (2.51)$$
$$\xi = 0, 2, 3$$

ξ is a parameter to denote specific mixing models. For $\xi = 0$ the resulting model is better known as the Maxwell-Garnett mixing model. Assuming the background constituent as the partially saturated pore, a mixture of soil air water can be achieved by a combination of two interlaced equations of the sort of (2.51). Here the resulting relative permittivity of the pore medium, i.e. mixture of water and air is inserted as the relative permittivity of the inclusion ε_2.

Another example for a structure-dependent model is the Bruggeman-Hanai-Sen model (Shen et al., 1985).

$$V_2 = \left(\frac{\varepsilon_s - \varepsilon_1}{\varepsilon_1 - \varepsilon_2}\right)\left(\frac{\varepsilon_1}{\varepsilon_s}\right)^{l_1} \tag{2.52}$$

The exponent l_1 is controlled by the shape of the inclusions. For spherical inclusions the exponent l_1 has a value of 1/3. Reorganizing equation (2.52) leads to

$$\varepsilon_s = \varepsilon_1 V_2^{\left(\frac{1}{1-l_1}\right)}\left(\frac{1-\frac{\varepsilon_2}{\varepsilon_1}}{1-\frac{\varepsilon_2}{\varepsilon_s}}\right)^{\left(\frac{1}{1-l_1}\right)} \tag{2.53}$$

Replacing V_2 with the porosity Φ, ε_1 with the resulting relative permittivity of the pore space ε_{pore}, and ε_2 with the relative permittivity of the soil particles ε_m the following relationships can be deduced.

$$\begin{aligned}\varepsilon_s &= \varepsilon_{pore}\Phi^{\left(\frac{1}{1-l_1}\right)}\left(\frac{1-\frac{\varepsilon_m}{\varepsilon_{pore}}}{1-\frac{\varepsilon_m}{\varepsilon_s}}\right)^{\left(\frac{1}{1-l_1}\right)} \\ \varepsilon_{pore} &= \varepsilon_w\left(\frac{\Theta}{\Phi}\right)^{\left(\frac{1}{1-l_2}\right)}\left(\frac{1-\frac{\varepsilon_a}{\varepsilon_w}}{1-\frac{\varepsilon_a}{\varepsilon_{pore}}}\right)^{\left(\frac{1}{1-l_2}\right)}\end{aligned} \tag{2.54}$$

ε_a is the relative permittivity of air, while assuming a pore space solely filled with water and air. For oblate ellipsoidal inclusions the exponents l_1 and l_2 have the value 0.5 (Greaves et al., 1996). Johnson and Poeter (2005) used this model successfully to determine volumetric water contents in sands in laboratory measurements.

Another example for a structure-dependent mixing model is a modified DeLoor model (Hübner, 1999):

$$\begin{aligned}\varepsilon_s &= \varepsilon_m + \sum_{n=1}^{3}\frac{V_n}{3}(\varepsilon_n - \varepsilon_m)\sum_{p=1}^{3}\frac{1}{1 + A_p\frac{\varepsilon_n}{\varepsilon^*} - 1} \\ \sum_n V_n &= 1\end{aligned} \tag{2.55}$$

In the case of the DeLoor model, the summations are performed over three summands since the depolarization factor A regards the effect of adsorption water. To do so, however, an additional relative permittivity ε^* has to be included. ε^* can be interpreted as a resulting relative permittivity at the interface of the ellipsoidal inclusions. By assuming ellipsoidal

inclusions for equation (2.55) Hübner (1999) presents a mixing model to derive the soil's relative permittivity regarding the volume fractions of soil particles, air, adsorption water and bulk water. Ellipsoids are generally assumed for well-cemented sandstones (Greaves et al., 1996) which makes it questionable if this is justifiable for application on soils.

Generally structure-dependent mixing models explain the resulting relative permittivity of a mixture from a physical perspective. However, by doing so, many generalizations have to be made to get a reasonable function. Here mixtures are postulated with inclusions of defined geometrical shapes, i.e. spheres or ellipsoids. Assuming a natural soil such assumptions concerning the shape of the constituents are only hypothetical. The three structure-dependent models briefly addressed here each require information, which is difficult to acquire in the field and can change with the degree of saturation. E.g. equation (2.55) requires a resulting relative permittivity at the interface of the inclusions or equation (2.54) requires the shape of the air enclosed in the pore water. Although structure-dependent mixing models can be successfully applied on field data (e.g. Dannowski and Yaramanci, 1999) more often simple mixing models requiring less initial information are utilized (e.g. Greaves et al., 1996, Turesson, 2006).

Volume-dependent model

Volume-dependent models try to determine the resulting relative permittivity of a mixture on the basis of the respective volume fractions. The most general version of a volume-dependent model is of the form:

$$\varepsilon_s = \left(\sum_n V_n \varepsilon_n^k \right)^{\frac{1}{k}} \tag{2.56}$$

with V_n the volume fraction of the n-th constituent and k an exponent in the range between (-1) and 1 (Roth et al., 1990). For the extreme values of k a layered dielectric medium inside a capacitor with stratification perpendicular to the electric field vector (k = -1) or parallel (k = 1) can be associated. For k = 0.5 the mixture can be assumed to be a series of independent constituents traversed successively by an EM wave. The corresponding distances are then given by the respective volume fractions. This special case of equation (2.56) is also known as the complex refractive index model (CRIM) (Shen et al., 1985) or the Birchak formula (Roth et al., 1990, Hübner, 1999). Assuming a three-phase soil consisting of soil particles, air and water, the following mixing model can be deduced from equation (2.56).

$$\varepsilon_s^k = (1-\Phi)\varepsilon_m^k + \Theta\varepsilon_w^k + (\Phi-\Theta)\varepsilon_a^k \tag{2.57}$$

Variations of equation (2.57) have wide acceptance for the determination of volumetric water contents (e.g. Dannowski and Yaramanci, 1999, Greaves et al., 1996, Huisman et al., 2003, Loeffler and Bano, 2004). Schmalholz (2000) successfully applied equation (2.57) to determine the volumetric water content of wet sands and the resulting electrical conductivity by inverting the measured spectral complex relative permittivity of the soil with respect to the relative permittivity of water given in equation (2.39).

Another example for a volume-dependent model is given by Peplinski et al. (1995) regarding the complex relative permittivity of the soil. They used a dataset of 19 different soil samples ranging from soils with sand fractions of 15 to 50 weight percent, silt from 35 to 65 weight percent and clay from 5 to 20 weight percent. The deduced mixing model is valid for a frequency range between 300 to 1300 MHz.

$$\varepsilon_s' = \frac{\left(1+\frac{\rho_b}{\rho_m}\varepsilon_m^k + \Theta^{\beta'}\varepsilon_w'^k - \Theta\right)^{\frac{1}{k}} + 0.68}{1.15}$$
$$\varepsilon_s'' = \left(\Theta^{\beta''}\varepsilon_w''^k\right)^{\frac{1}{k}} \tag{2.58}$$

Here ρ_b is the bulk mass density of the soil, ρ_m is the mass density of the soil particles and the exponents β' and β'' are given by the following relationships.

$$\beta' = 1.2748 - 0.519sa - 0.152cl$$
$$\beta'' = 1.33797 - 0.603sa - 0.166cl \tag{2.59}$$

with *sa* the mass fraction of the sand constituent and *cl* the mass fraction of the clay constituent. Although more additional information is needed to utilize mixing model (2.58) than to use (2.57) those can be acquired relatively easily in the field.

Statistical models are another type of volume-dependent models. Here three-dimensional circuits of capacitors with respect to the soil constituents are generated and the resulting relative permittivity is derived. The number of the respective capacitors is in accordance with the volumetric distribution of the corresponding soil constituents. The resulting circuits are generated stochastically, and to ensure objectivity a large number of models is analyzed. Hübner (1999) derived several scenarios and found good correlation for both the structure-dependent equation (2.55) and the volume-dependent equation (2.57). Friedman (1997) used a similar method and derived a relationship between the soil porosity and volumetric water content for the resulting relative permittivity of the soil. In his model the relative permittivity of the soil particle was assumed to be 4.

$$\varepsilon_s(\Phi,\Theta) = a_0(\Phi) + a_1(\Phi)\Theta + a_2(\Phi)\Theta^2 + a_3(\Phi)\Theta^3 \tag{2.60}$$

The form of this equation is quite similar to the earlier discussed empirical functions. The factors a_0 through a_3 are porosity-dependent and given by the following relationships.

$$a_0(\Phi) = 2.35\Phi^{-0.398}$$
$$a_1(\Phi) = -49.54 + 509.7\Phi - 1241.5\Phi^2 + 839.7\Phi^3$$
$$a_2(\Phi) = 513 - 3708.9\Phi + 9129.8\Phi^2 - 6562\Phi^3$$
$$a_3(\Phi) = -487.5 + 5605\Phi - 14717\Phi^2 + 11115\Phi^3 \tag{2.61}$$

Friedman (1997) found a good correlation between equation (2.60) and the empirical function (2.47). By assuming a relative permittivity of 4 for the soil particles, equations (2.61) are only valid for specific soils and would require new determinations for different soils.

An advantage of the volume-dependent models compared to the other discussed models is the flexibility concerning soil variations. The models concede variations of porosities or soil particles in their formulation. On the other hand, parameters which are difficult to acquire like geometrical structure of inclusions or resulting relative permittivities at interfaces do not need to be determined. For a three-phase mixture, i.e. soil particles, air and water, only the relative permittivity of the soil particles and the porosity need to be determined to derive the volumetric water content from the measured relative permittivity of the soil.

The porosity can be determined by the following relationship.

$$\Phi = 1 - \frac{\rho_b}{\rho_m} \tag{2.62}$$

Here a sample of defined volume has to be extracted in the field, and the dry mass density of the soil as well as of the soil particles has to be determined. To determine the relative permittivity of the soil particles Hübner (1999) uses a relationship of the following form.

$$\varepsilon_s = \left(1.01 + 0.44 \frac{\rho_m}{1 \frac{g}{cm^3}} \right)^2 - 0.062 \tag{2.63}$$

Alternatively the relative permittivity of the soil particles can be determined with calibration measurements (e.g. Robinson and Friedman, 2003).

Volume-dependent models appear to be best suited to determine the volumetric water content and volumetric water content changes.

- The required input parameters are comparably easy to acquire by simple soil sampling and the structure of the models are flexible for inclusion of additional variables such as temperature dependence or frequency of the relative permittivity of water.
- The complex relative permittivity of the soil can be taken into account.

Generally the determination of additional constituents, such as contaminations, cannot be calculated properly using mixing models if the relative permittivity of the contamination does not differ significantly from the other soil constituents (e.g. Schmalholz et al., 2001).

In the following chapters a CRIM model will be used to determine the volumetric water content of the investigated soils, since it features good flexibility and easy applicability.

$$\Theta = \frac{\sqrt{\varepsilon_s} - (1 - \Phi)\sqrt{\varepsilon_m} - \Phi\sqrt{\varepsilon_a}}{\sqrt{\varepsilon_w} - \sqrt{\varepsilon_a}} \tag{2.64}$$

Assuming a non-dispersive low-loss medium, this equation can also be written as

$$\Theta = \frac{\frac{c_0}{v_s} - \left(\frac{\rho_b}{\rho_s}\right)\sqrt{\left(1.01 + 0.44 \frac{\rho_s}{1 \frac{g}{cm^3}} \right)^2 - 0.062} - \left(1 - \frac{\rho_b}{\rho_s}\right)}{\sqrt{\varepsilon'_{eff\_w}} - 1} \tag{2.65}$$

with regard to equations (2.25), (2.42), (2.62) and (2.63). If no additional information is presented an average porosity of 0.4 and a relative permittivity of 5 for the soil particles are assumed.

3 Transmission methods

3.1 Parallel transmission measurements

One of the most elementary setups is the parallel transmission. Here the georadar antennas are placed on opposite sides of a medium under investigation. Using this layout, the distance between the transmitter and receiver d can be assumed to be equal to the travel path of the fastest EM phase through the object. The first arriving EM phase is commonly the EM phase traveling around the object through air, since the dimensions of the object under investigation most often are insufficient to assure a first arrival of the object traversing phase. Assuming a cylindrical object, radius r and length $l >> r$, and an antenna separation $2r$, the relative permittivity ensuring first arrival of the object passing phase can be calculated by:

$$\frac{2r\sqrt{\varepsilon_{eff}}}{c_0} \leq \frac{\pi r}{c_0}$$

$$\text{or} \qquad (3.1)$$

$$\varepsilon_{eff} \leq \frac{\pi^2}{4} \approx 2.5$$

Such a low relative permittivity is not plausible for natural soils (Figure 2.7).

Georadar generally records a time series which requires the identification of the traversing EM impulse in the radar section. To determine the exact propagation time of the EM wave, the arrival time as well as the initial time of the generation of the EM wave has to be known. The time of the generation of the EM wave at the transmitter antenna will be called initial time zero t_0 from now on. The georadar time $t = 0$ ns is not necessarily equal to t_0. With the knowledge of the propagation path of the first arrival EM phase, the relative permittivity of the medium can be derived according to equation (2.24):

$$\varepsilon'_{eff} = \left(\frac{c_0 (t - t_0)}{d} \right)^2 \qquad (3.2)$$

with t being the arrival time of the first phase and d being the propagation distance.

3.1.1 Experimental setup

An easy and concise experiment was performed to evaluate the potential of the parallel transmission measurement. A small standard aquarium, length 0.55 m, width 0.26 m and height 0.30 m, was filled with de-ionized water. The aquarium walls were 6 mm thick and made of glass. During the experiment the electrical conductivity was increased by adding sodium chloride. For this experiment water was used for its homogeneity and its well known electrical properties in the georadar frequency range (e.g. Ulaby et al., 1986, Kaatze, 1989, Hübner, 1999, Kupfer, 1997). The initial electrical conductivity of the water was $\sigma_0 = 0.3$ mS/m (see Table 3.1). Furthermore, no additional effects such as adsorption water relaxation, scattering of the EM wave or mixing models had to be consdered. The water was under permanent temperature control in the course of the experiment since the relative

permittivity of water features noticeable temperature dependence (Figure 2.4). All significant information concerning the experiment can be seen in Table 3.1.

Table 3.1: Parameters relevant for the parallel transmission measurement.

number	electrical conductivity σ_a [S/m]	$\log(\sigma_a)$ [S/m]	mass sodium chloride m_S [g]	salinity S [%]	temperature T [°C]
0	0.00029	-3.5	0	0	22.2
1	0.017	-1.8	2.97	0.009	22.3
2	0.035	-1.5	6.05	0.019	22.5
3	0.052	-1.3	9.1	0.029	22.3
4	0.068	-1.2	12.11	0.038	22.3
5	0.095	-1.0	17.04	0.053	22.7
6	0.15	-0.82	27.24	0.086	22.9
7	0.25	-0.60	47.94	0.151	22.9
8	0.46	-0.34	88.05	0.277	23.1
9	0.85	-0.070	168.10	0.529	23.0
10	1.6	0.20	328.55	1.033	23.0
11	2.9	0.46	648.62	2.040	22.8
12	4.3	0.63	994.87	3.129	23.0

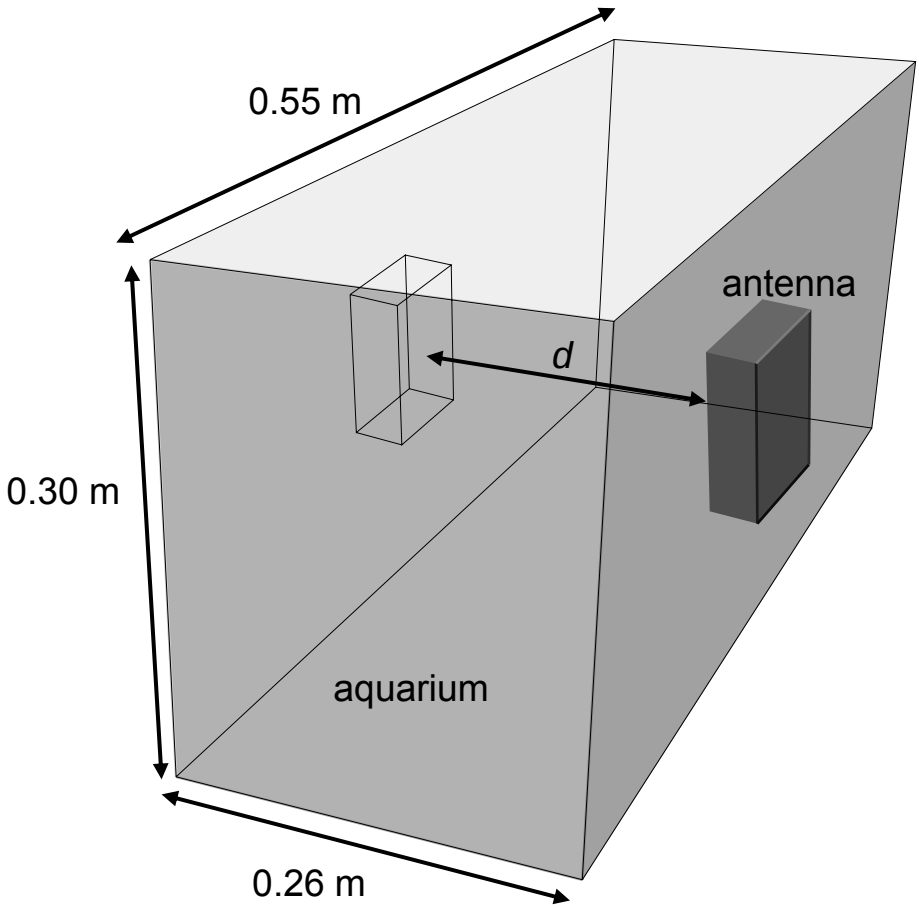

Figure 3.1: Setup of a parallel transmission measurement exemplarily shown with the aquarium used in 3.1.1.

The georadar measurements were performed with a set of 1 GHz antennas, RAMAC GPR-system, MALÅ GeoScience, Sweden, and a set of 1.5 GHz antennas, SIRveyor system, GSSI, USA. Both antenna sets were shielded minimizing the effect of air wave interferences as much as possible. For each measurement the antennas were placed at opposite sides of the aquarium with the transmission path of the EM wave being the smaller side of the rectangular base of the aquarium (Figure 3.1). Assuming a relative permittivity of 81 for water and the respective frequencies of the antennas, the propagation path is approximately 8 wavelengths for the 1 GHz antenna and 12 wavelengths for the 1.5 GHz antenna. Initial time zero was obtained through a calibration measurement in air. This calibration measurement ensured the precise determination of t_0 by:

$$t_0 = t - \frac{d}{c_0} \tag{3.3}$$

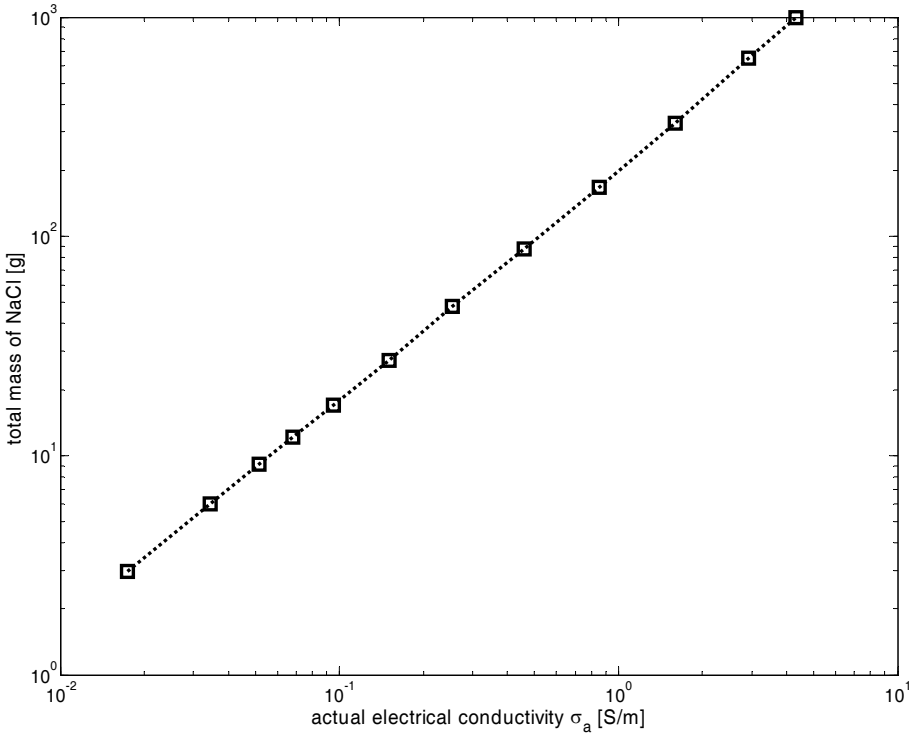

Figure 3.2: Determined relationship between measured electrical conductivity of water to the added mass of sodium chloride.

To acquire good data quality a stacking rate of 320 was applied. This means an identical measurement was performed 320 times and the recorded traces were used to derive one average trace. Therefore statistical noise is reduced whereas signal information is enhanced. In addition to the georadar measurements the actual electrical conductivity σ_a was determined by conductometers LF 597-S and LF 535 by WTW, Germany. After the measurements were performed sodium chloride was added to the water and homogeneity was restored by stirring. Then the measurement procedure was repeated. A total of 1 kg sodium chloride was dissolved resulting in a maximum electrical conductivity of over 4 S/m. The application of sodium chloride was performed in 12 steps to cover a large electrical conductivity range (Figure 3.2).

Using the georadar signal, three parameters were determined.

- propagation time
- center frequency
- attenuation

For short propagation paths significant wavelet dispersion can be excluded since the spectrum does not change strongly (Irving and Knight, 2003). The propagation time was determined by picking a well-recognizable event of the transmitted signal. In the dataset presented here the second deflection or first minima for the 1 GHz antenna and the first deflection for the 1.5 GHz antenna were picked. Although the first deflection for the 1 GHz antenna is a distinct maximum it is too small to be accurately picked for greater attenuations (Figure 3.3). The maximum value of the entire recorded dataset for each antenna was used to normalize the data for better comparability.

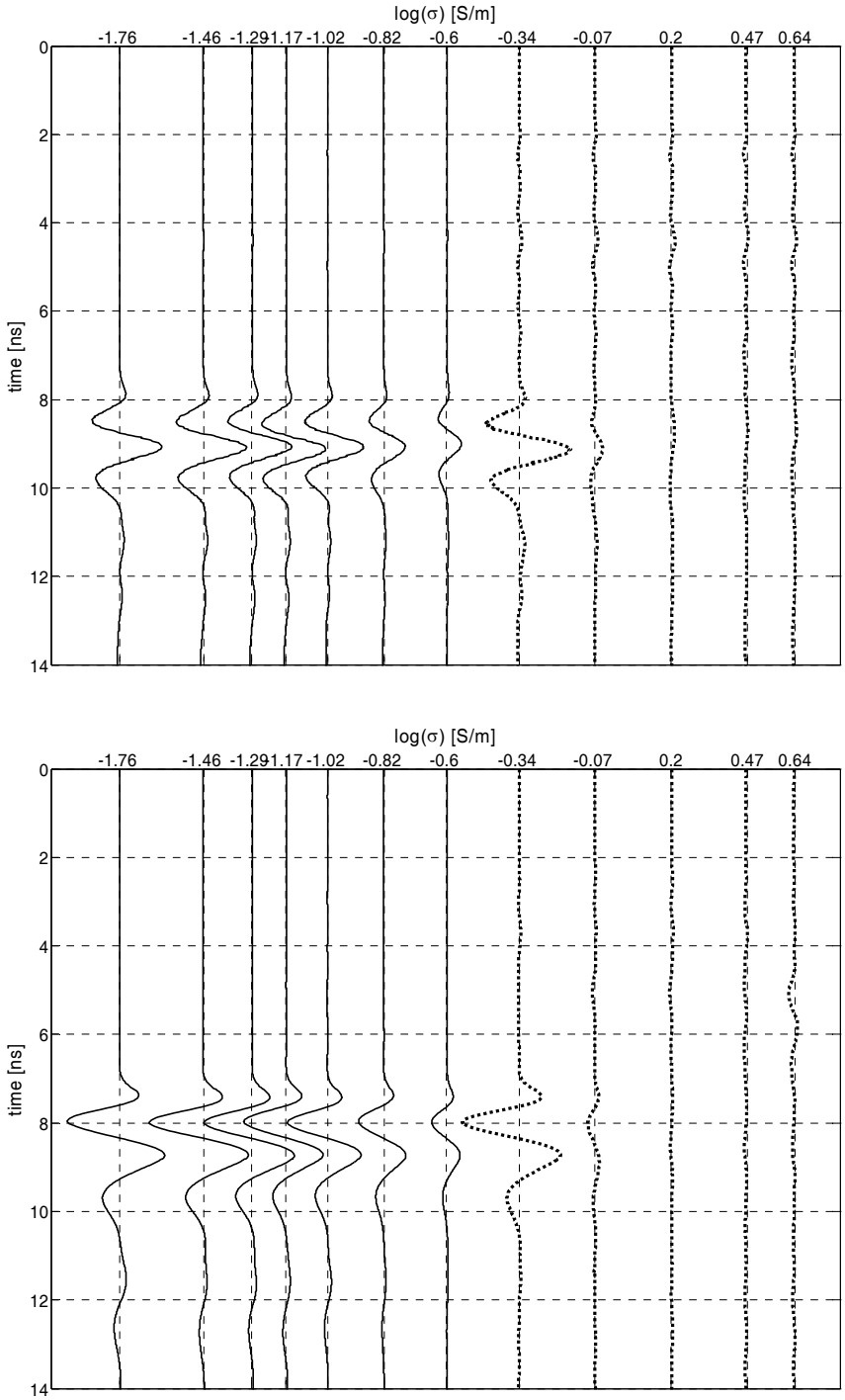

Figure 3.3: Recorded georadar signals of the aquarium experiment for the different electrical conductivities. MALÅ 1 GHz (above) and GSSI 1.5 GHz (below) amplitudes normalized to the respective maximum value of the entire radar section. Dashed lines are multiplied by ten.

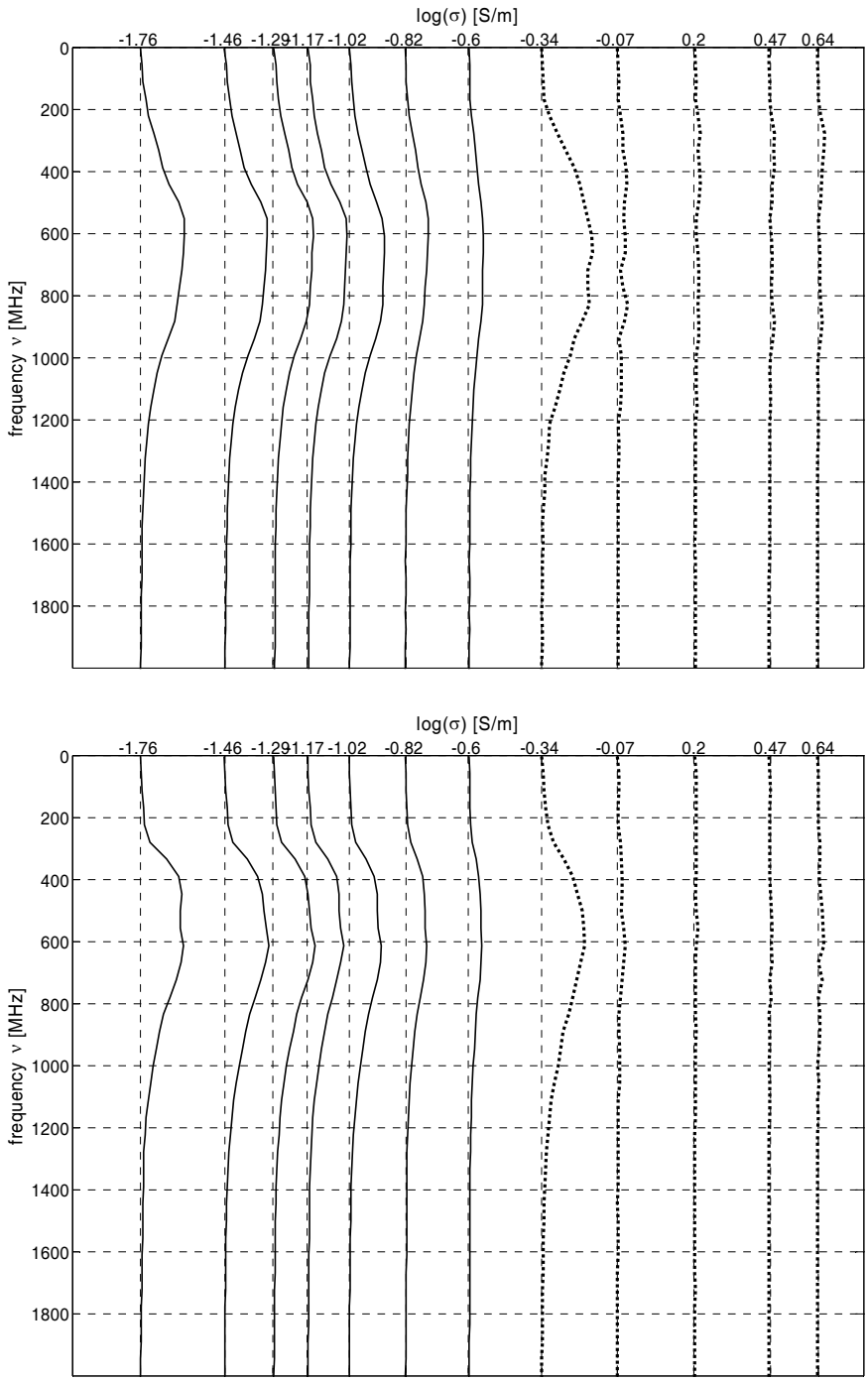

Figure 3.4: Frequency spectrum of the recorded georadar signals. MALÅ 1 GHz (above) and GSSI 1.5 GHz (below) amplitudes normalized to the respective maximum value of the entire radar section. Dashed lines are multiplied by ten.

The center frequency is the frequency with the maximum amplitude value in the frequency spectrum (Figure 3.4). The frequency spectrum is derived by Fourier transformation (2.1.1). Looking at the center frequencies no significant frequency shift can be registered at least for electrical conductivities below 0.5 S/m ($\log(\sigma) = -0.34$ [S/m]) (Table 3.1). Comparing two trace spectra for the 1 GHz antenna for 0.02 S/m ($\log(\sigma) = -1.8$ [S/m]) and approximately 0.5 S/m no significant dispersion is featured (Figure 3.4). Although a general shift of the whole frequency spectrum towards lower frequencies can be noticed, the center frequency

remains the same. For the further evaluation the center frequencies were used to determine the electrical conductivity.

To determine the attenuation, a handle of the decay of the EM energy has to be chosen. Although some sort of variation of deflection of the recorded signal can be used, the instantaneous amplitude or amplitude of the envelope (Figure 3.5) was analyzed (Buttkus, 2000).

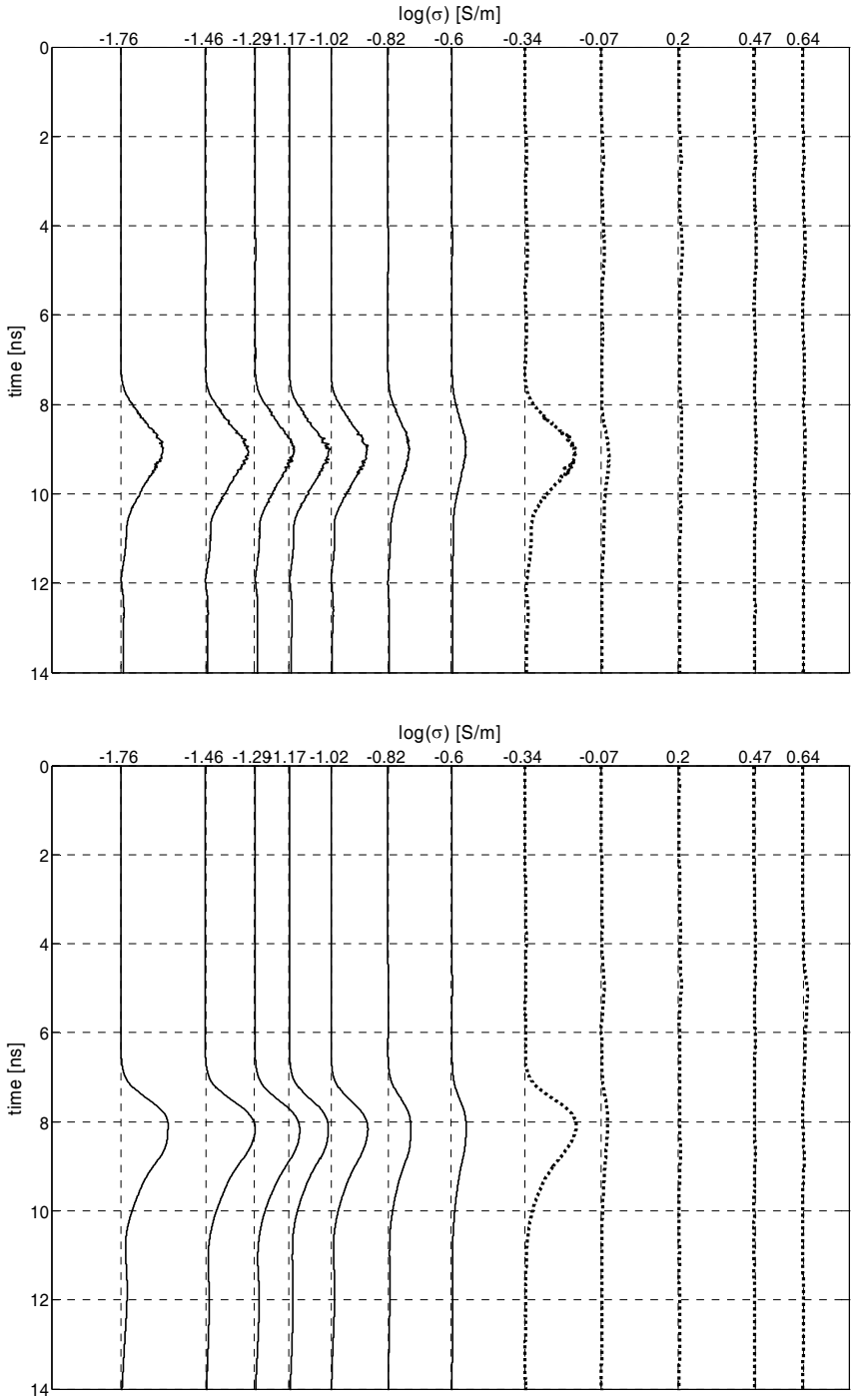

Figure 3.5: Instantaneous amplitudes for the respective electrical conductivities. MALÅ 1 GHz (above) and GSSI 1.5 GHz (below) amplitudes normalized to the respective maximum value of the entire radar section. Dashed lines are multiplied by ten.

Assuming a complex time-dependent function z:

$$z(t) = A(t)e^{i\theta(t)} = x(t) - i\,y(t)$$
$$\text{and } y(t) = \frac{P}{\pi}\int_{-\infty}^{\infty}\frac{x(\varpi)}{\varpi - t}d\varpi \equiv H(x(t)) \tag{3.4}$$

With P the principal value of the integral and H indicating the Hilbert transform. The modulus of $z(t)$ is called the instantaneous amplitude. The advantage of the instantaneous amplitude compared to just using signal intensities is its proportionality to the square root of the complete energy of the signal at an instant of time (Sandmeier, 2006). Here not only the values of one or a few deflections are considered, but the whole transmitted signal including possible wavelet dispersion. Secondary signals, e.g. data noise, superposing the actual signal are still disturbing events. But the effect is somewhat relativized since the whole signal is investigated and not only a few sampling points in the trace.

3.1.2 Data interpretation

Equation (2.39) neglects the effect of dissolved ions on the relative permittivity of water. In order to take this into account, an alternative relation has to be deduced. Those relationships are dependent on the ions dissolved in the water and can be derived by the equations provided by Ulaby et al. (1986). For a sodium chloride solution the relative permittivity can be determined as:

$$\varepsilon_{eff\_sw}(\omega,T,S) = \varepsilon_{w\infty}(T) + \frac{\varepsilon_{sw0}(T,0)a(T,S) - \varepsilon_{w\infty}(T)}{1 + i\omega\tau_w(T)b(T,S)} + i\frac{\sigma_{sw}(25°C,S)e^{-\chi(T,S)}}{\varepsilon_0\omega} \tag{3.5}$$

With ε_{sw0} being the relative permittivity of saline water in the static case, a and b being ion-specific polynomials, σ_{sw} the electrical conductivity of saline water at a temperature of 25 °C, S the salinity and χ a correction exponent. The salinity is the relation between the mass of sodium chloride m_S to the total mass of the solution.

$$S = \frac{m_S}{m_S + m_w} \tag{3.6}$$

with m_w the mass of water. According to equation (3.5) only the relative permittivity for the static case has to be determined differently from equation (2.40).

$$\varepsilon_{sw0} = 87.134 - 0.1949\zeta - 0.01276\zeta^2 + 2.491\cdot10^{-4}\zeta^3 \tag{3.7}$$

ζ is the normalized temperature to provide a dimensionless quantity. Equation (3.7) is not identical to the corresponding relationship in equation (2.40). The two ion-specific polynomials are given by the following relationships (Ulaby et al., 1986).

$$a(T,S) = 1.0 + 1.613\cdot10^{-5}S\zeta - 3.656\cdot10^{-3}S + 3.210\cdot10^{-5}S^2 - 4.232\cdot10^{-7}S^3$$
$$\text{and} \tag{3.8}$$
$$b(T,S) = 1.0 + 2.282\cdot10^{-5}S\zeta - 7.638\cdot10^{-4}S - 7.760\cdot10^{-6}S^2 + 1.105\cdot10^{-8}S^3$$

The corresponding electrical conductivity of the saline water can be derived by the following two equations.

$$\sigma(25°C,S) = S\left(0.18252 - 1.4619\cdot10^{-3}S + 2.093\cdot10^{-5}S^2 - 1.282\cdot10^{-7}S^3\right)\cdot\hat{\sigma}$$
$$\text{with } \hat{\sigma} = 1\frac{\text{S}}{\text{m}} \tag{3.9}$$

$$\chi(T,S) = \Delta_\sigma\left(0.02033 + 1.266\cdot10^{-4}\Delta_\sigma + 2.464\cdot10^{-6}\Delta_\sigma^2\right) - \\ - S\Delta_\sigma\left(1.849\cdot10^{-5} - 2.551\cdot10^{-7}\Delta_\sigma + 2.551\cdot10^{-8}\Delta_\sigma^2\right)$$
$$\text{with } \Delta_\sigma = \frac{25°\text{C} - T}{1°\text{C}} \tag{3.10}$$

Strictly speaking the polynomials provided by Ulaby et al. (1986) cover only the salinity range between 0.4 to 3.5 % or the last four mixtures in Table 3.1.

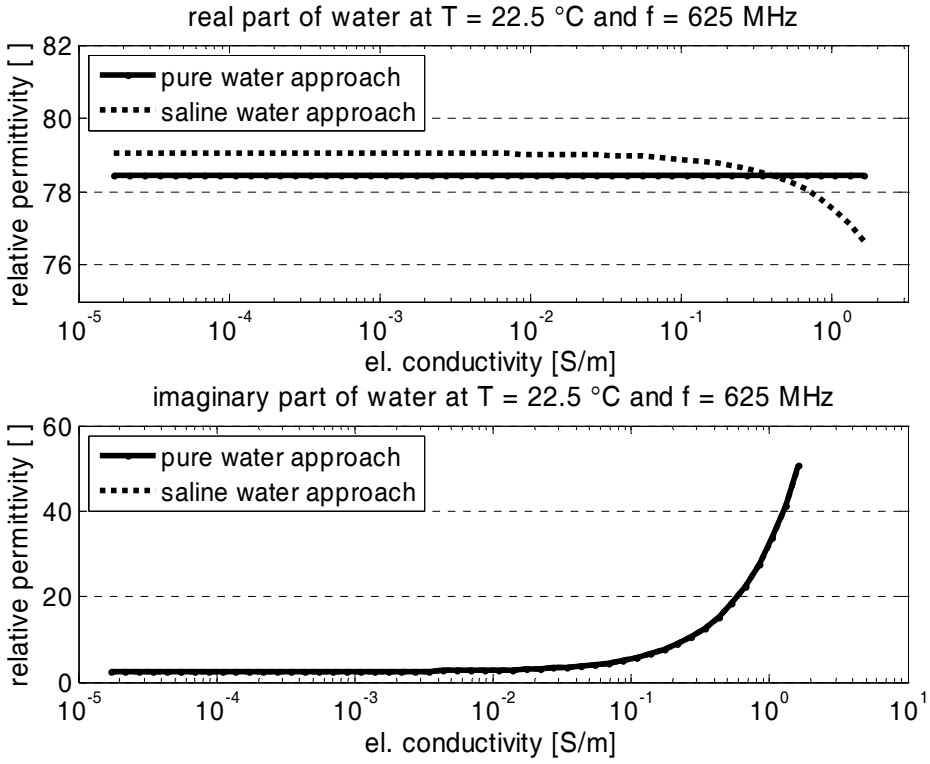

Figure 3.6: Comparison of relative permittivities calculated for pure water (equation (2.39)) (solid line) and saline water (equation (3.5)) (dashed line).

Deriving the relative permittivity of saline water with the approaches given in equation (2.39) and (3.5), a deviation from one another can be noticed for the real part of the relative permittivity (Figure 3.6). The imaginary part of the relative permittivity shows no noticeable difference for both equations for the chosen frequency. Due to the simple structure of (2.39), i.e. relative permittivity of water is not dependent on the electrical conductivity, the real part is constant for a given temperature over the whole electrical conductivity range. The real part of the relative permittivity derived with equation (3.5) features a slightly higher value outside

its range of validity and a strong decrease for higher electrical conductivities. Here the effect of additional relaxation processes due to stronger interactions of sodium chloride ions and water can be considered. Although an initial difference of approximately 0.5 in the relative permittivity can be noticed, this has only marginal effect on the derived EM propagation velocity (Figure 3.7). On the other hand, comparing the resulting EM propagation velocities derived from equation (2.24) and the simplified equation (2.25) reveal two important results. The simplified equation (2.25) can be assumed to be correct for electrical conductivities up to 0.1 S/m. For the investigated case the resulting error can be considered marginal for electrical conductivities up to 1 S/m.

Taking all the aforementioned into account and looking at the actual recorded georadar data, equation (2.24) has been chosen to calculate the real part of the relative permittivity. Therefore an additional case-specific query for electrical conductivities is not required. The electrical conductivity was calculated according to equation (2.45). The initial measurement number 0 (see Table 3.1) is assumed to be identical to a measurement with an electrical conductivity of 0 S/m. The assumption is valid since the resulting additional summand caused by the electrical conductivity for this case is 0.0083 according to equation (2.42). Therefore an initial attenuation coefficient can be derived according to the procedure provided in 2.2.2 and used for the succeeding determinations. For the following data interpretation only the datasets acquired with the 1 GHz antennas are discussed as the 1 GHz antennas were used for all measurements discussed in this work.

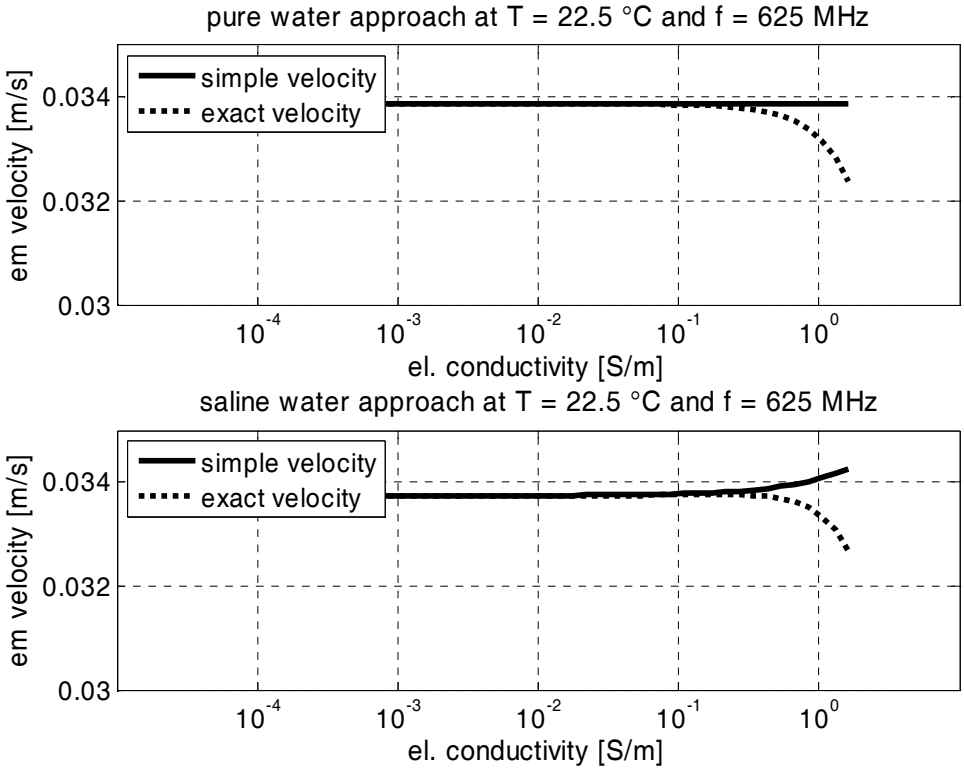

Figure 3.7: Comparison between simple velocity derivation after equation (2.25) (solid line) and exact velocity after equation (2.24) (dashed line) for the pure water approach after equation (2.39) (above) and the saline water approach after equation (3.5) (below).

Looking at the determined EM propagation velocities a very good correlation with the theoretical propagation velocity is achieved (Figure 3.8). The errors are well below

±0.00165 m/ns in the propagation velocity or ±5%. Only the measurements beyond 1 S/m feature bigger errors. Looking at the recorded wavelets (Figure 3.3) it can be assumed that this error is more a result of insufficient signal intensity than erroneous model assumptions.

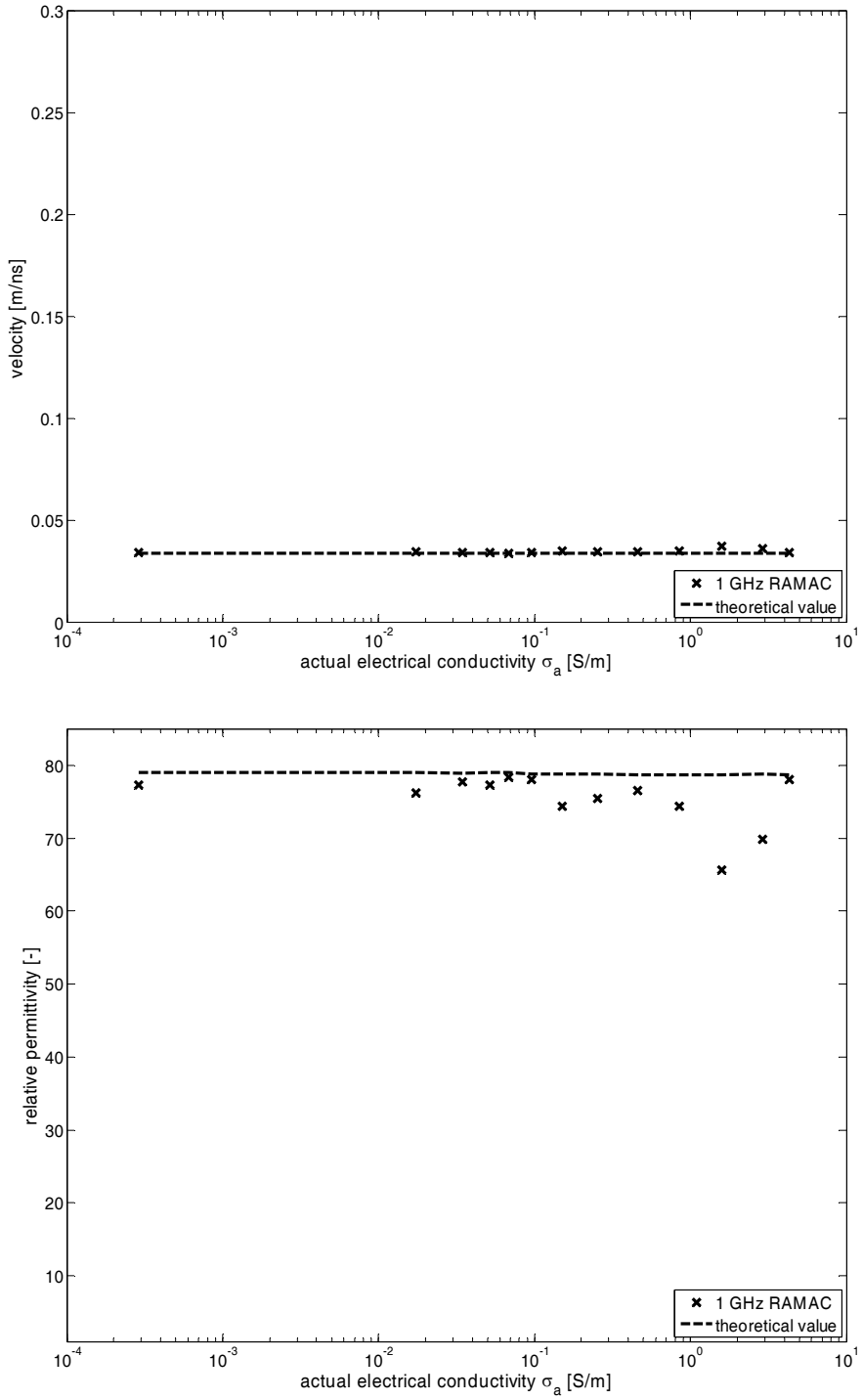

Figure 3.8: Determined and theoretical calculated EM velocities for the 1GHz antenna (above). Real part of the relative permittivity (below) calculated from the measured EM velocities.

The corresponding resulting real parts of the relative permittivity of water are equally well represented (Figure 3.8). Using the hypothesis of insignificant wavelet dispersion and

subsequently using a distinct feature of the wavelet instead of the first arrival of the EM wave appears justifiable. This is even more important since the time correction was made using EM wave transmission in air. According to several publications (e.g. Wollny, 1999, Lampe et al., 2003, Radzevicius et al., 2003, van der Kruk, 2004, Holliger et al., 2004) the antenna characteristics are strongly dependent on the electrical parameter of the media in the close vicinity. This effect appears to be rather a problem for amplitude analysis and should not have any influence on travel time analysis. Wollny (1999) encountered a frequency shift of the emitted wavelet to lower frequencies for media with electrical properties differing from those the antenna is originally matched for by its design. Additionally a shift of initial time zero to later times was noticed. This effect seems to be insignificant for the analysis of these measurements. Although a general shift of the propagation velocities to greater values are noticeable, a direct connection to the effect described by Wollny (1999) cannot be concluded. On the other hand, an obvious deviation of the nominal frequency given by the manufacturer from the actual center frequencies can be registered.

Looking at the measured amplitudes, a recognizable attenuation due to the electrical conductivity is noticeable (Figure 3.9). The amplitudes were normalized to the initial measurement. The theoretical model resembles the measured amplitudes quite well. Due to the 16 bit A/D converter of the RAMAC GPR System and the worse signal-to-noise ratio of the data, the amplitude bandwidth is only resolvable over two decades. Excluding a reliable quantitative evaluation of the last three measurements (number 10-12 or $\sigma > 1$ S/m).With the exception of measurement number 1 ($\sigma = 0.017$ S/m) the recorded amplitudes are all above the theoretically expected amplitudes. Additionally the amplitudes of measurements 1 and 4 are smaller than the succeeding amplitudes indicating a not-negligible inaccuracy of the recorded amplitudes. Looking at a reference dataset consisting of amplitude data from the air measurements strengthen the suspicion of erroneous amplitude data (Figure 3.9). Here identical measurements feature deviations from each other of over 20%. The cause of this can be various:

- Even though the georadar devices were operational the whole duration of the measurements, an effect of different operation temperatures cannot be excluded.
- Another possible cause could be slightly differing dipole orientations due to the placement by hand. Such an extensive effect seems unreasonable since no field measurements feature such precise placements. Amplitude analyses were performed successfully in the field and promising new interpretation methods are still in development (e.g. Holliger and Maurer, 2004).

The electrical conductivities were derived by equation (2.45). Looking at the determined electrical conductivities, a satisfying result is achieved (Figure 3.10). Due to the generally less attenuated amplitudes compared to the theoretical expected values, the derived electrical conductivities are lower than the actual ones. As expected measurements number 10 to 12 (i.e. $\sigma > 1$ S/m) are far too low. As the measured amplitudes are too high, measurement number 4 significantly distinguishes itself from the neighboring data points. All derived electrical conductivities have the correct magnitude. Utilizing the simplified equation (2.39) delivers sufficient accuracy for the measurements.

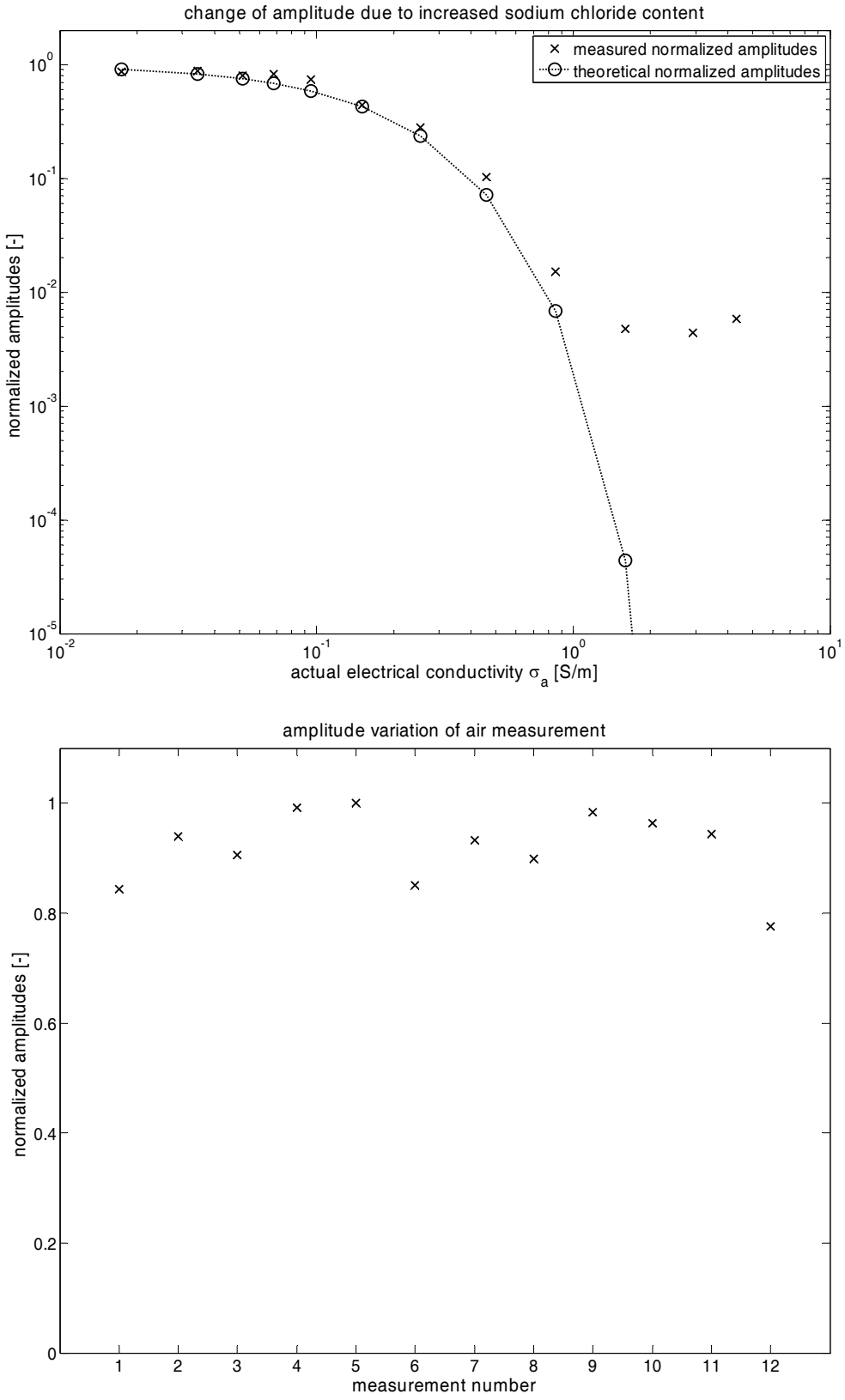

Figure 3.9: Comparison of determined normalized amplitudes of the 1 GHz antenna and the theoretical amplitude decay (above). Determined and normalized amplitudes from calibration measurements conducted in air (below).

Looking at the covered electrical conductivity range a direct extrapolation to field measurements seems difficult. The electrical conductivities are much too high for realistic georadar field measurements as georadar is not suited for soils with such electrical conductivities. But similar amplitude attenuations can be achieved for bigger propagation paths and lower attenuation coefficients (equation (2.43)). The best results will be achieved if significant amplitude attenuation is ensured. Due to the relatively poor amplitude resolution high physical parameter accuracies appear doubtful. Therefore a direct determination of the electrical conductivity is avoided in most applications. Depending on the application, qualitative evaluation of attenuation coefficients may be sufficient to illustrate interesting features in the investigated medium (Holliger et al., 2001).

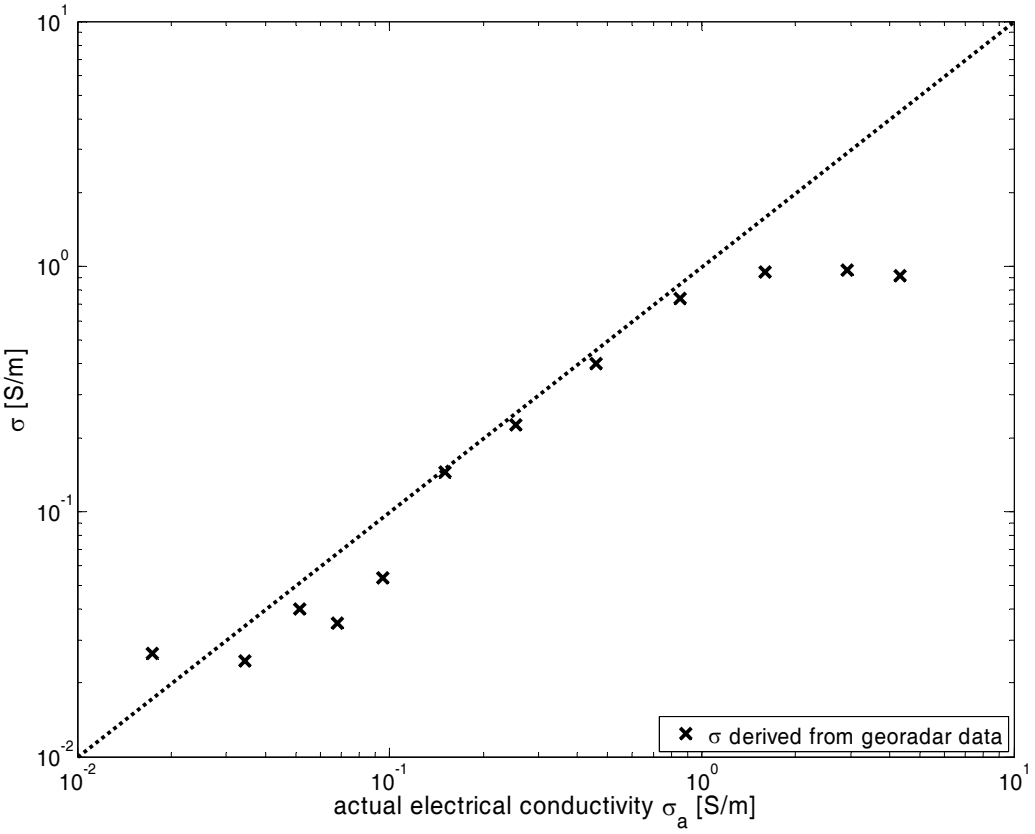

Figure 3.10: Crossplot of actual and derived electrical conductivities.

3.1.3 Application example

To investigate the parallel transmission measurements under more realistic conditions, a lysimeter was used. The lysimeter was located at the lysimeter facility of the Research Center Jülich, Germany. The lysimeter consists of a cylinder with a diameter of 1.2 m and a height of 1.5 m. The lysimeter is a property of the Institute of Chemistry and Dynamics of the Geosphere, Departement IV Agrosphere (ICG IV). The lysimeter was filled by pushing it into the subsurface and the soil inside the lysimeter can be assumed undisturbed. Further information concerning the soil or the lysimeter can be found in Pütz and Klimsa (1991) or Schmalholz et al. (2004b). Due to the extraction method and the storage of the lysimeter only 1.2 m of the full height was accessible for georadar measurements. The lysimeter was equipped with various sensors such as tensiometer, TDR probes and temperature sensors.

Although all these sensors were inserted and collected data during the georadar measurements no disturbing effects were noticed in the data.

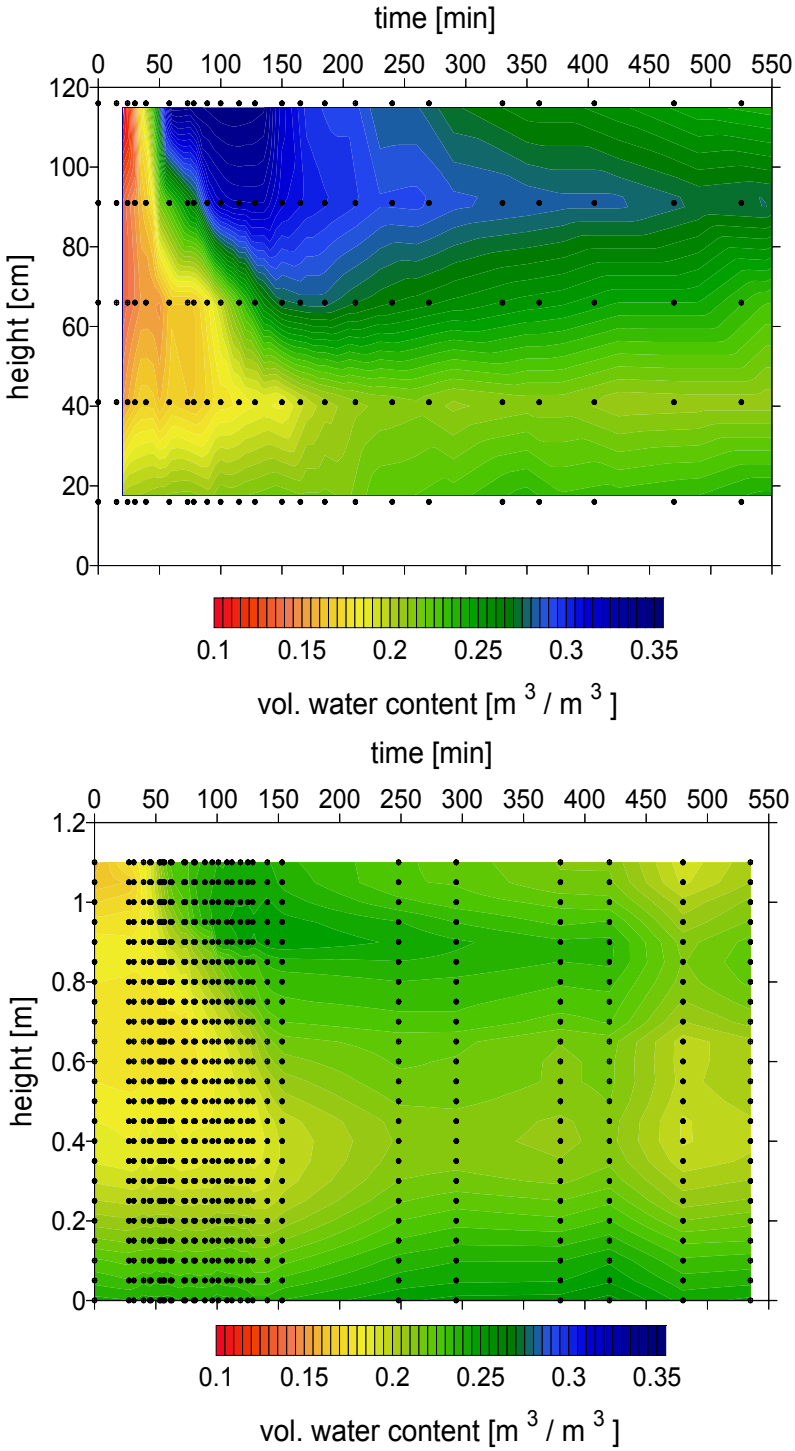

Figure 3.11: Determined volumetric water content dynamics of the irrigated side of the lysimeter with installed TDR probes (above). Integral determined volumetric water content dynamics with georadar for a plane crossing the irrigated region (below).

In Schmalholz et al. (2004b) a first parallel transmission experiment was performed. Here a sector irrigation was realized and the water seepage was traced using the parallel transmission measurement. Encouraged by the good results and the fast data acquisition an additional

experiment was performed. Again a sector irrigation experiment was chosen with 0.0327 m^3 water irrigated on approximately 0.25 m^2. After 116 min the water was totally infiltrated into the lysimeter, i.e. approximately 131 mm rain equivalent. This corresponds to an infiltration rate of 68 mm/h. Due to the fast data acquisition one dataset consisting of a vertical profile from $z = 0$ m to $z = 1.1$ m and steps of $\Delta z = 0.05$ m took far less than 1 min. Initial time zero was determined by placing transmitter and receiver antenna next to each other. The covered time span was from start of the irrigation until 535 min after start of irrigation. Two vertical planes were investigated. One plane was chosen to directly cross the sector-irrigation and one perpendicular to the other plane. This way horizontal diffusion could be detected and considered in later analysis. The volumetric water content was calculated by the CRIM mixing model according to equation (2.65). The average mass density of the soil particles was derived using the soil density ρ_s and the porosity Φ in equation (2.62).

A general correlation is noticeable when comparing the volumetric water contents determined by georadar and TDR. The effect of the irrigation is relatively small on the integral volumetric water content (Figure 3.11). The black markers in Figure 3.11 indicate the vertical location and acquisition time of the data, whereas a simple linear interpolation between the data points was used to determine the remaining areas. Since the georadar propagation path travels through the whole diameter of the lysimeter, the effect of the irrigation is interpreted as an integral wetting of the lysimeter. With the additional perpendicular dataset, a more localized interpretation can be made (Figure 3.12). This way, the increasing relative permittivity of the soil is accredited to the irrigated half of the plane. If the relative permittivity of the perpendicular plane changed, this change was used as an integral value for the half plane not directly irrigated. This half plane should not be affected by the irrigation.

$$\sqrt{\varepsilon_{s\_irr}(t)} = 0.5\sqrt{\varepsilon_{s\_irr}(0) + \left(\Delta\varepsilon_{s\|}(t) - \Delta\varepsilon_{s\perp}(t)\right)} + 0.5\sqrt{\varepsilon_{s\_irr}(0) + \Delta\varepsilon_{s\perp}(t)} \qquad (3.11)$$

With ε_{s_irr} being the relative permittivity of the irrigated half plane, $\Delta\varepsilon_{s\perp}$ and $\Delta\varepsilon_{s\|}$ the change of the relative permittivity not crossing the irrigated area and traversing through the irrigated area.

Looking at the resulting volumetric water contents in Figure 3.12, a rough division into three areas can be made. From $z = 0$ m to $z = 0.25$ m a zone with increased volumetric water content is present. This higher volumetric water content, compared to the other vertical water content distribution, is caused by the gravity. The lysimeter was not equipped with a base plate with applied suction. Therefore water is accumulated at the bottom of the lysimeter. Between $z = 0.25$ m and $z = 0.85$ m the volumetric water content changes only slightly. The last area is above $z = 0.85$ m. Here the volumetric water content changes relatively fast and is somewhat hindered to seep into the lower area.

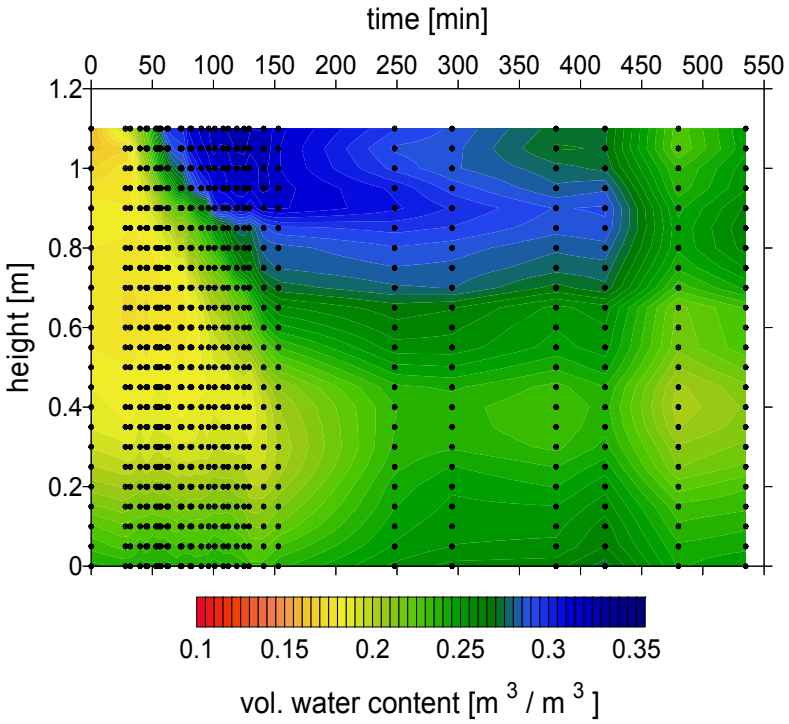

Figure 3.12: Determined volumetric water content dynamics of a plane crossing the irrigated region with georadar. Here the volumetric water content dynamics of a perpendicular plane was used to restrict the actual effect of the irrigation to the irrigated area.

The amplitudes were analyzed by deriving the instantaneous amplitude for each data point and subsequently normalized to its initial value at t = 0 min. This was necessary since a unified normalization over the whole initial vertical profile would result in too strongly varying values. By using such normalization each height point time series can be treated like the aquarium experiment discussed earlier. Generally an increase in the volumetric water content leads to an increase in electrical conductivity (Schön, 1996). With the determined volumetric water contents in Figure 3.12 a general decrease in the recorded amplitudes can be expected.

Looking at the resulting amplitude distribution (Figure 3.13) a more complex structure than in Figure 3.12 is revealed. The area between $z = 0$ m and $z = 0.10$ m features a slight decrease in the amplitude. Since the change is greater than 0.2 and constant over time, an error in the measurement can be excluded. The area between $z = 0.10$ m and $z = 0.45$ m features only marginal changes and even an increase in the amplitude in the lower part. The area between $z = 0.45$ m and $z = 0.80$ m features first a distinct decrease in the amplitude for lower z-values, followed by almost no change at all at $z = 0.60$ m. It is not apparent if the measurements at $t = 250$ min are erroneous or not. Above that constant amplitude area, the amplitude shows a marginal decrease. The next area between $z = 0.80$ m and $z = 1.0$ m dislays a relatively strong decrease in the amplitude. This corresponds to the high volumetric water contents at this height. For $z = 1.0$ m and above an overproportional increase in the amplitude is recognizeable. The last area is more likely to be effected by the interface wet soil to air than really by the change of attenuation.

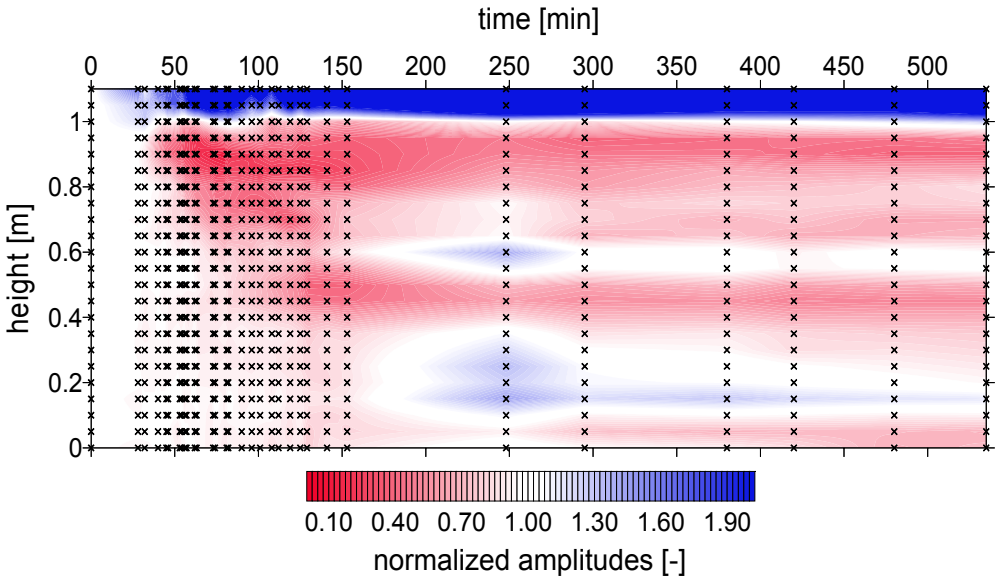

Figure 3.13: Determined individually normalized amplitude variations due to the lysimeter irrigation.

By combining the results displayed in Figure 3.12 and Figure 3.13, one can deduce an interface at $z = 0.8$ m and $z = 0.5$ m. Additionally, the areas between 0.8 m and 0.5 m, and 0.5 m and 0 m appear to feature a soil which is traversed quicker by the water front. In Figure 3.12 this property is indicated by the high volumetric water content contrast above and below 0.8 m and above and below 0.5 m. In Figure 3.13 this characteristic is indicated by absence of amplitude changes, with the exception of early times, where the initial water front passed through this area. Due to less vertical coverage with TDR probes such interfaces cannot be imaged using the determined volumetric water contents with TDR (Figure 3.11).

3.2 Tomographic transmission measurements

The tomographic transmission measurement is one of the most commonly utilized tools for georadar. The tomography is generally used for the interpretation of ray-based methods such as seismics or georadar (Sheriff, 1997) but is getting more and more usage in its common meaning as an imaging technique. Therefore non classical tomography methods, such as 2D geoelectrics measurements are called electrical resistivity tomography (ERT) (e.g. Kemna et al., 2002). In the classical sense, tomography is used to determine velocity, attenuation, or reflectivity distributions of an observation area (Sheriff, 1997). This is achieved through the combination of several transmitter-receiver positions and their combined evaluation. Generally a velocity or attenuation factor is assigned to each cell traversed by the rays and their respective values are derived from the combined minimization of each data misfit. This enables a one-dimensional, two-dimensional, or three-dimensional determination of the investigated medium.

For georadar the tomography can be divided into ray tomography and wave tomography. Ray tomography reduces the investigated waves to rays, and consequently only propagation properties are investigated. These properties are the velocity and the attenuation of the investigated medium. Ray tomography is generally linked to transmission tomography (e.g. Binley et al., 2001), but includes reflection tomography as well (e.g. Tronicke et al., 2001). Wave tomography takes into account the wave nature of the used method. This includes for example diffraction phenomena. The advantage of wave tomography, e.g. diffraction tomography or migration tomography, is the combined inversion of amplitude and phase information (Valle et al., 1999), whereas ray tomography generally inverts velocity or attenuation data.

Tomographic datasets are commonly inverted with respect to the propagation paths of the individual transmitter-receiver location. For transmission tomography the straight connection between the transmitter and receiver can be used. If strong velocity contrasts are present, curved rays according to the Fermat's principle should be used (Valle et al., 1999). Depending on the velocity contrast and the length of the propagation path, great differences between the straight ray assumption and the curved rays can be registered. Then high velocity anomalies are overestimated, i.e. their dimensions are interpreted to be bigger than they actually are, whereas low velocity anomalies are underestimated or even undetectable (Valle et al., 1999).

3.2.1 Application Example: Setup and Interpretation

Since tomography is a geophysical tool with a wide array of applications (see e.g. Knödel et al., 1997, Witten et al., 1994, Herman and Kuba, 1999), a comprehensive introduction of tomography will be forgone. The focal point will be placed on the application to small scale problems and their evaluation. This will be presented for an application example conducted in cooperation with the Institute of Chemistry and Dynamics of the Geosphere (ICG), Forschungszentrum Jülich GmbH, Germany. In the lysimeter facilities of the ICG a lysimeter with plastic housing is accessible and enables georadar transmission measurements (see 3.1.3, Schmalholz et al., 2004b) (Figure 3.14).

The first recorded signal for a tomographic measurement on a small object will be the phase traveling around the object in air. In case of the lysimeter with a diameter of 1.2 m and a height of approximately 1.5 m several combinations of wave paths through air are possible. Since the lysimeter is situated in a facility, additional reflecting objects are present in the vicinity of the lysimeter. One prominent reflector is the metallic stand on which the lysimeter is placed. Another reflector is the circular cut-out in the ceiling. This cut-out has two functions. First it enables the installation of the lysimeter into the lysimeter facility. Second the lysimeter can be treated in near-natural conditions, i.e. exposing the lysimeter to

evapotranspiration and precipitation. Although such effects were not investigated with the used lysimeter, the topside of the lysimeter still extended well into the cut-out in the ceiling. In this cut-out was a metallic casing to protect the concrete ceiling from damage during insertion of the lysimeter. To exclude precipitation during the experiments a metallic cover was placed on the cut-out. These metallic objects acted as an EM wave trap generating several multiple reflections of air waves and presented severe disturbing events in the recorded data.

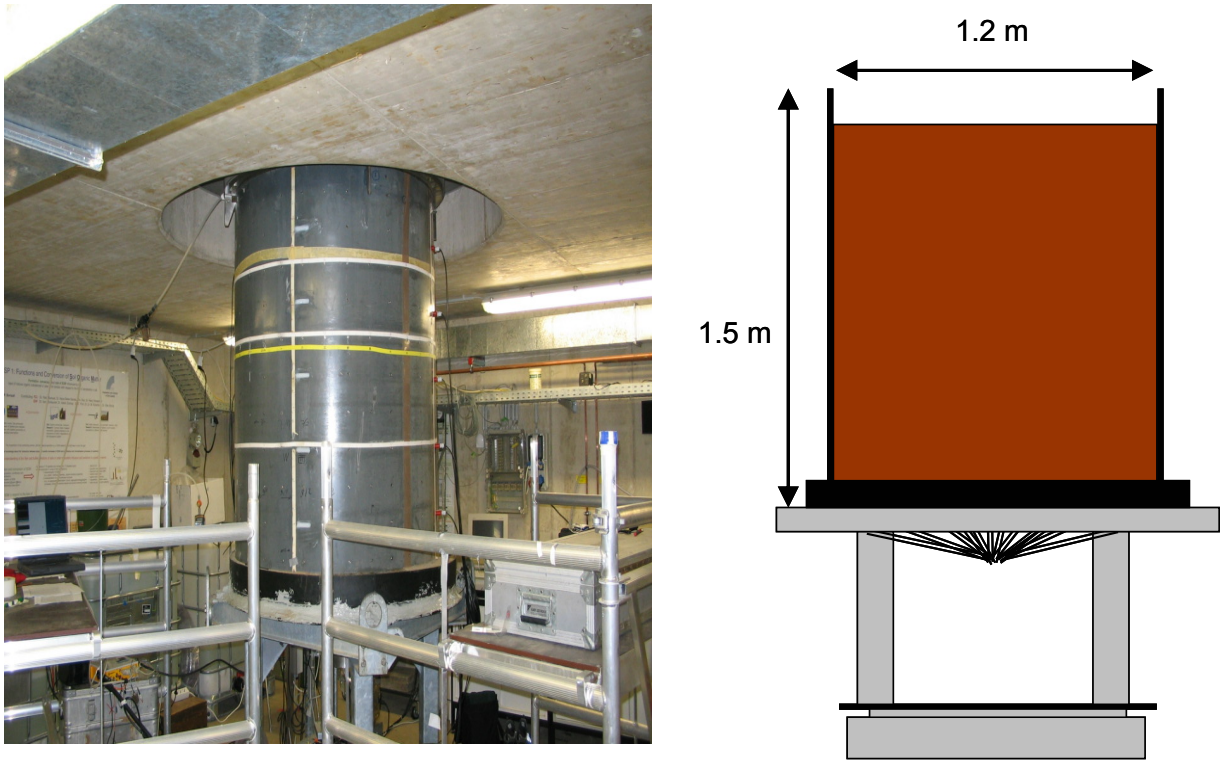

Figure 3.14: Picture of the lysimeter situated in the lysimeter facility at the ICG, Forschungszentrum Jülich GmbH, Germany (left). The scaffolds were necessary to reach all antenna positions at the lysimeter. Layout of the lysimeter (right).

Due to the poor ray coverage mentioned in Schmalholz et al. (2004b) the vertical sections will be neglected. In this evaluation only horizontal planes will be discussed. An example for the horizontal ray coverage is given in Figure 3.15. The gap at approximately x = -0.58 m and y = -0.10 m was caused by inserted TDR probes. At this position the utilized georadar antennas were too big to be placed between the TDR probes. To ensure that the picked arrival times are sufficiently free of distortion by the first air waves, only transmitter-receiver combinations of at least 0.5 m straight propagation paths through the lysimeter body were used. This exclusion corresponds to an angle restriction of less than approximately 66° to the surface normal. Since transmission intensities are expected to be relatively low for angles larger than 66° (e.g. Radzevicius et al., 2003), this exclusion is not so dramatic as the resulting poor quality of this data would not enhance the results. The data was collected with transmitter positions varying at positive x-axis locations and receiver positions varying at negative x-axis locations (see Figure 3.15). Due to the reciprocity of the transmission paths a complete all around measurement with both transmitter and receiver antenna was not necessary.

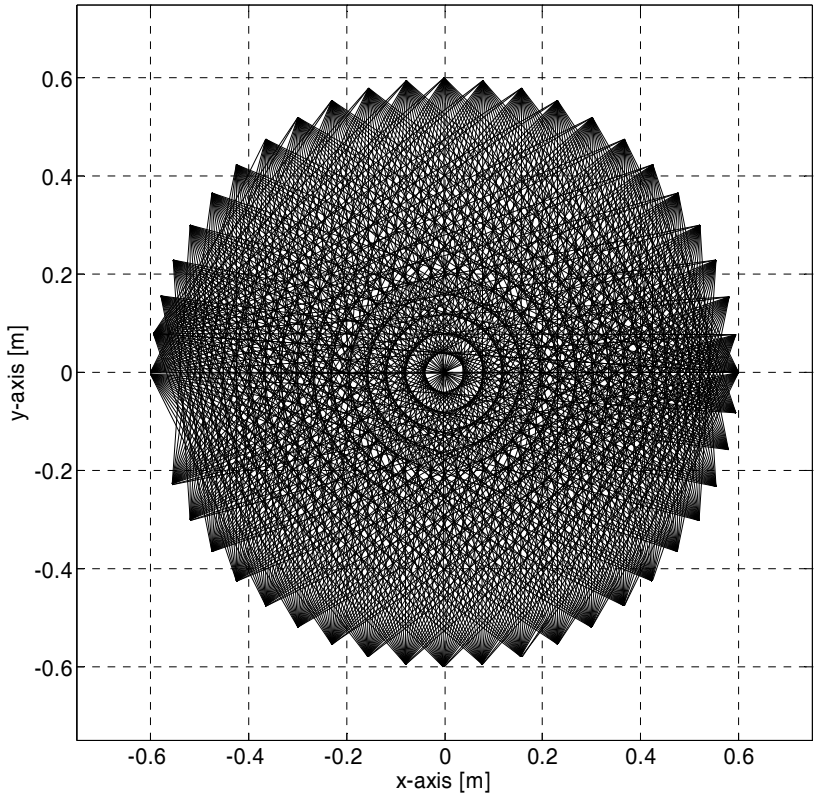

Figure 3.15: Exemplary straight-ray distribution described in Schmalholz et al. (2004b) for a horizontal tomographic plane used for the lysimeter at the lysimeter facility of the ICG, Forschungszentrum Jülich GmbH, Germany.

In Figure 3.16 a typical horizontal plane radar section, recorded with a 1 GHz georadar antenna from MALÅ GeoScience, Sweden, is displayed. The transmitter was fix at the circumference location 0 m, corresponding to $y = 0.6$ m and $x = 0$ m in Cartesian coordinates in Figure 3.15. The two dotted traces in Figure 3.16 are dummy traces since a TDR probe was installed in the lysimeter denying the positioning of the georadar antenna at its position. The traces were still recorded for simplification reasons and were disregarded in later interpretations. The recorded travel times resemble absolute travel times. This was achieved by determining initial time zero via placing transmitter and receiver directly next to each other, at the beginning and at the end of every radar section. This enabled the identification and correction of small shifts of the system recording time. Due to the positioning of the two antennas immediately next to each other, the actual travel time of the EM wave can be assumed almost zero. Each horizontal tomography dataset consisted generally of 25 transmitter and 25 receiver positions. Owing to the presence of installed TDR probes and the restriction to propagation paths greater than 0.5 m, the 625 possible transmitter-receiver combinations were reduced to approximately 550 combinations. The displayed dataset in Figure 3.15 shows 547 combinations. This enables a model raster of 0.05 m squares and still ensuring an over-determined system of equations. It has to be noted that those model squares are not to be mistaken with the spatial resolution of the tomography.

Looking at the single traces in Figure 3.16, the effect of the air waves is visible. The traces recorded relatively close to the transmitter, i.e. the first and last traces in Figure 3.16, show distinct deflections at earlier recording times. Although relatively small in intensity compared

to the direct signal, those air signals present severe problems for automatic picking algorithms. This is especially problematic since the air signals are of similar spectral and shape characteristic as the direct signal traversing the lysimeter body. Although noise caused by sources of interference or by simply a poor signal to noise ratio can be corrected relatively easily (Messinger, 2004), signals from the same transmitter are still problematic (Tronicke and Knoll, 2005). On the other hand, picking a dominant feature of the georadar signal proved to be accurate enough for small-scale analysis with insignificant wavelet dispersion (see 3.1.2). The effect of wavelet dispersion can be neglected even though the propagation path is at least two and up to four times longer than for the aquarium measurements. This is mainly caused by the much inferior expected electrical conductivities inside the lysimeter. By using a dominant feature of the wavelet one has to consider the potentially different signal transmitted and received as a result of assembling both georadar antennas directly next to each other. Such an aberration would result in a constant error in the propagation time determination and could be corrected relatively easily.

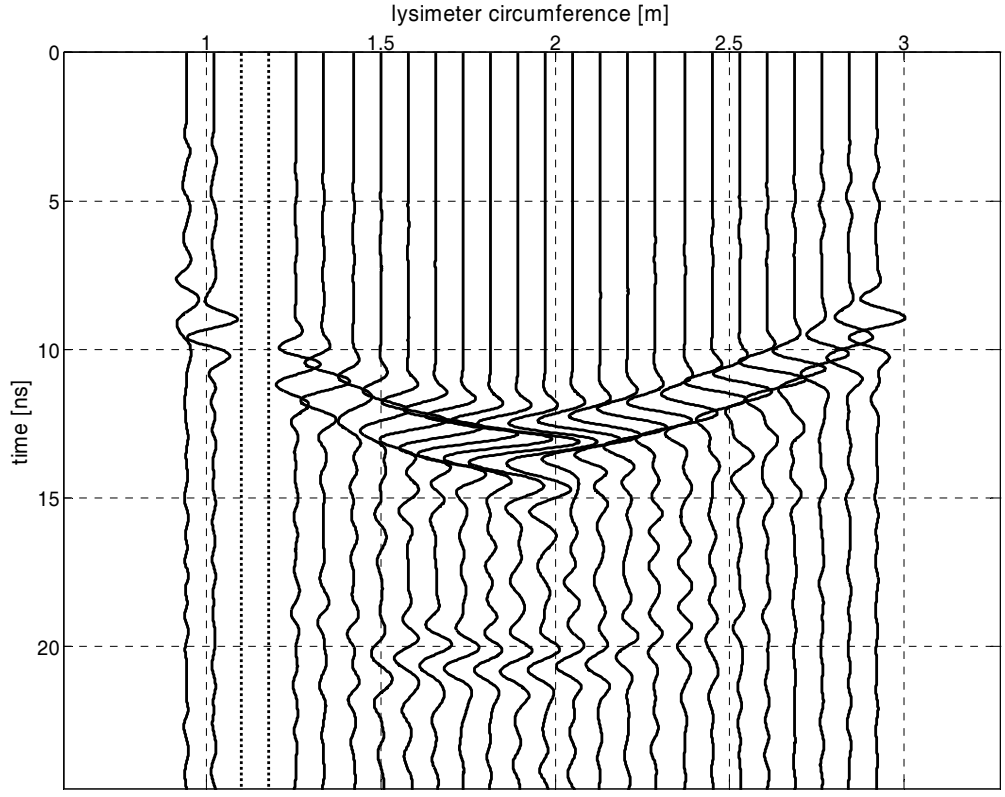

Figure 3.16: Exemplary radar section for one transmitter position of a horizontal tomographic plane. In the present case the transmitter was situated at circumference 0 m with circumference 1.88 m the opposite receiver location. The dotted traces are dummy traces since a TDR probe was installed at the respective receiver position.

3.2.2 Short-term experiment

To check the applicability of the georadar tomography for small-scale investigations an experiment was conducted. A short-term experiment was performed to check the time and spatial resolution. For the short-term measurement a sector irrigation was conducted which is described in 3.1.3. Due to the fact that the transmitter antenna was mounted on a wooden skid and the receiver antenna was placed by hand, the acquisition of one horizontal tomography dataset, identical to Figure 3.15 utilized in Schmalholz et al. (2004b), would have taken too

long. To acquire one standard horizontal dataset takes approximately 1 h. This long duration is caused by various reasons.

To ensure a good data-to-noise ratio of the recorded data a relatively high stacking is required. Here the recording of one trace requires approximately 1.5 s. This alone sums up to more than 15 min of data recording time. The bulk of the required time is then distributed on antenna placements, data quality assurance after data acquisition and repeat measurements if necessary. Additionally, the measurement documentation is essential for later interpretation and resorting, and the georadar control-unit controller program has to be operated for each data recording.

Since the latter activities are fix time consumers, only the number of transmitter-receiver combinations are the logical items to cut down the data acquisition time. Therefore only a total of 140 combinations were recorded (Figure 3.17), decreasing the spatial accuracy but enabling the acquisition of a horizontal tomographic plane in less than 30 min. A recording of all transmitter-receiver combinations into one data file and consequently reducing acquisition time was not advisable for several reasons. The most important is the independent power supplies for the two antennas and the control unit. The failure of one or both power supplies of the antennas would be difficult to identify during data acquisition. Additionally a rerecording of data with poor signal-to-noise ratio would be extremely difficult since its receiver-transmitter combination is difficult to reacquire in that short amount of time. Therefore each data file contained two transmitter locations and their respective receiver positions, enabling a quick data quality inspection and quick intervention if necessary.

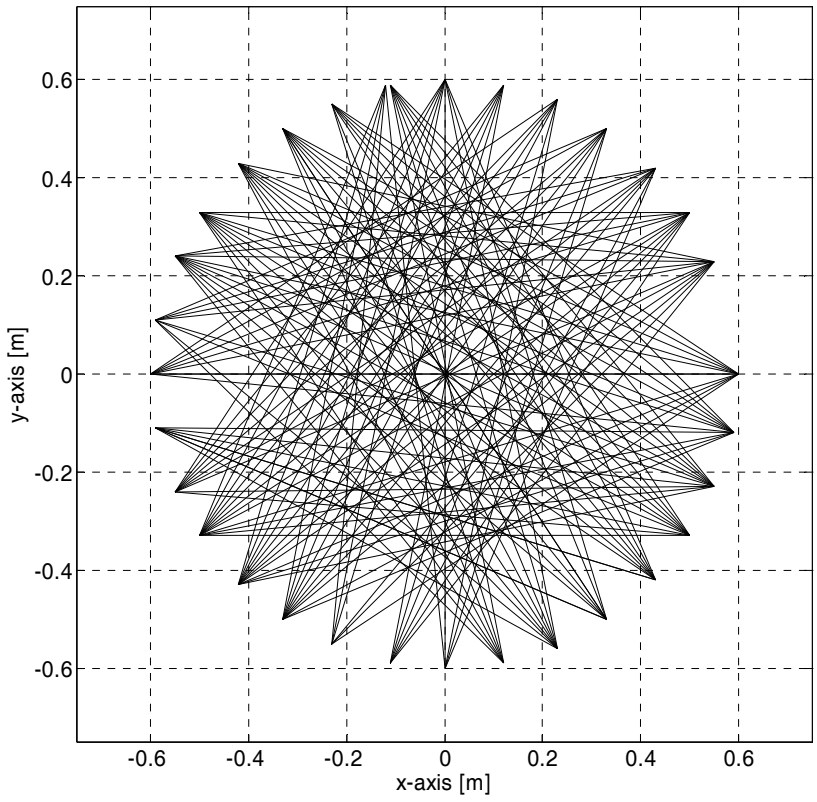

Figure 3.17: Time-optimized ray distribution for the short-term measurements. The two gaps at opposite sites are caused by installed TDR probes, preventing the positioning of the georadar antennas.

To record a tomographic section the medium under investigation needs to be in a state of equilibrium. If equilibrium is not guaranteed the parameters of the traversed cells in the tomographic inversion are not time-constant anymore. This makes a successful application of the tomographic inversion impossible. This problem resulted in a dead-time for the acquisition of the first horizontal tomographic dataset. Looking at the determined water contents by TDR (Figure 3.11) and the water contents determined by the optimized georadar parallel transmission measurements (Figure 3.12) fast changes are observable up to approximately 150 min. Therefore the acquisition of the first tomographic datasets had to start after 150 min at best. Before the start of the irrigation an additional tomographic dataset was collected to determine the initial state of the lysimeter (Figure 3.18). The utilized inversion algorithm is integrated in the software package REFLEXW by Sandmeier (2006) and is based on a Semi Iterative Reconstruction Technique (SIRT) introduced by Dines and Lytle (1979). The horizontal plane was situated at $z = 0.85$ m (see Figure 3.11). This plane was chosen based on the results of the preceding experiments in Schmalholz et al. (2004b). For this plane effects of the air waves were minimal and the water seepage was expected still significant enough to produce distinct relative permittivity changes.

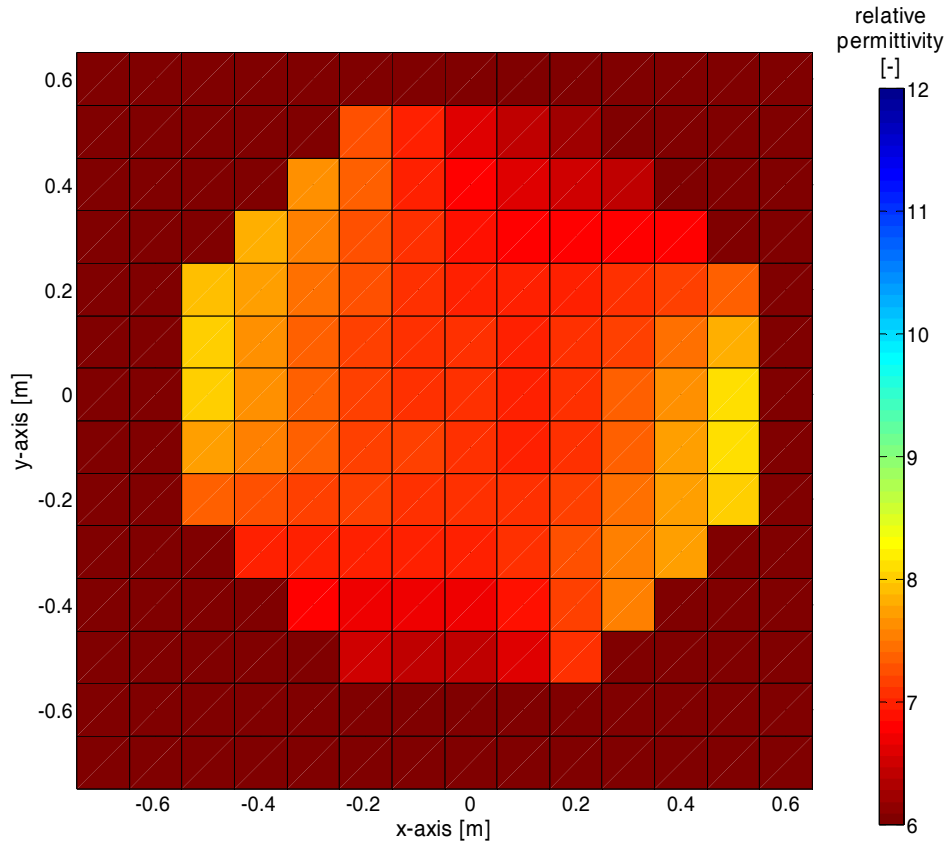

Figure 3.18: Determined relative permittivity distribution inside the lysimeter at the height $z = 0.85$ m before start of irrigation.

The result in Figure 3.19 shows the problem of the equilibrium requirement quite well. Although the irrigated region is well distinguishable an area at the opposite side is recognizable with decreasing relative permittivities. Looking at the determined volumetric water contents in Figure 3.11, decreasing volumetric water content is noticeable over the

course of time, required to collect the tomographic dataset. This vertical water seepage through and out of the investigated horizontal plane resulted in generally lower relative permittivites for later transmitter-receiver combinations. Nevertheless the bulk of the change is correctly attributed to the irrigated half of the horizontal plane.. Due to the relatively poor ray coverage at the lysimeter's boundary, the tomographic results were truncated by 0.1 m, i.e. one tomographic inversion cell. Since the used tomographic algorithm, implemented in the software REFLEX (Sandmeier, 2006), determines squares, additional areas were not considered for the interpretation due to geometrical reasons.

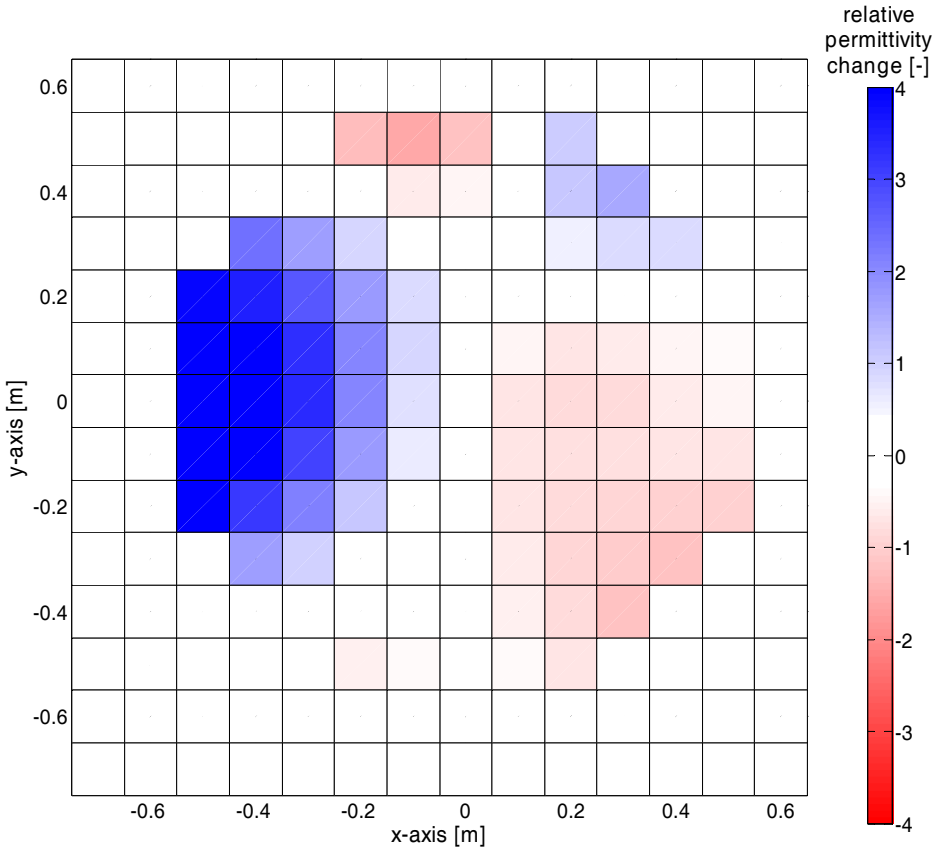

Figure 3.19: Determined change of relative permittivity distribution for the first horizontal plane finished 226 min after start of irrigation compared to the initial state.

In Figure 3.20 the determined relative permittivities over the whole span of tomographic data acquisition are displayed. In this case only isolines are drawn to enhance the overall comprehensibility. Additionally, an isobody was included to illustrate the dynamical processes. Only relative permittivity values of significance were chosen to focus on the irrigation and its effects. Note that no relative permittivities beyond 9 were present at the initial state of the lysimeter (Figure 3.18). In the presented case the isobody indicates a distinct flow through the investigated plane at $z = 0.85$ m with a maximum of the volumetric water content at approximately 270 min. Of course, this has to be evaluated quite precautiously due to the dynamical effect in Figure 3.19. Since the earliest tomographic plane, i.e. at a time of 226 min, denotes erroneous values, it is expectable that the maximum volumetric water content actually passed through the plane at earlier times. The water seepage out of the plane is well traceable nevertheless. Figure 3.20 depicts a decreasing volumetric water content at the center of irrigation, and a long-lasting increased volumetric water content

zone. This area of relative permittivity of 9 (or 0.188 m^3/m^3) and higher is restricted to the region with $x < 0$ m. This is in good accordance to the parallel transmission measurements (see 3.1.3) and earlier experiments (Schmalholz et al., 2004b).

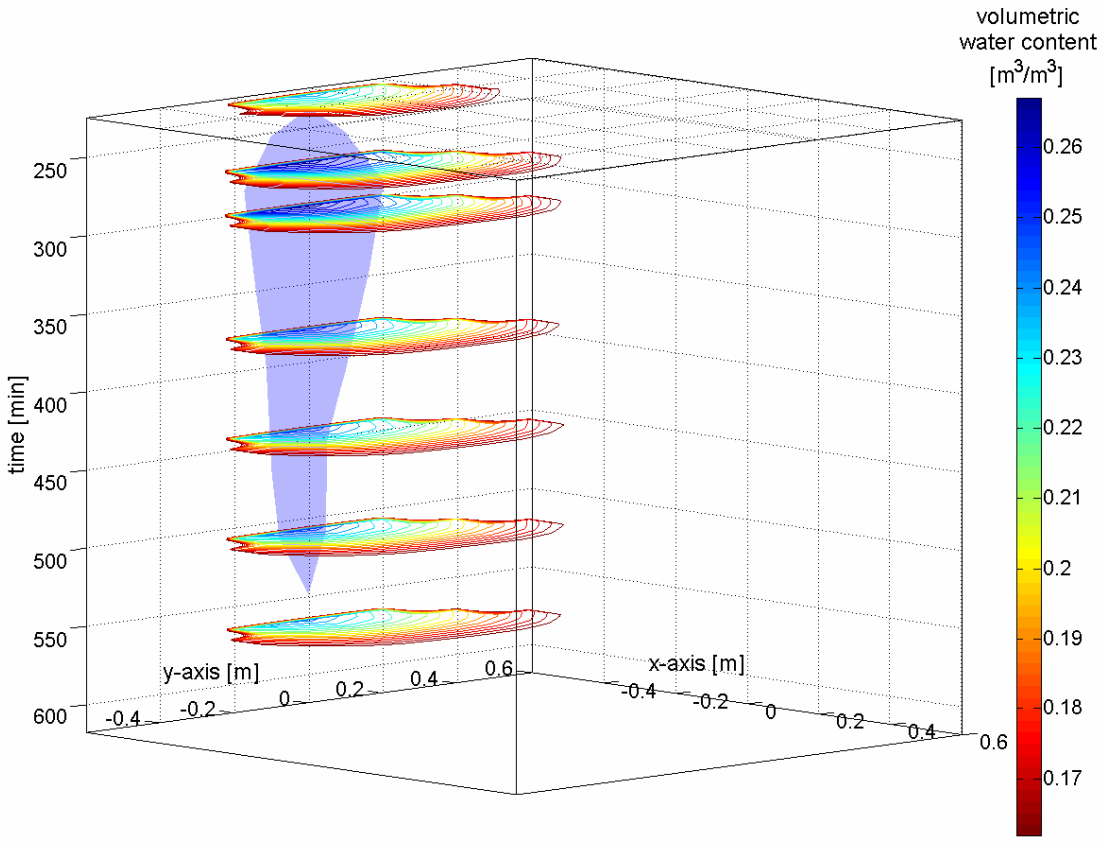

Figure 3.20: Detemined volumetric water content dynamics inside the lysimeter following the irrigation experiment. The isolines range from 0.16 m^3/m^3 to 0.30 m^3/m^3 and the isobody represents 0.25 m^3/m^3.

Comparing the tomographic results with the volumetric water contents determined with TDR, a good correlation is visible (Figure 3.21). With the exception of the result at 226 min, all determined volumetric water contents provide values of less than 0.03 m^3/m^3 discrepancy. Since the tomographic results were truncated, i.e. excluding the outermost 0.1 m circular section of the cylinder, and the TDR probe was situated 0.06 m above the tomographic plane, an exact transfer is not possible anyway. The initial volumetric water contents are in excellent conformance, which suggests relative homogeneous conditions inside the lysimeter in the area of the TDR probe. Furthermore, a good correlation between TDR and georadar is reaffirmed. Looking at Figure 3.21, the difference between the TDR results and the tomographic results for acquisition times greater than 250 min appear to be relatively constant. This can have various causes.

One cause for this difference could be the truncating of the tomographic plane. Due to the extraction procedure of the lysimeter a differing porosity can be expected at the outermost regions from those in the inside regions. On the other hand, preferential flow can be expected for the immediate regions at the hull of the lysimeter. This indicates differing flow properties of the soil, but not necessarily significantly higher volumetric water contents for the outermost 0.1 m.

Another reason mentioned earlier is the error caused by arrival time picking of a dominant feature of the georadar signal. This picking error would consequently influence the inversion and its results. But as displayed in Figure 3.21, this error should also be present for the initial tomographic measurement immediately before the start of the irrigation. Since the initial time zero determination was performed by holding the receiver antenna to the mounted transmitter antenna, which was always positioned at the unwatered side of the lysimeter, strong changes of the antenna characteristics are not very likely. More importantly, looking at (Figure 2.7) and equation (2.25), a constant error for the arrival time picking would be more rigorous for low volumetric water contents than high volumetric water contents. The non-linearity of the relationship between the volumetric water content and the relative permittivity indicates bigger discrepancies for the volumetric water content due to error margins for lower relative permittivities.

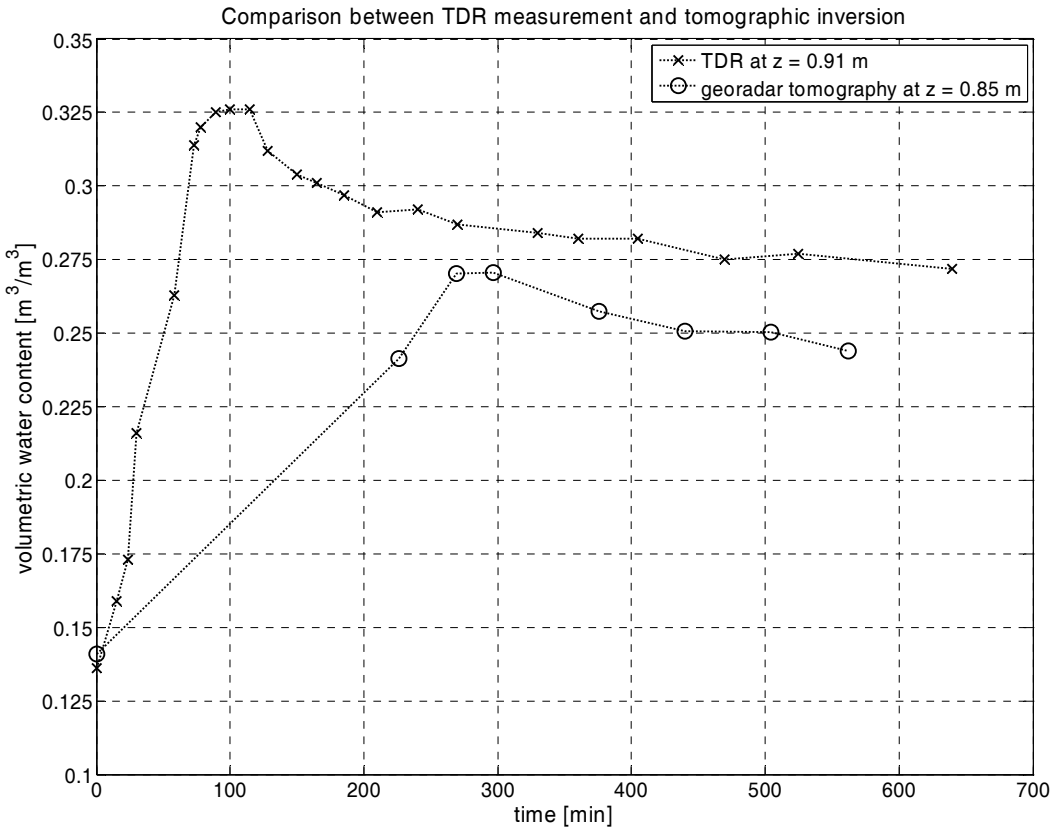

Figure 3.21: Comparison between the volumetric water contents determined by the nearest TDR probe 0.06 m above the horizontal tomographic plane and a corresponding region in the horizontal tomographic plane. The corresponding tomographic region is a rectangular of 0.1 m times 0.1 m since the poor ray coverage required truncating the outermost 0.1 m circular section of the cylinder.

The soil region covered by the TDR probe is generally wetter due to the seepage of water and the retention of water in higher regions of the soil. However, since both methods show constantly decreasing volumetric water contents after 300 min, this reason does not appear very likely. On the other hand, the parallel transmission measurements indicate the presence of an interface at this height. In the case of an interface, the vertical offset between the TDR probe and the georadar plane could be responsible for the differing volumetric water contents.

This would be in accordance with the parallel transmission measurements, where the region above the interface is wetter than the region below the interface.

The most likely reason for the lower volumetric water contents derived by georadar tomography appears to be the regularization. Similar to Figure 4.14, different regularizations can be chosen to produce chiseled or smooth results. In the present case a smooth variant was chosen for two reasons. First, the tomographic inversion was conducted with a neutral mindset, i.e. additional constraints were not applied. Second, with the poor ray coverage and the two missing antenna positions (see Figure 3.17) a chiseled regularization would result in strong artifacts in those two regions. This, of course, would result in a bigger overall error since this region is compared to the TDR results.

4 Ground wave method

4.1 Ground wave of the georadar signal

The ground wave of the georadar signal is an interface wave. It appears at the interface air subsurface. For georadar antennas being placed at the interface, the registered ground wave signal is a secondary wave generated by the EM wave propagating in the subsurface (Figure 4.1). Therefore, the generally known ground wave (Du, 1995; Sperl, 1999; Wollny, 1999; Huisman et al., 2001; Grote et al., 2003; Galagedara et al., 2005a) is actually an air wave excited by the EM wave in the ground. Due to consistency matters, the ground wave is an inhomogeneous wave with finite reach into air. The ground wave is restricted to the nearest vicinity of the interface and features an exponential attenuation rectangular to the interface.

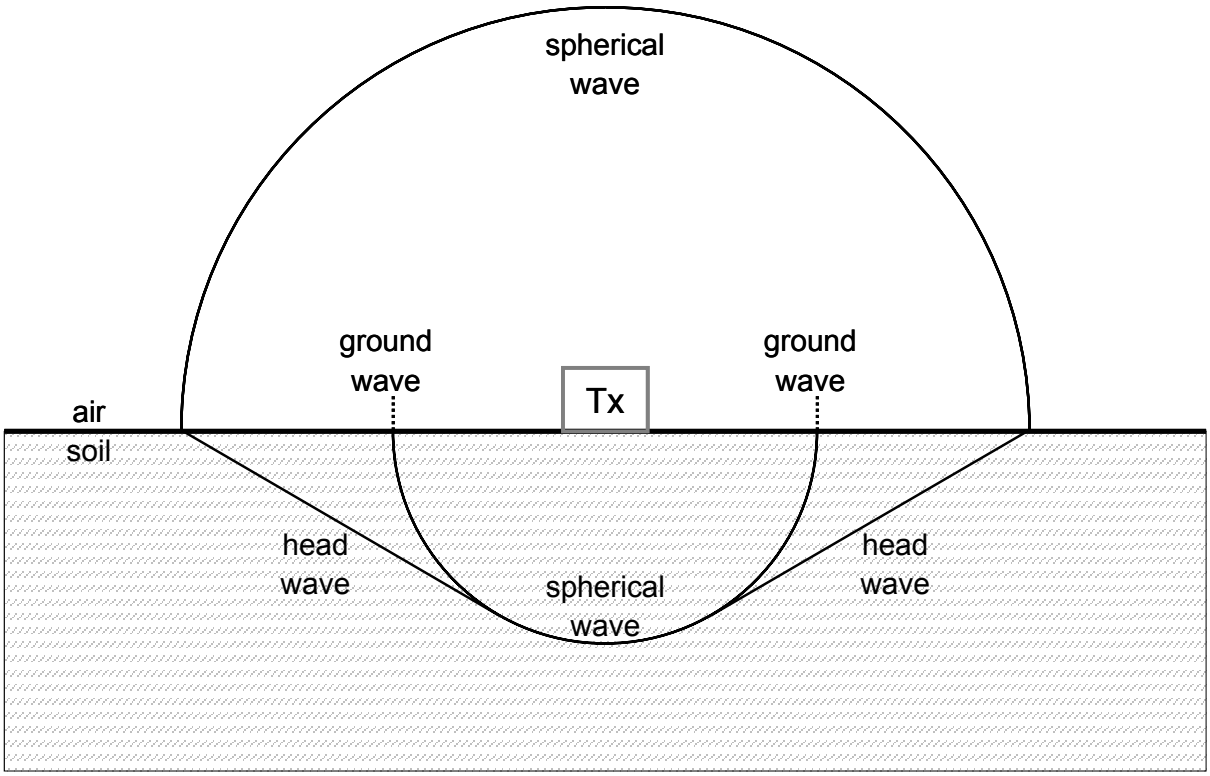

Figure 4.1: Schematic snapshot of the EM wave front generated by a georadar antenna (Tx).

The ground wave of the georadar signal is of great interest for a variety of problems. For one, the ground wave can be an interfering event for more conservative investigation methods such as CMP or CO reflection measurements. The ground wave commonly arrives as the second wave after the direct air wave. Due to the finite character of the georadar signal, reflection events immediately after the ground wave can be difficult to distinguish. This makes it hard to identify shallow reflection events. Since the ground wave occurs as a linear event in CMP measurements, common interpretation techniques such as normal moveout (NMO) or semblance analysis (e.g. Greaves et al., 1996) cannot be used in the time range affected by the ground wave. On the other side, the ground wave presents the opportunity to investigate shallow regions of the subsurface. The propagation velocity of the ground wave is directly correlated with the electrical properties of the soil due to its propagation path *d*.

This is especially beneficial since conventional reflection measurements for shallow investigations feature extremely short EM propagation times. Assuming a reflector depth z of 0.1 m and a relative permittivity of 9 for a homogeneous soil, a propagation time t of 2 ns can be derived using equation (2.25).

Assuming a picking error of 0.1 ns the interpreted relative permittivity ranges from 8.1 to 9.9. Due to the square root of ε in equation (2.25) a picking error of 5% leads in this case to an error of 10% for the relative permittivity. Ground wave measurements cover a comparable depth. Additionally the propagation path d can be increased, minimizing the effect of the picking inaccuracy significantly but reducing spatial resolution.

Du (1995) and Wollny (1999) tried to explain the ground wave in their respective works. They both assumed infinitesimal small electrical dipoles as antennas. Du (1995) formulated an equation for the component of the electrical field E_y parallel to the dipole orientation for both transmitter and receiver dipole. The dipoles were placed directly at the interface and were oriented perpendicular to their connecting line as well as the normal of the interface.

$$E_y = \frac{i\omega\mu_0}{2\pi\left(k_s^2 - k_a^2\right)} \quad \frac{\left(k_a\, e^{ik_a r} - k_s\, e^{ik_s r}\right)}{r^2} \tag{4.1}$$

with k_a and k_s the respective wave numbers for air and soil.

Wollny (1999) used another formulation to explain the ground wave. In his work the transmission of an EM wave field through an interface is observed. Here the transmitter is placed in one half-space and the receiver in the other. The transmitter and receiver are then approached to the interface until the respective distances to the interface are equal to 0 m. Assuming the same dipole orientations as used by Du (1995), the electrical field can be described by the following formula.

$$E_y = \frac{\omega\mu_0}{2\pi k_s^2}\left(k_a\, e^{ik_a r} f - k_s e^{ik_s r}\left(\frac{1}{r^2} + \frac{i}{k_s r^3}\right)\right)$$

$$f = \left(\frac{2}{r^2} + \frac{2i}{k_a r^3} + \frac{ik_a^2}{k_s r}\sqrt{\frac{\pi}{k_a r}}\, e^{ir}\left(\frac{1+i}{2} - \int_0^P \frac{e^{iu}}{\sqrt{2\pi u}}\, du\right)\right) \tag{4.2}$$

$$P = \frac{k_a^3 r}{2k_s^2}$$

Both equations (4.1) and (4.2) differ in their formulation and deduction. But the fact that the propagation velocity depends on the relative permittivity of the subsurface still remains. These formulations are important for the analytical interpretation of the penetration depth of the ground wave. In this context the penetration depth of the ground wave can be described as the vertical segment below the interface having a noticeable effect on the recorded propagation velocity of the ground wave. The vertical penetration depth is of interest when dealing with shallow vertical heterogeneity. To estimate the penetration depth of the ground wave of the georadar, several investigations have been performed experimentally and/or synthetically (Galagedara et al., 2005a, Galagedara et al., 2005b; Sperl, 1999; Wollny, 1999; Voss, 2006). Generally a penetration depth in the range of one wavelength and smaller is concluded. Depending on the definition of the penetration depth some relationships can be given.

Sperl (1999) defined a “Schwerpunktstiefe” or centroid depth z_c. Here the determined relative permittivity from ground wave measurements was directly assigned to the respective depth.

$$z_c(\varepsilon_s) = 0.145 \sqrt{\frac{c_0}{\upsilon\sqrt{\varepsilon_s}}} \quad [\text{m}] \tag{4.3}$$

Assuming a gradual increase in the relative permittivity of the subsurface the penetration depth is not allocated to the resulting covered vertical range. The big disadvantage of such a centroid depth is its dependence on the respective relative permittivity distribution in the subsurface. Therefore equation (4.3) should not be interpreted as a general rule but more of a case-specific relationship deduced for the test site used by Sperl (1999).

Another possible definition of the penetration depth is given by Galagedara et al. (2005b). Here the sampling depth z_{sa} was determined by numerical simulations. Several two-layered subsurface models were generated and the thickness of the upper layer was varied. Galagedara et al. (2005b) defined the sampling depth as the maximum depth of the interface in the subsurface when the determined relative permittivity of the ground wave differed by more than 5% from the relative permittivity of the upper layer. The sampling depth was then determined.

$$z_{sa}(\varepsilon_s) = 0.6015 \frac{c_0}{\upsilon\sqrt{\varepsilon_s}} + 0.0468 \quad [\text{m}] \tag{4.4}$$

The sampling depth in equation (4.4) resembles only the case investigated by Galagedara et al. (2005b), i.e. a two-layered subsurface. Furthermore by defining a 5% cut-off, equation (4.4) is dependent on the relative permittivity contrast of the interface chosen in the numerical simulation. Although Galagedara et al. (2005b) compared equation (4.4) with results from a field experiment, it was pointed out that additional numerical simulations were needed to formulate a more universal relationship.

To obtain the vertical section influencing the ground wave Voss (2006) performed an averaging of the covered vertical relative permittivity distribution. Assuming a penetration depth z_p and a vertical relative permittivity distribution ε_s, the resulting averaged relative permittivity $\bar{\varepsilon}_s$ can be derived by:

$$\bar{\varepsilon}_s(z_p) = \frac{1}{n}\sum_{i=1}^{n} \varepsilon_s(z_i) \quad \text{with } z_n = z_p \tag{4.5}$$

In equation (4.5) no weighting of the relative permittivity distribution was included but could be supplemented if necessary. Deriving the resulting relative permittivity of all possible penetration depths according to equation (4.5) and comparing them to the determined relative permittivity of the ground wave measurement provides the penetration depths. This method was used by Voss (2006) to estimate the penetration depth of the ground wave under defined natural conditions.

A direct comparison between the results of Sperl (1999), Galagedara et al. (2005b), and Voss (2006) is difficult to draw since all three authors defined the relevant region differently and all three used different soils. Although the vertical coverage of the ground wave is still subject of various researches, the high accuracy for homogeneous problems is well documented

(Huisman et al., 2001, Grote et al., 2003, Galagedara et al., 2005a, Müller et al., 2003). To minimize the covered volume of the ground wave for small-scale investigations the measurement layout has to be reworked. Performing a profile measurement, only one of three dimensions can be optimized. One dimension is predetermined by the antenna dimension (Sperl, 1999), whereas the sampled vertical dimension appears to be predetermined by the wavelength of the georadar signal.

4.2 Ground wave measurement layout

The most common application for ground wave measurements are moveout (MO) measurements (e.g. Huisman et al., 2001). Here one antenna is placed at a fixed location and the other antenna is successively moved away. Since the ground wave travels along the surface of the underground it can easily be identified as a linear phase in a MO radar section. Although lateral heterogeneities cause an aberration from the linearity of the ground wave phase, this effect is mostly negligible. The big advantage of the MO measurement is that no absolute time zero is necessary. Therefore, the propagation velocity of the ground wave can easily be derived by:

$$v_{GW} = \frac{s_2 - s_1}{t_2 - t_1} \tag{4.6}$$

with v_{GW} the ground wave velocity, s_i the antenna separation at position i and t_i the propagation time for position i in the radar section (Figure 4.2).

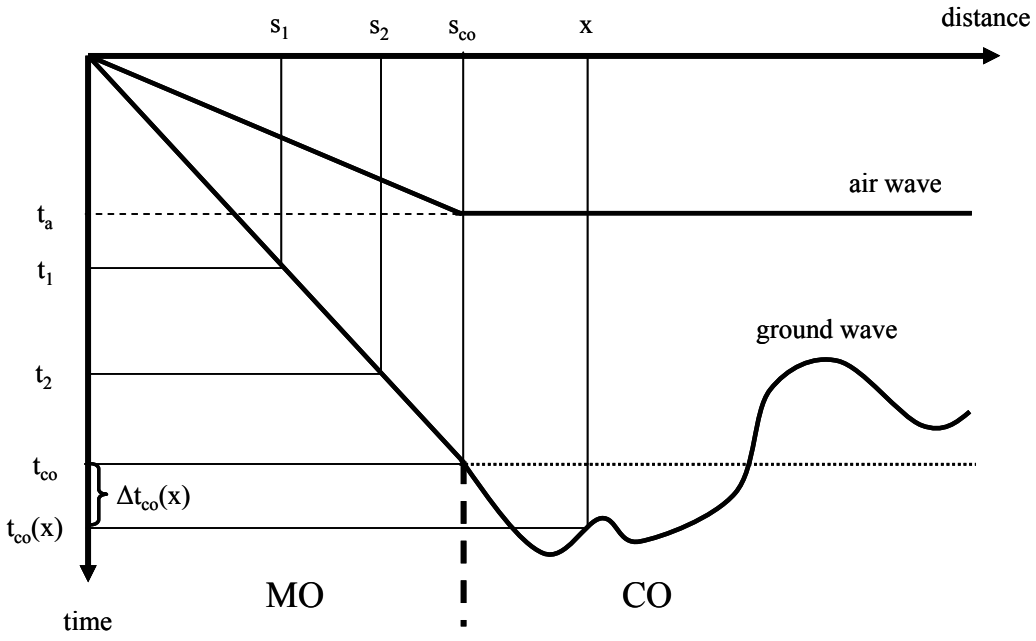

Figure 4.2: Schematic travel time diagram of a ground wave measurement consisting of a MO and CO measurement. Until the separation s_{co} the transmitter and receiver antennas are separated from each other (MO). After that the antennas are moved at a fixed antenna separation s_{co} along the profile.

Another method is the constant offset (CO) measurement, where transmitter and receiver are separated by an appropriate but fixed distance and dragged along a profile (e.g. Grote et al.,

2003). This method is more suitable for the coverage of larger areas, but implies the problem of identifying the ground wave in the radar section with the absence of a MO and the necessity to determine initial time zero. Commonly the propagation time of the air wave is used to determine initial time zero. With the well-known propagation velocity of EM waves in air c_0, the propagation velocity of the ground wave can be derived by:

$$v_{GW} = \frac{s_{co}}{t_{co} - \left(t_a - \frac{s_{co}}{c_0} \right)} \tag{4.7}$$

with s_{co} the antenna separation, t_{co} the recording time of the ground wave and t_a the recording time of the air wave (Figure 4.2). A big disadvantage of the CO measurement is the uncertainty whether the correct ground wave phase of the georadar signal is used. In the field various phases like reflected waves or critical refracted waves can be identified (Huisman et al., 2001) and are interfering with the recorded ground wave signal. These interferences basically result in erroneous time picking and consequently wrong interpreted soil moisture contents. On the other hand, shielded GPR antennas often lack an air wave due to their shielding.

A third and most useful method was proposed by Du (1995) and is a combination of the MO and CO measurements. An MO is performed at the beginning of a radar section until the ground wave can be easily separated from the air wave and is then followed by a CO measurement in the same radar section without stopping the measurement. This ensures two very important issues. First, the propagation velocity can be determined without the necessity of initial time zero and second, the measurement layout enables quick coverage of large areas. The resulting ground wave velocity distribution is given by:

$$v_{GW}(x) = \frac{s_{co}}{\left(\frac{s_{co}}{\frac{s_2 - s_1}{t_2 - t_1}} \right) + \Delta t_{co}(x)} \tag{4.8}$$

with $v_{GW}(x)$ the ground wave velocity at the location x, generally the midpoint between transmitter and receiver. Δt_{co} denotes the arrival time difference between $t_{co}(0)$ and $t_{co}(x)$.

Often the combined MO and CO measurement is separated into two single measurements. First a MO measurement is performed to determine the optimal antenna separation and the initial ground wave velocity. After that a CO measurement with the previously determined antenna separation is carried out. This procedure is often reasoned by the necessity to fix the antennas to sleds or other similar devices. This may be justifiable for measurements on homogeneous sites where no strong variations of the soil moisture are expected. For measurements on a heterogeneous subsurface with strong electric property variations in a spatial range of a decimeter, this procedure is not advisable. To be sure to gather correct data, the combined MO and CO measurement in the same data recording should be mandatory. Depending on the electrical parameters of the subsurface and the antenna characteristics the identification of the correct ground wave phase can be difficult.

4.3 Data interpretation

Using the combined MO and CO measurement provides only integral ground wave velocities for the covered distance between transmitter and receiver. This antenna separation is dependent on various parameters such as the electric properties of the subsurface, antenna characteristics, antenna housings etc. Assuming the most rudimentary model for the ground wave propagation path, i.e. direct connection between transmitter and receiver antenna moved into the subsurface, the propagation distance d of the air wave and the ground wave is the same. Consequently, the propagation times for both direct air wave and ground wave intersect at initial time zero for an antenna offset of 0 m. For an inline CO profile measurement of a lateral heterogeneous soil the corresponding arrival time t of the ground wave can be derived by:

$$t(x) = \sum_{i=1}^{n} t_i(x) = \sum_{i=1}^{n} \frac{d_i \sqrt{\varepsilon_i(x)}}{c_0} = d \frac{\sqrt{\varepsilon(x)}}{c_0} \tag{4.9}$$

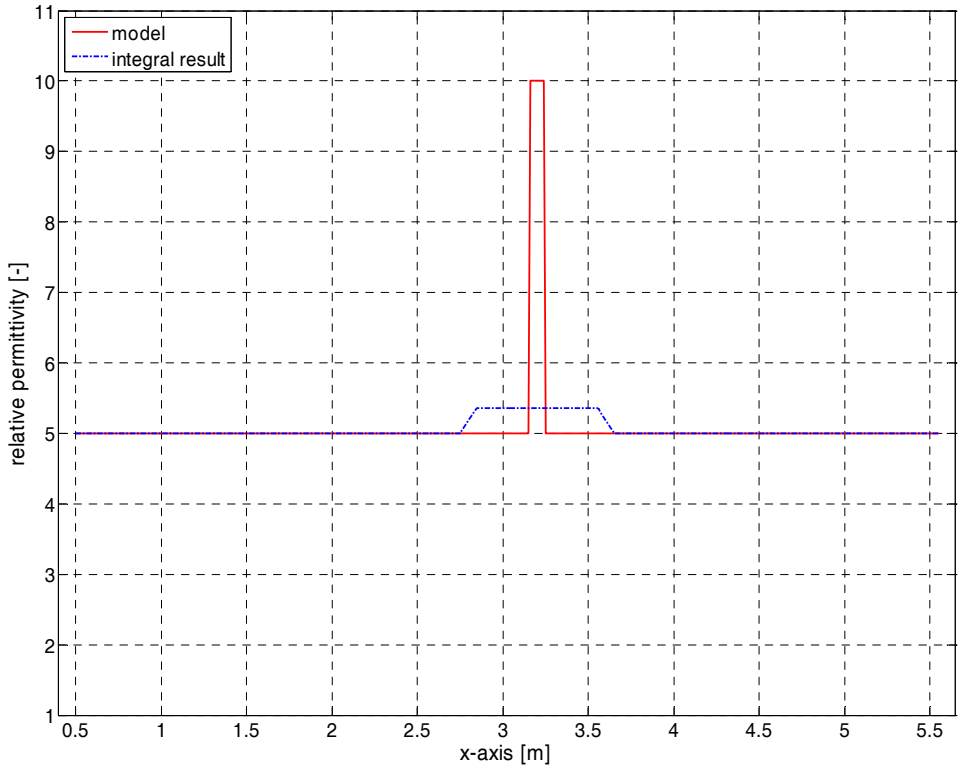

Figure 4.3: Determined relative permittivity due to ideal ground wave measurement data and its integral result for a 0.1 m anomaly and 0.8 m antenna separation. The resulting correlation coefficient is R = 0.31 and the standardized RMS error (see (4.11)) RMS_{std} = 13.8%.

Based on equation (4.9) the propagation times for a simple three-region model can be derived. In this case a 0.1 m anomaly with a relative permittivity of 10 ($\Theta \approx 0.209$ m^3/m^3) is enclosed by a background relative permittivity of 5 ($\Theta \approx 0.093$ m^3/m^3) (Figure 4.3). Assuming a step width Δx smaller than the antenna separation d, each segment of the soil $\varepsilon_i(x)$ is covered multiple times. In the presented case an antenna separation of 0.8 m is used and the corresponding step width is 0.01 m.

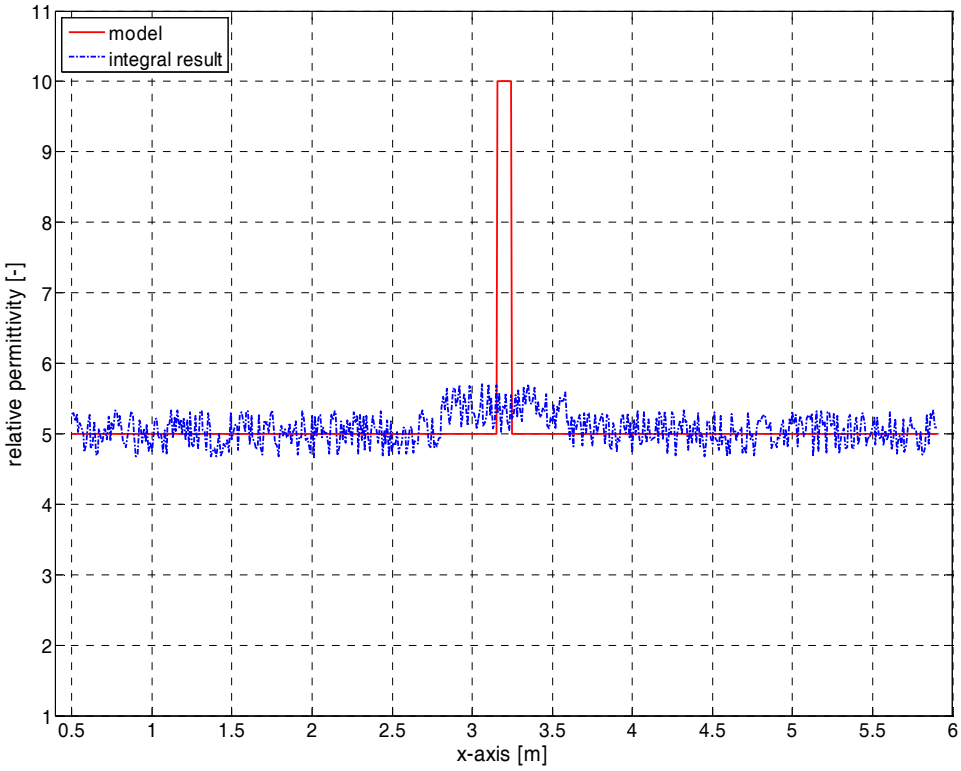

Figure 4.4: Determined relative permittivity due to ideal ground wave measurement data and its integral result for a 0.1 m anomaly and 0.8 m antenna separation with 0.2 ns white noise. The resulting correlation coefficient is R = 0.15 and the standardized RMS error (see (4.11)) RMS_{std} = 12.7%.

To increase the spatial accuracy the antenna separation is generally decreased (Grote et al., 2003). Using for example an antenna separation of 0.4 m as opposed to the aforementioned 0.8 m, the maximum effect of the anomaly is 0.76 in the relative permittivity (Figure 4.5) and reproduces only 57.6% of the actual anomaly value. Paired with the narrower maximum due to the smaller antenna separation, the perceptibility of the anomaly is enhanced (Figure 4.5). On the other hand, a time picking error of 0.2 ns is enough to nearly mask the anomaly (Figure 4.5). This is caused by the stronger effect of the picking error since the propagation time decreases with decreasing propagation distance. Therefore a reduction of the antenna separation is only reasonable if the propagation time can be determined with sufficient accuracy.

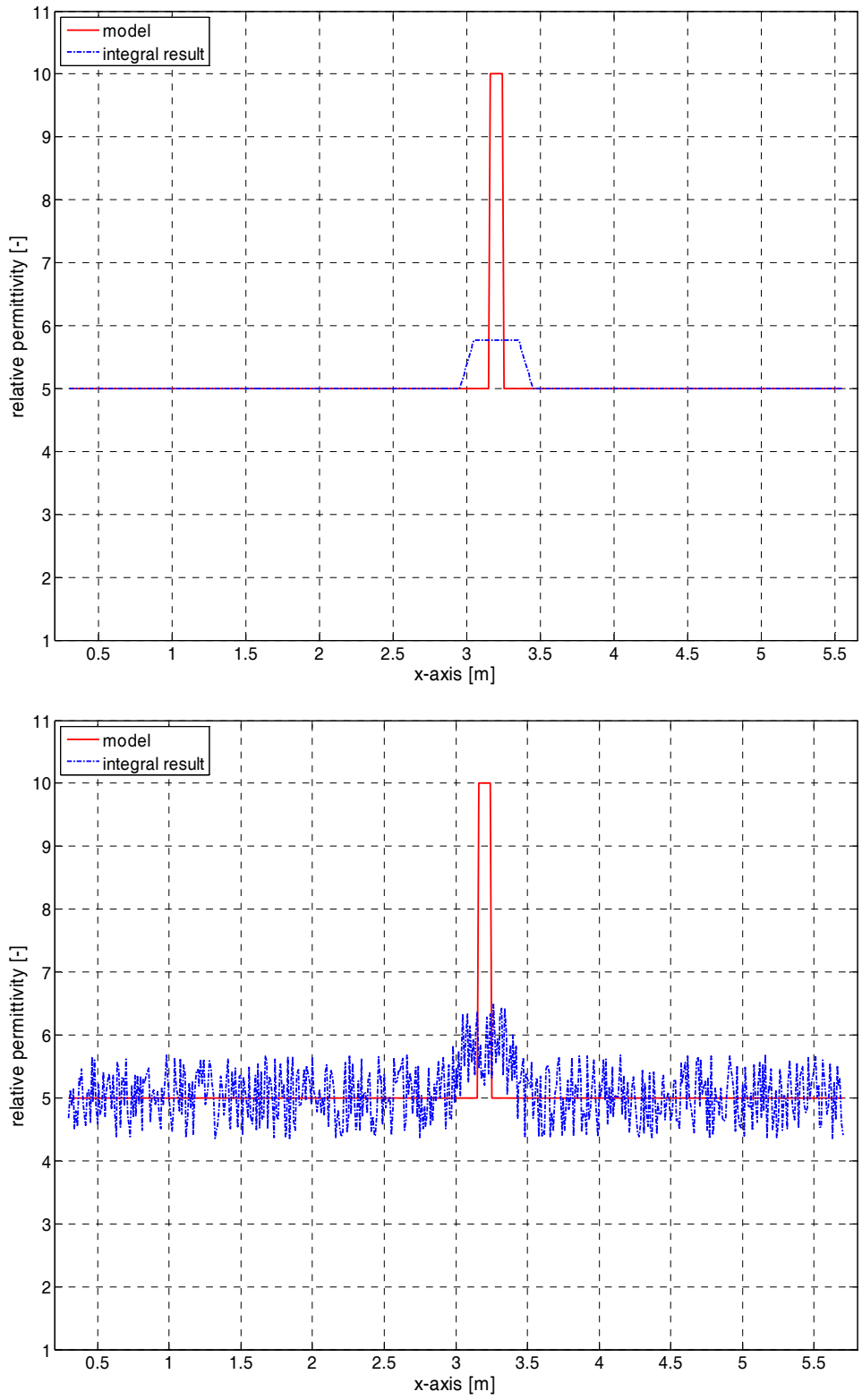

Figure 4.5: Resulting integral relative permittivities for an antenna separation of 0.4 m (above). The resulting correlation coefficient is R = 0.48 and the standardized RMS error (see (4.11)) RMS_{std} = 11.4%. Relative permittivities calculated after additional application of 0.2 ns white noise (below). The resulting correlation coefficient is R = 0.18 and the standardized RMS error (see (4.11)) RMS_{std} = 13.9%.

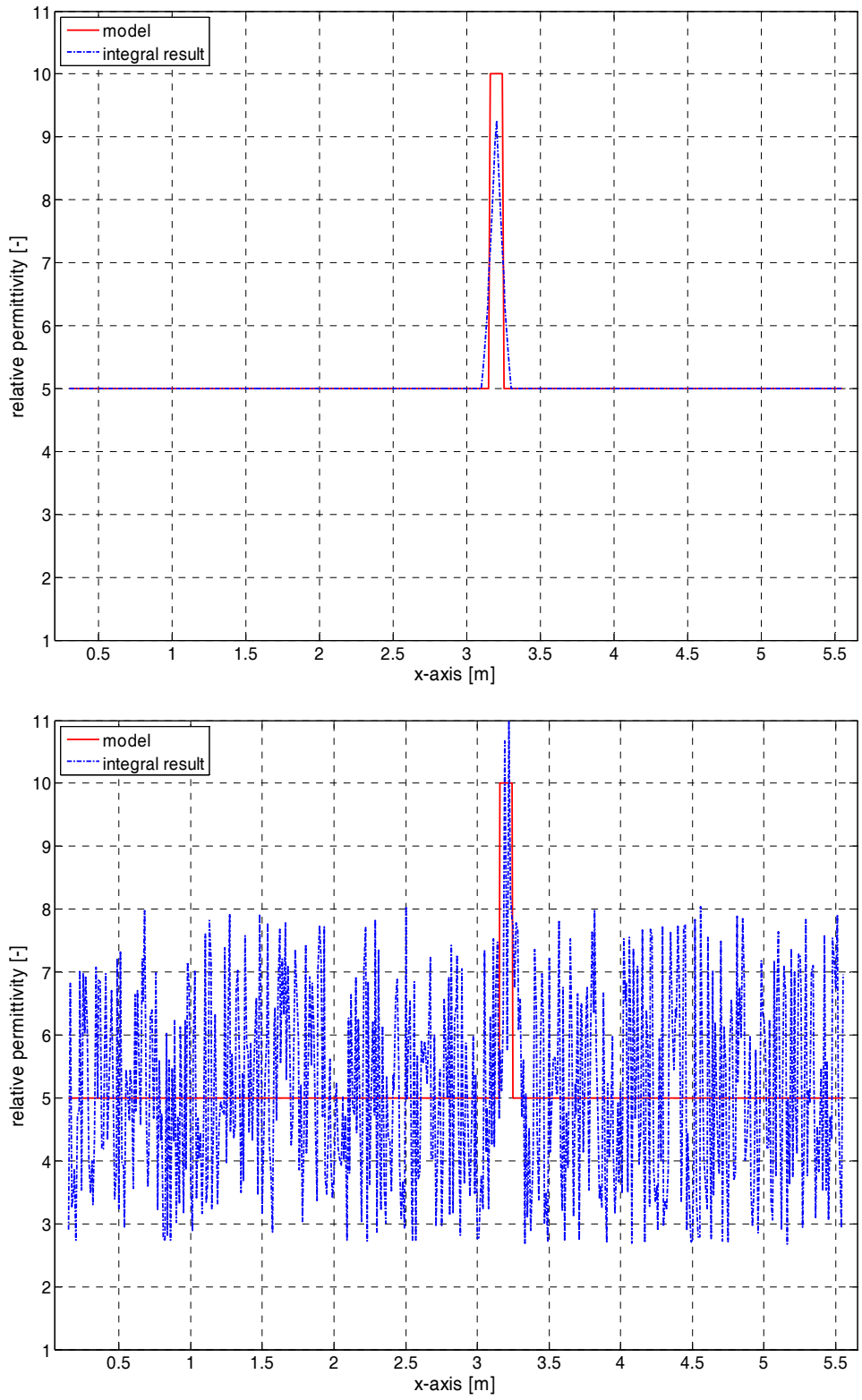

Figure 4.6: Resulting integral relative permittivities for an antenna separation of 0.1 m (above). Due to the simulated step width of the measurement the relative permittivity of the anomaly is not reproduced to its actual value since no measurement was situated at the necessary location. The resulting correlation coefficient is R = 0.92 and the standardized RMS error (see (4.11)) RMS_{std} = 6.2%. Relative permittivities calculated after application of 0.2 ns additional white noise (below). The resulting correlation coefficient is R = 0.20 and the standardized RMS error (see (4.11)) RMS_{std} = 31.2%.

In this case, even a reduction of the antenna separation to 0.1 m (Figure 4.6), or the dimension of the anomaly, and a picking inaccuracy of 0.2 ns masks the anomaly. Although a visible effect of the anomaly is present, a quantitative evaluation is extremely difficult if not impossible. In the present case, the full value of the anomaly is not reproduced since the antennas would require to be placed at one exact position combination. This is not the mandatory case when performing a ground wave measurement and hence the relative permittivity of the anomaly is not represented by the integral result.

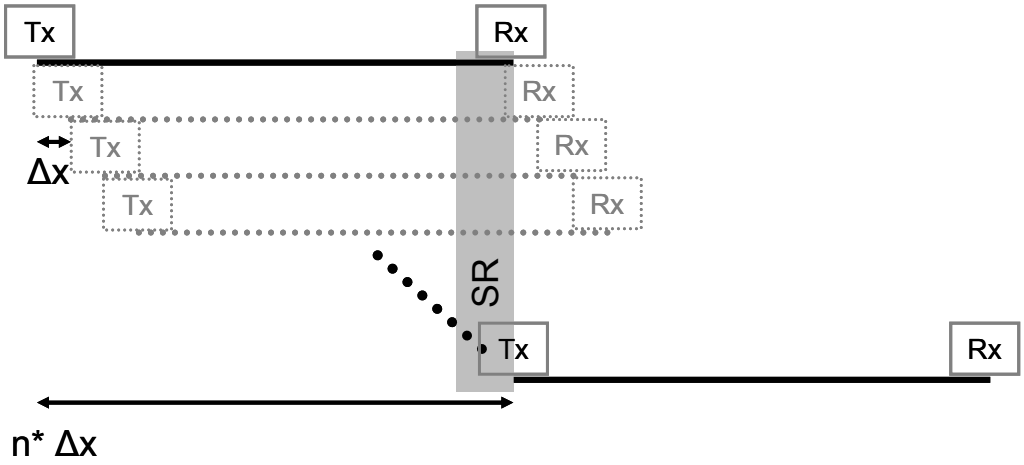

Figure 4.7: Schematic drawing of a profile measurement with constant step width Δx over a soil region SR. In the present case the transmitter Tx reaches the initial location of the receiver Rx after n steps. For better presentation reasons the presented profile measurement is not totally in line.

Due to the utilized measurement layout, i.e. inline CO profile measurement with step width smaller than the antenna separation, an alternative interpretation can be made. Dividing the soil covered by the ground wave in equidistant parts of the size of the step width Δx with:

$$d = \sum_{i=1}^{n} \Delta x_i \tag{4.10}$$

and using equation (4.9), each soil region is covered n-times in a CO profile measurement (Figure 4.7). Therefore an inversion measurement of the travel times can be performed, similar to tomographical measurements. The inversion algorithm is integrated in the software package REFLEXW by Sandmeier (2006) and is based on a Semi Iterative Reconstruction Technique (SIRT) introduced by Dines and Lytle (1979). Even though such a tool is not necessary for this problem since only a one-dimensional inversion is performed, the tomographical tool provides flexibility. The ground wave measurement can be performed in various ways, including 2D measurements with freely distributed profiles, since the georadar is most flexible and presents no restrictions.

Applying the inversion on the initial dataset, i.e. 0.8 m antenna separation, a distinct maximum is reproduced (Figure 4.8). The center of the anomaly correlates very well with the anomaly derived from the tomographical inversion. Although the value of the anomaly is not reproduced, the maximum relative permittivity of the tomographical inversion result of 7.69 represents a 53.8% excitation from the background or 76.9% of the actual anomaly value. The width of the interpreted maximum of 0.2 m or approximately 0.15 m, when including a 10%

threshold for the anomaly identification, correlates well with the actual anomaly width of 0.1 m.

On the other hand, several artifacts can be recognized. The two closest artifacts to the actual anomaly at 2.4 m and 4.0 m also display an additional feature of the applied inversion. Here a restricting condition was implemented. This can be a handy feature if additional information of the investigated soil is known. An example could be minimum or maximum expectable volumetric water contents. In the present case a lower boundary for the propagation velocity, and consequently for the relative permittivity, was implemented for the inversion.

Deriving the correlation coefficient R for the integral and the inversion results, an improvement is noticeable. The integral result only produces $R_{int} = 0.31$, whereas the inversion result produces a much better correlation with $R_{inv} = 0.88$. Since the correlation coefficient only presents the linear relationship between two parameters, in this case the actual relative permittivity and the determined relative permittivity, an additional examination parameter is used. The standardized root mean square (RMS_{std}) error, or coefficient of variation (Sheriff, 1997), is given by:

$$RMS_{std} = \frac{\sqrt{\frac{1}{n}\sum_{i=1}^{n}(M_i - I_i)^2}}{\frac{1}{n}\sum_{i=1}^{n} M_i} \tag{4.11}$$

with M the model value and I the integral, respectively inversion value. This way, the root mean square error for different models is better comparable, since the general RMS error is difficult to translate when comparing different models. Here the RMS_{std} is enhanced from 13.8% for the integral result to 7.4% for the inversion result.

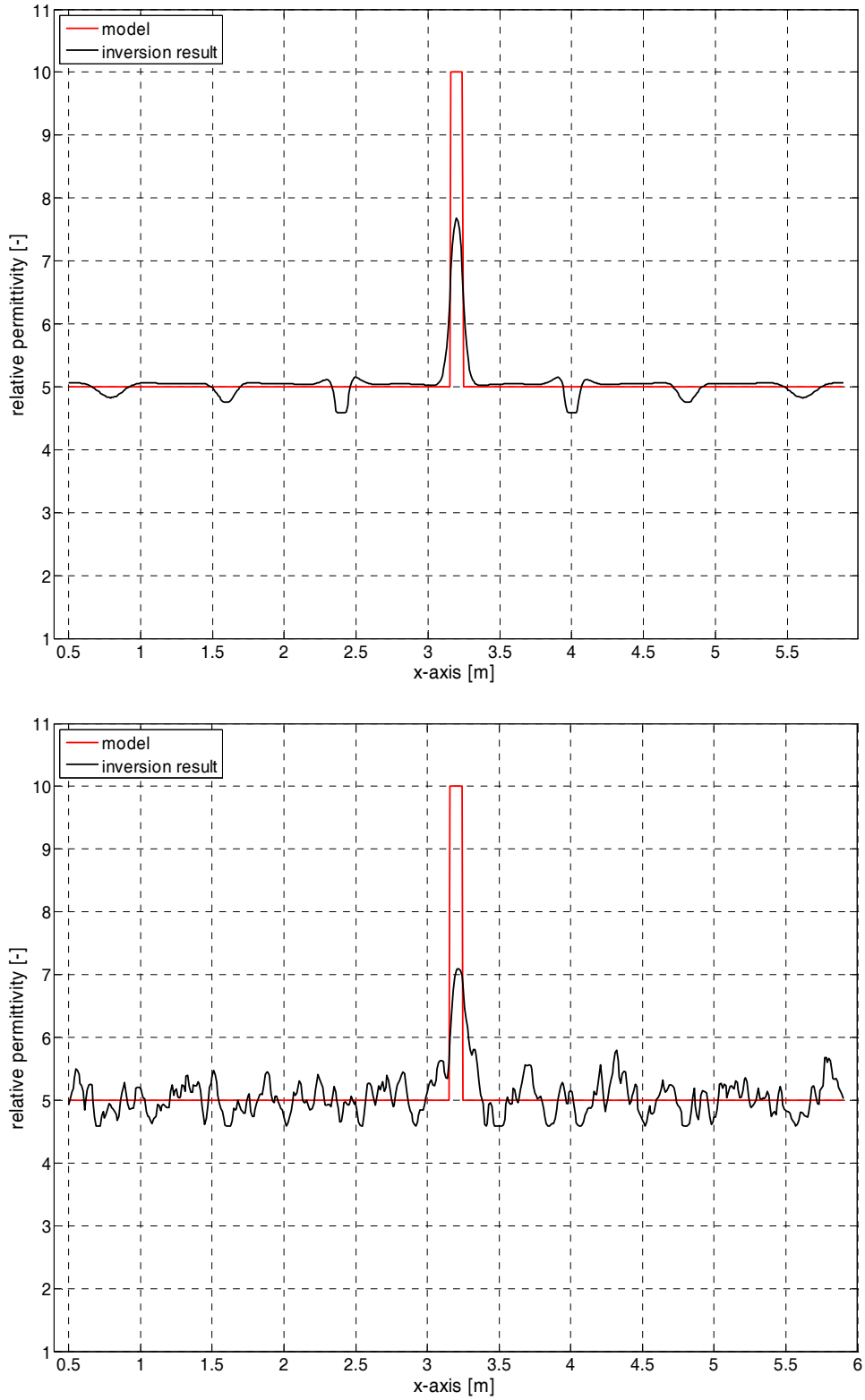

Figure 4.8: Determined relative permittivities due to ground wave travel time inversion for an antenna separation of 0.8 m (above). The resulting correlation coefficient is R = 0.88 and the standardized RMS error (see (4.11)) RMS_{std} = 7.4%. Relative permittivities after the travel time inversion and an additional 0.2 ns white noise (below). The resulting correlation coefficient is R = 0.60 and the standardized RMS error (see (4.11)) RMS_{std} = 10.1%.

Applying a noise of 0.2 ns to the time picking, the tomographical inversion features again a distinct maximum (Figure 4.8). The center of the anomalies correlates very well, although the inversion somewhat shifts the base of the anomaly in x-direction. This is caused by the noise, which features no symmetry around the anomaly (see Figure 4.4). The maximum of the interpreted anomaly with 7.09 is still a distinct feature. The other spikes do not exceed a 10% threshold, with the lone prominent exceptions at approximately 4.3 m and 5.8 m. Although the actual relative permittivity of the anomaly is not reproduced, the anomaly of only an eighth of the antenna separation is easily detectable. In this case the correlation coefficient has increased from $R_{int} = 0.15$ to $R_{inv} = 0.60$. The standardized RMS is still enhanced from 12.7% to 10.07%. This lower degree of data correctness is caused by the increased occurrence of artifacts in the inversion interpretation due to the data noise. The bandwidth of the artifacts caused by the data noise does not feature significantly higher undulations in the interpreted relative permittivities. One noticeable effect is a lowpass filtering of the data. This can be changed due to the implemented regularization. Generally the rule can be made that the lower the regularization the noisier the interpreted relative permittivities will get. The regularization should be applied in the way that anomalies of the aspired spatial dimension can still be identified. This means for the current case that anomalies of 0.1 m should still be distinguishable which is successfully achieved.

The accompanying artifacts caused by the noise are noticeable but can be qualified by a reasonable criterion. In this case an implementation of a threshold derived from the average relative permittivity ε_{av} over 0.8 m, i.e. the antenna separation d, would be suitable to identify the anomaly (Figure 4.9). If additional information is available such as a variogram, twice the data range, a reference value for the spatial dimension of the heterogeneity, could be used instead. In this case, without any additional information, the threshold was chosen as follows. Based on the average propagation velocity, in this case $v_{mean} = 0.1342$ m/ns, and the picking uncertainty of $\Delta t = 0.2$ ns, the threshold was derived by:

$$\varepsilon_{thres}(x) = \varepsilon_{av}(x) \pm \varepsilon_{\mathrm{var}} = \varepsilon_{av}(x) \pm \left(\frac{c_0}{\frac{d}{\frac{d}{v_{mean}} \pm \Delta t}} \right) \approx \varepsilon_{av}(x) \pm 0.08 \cdot \varepsilon_{av}(x) \qquad (4.12)$$

Utilizing a threshold such as in equation (4.12) anomalies with smaller relative permittivity contrasts cannot be detected. On the other hand, it appears to be reasonable to use a coarser discretization of the relative permittivity. Depending on the aspired goal, an exact quantitative determination of the relative permittivity is not necessary. Localizing e.g. water repellent and wettable areas, or detecting preferential flow paths, a qualitative evaluation of the relative permittivity may be sufficient.

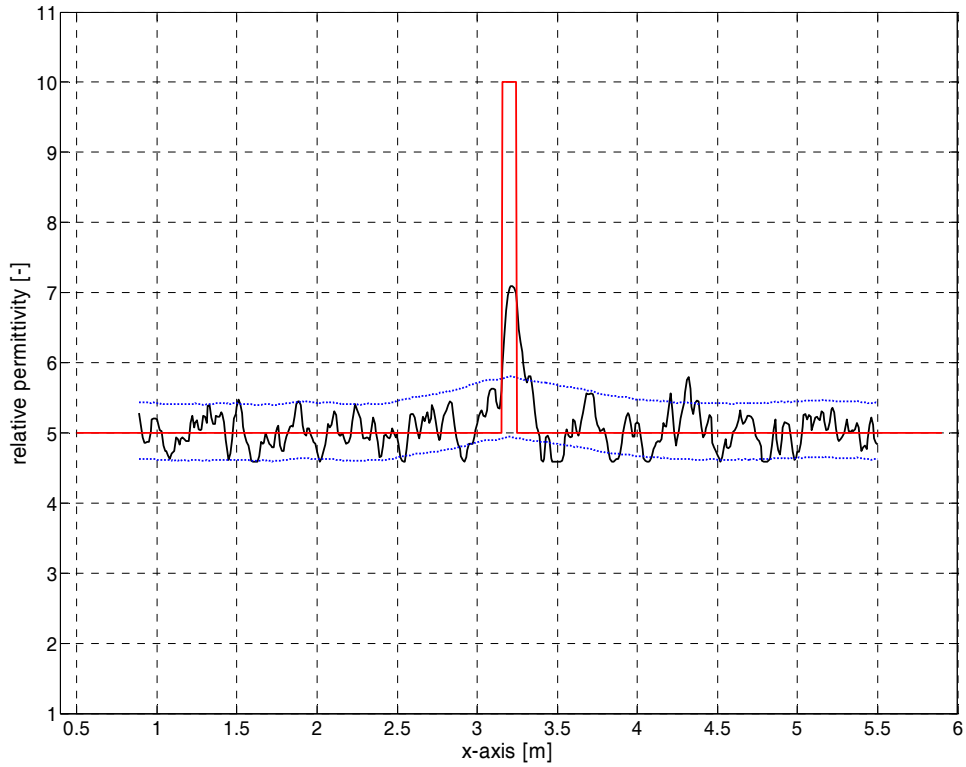

Figure 4.9: Determined relative permittivities due to ground wave travel time inversion for an antenna separation of 0.8 m with 0.2 ns white noise and a threshold of ± 0.08 ε_{av}.

Until now, only ideally derived propagation times were used and additionally perturbed by white noise. In the next step the ground wave measurement was synthetically simulated. This simulation was derived from a finite difference time domain (FDTD) module implemented in the software package REFLEXW by Sandmeier (2006). This modeling algorithm was also used by Sperl (1999) in his evaluation of the penetration depth of the ground wave. In his investigations Sperl (1999) placed the transmitter in the air, whereas the receiver was placed inside the soil. This way he achieved best data quality for his analysis. The air wave was still recognizable, although in the form of the head wave. In this work both the transmitter and receiver are placed in air near the soil-air interface with at least one raster point between transmitter and receiver, respectively, and the interface. The data quality is sufficient to successfully pick the dataset (Figure 4.10) and by using this layout a more realistic simulation can be performed.

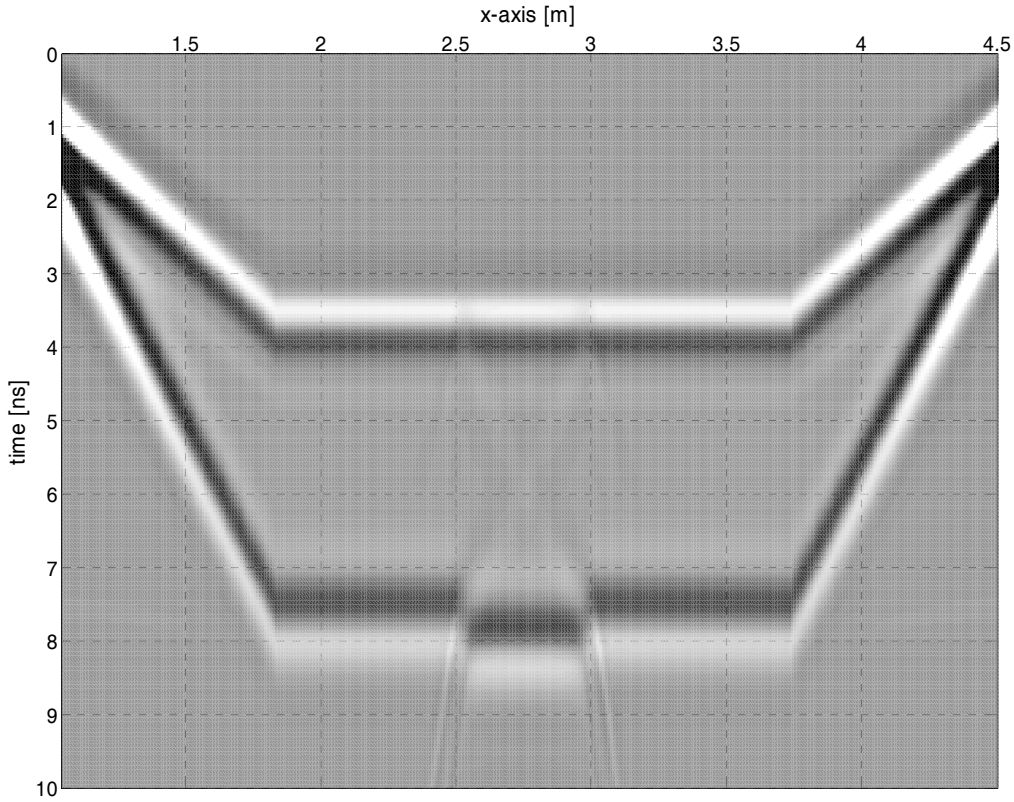

Figure 4.10: Synthetic radar section for a ground wave measurement over a 0.1 m wide anomaly with MO at the start and the end of the recording. The first arriving signal corresponds to the air wave, the second to the ground wave. Due to the distinct lateral relative permittivity change a reflection is generated for both the air wave and the ground wave. These reflections can be traced to later arrival times.

Comparing the interpreted integral relative permittivities (Figure 4.11) for the theoretical derivation and the simulated one, two significant differences can be recognized.

First the integral relative permittivities derived from the FDTD modeling feature undulations at the anomaly. This is caused by the fact that the transition from the background of 5 to 10 is a distinct one without a gradual increase. Therefore, the EM wave is reflected and generates a disturbing wavelet superposing the actual ground wave signal (Figure 4.10). This superposition results in an additional reduction of the time-picking accuracy. Although such distinct lateral transitions are doubtful for field ground wave measurements, several other similar disturbances of the recorded signal can occur. Such interfering events could be caused by objects in the soil or in air and have both effects on the quality of the time picking (van der Kruk and Slob, 2004).

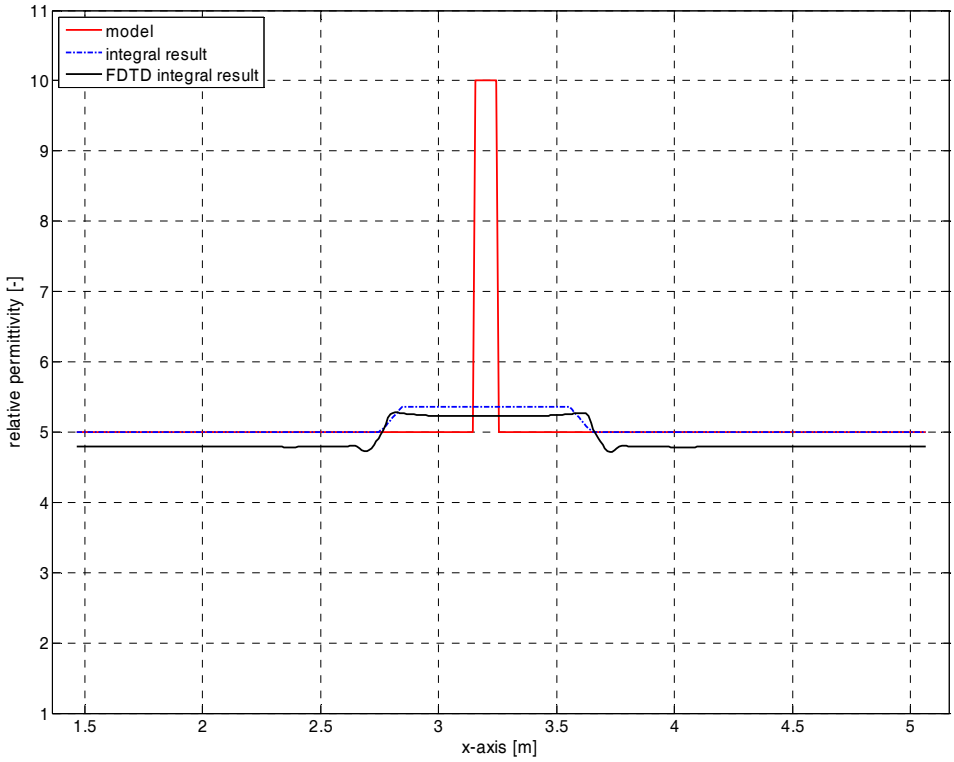

Figure 4.11: Comparison between integral relative permittivities derived with simple propagation times (blue dash-dotted) and determined FDTD propagation times (black solid).

Second the FDTD simulation underestimates the relative permittivity of the subsurface with the used transmitter and receiver combination. In this case, the difference between theoretical derived and simulated determined relative permittivity is approximately 0.2 or 4%. This error appears not to be caused by false relative permittivity discretization in the algorithm or varying antenna separation due to the raster increment. Therefore this aberration can be either caused by a systematic picking error or by a differing propagation path. Using the relative permittivity of the soil ε_s of 5 ($\Theta \approx 0.093$ m^3/m^3) and the determined relative permittivity ε_{sd} of 4.78 ($\Theta \approx 0.087$ m^3/m^3) the propagation path through air can be derived. Assuming a symmetrical propagation from transmitter into the soil and from the soil to the receiver (Figure 4.12) the following equations are valid.

$$\sqrt{\varepsilon_{sd}} = s_a\sqrt{\varepsilon_a} + s_s\sqrt{\varepsilon_s}$$
$$\text{and} \qquad (4.13)$$
$$s_s + s_a = 1$$

with s_s and s_a the respective relative propagation path through soil and air. Postulating an EM propagation following ray optics, the EM ground wave has a maximum under the following incident angle Wollny (1999):

$$\sin\vartheta_c = \sqrt{\frac{\varepsilon_a}{\varepsilon_s}} \qquad (4.14)$$

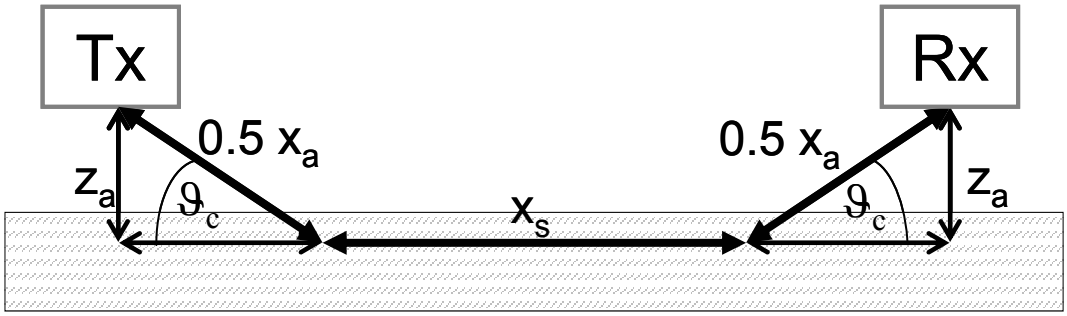

Figure 4.12: Schematic propagation path of the ground wave assuming ray optics.

With this relationship, the actual propagation path can be derived as (see Figure 4.12):

$$x = x_s + x_a = d - 2\frac{z_a}{\tan \vartheta_c} + 2\frac{z_a}{\sin \vartheta_c} \tag{4.15}$$

In the present case, the elevation of the transmitter and the receiver is 0.01 m, respectively, and the antenna separation is 0.8 m. Therefore, the propagation path x can be derived to 0.8047 m with 0.7600 m in the soil and 0.0447 m in air. The resulting propagation time can be derived by:

$$t = t_a + t_s = \frac{x_a\sqrt{\varepsilon_a}}{c_0} + \frac{x_s\sqrt{\varepsilon_s}}{c_0} \tag{4.16}$$

In this case the propagation time according to ray-optical assumptions would be 5.81 ns (or $\varepsilon_{sd} = 4.75$), which is well matching the determined propagation time of 5.83 ns (or $\varepsilon_{sd} = 4.78$). Although an exact interpretation of real ground wave measurements using ray optics appears far fetched (Wollny, 1999), explaining the travel time reduction of the FDTD simulations with ray optics appears reasonable.

Again a white noise of 0.2 ns was applied to the picked EM propagation times. Comparing the determined relative permittivities for the integral result and the inversion result, an enhancement in the perceptibility of the anomaly is registered (Figure 4.13). The correlation coefficient has increased from 0.15 to 0.73, whereas the standardized RMS error has decreased from 14.90% to 11.17%. In this case the validity of the RMS error may be a little bit relativized, since the used propagation times do not match exactly the assumed theoretical propagation times (see equation (4.16)). On the other hand, the anomaly can easily be distinguished when applying a threshold criterion (Figure 4.14). Even better matches can be achieved depending on the applied regularization on the inversion parameters (Figure 4.14). However reducing the regularization will feature stronger artifacts originated from the data noise as well as the inversion algorithm itself.

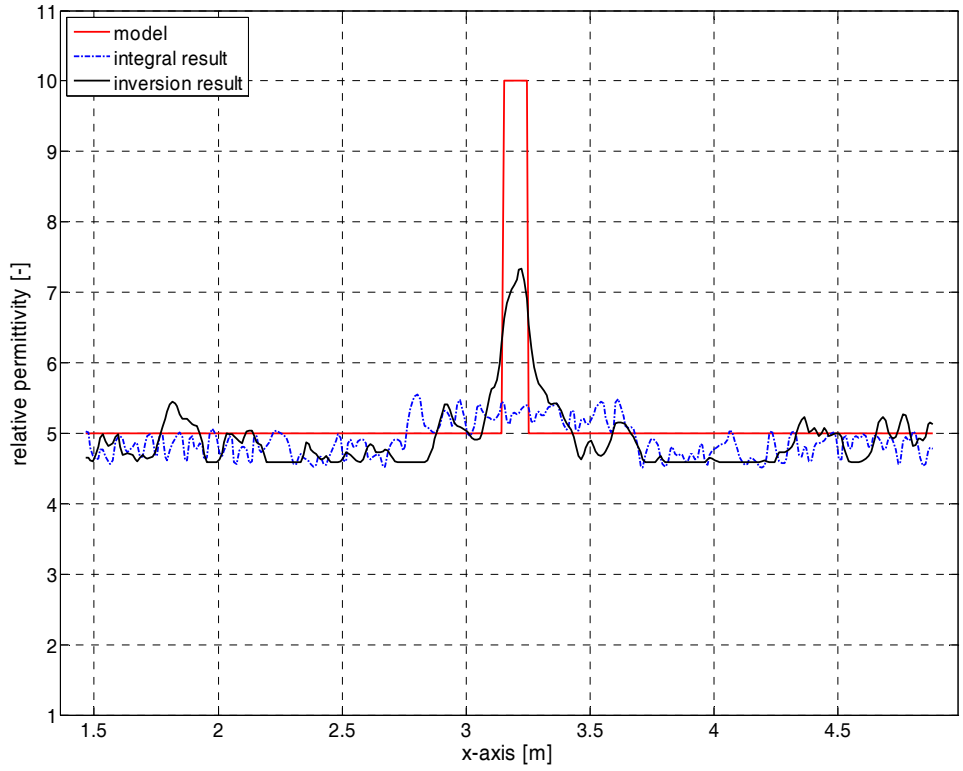

Figure 4.13: Comparison of determined integral (blue dash-dotted) and propagation time inverted (black solid) relative permittivity using FDTD data for an antenna separation of 0.8 m with 0.2 ns white noise.

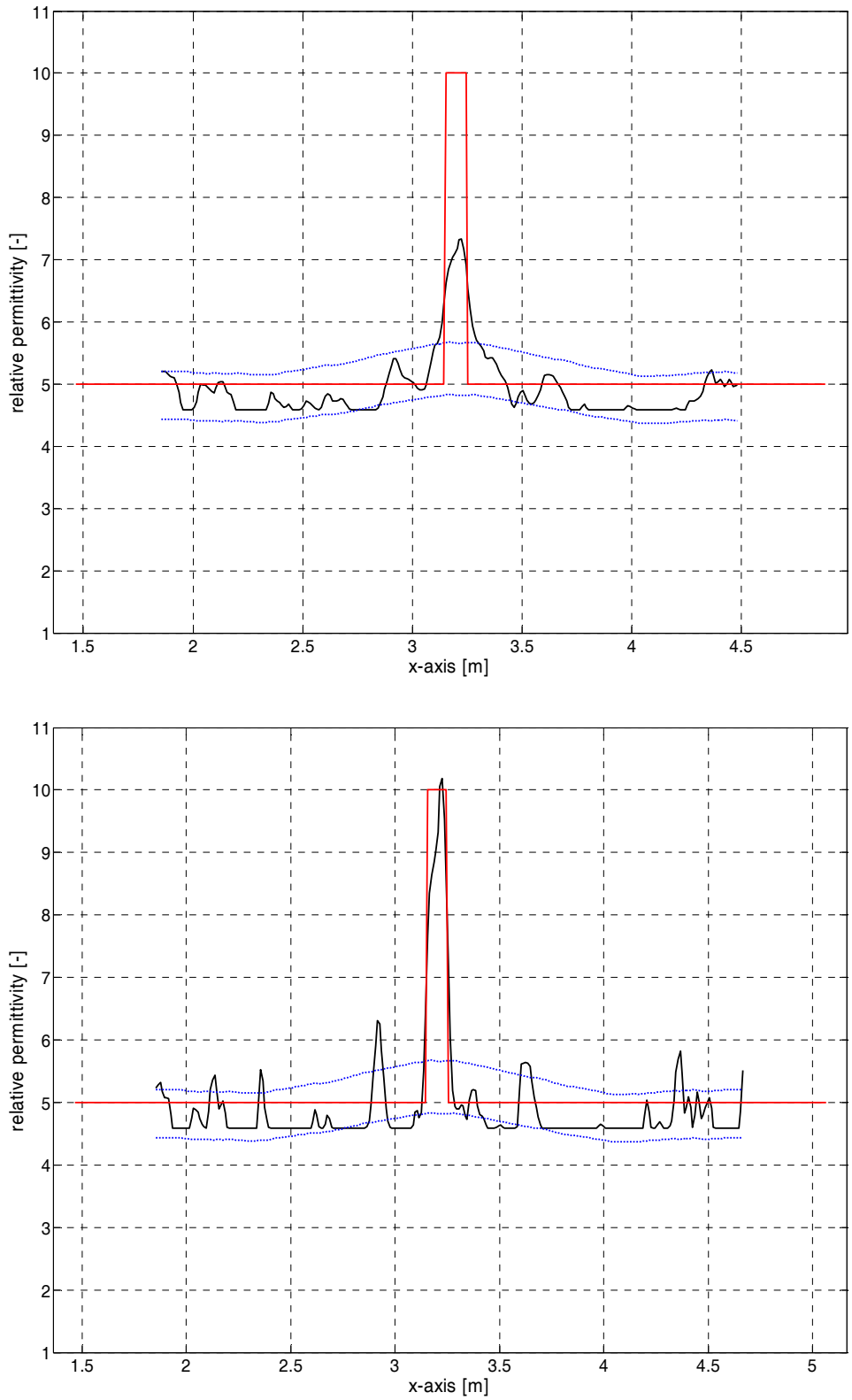

Figure 4.14: Identification of the anomaly using a threshold criterion and two different regularizations. The upper graph features a smoother regularization whereas the lower graph presents an accentuation of narrower but stronger incidents. Both data sets were derived by FDTD modeling for an antenna separation of 0.8 m with 0.2 ns white noise.

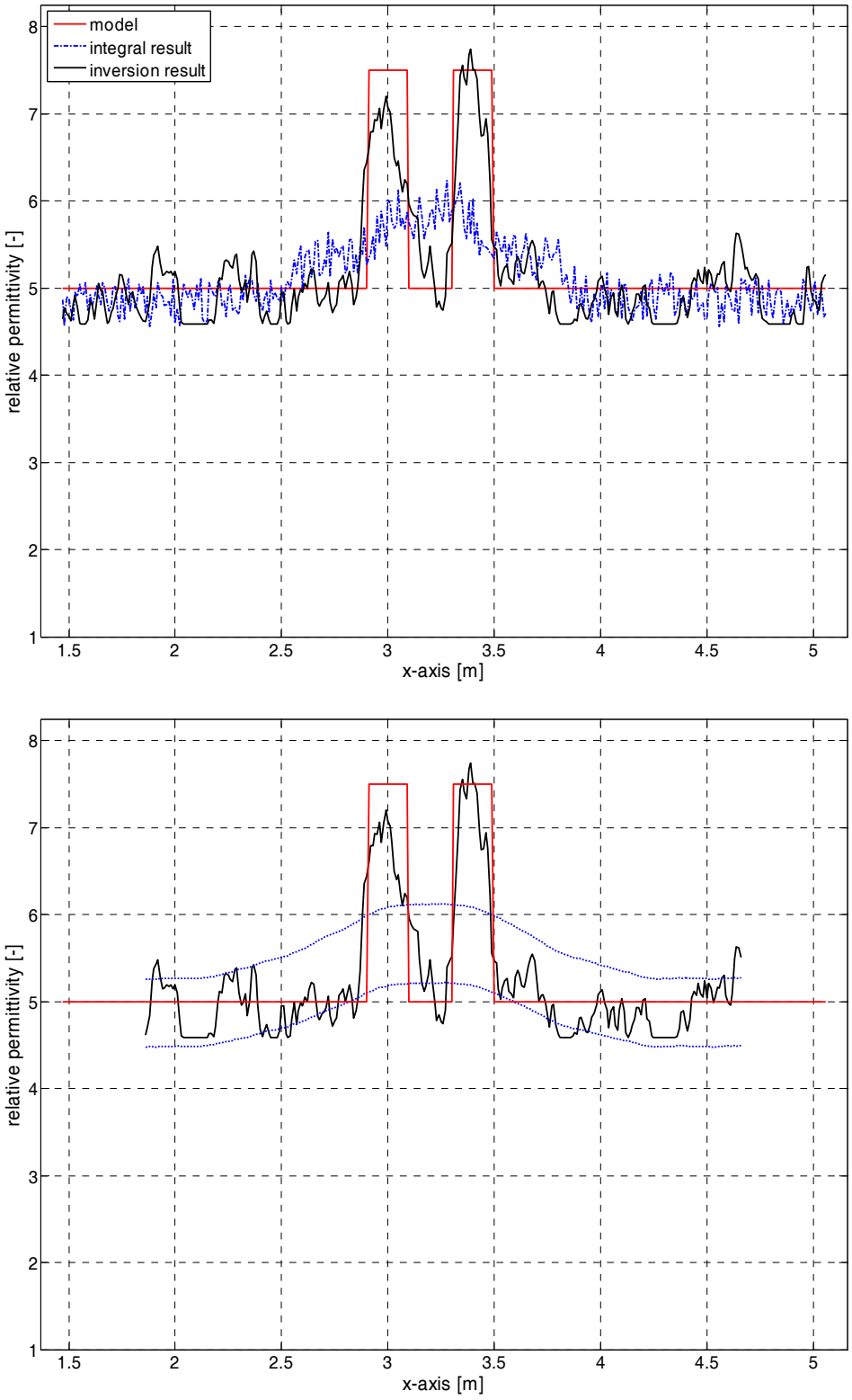

Figure 4.15: Comparison of integral results and inversion results for a model with two anomalies (above). Identification of the anomalies for the inversion results by applying a threshold. The data set was derived by FDTD modeling for an antenna separation of 0.8 m with 0.2 ns white noise.

An additional model is used to check the spatial resolution. In this case two 0.2 m wide anomalies separated by 0.2 m are investigated. The background relative permittivity is 5

($\Theta \approx 0.093$ m^3/m^3) and the relative permittivities of the anomalies are 7.5 ($\Theta \approx 0.159$ m^3/m^3). The propagation times were determined from a FDTD simulated synthetic radar section and a white noise of 0.2 ns was applied additionally. Comparing the resulting interpreted relative permittivities, the inversion produces again a better and more distinguishable match (Figure 4.15). In this case both the correlation coefficient with 0.86 compared to 0.54 for the integral interpretation as well as standardized RMS errors of 7.77% compared to 12.66% indicate a better fit. More important, the integral interpretation indicates the presence of one anomaly, negating the existence of two distinct anomalies. Although the presence of the two anomalies can be guessed due to the podium-like trend of the relative permittivity, it is doubtful that this would be resolvable for a field dataset. The inversion interpretation features two distinct anomalies in contrast to the integral interpretation. Because of the applied regularization the anomaly values are in the correct magnitude, whereas the artifacts can be widely neglected due to the threshold (Figure 4.15).

4.4 Application example

To check the advantages of the propagation time inversion compared to the integral determination, a field test was performed. In this case a location had to be found featuring shallow soil moisture heterogeneity. Both global trends as well as small-scale heterogeneities had to be present. The INTERURBAN test-site Tiergarten, an urban recreation area in Berlin, Germany (Müller et al., 2003) appeared to be ideal since this site features an approximately 30 m profile suitable for investigations. The Tiergarten is a park in the center of Berlin and was created between the 17^{th} and 20^{th} century. As common for an urban park the soil is in a steady evolution process. After World War II many craters were filled with surrounding debris resulting in sometimes strong anthropogenic layering (Figure 4.16). Otherwise the humus layer of the soil is a sandy soil with generally above 80% sand, less than 15% silt and less than 5% clay content. Below this 0.4 m to 0.6 m thick humus layer a soil with a sand fraction above 95% reaches down beyond the ground water table. Depending on topography the ground water table lies between 1.5 m and 2.5 m below soil surface. The humus layer has approximately 5% C_{org} content and features water repellent regions with actual repellencies of up to 10 h (Huraß and Schaumann, 2006). The lateral size of those repellent areas is in the range of few decimeters.

Figure 4.16: Exemplary soil profile of the INTERURBAN site Tiergarten, Berlin, Germany. Although the inclusions are not representative for the whole area, high soil heterogeneity is universally present.

The data was recorded in four interlacing parts. This division in smaller parts was necessary since the utilized cables of the georadar antennas, 1GHz RAMAC, MALÅ GeoScience, Sweden, were too short for a single recording. Moving the radar control unit was no option, since even slight stress on the glass fiber cables can result in unpredictable shifts in the recorded radar sections. At the beginning of each of the four profiles a MO was performed to ensure the correct identification of the ground wave. The used antenna separation was 0.65 m and the step width was 0.04 m. The profile itself features a small topography of approximately 0.5 m with profile meter 150 m at the lowest and 179 m at the highest point.

Looking at the integral result of the ground wave measurement (Figure 4.17), a general trend is visible. The volumetric water content decreases gradually from an approximate range between 0.44 m^3/m^3 and 0.50 m^3/m^3 at 150 m to below 0.21 m^3/m^3 at 179 m. In between several small-scale variations can be registered. To get an estimate of the small scale volumetric water content, several TDR measurements were performed. The volumetric water content determined with the TDR probes is representative for a soil cylinder of approximately 0.03 m of diameter and 0.10 m of height. Assuming the geometrical area spanned by the antenna widths of 0.10 m and the antenna separation of 0.65 m as the corresponding spatial reference, then the ratio between TDR to georadar is approximately 1:23. Depending on the volumetric water content the corresponding volume covered by the ground wave could be derived using equation (4.4). Both the TDR and georadar volumetric water contents feature

similar trends although the TDR indicates by far stronger local variations. This is of course an effect of the smaller covered soil volume resulting in more distinct events. Looking at the areas denser sampled with TDR at 154 m to 155 m and 174 m to 176 m, again TDR and georadar are quite similar. Larger trends such as the decrease of the relative permittivity at approximately 175.25 m are well resolved, whereas the ones at approximately 174.5 m or 154.5 m are not distinguishable from the georadar data. A thresholding criterion similar to (4.12) could be formulated. This could be based on statistical analysis of the acquired TDR data or similar to the earlier used geometrical assumption.

Comparing the volumetric water contents from the propagation time inversion and the TDR measurement, a similar good correspondence with the general trend can be found (Figure 4.17). The corresponding spatial accuracy of the inversion result is still approximately 6 times larger than the TDR. In (Figure 4.17) some segments feature conspicuous differences.

- The segment between 152 m and 153 m features two maxima surrounding one minimum whereas the inversion indicates two minima enclosing one maximum.
- The segment between 157 m and 158 m features wide diverging values as well as the wrong affiliation of maximum and minimum.
- The two segments between 174.5 m to 175 m and 175.5 m to 176 m feature such a high heterogeneity in the TDR data that a correct reproduction with the georadar is not expected.
- The last segment is situated between 178 m and 178.5 m and features diverging volumetric water contents.

Therefore, taking the extremely small sampling volume of the TDR into account, the propagation time inversion produces well-fitting volumetric water content values with smaller related soil regions than the integral results.

The georadar appears to be better suited for the estimation of the volumetric water content of soils than TDR probes. The big advantage of the TDR, localized point-like measurement, can also be its big disadvantage. Performing field measurements at a large site, numerous measurements have to be performed with TDR. Assuming small scale heterogeneity in the range of decimeters, too few measurements can result in erroneous spatial interpretations. In the present case, the acquired TDR data cannot be used to interpolate between the data points, since the denser sampled segments indicate a strong heterogeneity. Therefore TDR data collected few centimeters away from the initial location may feature strongly varying values. On the contrary, integral georadar measurements may mask anomalies smaller than the antenna separation. This disadvantage can be revised to a certain extent by inverting the propagation times of the ground wave. Although smallest anomalies may not be identified and the exact values may not be reproduced, a sufficient accuracy can be achieved to identify small-scale variations. This may be especially valuable if small anomalies are to be detected in an otherwise relatively homogeneous environment, e.g. inclusions or water intrusions in pavements.

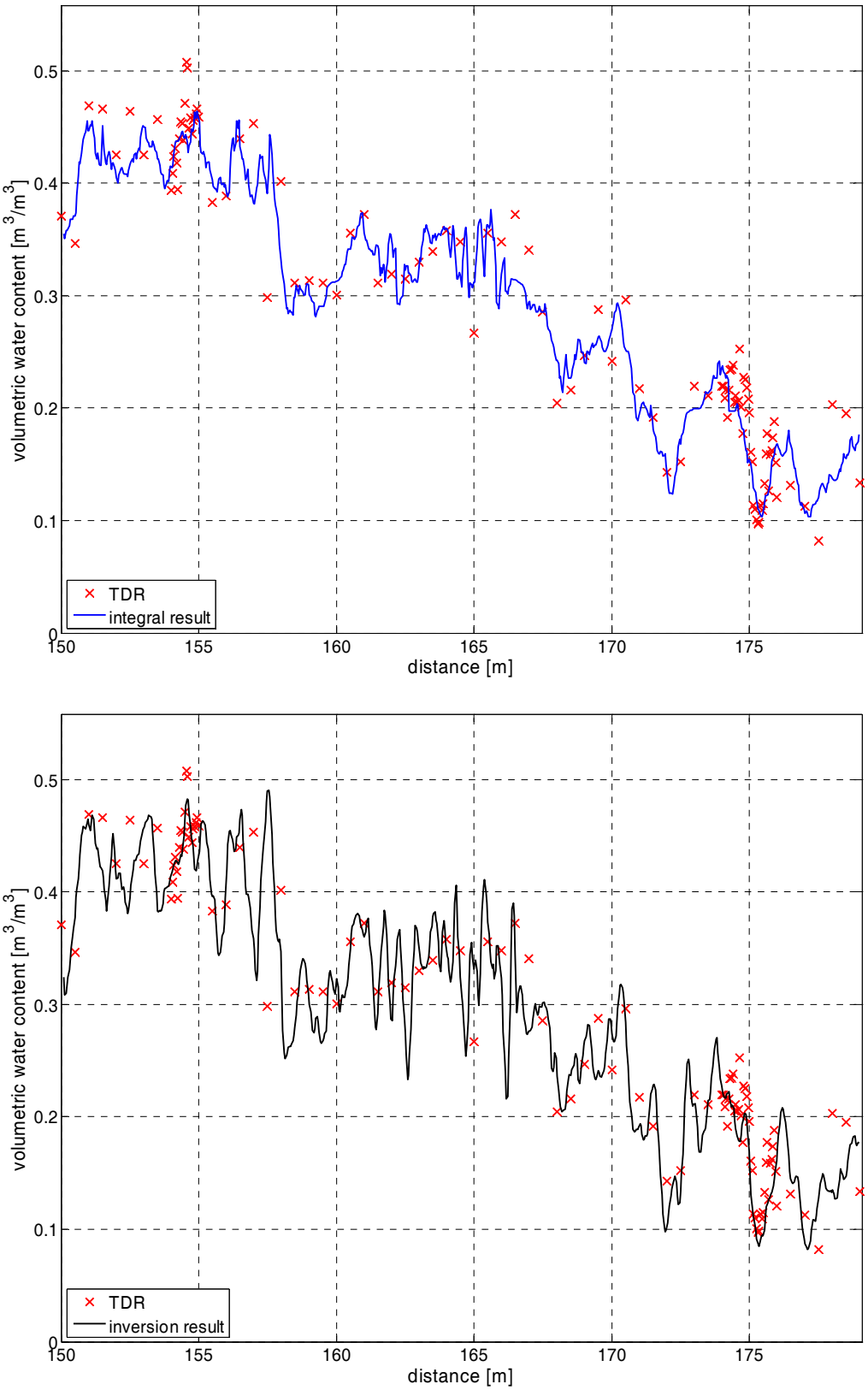

Figure 4.17: Comparison of determined relative permittivities by TDR (red crosses) and georadar ground wave measurements (blue line) (above). Comparison of determined relative permittivities by TDR (red crosses) and georadar ground wave measurements using the travel time inversion (black line) (below)

5 Radar Based – Time Domain Reflectometry (RB-TDR) method

Using the ground wave of the georadar signal, an easy and concise determination of the shallow distribution of the relative permittivity can be obtained (see chapter 4). To acquire the vertical distribution of the relative permittivity is another task. Most often one of three different georadar layouts is used to assess the vertical relative permittivity distribution.

- CMP measurements utilize reflections generated by interfaces in the subsurface (e.g. Greaves et al., 1996). CMP measurements provide accurate integral relative permittivities for the soil above the interface if plane reflectors are present, i.e. no steeply dipping interfaces and no significant lateral variations can be assumed. With the presence of a vertical layering with sufficient contrast of their respective electrical parameters (see equations (2.31) and (2.32)), a vertical distribution of the relative permittivity can be obtained. Here, the vertical resolution is one fourth of the wavelength (Jol, 1995), restricting the applicability further. Taking the antenna characteristics into account, additional information such as the relative permittivity of the lower layer or the electrical conductivity of the upper layer, can be gathered (e.g. Gregoire and Hollender, 2004, Helm, 1998).
- Another possibility is a parallel transmission measurement similar to the application described in 3.1.3. Since such accessibility is scarce for field investigations, boreholes are used instead. Parallel transmission measurements as well as tomographical measurements can be performed (e.g. Binley et al., 2001).
- Since boreholes are relatively expensive, another possibility is the VRP which requires the presence of only one borehole. Both borehole methods have the same disadvantages. The uppermost parts of the soil cannot be determined precisely since disturbing refracted georadar signals occur (Tronicke and Knoll, 2005). Small-scale variations in the range of few decimeters cannot be resolved, since commercial borehole georadar antennas are mostly low-frequency antennas below 100 MHz nominal frequency.

To acquire a local vertical distribution of the uppermost regions of the soil in a minimal invasive manner, specialized probes are mainly used. Such tools can be TDR probes (e.g. Scheuermann et al., 2002), radioactive logs (e.g. Bohrleber, 1992) or other similar devices (e.g. Hübner, 1999). These devices commonly require the presence of a coated borehole. All devices generally consist of a control unit and a specialized probe being lowered into the borehole. One risk in such operations is that the probe could tilt in the borehole. This could result in the loss of the probe, the borehole, or extensive services to recover the tilted probe, especially in the case of radioactive logs.

In the present case two main requirements were to be met. A robust georadar layout should be found to obtain small-scale vertical relative permittivity profiles even without the presence of distinct reflectors. On the other hand the layout should be flexible enough to be used for monitoring experiments as well as scanning measurements to acquire a map of the vertical relative permittivity distribution of the uppermost soil.

5.1 RB-TDR layout

The Radar Based Time Domain Reflectometry (RB-TDR) layout was first discussed by Igel et al. (2001). In Müller et al. (2003) and Schmalholz et al. (2004a) this layout was also denominated Local Moisture Sounding (LMS). For a RB-TDR measurement a common georadar system and a metallic rod are required. The metallic rod is inserted in part into the

subsurface and the georadar antennas are placed next to the rod (Figure 5.1). The transmitter antenna emits an EM impulse which propagates into the subsurface but gets also coupled to the metallic rod. The coupled EM wave travels along the metallic rod as a guided EM wave and which is partly reflected at the end of the rod. The reflected EM wave travels back to the surface and is registered by the receiver antenna. Here the analogy to the TDR method is obvious. By pushing the metallic rod gradually deeper into the subsurface and recording further georadar traces, the reflection at the end of the rod appears at later recording times, whereas every other reflection of additional interfaces remains at the same recording time. This makes it very easy to identify the reflection of the rod even in the unprocessed radar section (Schmalholz et al., 2004a). By lowering the position of the reflecting end of the metallic rod, the RB-TDR layout can be additionally compared to a VRP measurement. With the benefit that RB-TDR does not require a borehole big enough to lower a georadar antenna.

The metallic rod can also be placed inside an electrical insulating tube inside the subsurface. By using a tube, the rod can be lowered repeatedly into the subsurface enabling monitoring at that location. By using the RB-TDR layout in addition to an electrical insulating tube, a vertical profile measurement can be performed in a short period of time. For example a vertical measurement down to 1.0 m with 0.02 m steps requires less than 3 min, resulting in a dataset of 51 data recordings.

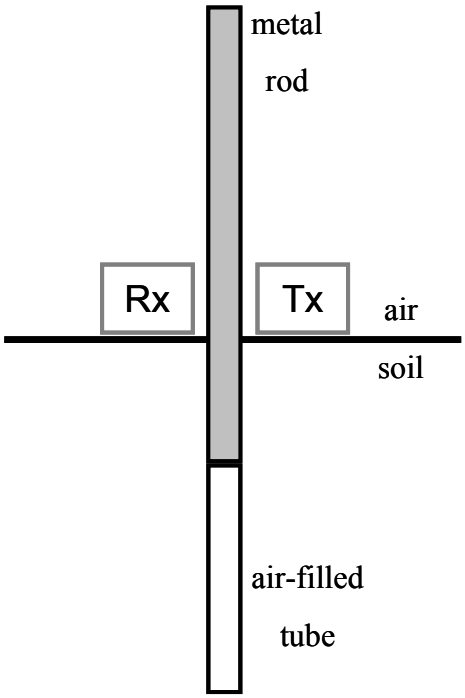

Figure 5.1: Schematic layout of a typical RB-TDR measurement.

To discuss the RB-TDR layout the propagation of the EM wave can be split into two parts. The first is the generation of the georadar wavelet and its characteristics depending on the electrical parameters in the vicinity of the antenna. The second part is the propagation of the guided EM wave along the metallic conductor as well as the reflection at the end.

The transmission characteristics of georadar antennas are mostly divided into three spatial regions. In the far field the georadar antenna can be assumed to be an infinite small dipole (Arcone, 1995). In this case the EM wave can be assumed as a plane wavefront. In the near field various parameters, such as type of antenna dipole, presence of antenna shielding, etc., have to be considered and have significant influence on the antenna characteristics (Lampe et

al., 2003, Radzevicius et al., 2003). The electrical field cannot be assumed planar in the near field. The third and most proximal region is the so called reactive near field where the physical properties of the surrounding directly interfere with the antenna characteristics (Serbin and Or, 2003). The field intensities are dominated by fractions proportional to drop-offs of r^{-2} and r^{-3} (Wollny, 1999). In recent time a lot of effort has been put into the understanding of antenna characteristics in the near field (Holliger et al., 2004, van der Kruk, 2004). Here different scenarios of antenna dipole shapes, resistive loading of antennas and shielding can be analyzed and used for the interpretation of field measurements (Holliger and Maurer, 2004).

In the case of the RB-TDR layout, the georadar antenna is placed directly next to a metallic rod indicating that the coupling of the EM wave has to be considered a reactive near-field problem. According to Wollny (1999) the dimension of the reactive near field r_{rnf} can be approximated by:

$$r_{rnf} = \frac{\lambda}{2\pi} = \frac{\mathrm{v}}{2\pi\upsilon} \tag{5.1}$$

Assuming a 1 GHz antenna, the reactive near field ranges approximately 0.048 m in air. Using more realistic center frequency of 0.6 GHz for the applied 1 GHz antenna in equation (5.1), the range of the reactive near field is circa 0.08 m.

As the reactive near field of a georadar antenna is still an unknown problem, the resulting antenna characteristics caused by the adjacent metallic rod cannot be described here. Since the results for the near field problem indicate a strong dependence of the antenna characteristics on various parameters such as shape of the dipole, loading of the dipole, shielding of the antenna, etc., it seems very difficult to solve the reactive near field problem in a satisfying way in the near future. On the other hand the antenna characteristics can be assumed constant for at least one vertical profile because of the RB-TDR layout. The antenna characteristics should remain the same because the measurement is conducted under identical conditions.

Igel et al. (2001) successfully showed that part of the emitted EM wave was guided along the metallic conductor inside the subsurface. When discussing guided waves in relation to soil property investigation, the first association is the TDR measurement. A TDR measurement is mainly realized by applying an electrical impulse, commonly a step function, on a transmission line (e.g. Robinson et al., 2003). At the TDR probe the generally coaxial transmission line is split up into metallic rods connected to either the inner or outer conductor of the transmission line. When propagating inside the transmission line, the EM wave is a transverse electro-magnetic (TEM) wave. Therefore the electric as well as the magnetic field vectors are perpendicular to the propagation direction, i.e. the coaxial transmission line. When propagating along the probe rods, the EM field no longer is a rotational symmetric field as in the transmission line. Here the propagation characteristics, i.e. the propagation velocity and the attenuation, are completely affected by the media surrounding the metallic probe rods. Sommerfeld (1899) provided the formulation that the skin depth of the electrical field inside a metallic conductor is negligible. The region of influence for TDR probes is described as the region around the probe rods, where most of the EM energy is focused. Here the propagation characteristics are mainly influenced. For example Oswald et al. (2004) defined it as the soil cylinder around their probe, where 70% of the electromagnetic power of the dominant guided EM mode is concentrated.

5.2 Estimation of RB-TDR reach

To get at least an estimate of the region around the metallic rod responsible to alter the propagation characteristics of the EM wave, some additional investigations were performed. The utilized modeling tool does not even support rudimentary antenna characteristics and consequently will be used only for a first rough estimate.

In Figure 5.2 a bird's eye view of a synthetic 3D RB-TDR data set is displayed. The model itself resembled a homogeneous half space model with relative permittivites of 1 and 5 ($\Theta \approx 0.093$ m^3/m^3), respectively. The center frequency of the transmitted signal was 750 MHz which corresponds to a wavelength of approximately 0.18 m ($\varepsilon_s = 5$). The location of the transmitter is indicated by the marker and resembles approximately the transmitter location of a 1 GHz antenna for field measurements. In this dataset only intensities of at least 15% of the maximum intensity are displayed. Although this presentation does not feature any indication of the region of influence, other important information can be gathered. According to the amplitude distribution at the surface depicted in Figure 5.2, the side of the rod opposite the transmitter appears to feature better data quality and perhaps farther reach than the side close to the transmitter. The region of similar EM behavior due to the guided wave will be called reach. Generally, the field intensity appears to be unsymmetrical distributed around the rod. Therefore the perceptibility of the reflected signal may vary depending on the receiver location. The size of the region opposite of the transmitter appears to be approximately one wavelength, whereas the region at the transmitter side is approximately half a wavelength. In Figure 5.3 the corresponding radar section to Figure 5.2 for negative x-values and $y = 0$ m and a rod depth of 0.2 m is presented. The RB-TDR phase is well visible and additional signals can be seen. Those registered signals farther away from the rod indicate the existence of a body wave as well. This body wave is generated at the end of the rod. Contrary to the guided RB-TDR phase, the body wave is attenuated much stronger due to spherical spreading. As mentioned earlier, the signal intensity inside the rod (traces with x-values greater than -0.025 m in Figure 5.3) is zero.

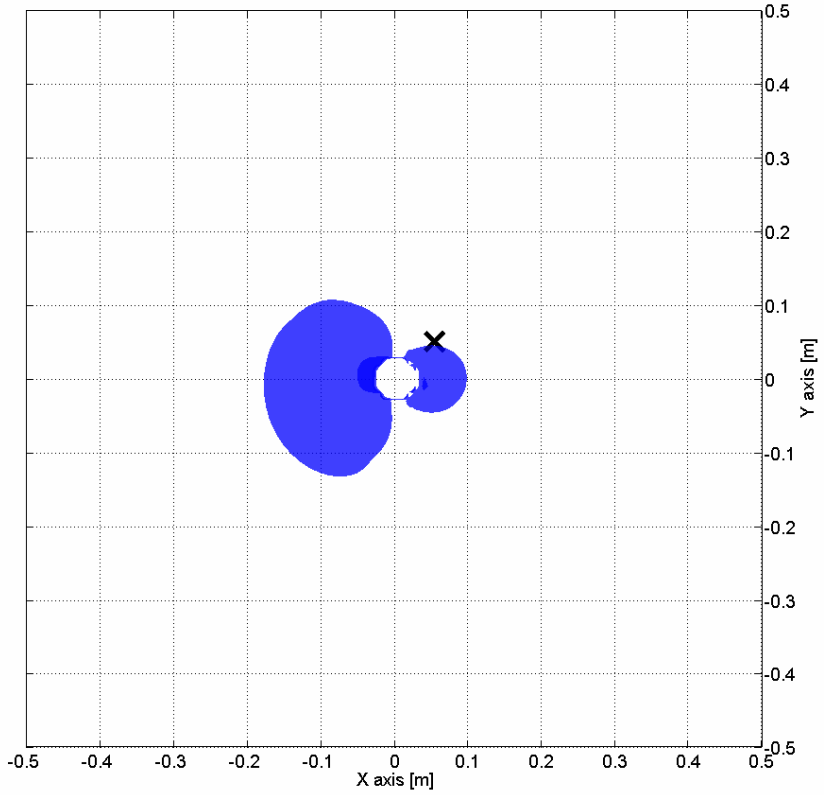

Figure 5.2: Derived area of at least 15% maximum amplitude intensity as a bird's eye view for a three-dimensional synthetic model. The location of the source, an infinitesimal dipole, is indicated by the cross. The rod was inserted 0.2 m into the subsurface ($\varepsilon_s = 5$). The isobody represents the resulting intensities at the surface.

To check the results from the synthetic data a field experiment was conducted. Here two different antenna combinations were used based upon the simulation results (Figure 5.4). The first one is the standard layout used by Igel et al. (2001), Müller et al. (2003) or Schmalholz et al. (2004a). Here the antenna, with transmitter and receiver in a single housing, is placed next to the rod. The big advantage of this layout is that it requires only one antenna since shielded antennas often consist of transmitter and receiver in one housing. Looking at Figure 5.2 this layout resembles a receiver position by mirroring the transmitter at the $y = 0$ m line. Therefore the signal intensity should be relatively high. The second antenna combination is based on the synthetic simulation. In this case the receiver position resembles a mirroring of the transmitter to the center of the rod. Here transmitter and receiver are at opposite sides and according to the numerical simulation good signal intensity should be achieved.

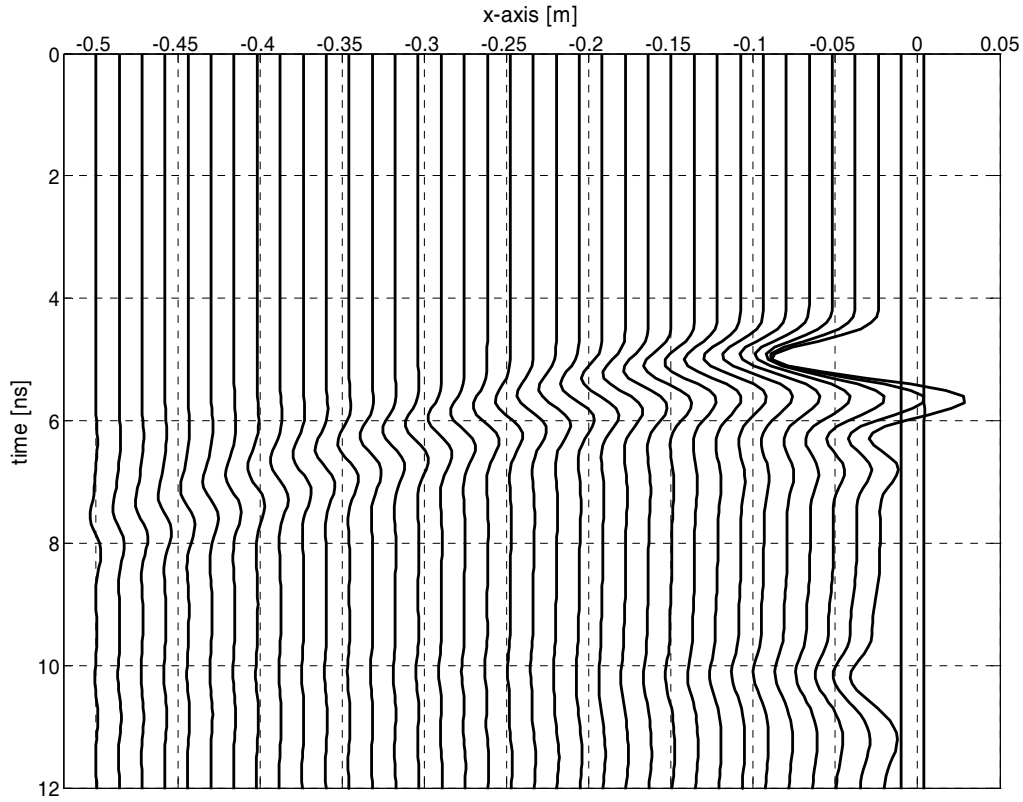

Figure 5.3: Synthetic radar section according to a y-coordinate of $y = 0$ m (see Figure 5.2) and a rod depth of 0.2 m. Positive x-values are not displayed and amplitudes are normalized to the maximum value in the radar section. The radar section represents a georadar measurement with fixed transmitter and receiver pulled towards the rod.

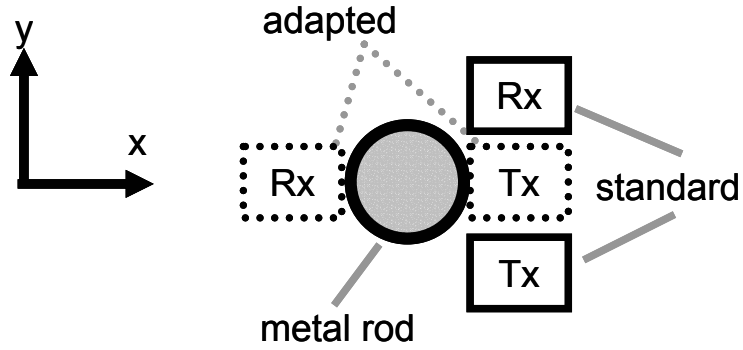

Figure 5.4: Schematic layout of the standard antenna combination (solid boxes) and the adapted antenna combination (dotted boxes).

Comparing the two radar sections corresponding to the antenna combinations, significant differences can be seen (Figure 5.5). Due to the different transmitter-receiver separation diverging absolute amplitudes are recorded. To ensure qualitative comparability both radar sections were normalized to their respective maximum amplitude value. Using the standard layout, only the direct wavelet, i.e. the signal propagating from the transmitter directly to the receiver, can be seen. The reflected signal from the rod cannot be detected in the unprocessed data, at least in the chosen form of presentation. Contrary to the standard layout, the adapted layout clearly displays the descending reflection from the rod (Figure 5.5). Additionally an

ascending phase can be identified. This reflection corresponds to a reflection at the upper end of the rod, which is in air and features a descending distance to the antennas for each successive step. The significant better perceptibility is mainly caused by the reduced intensity of the direct wave from the transmitter to the receiver. This can be explained by the inferior energy transmitted in this direction (e.g. Radzevicius et al., 2003) and the metallic rod shielding the direct path due to its high electrical conductivity. By deriving an average trace for the radar section and subtracting it from each trace, the reflection of the rod can be isolated (Figure 5.6). This procedure is referred to as a background removal (Sandmeier, 2006). By applying the background removal, the two reflections can be identified in both datasets. Since the background removal acts as a horizontal filter, only the horizontal reflections, e.g. the direct wavelet, are subtracted, but the inclinated events remain unaffected. This of course implies a data set with a sufficient number of traces. Due to the high intensity of the direct wavelet in the standard layout, the data quality at earlier arrival times is still inferior compared to the adapted layout.

To eliminate the reflection of the rod end in air, a transformation of the radar section into the frequency wavenumber (f-k) domain and a subsequent elimination of the phase can be performed (e.g. Sheriff, 1997). Here the two reflections originated at different ends of the rod clearly distinguish themselves since their corresponding velocities have opposed algebraic signs. Comparing the resulting radar sections after the f-k filtering, both layouts feature distinct reflections from the end of the rod inside the soil (Figure 5.7). To minimize wavelet altering effects as much as possible only the air reflection was eliminated with the f-k filtering.

Using the adapted layout, an additional measurement was performed. Here a conventional RB-TDR measurement was conducted with supplementary moveout measurements at specific rod depths. Starting at a depth of 1.2 m, the receiver was gradually moved away from the rod. The step width was 0.02 m and the maximum distance away from the rod was 0.3 m. After the moveout was performed, the receiver antenna was placed back next to the rod and the rod was gradually raised 0.2 m in 0.02 m steps. Then another moveout was performed. This procedure was repeated until the rod was at the soil surface. By performing these moveout measurements both the dependence of the interval velocity from the distance receiver to rod as well as the intensity of the reflected wave from the separation receiver rod can be determined.

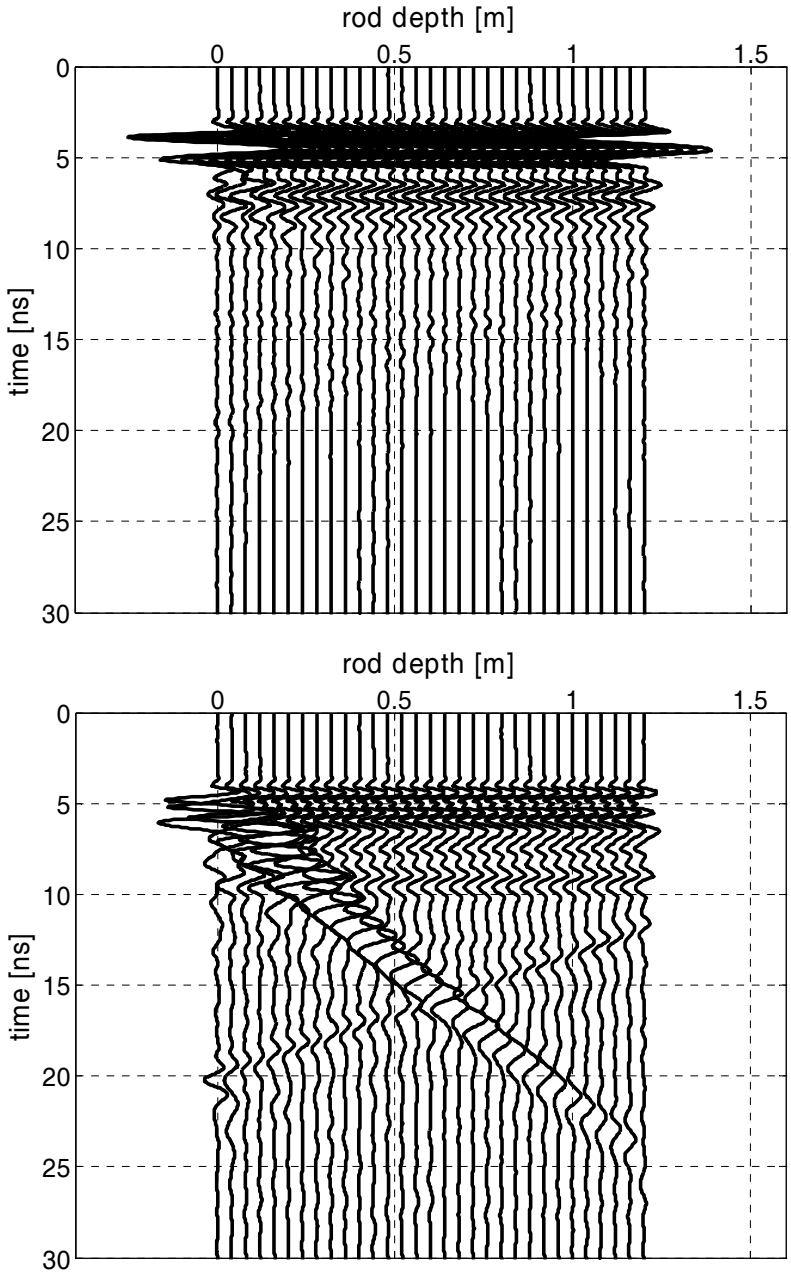

Figure 5.5: Recorded unprocessed RB-TDR dataset for the standard (above) and the adapted antenna combination (below). Amplitudes are normalized to the respective maximum value of the whole radar section.

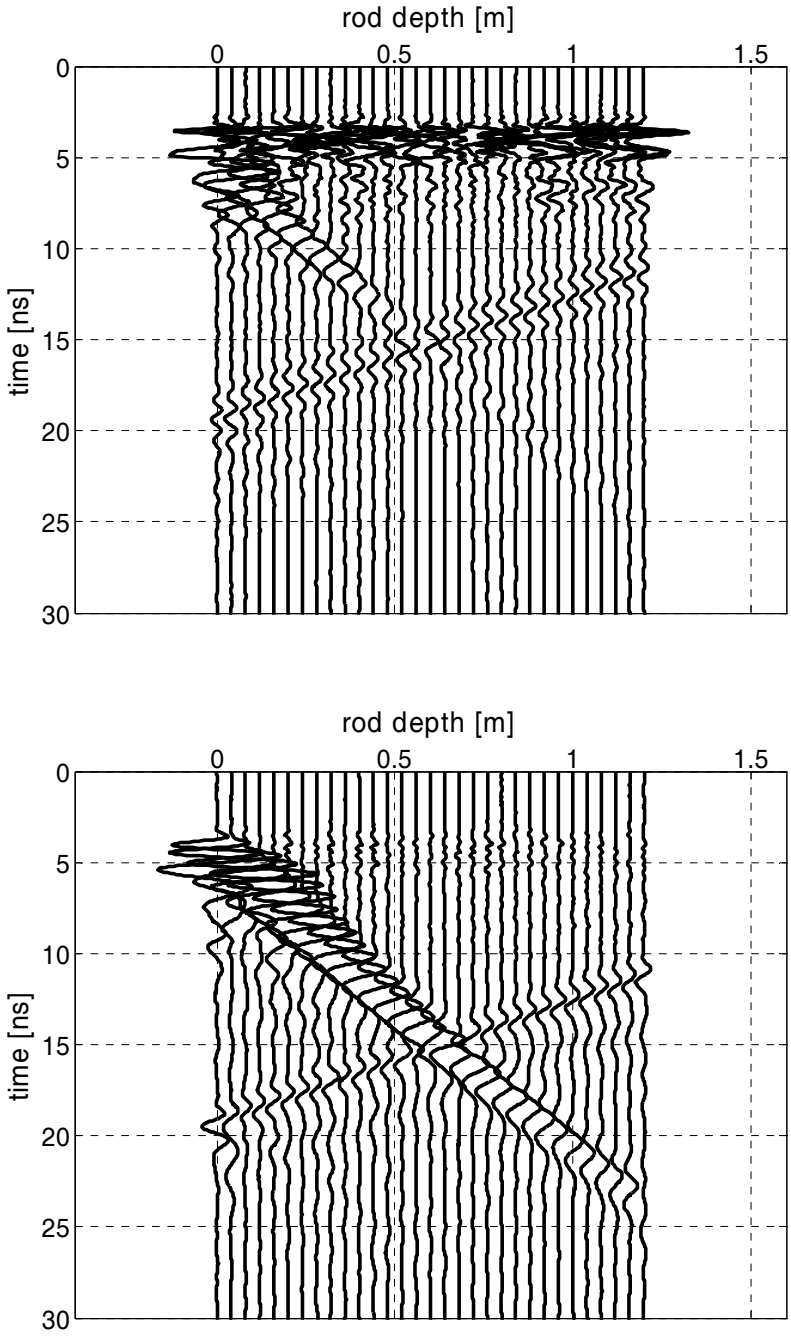

Figure 5.6: Recorded RB-TDR dataset for the standard (above) and the adapted antenna combination (below) after the application of a background removal. Amplitudes are normalized to the respective maximum value of the whole radar section.

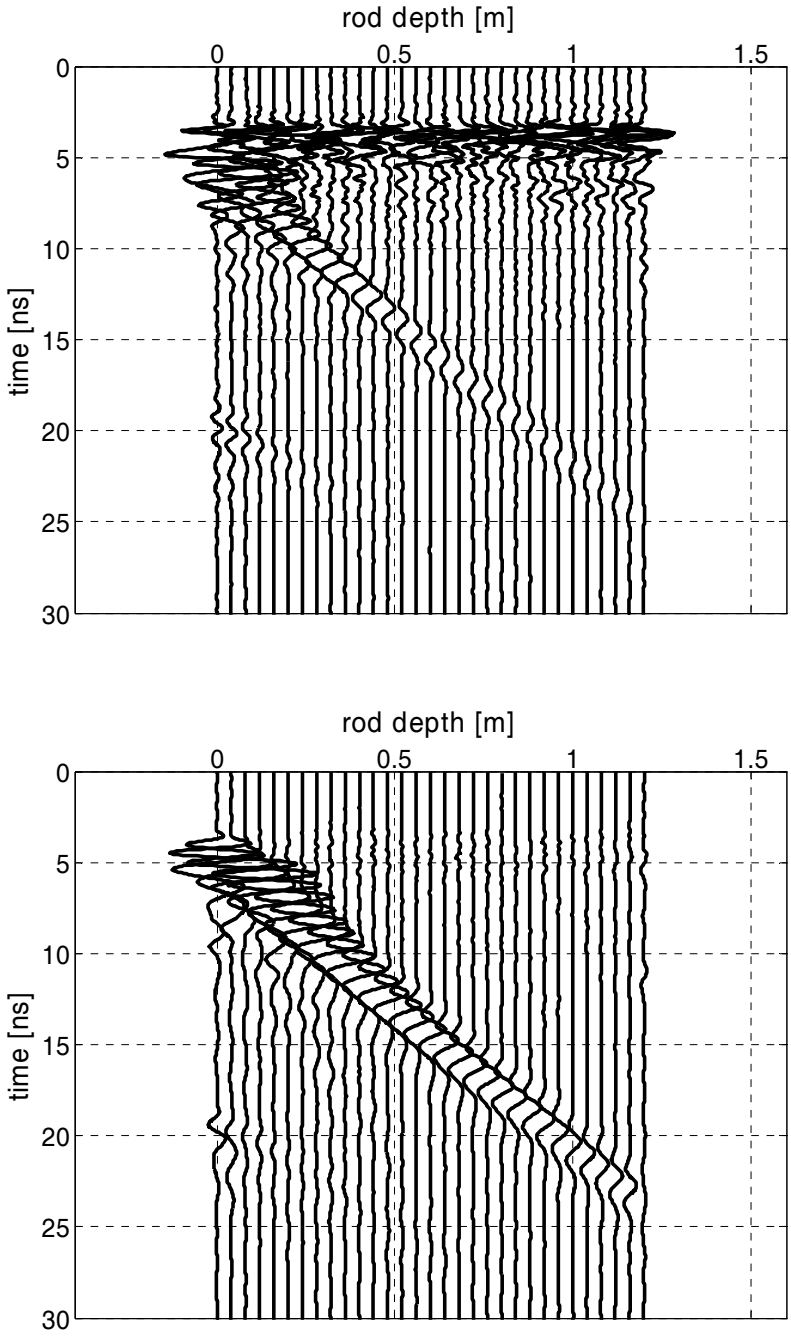

Figure 5.7: Recorded RB-TDR dataset for the standard (above) and the adapted antenna combination (below) after the application of a background removal and f-k filtering. Amplitudes are normalized to the respective maximum value of the whole radar section.

In Figure 5.8 the respective normalized amplitudes of the various moveouts are displayed. The amplitudes were determined by deriving the instantaneous amplitude of the reflected georadar signal (see 3.1.2). A relative decay of the amplitude with increasing distance from the rod is clearly visible. The two general exceptions are the measurement of the deepest rod position at 1.2 m depth and the shallowest at 0.2 m depth. In case of the deepest rod position the reason is quite simple. Here the signal intensity was insufficient to be analyzed quantitatively. All other rod positions, without the aforementioned shallowest, show the same behavior at least up to a receiver rod distance of 0.25 m. In case of the shallowest position a

stronger attenuation is determined to a rod receiver distance of approximately 0.15 m. For distances greater than 0.15 m a slight increase in the instantaneous amplitude is registered. Looking at Figure 5.5 one can see that the RB-TDR phase of the 0.2 m deep rod is superposed by the direct air wave. Since the moveout measurement was not treated with the same processing steps as for the RB-TDR measurement, i.e. no background removal or f-k filtering, the direct air wave was not eliminated. This is caused because the antenna layout did not conform to the RB-TDR assumption, i.e. additional reflection events appear at constant times. To investigate the reach only the reflection depths of 1.0 m and 0.4 m are investigated, since they represent the biggest propagation distance differences.

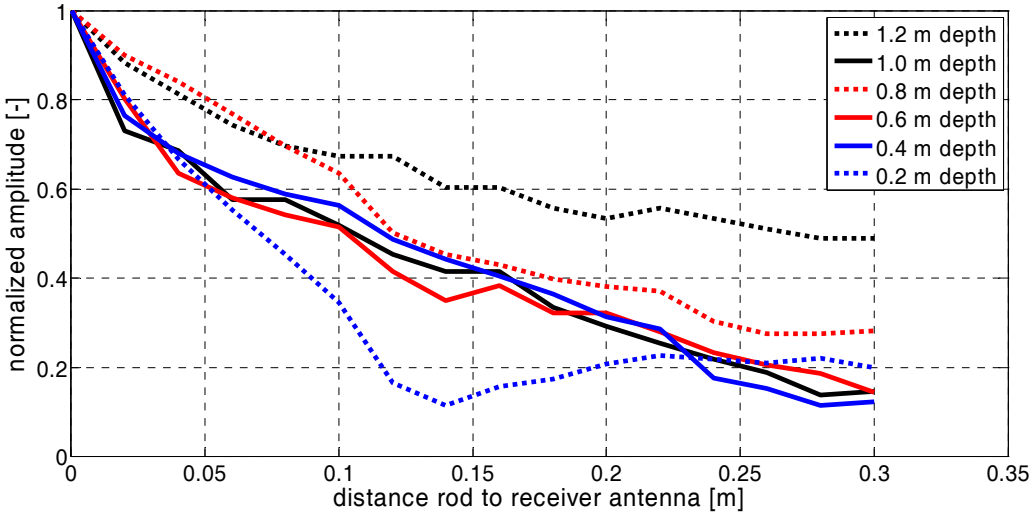

Figure 5.8: Normalized amplitudes for the respective moveout measurements for different rod depths.

Assuming the rod end as the origin of an elementary (Huygens) wave, the respective propagation path differences can be derived by simple geometrical computation.

$$\Delta d(x) = \sqrt{x^2 + z^2} - z \tag{5.2}$$

with x the distance rod receiver and z the depth of the end of the rod. In Figure 5.9 strong differing decays can be seen. Comparing for example the graphs for depths of 1.0 m and 0.4 m, an additional propagation path of 0.04 m results in an attenuation to less than 0.15 of the initial signal for a depth of 1.0 m, whereas the same additional propagation path results in an attenuation to approximately 0.4 for a depth of 0.4 m. To attenuate the signal of the rod depth of 0.4 m to less than 0.15 of the initial signal, an additional propagation path of 0.1 m, or 125% of the initial propagation path, is required, compared to only 104% for a depth of 1.0 m. Since the EM wave at the depth of 0.4 m would not travel through soil regions not traversed by the EM wave originated at 1.0 m differing attenuations caused by different soil properties can be excluded.

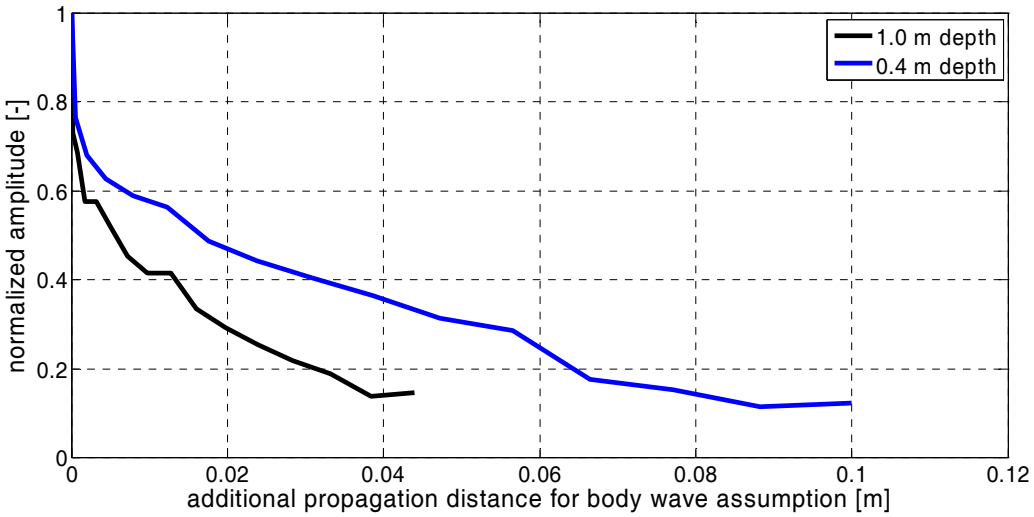

Figure 5.9: Dependence of the attenuation of the recorded amplitudes for different rod depths. The amplitudes are plotted against the additional geometrical propagation path for the body wave assumption.

Another potential explanation could be the transmission characteristic of the reflection at the end of the rod. If an elementary wave was generated at the end of the rod, a homogeneous energy distribution must not be assumed. In Figure 5.10 a transmission angle of approximately 15° for a rod depth of 1.0 m, causes a decay of the EM intensity to less than 0.15 compared to the normal incident. The same angle causes a decay of only approximately 0.55 for a rod depth of 0.4 m.

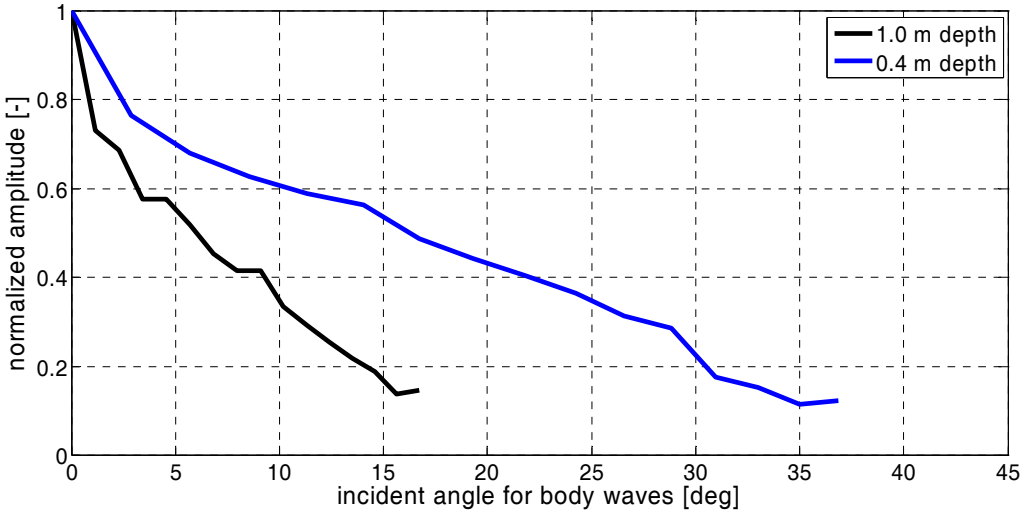

Figure 5.10: Dependence of the attenuation of the recorded amplitudes for different rod depths to the incident angle for the body wave assumption.

Combining all these observations the assumption of body waves as the source of the registered wave is not plausible. Indication towards guided waves is fortified when looking at the resulting interval velocities for successive depth intervals (Figure 5.11). Over a distance of 0.20 m between the receiver and the rod, all interval velocities vary less than ±0.0025 m/ns. In

5.3 the determination of interval velocities will be explained. The sole exception is the shallowest interval between 0.20 m and 0.40 m. Since the air wave interferes with the reflected phase of the 0.20 m dataset, errors due to inaccurate time picking may occur. Assuming a center frequency of the georadar signal υ of 600 MHz for the measurement, the interval velocity v_i of approximately 0.13 m/ns and the distance of sufficiently constant interval velocities x of 0.20 m, the reach of the RB-TDR signal can be estimated.

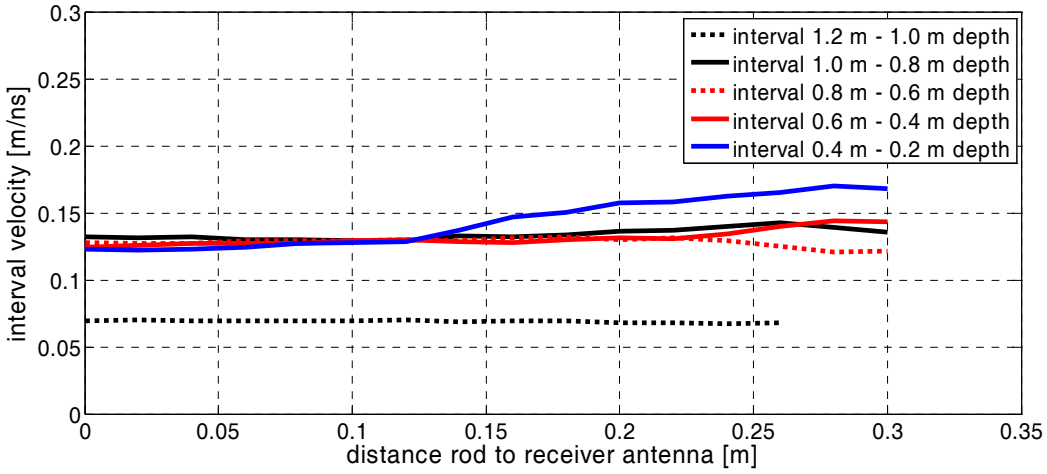

Figure 5.11: Comparison of derived interval velocities for successive depth intervals and their dependence on the distance rod receiver antenna.

$$x = a\lambda = a\frac{v_i}{\upsilon} = a\frac{c_0}{\upsilon\sqrt{\varepsilon_s}} \tag{5.3}$$

In the present case the reach a would be approximately 1.15 times the wavelength. In this case the smaller rod to receiver distance of 0.2 m determined from the interval velocities was used since the reach is only a rough qualitative estimate and cannot be compared to other characteristics like the region of influence. The reach of the RB-TDR can be assumed approximately one wavelength, although further investigations need to be performed. Numerical simulations additionally indicate a strong dependence on the transmitter and receiver locations at the rod. This dependence could potentially be used to determine relative permittivitties surrounding the rod depending on their azimuthal direction and not only their vertical location.

5.3 Propagation time analysis

To estimate the effect of the metallic rod body on the registered travel times of the rod reflection a series of numerical simulations using a 3D modeling tool implemented in the software package REFLEXW by K.J. Sandmeier (Sandmeier, 2006) were performed. Although this modeling algorithm does not support any antenna-specific characteristics such as the more sophisticated algorithms introduced by Radzevicius et al. (2003) or Lampe et al. (2003), this simple algorithm is justifiable under the following conditions.

- By looking strictly at propagation times for quantitative analysis, the radiation patterns are irrelevant.
- Although the intensities of the propagated waves can be expected to be different, the general propagation paths should stay the same. Therefore, by analyzing the derived wave paths, general conclusions can be made.

The model is a half-space model with a relative permittivity of 7.5 ($\Theta \approx 0.156$ m^3/m^3) for the subsurface and 1 for air. The metallic rod, diameter 0.05 m, was inserted perpendicular to the ground surface. The metallic rod was assumed of infinite height in air and reached down to three different depths (0.15 m, 0.20 m and 0.25 m) in the subsurface. Simulating the insulating air-filled tube usually used for the RB-TDR layout, a relative permittivity of 1 was assumed directly below the metallic rod (Schmalholz et al., 2004a). In this first approximation a simple point source was used simulating an infinite small dipole located 0.08 m away from the rod's symmetry axis and 0.01 m above the ground surface. This distance corresponds approximately to the separation of the rod to the mid point of the antenna dipole in the field using the adapted layout and a 1 GHz antenna, RAMAC GPR-system, MALÅ GeoScience, Sweden.

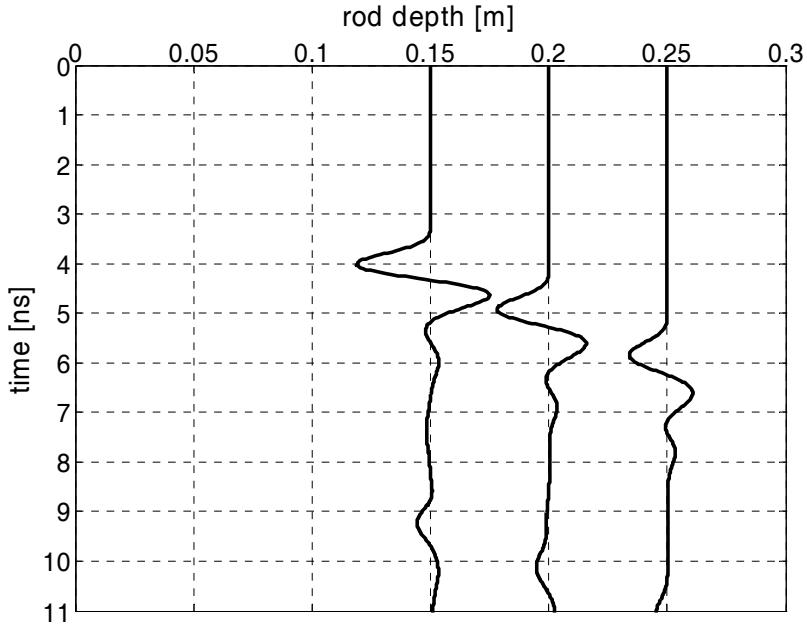

Figure 5.12: Synthetical derived georadar traces for different rod depths. Amplitudes are normalized to the respective maximum value of the whole radar section.

Figure 5.12 displays a synthetic radar section for the three rod depths. The direct wavelet from transmitter to receiver was eliminated and therefore not present in Figure 5.12. The receiver was assumed at the transmitter opposite side of the rod with a distance of 0.08 m. This would correspond to a measurement with the metallic rod sandwiched between a transmitter and receiver antenna. The recorded absolute two-way travel times are not identical to theoretical travel times for EM waves directly coupled to the metallic rod. This is caused by the lateral offset of transmitter and receiver from the rod. To evaluate the vertical distribution of the relative permittivity, travel-time differences of rod reflections of different depths are used instead (Schmalholz et al., 2004a). In the present case the travel-time difference was derived for the depth intervals 0.15 m to 0.20 m, 0.20 m to 0.25 m and 0.15 m to 0.25 m (Figure 5.13).

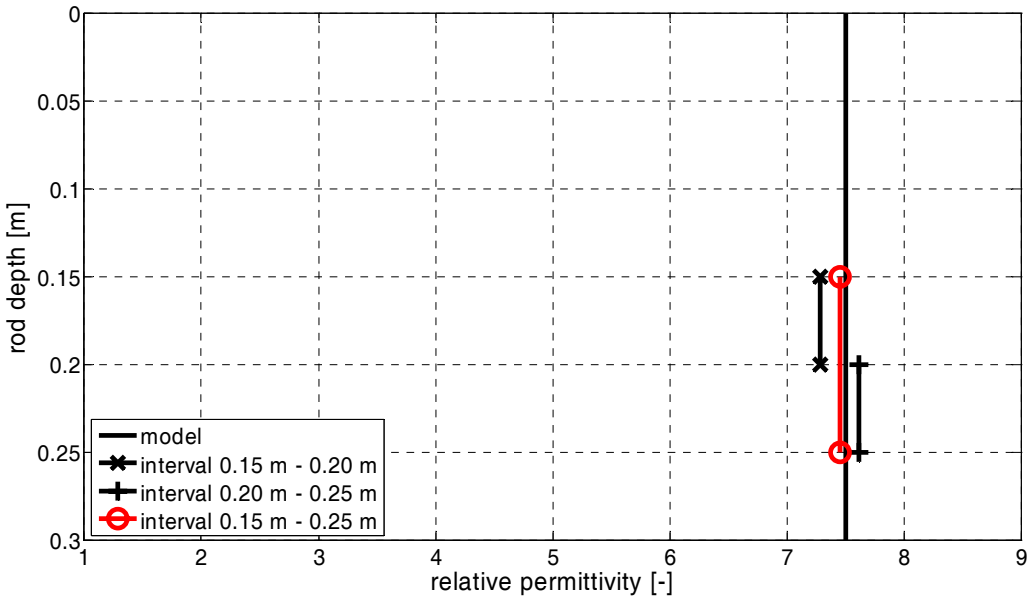

Figure 5.13: Derived relative permittivities for the respective depth intervals.

All three interpreted relative permittivity intervals represent the relative permittivity of the medium quite well (Figure 5.13). Both smaller intervals are of lower accuracy than the bigger interval. This is caused by two obvious reasons. First, the FDTD model possesses a finite raster increment, in this case 0.007 m. By lowering the increment, the raster files and hence the memory requirements and calculating times increase for the numerical FDTD simulation. Since the used modeling algorithm is run on a conventional personal computer, the maximum raster file size is restricted. This finite spatial raster results in a localization uncertainty in the range of 0.014 m, or 14% of the propagation difference, since two-way travel times are investigated. Second, the radar section is recorded with a sampling in time of 0.02 ns. This time discretization Δt additionally results in an uncertainty. If the reflected phase was correctly determined this Δt still produces an error of 2% for the two-way travel time for the smaller intervals. In this numerical study the first case is of course dominant. But for field measurements the second case increases drastically since the determination accuracy for arrival times decreases and is well below that for synthetic radar sections. Therefore, Igel et al. (2001) used bigger depth intervals (0.2 m for difference picking) and suggested a moving average interpretation for the smaller measured depth steps (0.02 m), similar to ground wave measurements.

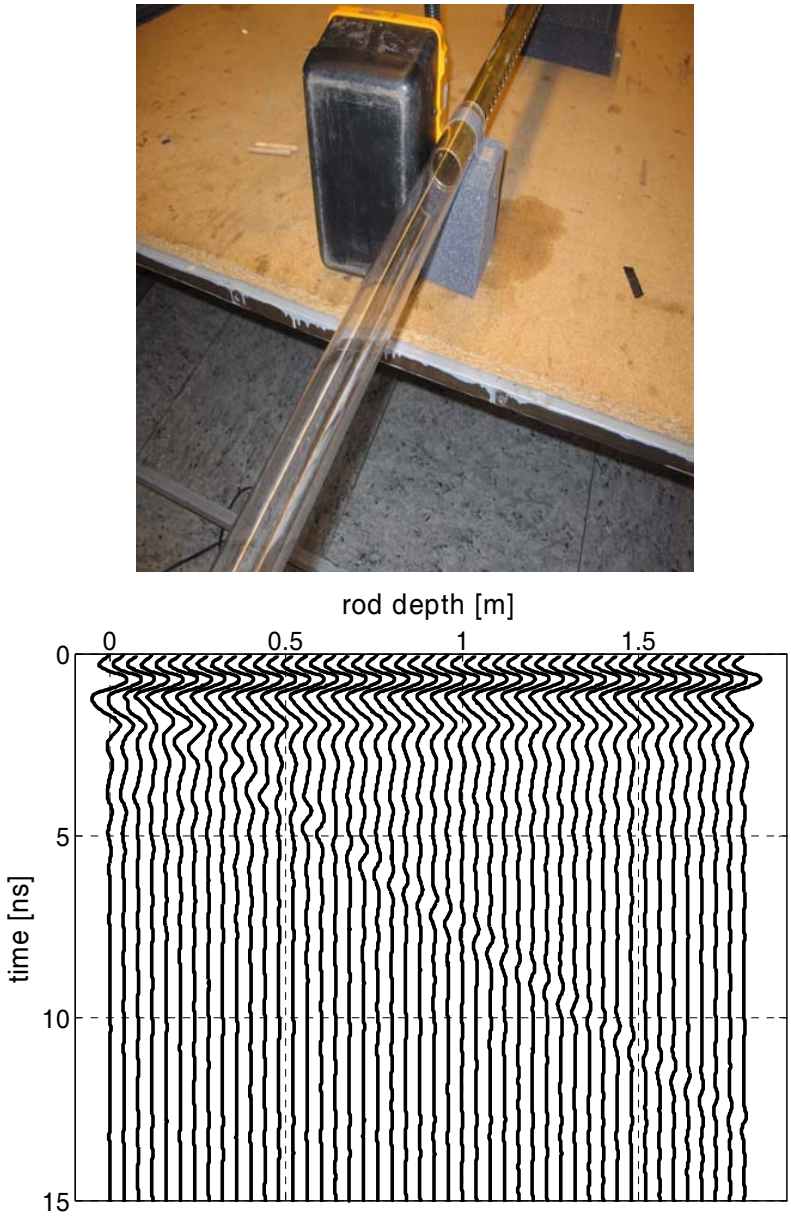

Figure 5.14: Picture of the RB-TDR measurement using the standard antenna combination in air (above). Data recording of the measurement in air without any processing applied (below). Amplitudes are normalized to the respective maximum value of the whole radar section.

To check the result from the FDTD simulation, two RB-TDR measurements on homogeneous media were performed. The first medium was air. Here the propagation velocity of the EM wave is well known. To perform the measurements, one 1 GHz georadar antenna (MALÅ, GeoScience, Sweden) was placed next to a metallic rod (Figure 5.14), resembling the standard RB-TDR layout. The metallic rod was placed horizontally into a plastic tube, simulating field conditions. The tube additionally ensured defined positioning of the rod without risking changes of the rods inclination to the antenna. The measurement itself was performed in a room without any elimination of potential disturbing reflectors, e.g. furniture or cables, since such events should be eliminated due to the attributes of the RB-TDR layout. In Figure 5.14 the radar section of the unprocessed data is shown. Each recorded time series or trace represents the data recording for a respective depth of the end of the rod. One can clearly see

the initial signal transmitted directly from the transmitter to the receiver in the time between 0 ns and 2 ns. Otherwise only a faint descending phase can be seen. This phase corresponds to the descending end of the rod. Applying the background removal processing, the reflecting phase can be isolated (Figure 5.15). An additional f-k filtering was not necessary. The only reflection changing over the course of the measurement is originated at the end of the rod. The reflection of the opposite end of the rod is not visible. Since the interface soil air is not present, no signal is reflected directly next to the georadar antenna. This could be an indication that the georadar antennas are shielded well due to the elimination of signals coming from above.

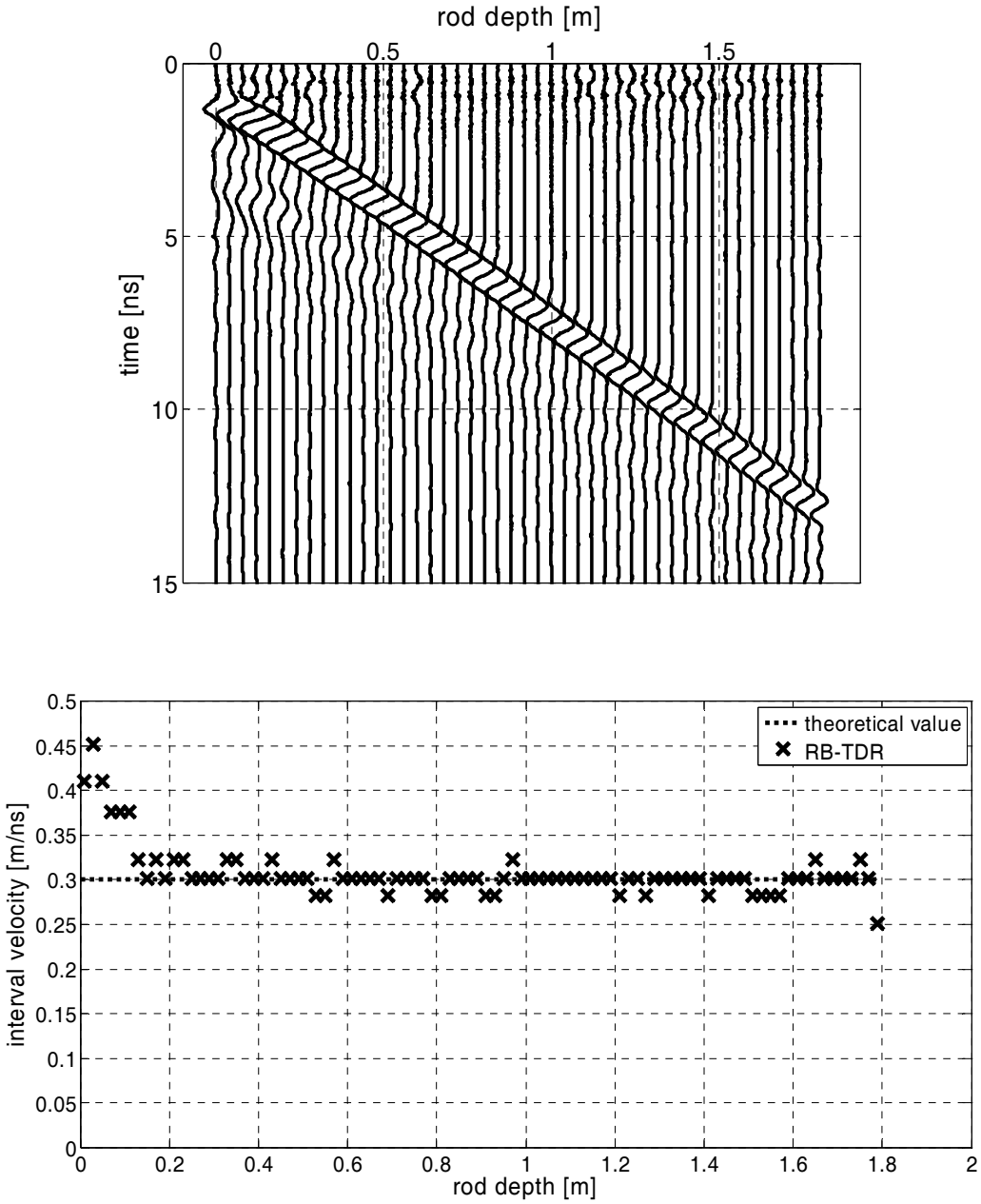

Figure 5.15: Processed dataset of the air measurement after application of the background removal (above). Amplitudes are normalized to the respective maximum value of the whole radar section. Interval velocities determined for depth intervals of 0.04 m (below).

The descending phase in (Figure 5.15) resembles a linear phase since the time difference Δt between two successive depths should be constant at:

$$\Delta t = \frac{2\Delta z}{\mathrm{v}} \tag{5.4}$$

In the present case the time difference should be 0.26 ns, for v = 0.3 m/ns and Δz =0.04 m, i.e. averages over three traces.

Reorganizing equation (5.4), the respective resulting interval velocities can be derived. After an initial aberration for the uppermost 0.15 m, the actual velocity of 0.3 m/ns is well reproduced. The high error for the uppermost region has two origins. Due to the distinct and dominating direct wavelet from the transmitter to the receiver (see Figure 5.14) inaccuracies for picking the reflected wave from the rod are possible. This is quite obvious since the uppermost 2 ns in (Figure 5.15) are still noisy, indicating that the direct wavelet could not be totally erased with the background removal. The other unknown is the coupling of the EM wave to the rod.

Looking at the determined velocities beyond 0.2 m depth (Figure 5.15), two additional striking features can be seen.

- On the one hand, the effect of the time discretization is recognizable. When picking the arrival time of the EM wave one sample (or 0.0177 ns) too early, the resulting determined velocity is 0.33 m/ns. When picking one sample too late, the velocity is lowered to 0.288 m/ns. The aberrations in (Figure 5.15) are only originated by picking one sample too early or too late.
- On the other hand, even the correctly picked arrival times result in slightly wrong velocities. This is again an effect of the time discretization since the exact velocity can only be determined with the exact arrival time. Due to the discretization of the recorded signal, only an approximated value can be used.

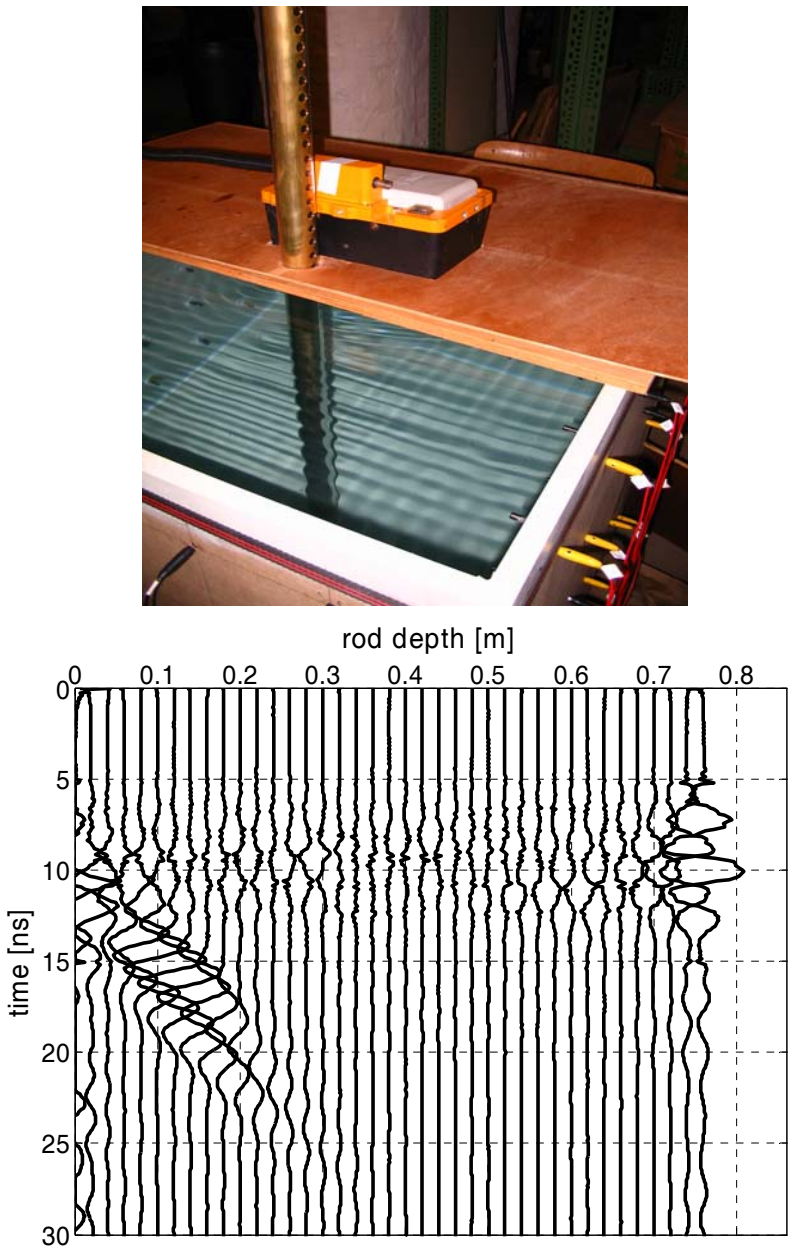

Figure 5.16: Picture of the RB-TDR measurement using the standard antenna combination in water (above). To visualize the water surface mechanical waves were produced. Data recording of the measurement in water after the background removal processing step was applied (below). Amplitudes are normalized to the respective maximum value of the whole radar section.

The second homogeneous medium was water ($\sigma = 0.32$ mS/m). The same antenna was used, although the realization was a bit more difficult. The metallic rod was placed inside an insulating tube. The measurement was conducted in a water filled wooden cube with 0.8 m side length. The antenna was placed inside a wooden pattern enabling positioning of the antenna next to the rod (Figure 5.16). Looking at the isolated reflection of the reflected wave, the inferior data quality is obvious (Figure 5.16). Due to the stronger attenuation of the EM wave only the uppermost, i.e. earliest, reflections are well recognizable. Even then a stacking of 8192 traces was required to acquire adequate data quality. To reduce the acquisition time,

the time sampling was increased to 0.106 ns. Assuming a relative permittivity for water of 81, the expected propagation time difference between two depth points with $\Delta z = 0.02$ m is approximately 1.2 ns. Therefore a time sampling of 0.0177 ns as for the air measurements would not be necessary anyway. Nevertheless, looking at the results (Figure 5.17) a good correlation with the expected propagation velocity can be registered. The determined velocities mainly stay within one sample interval around the correct value even though the data quality appeared inferior. The data for small rod depths is again erroneous and shifted to higher velocities.

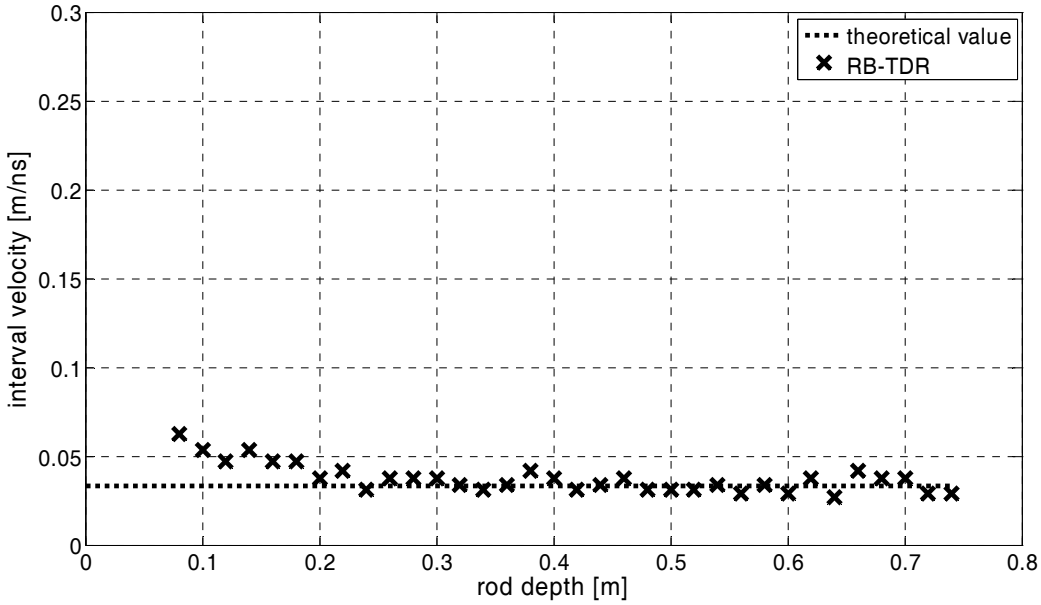

Figure 5.17: Interval velocities of water determined for depth intervals of 0.02 m.

Both experiments proved to be successful and supported the previous assumptions and simulations. Using the two media, i.e. air and water, the two most extreme relative permittivities to be encountered in the field were chosen. By deliberately refusing to reduce the number of existing disturbing reflectors, e.g. furniture, cables, or the wooden pattern, the proposed reduction of inevitable reflections in the field was included. The achieved accuracy appears to be sufficient for water content determination.

5.4 Application example

To check the applicability of the RB-TDR for monitoring purposes, a field experiment at the INTERURBAN test site Buch (Müller et al., 2003, Täumer et al., 2006) was conducted. This test site is located at the northern city limit of Berlin, Germany. The area is a former sewage field, where untreated waste water was irrigated from 1890 to 1985. In 1985 sewage was stopped and the area was leveled and reforested with trees and grassland. Due to heavy metal contaminations and water shortage in summer, most of the trees died (Täumer et al., 2006). The present dominating vegetation is dry grassland. The soil consists of 0.4 m to 0.6 m of organic topsoil with mostly dense rooting. Below the topsoil a medium-sized sand ranges below the ground water table in approximately 3 m depth. The sand content in the topsoil is generally above 94% with silt contents less than 6% and clay contents less than 1% (Huraß and Schaumann, 2006). Little deviations may occur due to the waste water sewage. The

organic matter content in the topsoil is mostly in the range of 4 to 6% with some spot-like exceptions of up to 30% (Täumer et al., 2006).

In this experiment two short but intensive rain events were simulated. Both events consisted of $5 \cdot 10^{-3}$ m^3 water on an area of approximately 0.16 m^2, or approximately 30 mm rain equivalent. The center of the irrigation area was at an isolating tube to conduct the RB-TDR measurements. Here the area covered by the antenna was not irrigated identically to the rest of the surface. Irrigation was started at 0 min and 115 min and lasted only a few minutes. The measurements were conducted with the standard layout because the measurements were also conducted during the irrigation and the covered area with the georadar antenna was minimal. The water was applied with a watering pot. The recorded radar sections were only processed with the background removal to eliminate horizontal events and f-k filtering to remove the reflection originated by the end of the rod in air.

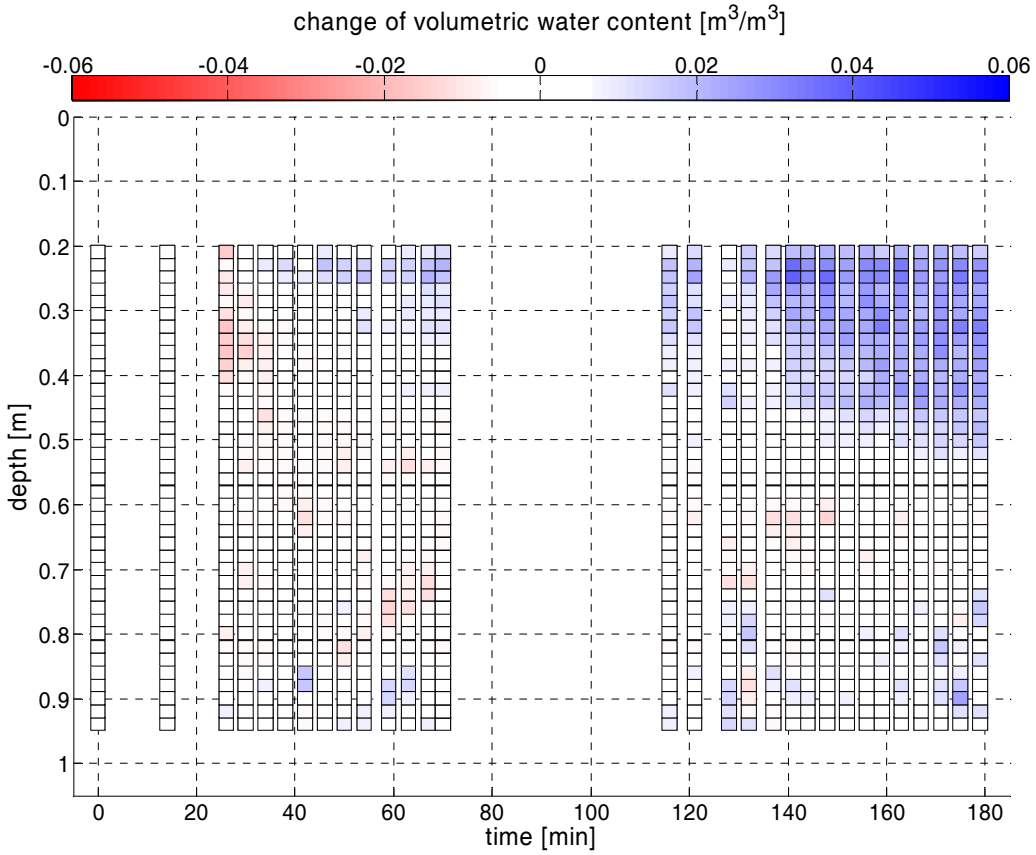

Figure 5.18: Determined vertical volumetric water content dynamics after two irrigations at 0 min and 115 min were conducted.

Looking at Figure 5.18, a clear increase of the volumetric water content in the uppermost region down to approximately 0.5 m is noticeable. The uppermost 0.2 m were excluded, since the coupling process of the EM wave is not resolved and the interpretation of the recorded reflections is difficult (see 5.3). Immediately after the first irrigation no change of the volumetric water content is recorded. At approximately 30 min a slight decrease in the determined volumetric water content is interpreted. This may be caused by changes of the volumetric water content in the corresponding depth region too fast to be exactly interpreted. The static background assumption is not valid for fast dynamical processes. The vertical volumetric water content distribution cannot be assumed constant in the course of one measurement, which affects the quality of the processing with the background removal as

well as the f-k filtering. In the time span between 40 min and 70 min, a distinct seepage is noticeable. No RB-TDR data was recorded during 70 min and 115 min because additional measurements with other geophysical methods were conducted.

After the second irrigation further seepage can be observed and a barrier-like effect at a depth of approximately 0.45 m is visible. In this depth the transition from the humus layer to almost pure sand layer is expected (Täumer et al., 2006). Here the underlying coarser sand acts as a capillary barrier to the finer humus layer, similar to sealings sometimes used at waste disposals (Zischak, 1997).

One striking result are the relatively low changes in the volumetric water content although strong water content changes were expected due to the intensive irrigation. Such moderate water content changes may be caused by the water retention in the uppermost 0.2 m due to plant roots. Another possibility may be horizontal water movement due to pressure head differences in the soil. But this appears to be unlikely to affect the vertical movement that drastically, since Täumer et al. (2006) did not experience such movements. A third and likely cause might be the antenna-dependent nature of the RB-TDR. Since the standard layout was used and the georadar antenna was placed at the tube during irrigation, the water seepage below the antenna is expected to be less than for other locations. Based on previous observations, the standard layout might be most sensitive for the soil region directly below the antenna along the rod. This of course would explain the relatively slight changes in the determined volumetric water content. Still, the RB-TDR layout proved to be capable of monitoring relatively fast dynamical events with high accuracy. According to the collected data, the reproducibility is in the range of 0.01 m^3/m^3 in the volumetric water content over long periods of time.

6 Reflection method with Diffraction Velocity Analysis (DVA)

The most common way to perform a georadar reflection measurement is to use the CO layout. For a CO measurement, the transmitter and receiver antennas are pulled along a profile at the surface with a fixed antenna separation. Although various antenna offsets are sometimes used for special investigations (Fisher et al., 1992) mostly small antenna separations compared to the investigated region are used. Ideally an antenna offset of zero is aspired. Generally, the antenna dipole is perpendicular to the profile direction. Other dipole orientations and combinations may present advantages for specific problems (van der Kruk et al., 2002), but are used far less often. The CO method is one of the most common applications of GPR and provides a quick coverage of the whole surveyed area (e.g. Grasmueck et al., 2005). A big problem for reflection measurements is the requirement of spacious interfaces with distinct electrical property changes. As mentioned in (2.1.3), such reflectors need to be at least in the range of the first Fresnel zone to be used for additional investigations. If such reflectors are present, evaluations of amplitude behavior of the EM wave (e.g. Gregoire and Hollender, 2004, Helm, 1998) can be performed. Objects smaller than the first Fresnel zone are mostly referred to as diffractors. Such objects are often unwanted sources of diffraction events in the radar section and sometimes produce errors for reflection analysis (e.g. Turesson, 2006). On the other hand, since only less than 2% of an average radar section includes interpretable reflections for standard interpretation (Shihab and Al-Nuaimy, 2004), the evaluation of diffracting events can present a valuable addition. This is even more important for investigations of the uppermost soil due to the generally absent reflectors in this region of the soil.

6.1 Experimental Setup

By analyzing diffraction hyperbolas (Figure 6.1), the location of a diffractor can be derived and dielectric property information on the overlaying soil can be acquired. This is also valid for reflectors with finite dimensions. At the edges of those reflectors diffractions occur, too. The arrival time t of the EM wave at the antenna location x is thereby defined by:

$$t(x) = \frac{2}{v_s}\sqrt{(x - x_0)^2 + z_0^2} \tag{6.1}$$

with x_0 and z_0 the coordinates of the diffractor in the subsurface and v_s the EM propagation velocity of the soil above the diffractor. If the depth z_0 is known, the velocity v_s can be directly determined from equation (6.1). The horizontal location of the diffractor x_0 can be easily determined from the radar section. For the most common case, i.e. unknown vertical location of the diffractor, several diffraction hyperbolas have to be derived by varying the value of v_s. The best fitting hyperbola can be used to determine v_s and z_0 since only one combination can fulfill the requirement to match the recorded diffraction hyperbola in the radar section.

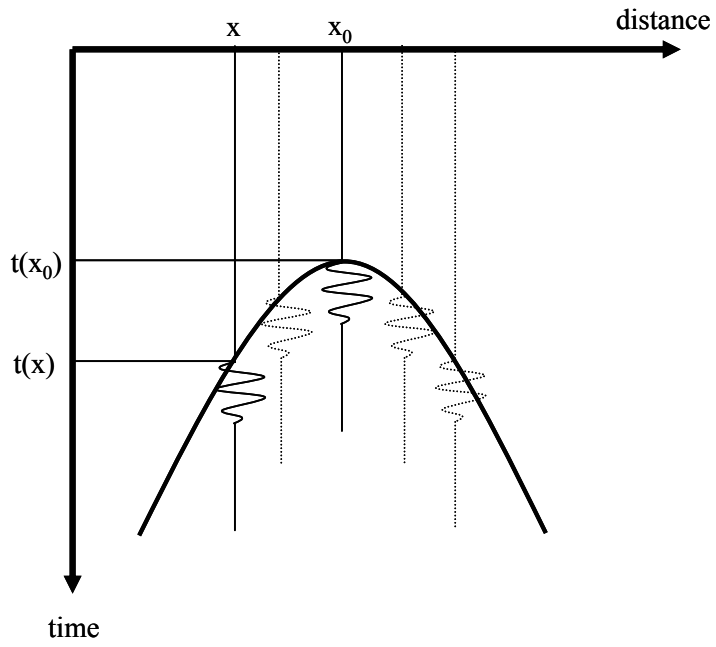

Figure 6.1: Schematic diffraction hyperbola for a CO measurement above a diffractor.

The exact location of the diffractor can be determined by locating the apex of the hyperbola at x_0 and deriving the depth z_0 by:

$$z_0 = \frac{v_s t_{x_0}}{2} \quad \text{with } t_{x_0} = t(x_0) \tag{6.2}$$

Using this method Loeffler and Bano (2004) were able to estimate one-dimensional volumetric water content changes inside a sandbox. In equations (6.1) and (6.2) a monostatic antenna layout, i.e. transmitter and receiver are located at the identical position, is assumed. Using a bistatic antenna system, a quasi-monostatic situation can be assumed for diffractor depths greater than 500% of the antenna offset d. In this case the true propagation path p_t for a bistatic measurement and normal incident can be derived by:

$$p_t = 2\sqrt{\left(\frac{d}{2}\right)^2 + z_0^2} \tag{6.3}$$

Assuming an antenna separation d of 0.11 m and a diffractor depth z_0 of 0.55 m, the true propagation path p_t is 0.0055 m longer or 100.5% of the monostatic propagation path. Most standard processing procedures assume zero offset assumptions since they were originally from seismic data processing. Here data sets were normal moveout (NMO) corrected due to computational restrictions.

Bigger errors occur when investigating diffraction hyperbolas originated from shallower diffractors. For a homogeneous half space with constant propagation velocity of 0.10 m/ns, the errors for propagation velocity determinations are displayed in (Figure 6.2). On the other hand, by assuming a picking error for the propagation time determination of 0.2 ns, the error caused by the erroneous assumption of the monostatic case is inferior for depths beyond 0.15 m. When combining both sources of errors, accurate velocity determination of less than

10% error can be expected for diffractors at depths of 0.2 m and beyond. Knowing the antenna separation d, the arrival time t of the EM wave for the same diffractor at x_0 and z_0 can be derived by:

$$t(x) = \frac{1}{\mathrm{v}_s}\left(\sqrt{\left(x + \frac{d}{2} - x_0\right)^2 + z_0^2} + \sqrt{\left(x - \frac{d}{2} - x_0\right)^2 + z_0^2}\right) \tag{6.4}$$

In this case the sole source of error is the inaccuracy of arrival time picking.

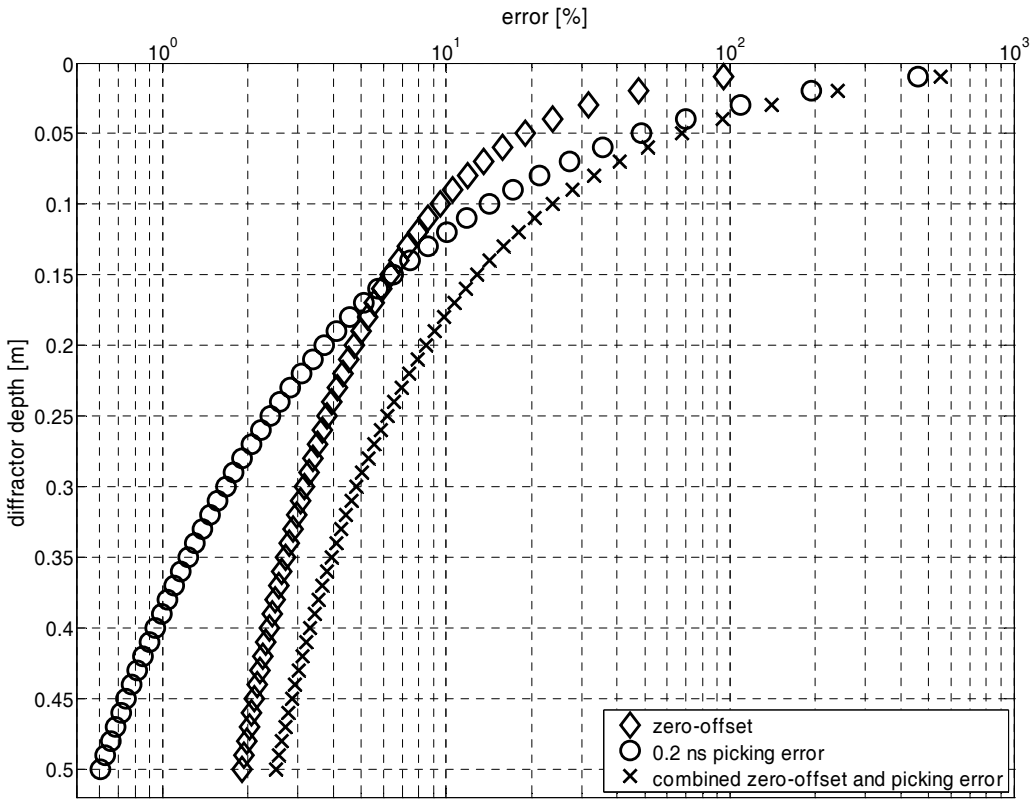

Figure 6.2: Comparison of velocity errors generated by the zero-offset assumption (rhomb), a constant picking error of 0.2 ns (circles) and both (crosses) for a background model with a relative permittivity of 10 and an antenna separation of 0.11 m.

For field measurements the error of the velocity determination can be estimated by:

$$\Delta \mathrm{v} = \frac{\partial \mathrm{v}}{\partial x}\Delta x + \frac{\partial \mathrm{v}}{\partial t}\Delta t \tag{6.5}$$

The local uncertainty Δx is usually the step width of the measurement, whereas the temporal uncertainty Δt can be estimated by the accuracy of arrival time picking.

Until now, only homogeneous half spaces were assumed. In case of a smooth transition of the electrical parameter in the subsurface, the propagation velocity v_s cannot be assumed constant. A smooth transition is assumed, since strong parameter changes would result in reflections and the recognition of the resulting interface in the radar section. In the first model a point-like diffractor at $x = 0$ m and at a depth of 0.75 m is assumed. The relative permittivity

directly above the diffractor has always the value 10. First a horizontal relative permittivity gradient of $d\varepsilon/dx = \pm 1/\text{m}$ is assumed. This gradient is relatively small compared to field conditions but is meant to be exemplary. Considering ray optics and the Fermat's principle (e.g. Fließbach, 1997, Sheriff, 1997), i.e. the ray travels along the path of the shortest travel time, the resulting diffraction hyperbola can be derived (Figure 6.3). The numerical solution of the Fermat's principle is also known under the generic name ray tracing.

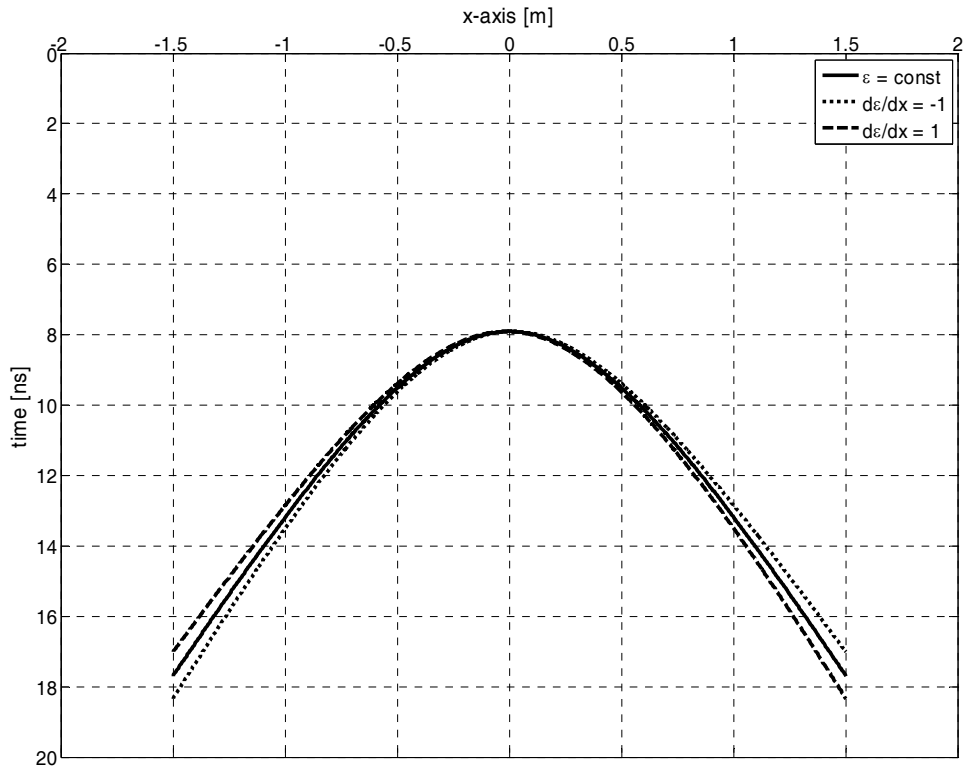

Figure 6.3: Comparison of numerical calculated diffraction hyperbolas for a constant relative permittivity of 10 (solid line), a negative gradient in x-direction (dotted line), and a positive gradient in x-direction (dashed line).

In Figure 6.3 the resulting diffraction hyperbolas are compared to the hyperbola for the homogeneous case. Here the aberration between the travel times for the homogeneous case and the two horizontal transitions are negligible for horizontal offsets smaller than 1 m. Although larger offsets produce recognizable variations in the travel times, the recorded intensities in the radar section will decrease. This is caused by the longer propagation path and the antenna characteristics of the georadar. Here the main direction of the transmitted EM energy is focused more and more to the normal of the surface (Radzevicius et al., 2003) for increasing relative permittivities. For a bow-tie antenna, normally utilized for shielded impulse georadar antennas, an energy maximum in profile direction is present at approximately 40° to the normal for $\varepsilon_s = 5$ or approximately 17° for $\varepsilon_s = 80$ (Radzevicius et al., 2003). Due to the resulting low intensity of the diffracted signal for greater horizontal offsets, an exact determination of the arrival times cannot be executed anyway. In the case of the first model in (Figure 6.3), the effect of the horizontal gradient can be neglected and a precise determination of the integral velocity for the apex of the hyperbola can be obtained.

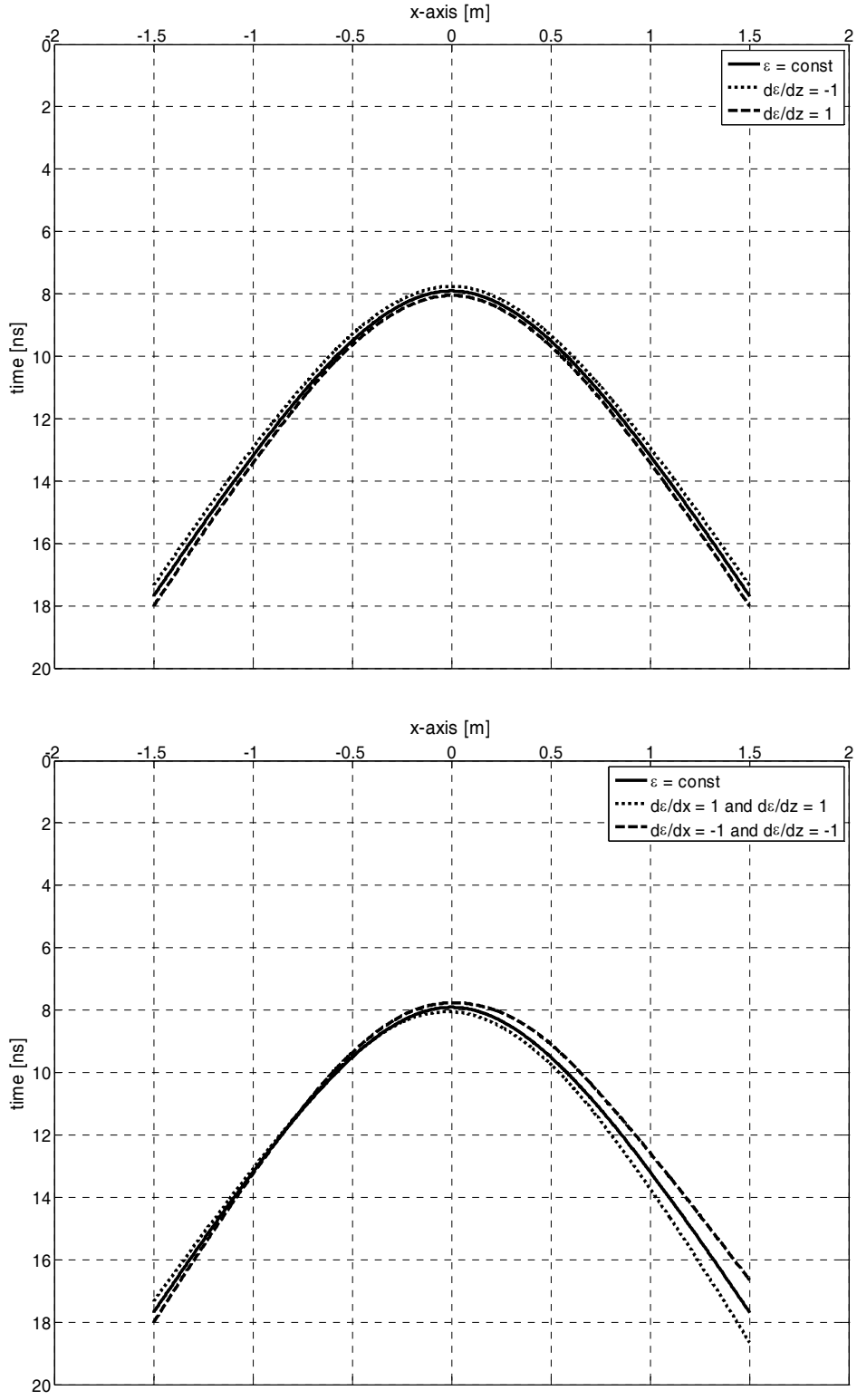

Figure 6.4: Comparison of numerical calculated diffraction hyperbolas for a constant relative permittivity of 10 (solid line), a negative gradient in z-direction (dotted line), and a positive gradient in y-direction (dashed line) (above). Comparison of numerical calculated diffraction hyperbolas for a constant relative permittivity of 10 (solid line), a negative gradient in x- and y-direction (dotted line), and a positive gradient in x- and z-direction (dashed line) (below).

Deriving diffraction hyperbolas for a vertical gradient of $d\varepsilon/dz = \pm 1/m$ (Figure 6.4), an even inferior effect can be recognized. Here the hyperbolas are only shifted to smaller respectively larger arrival times with no noticeable change of the hyperbola's shape. This is a good indicator for the achievable accuracy in the velocity determination. In the present case an average velocity of $\overline{v}_s = 0.0967\,\mathrm{m/ns}$ or $\overline{v}_s = 0.0931\,\mathrm{m/ns}$ is equally well fitted, at least when fitting the data by hand. A velocity determination can be expected to be of less accuracy than ± 0.002 m/ns. A successful determination of the integral relative permittivity would be achievable. In this case, the vertical location of the diffractor would be under- or overestimated respectively, but far less than being problematic for the evaluation of the diffraction hyperbola. By combining the horizontal as well as the vertical gradient of the relative permittivity, the resulting diffraction hyperbolas are deformed more strongly (Figure 6.4). Depending on the combination of the gradients an exact allocation of the diffractor would be difficult. But in this case the uncertainty would only be a few centimeters in horizontal and vertical direction. This error would then cause only minor aberrations in the localization of the corresponding water contents.

6.2 Data Interpretation

To check the potential of this method a simple two-dimensional model is assumed. The model resembles a typical relative permittivity distribution for the INTERURBAN Tiergarten site (see 4.4). Here the uppermost 0.6 m resembles the humus layer (Figure 6.5). Although not universally valid for the Tiergarten site, this humus distribution sometimes occurs due to the dense rooting of the grass in the uppermost part and the abrupt transition from humus to sand in the lowermost part of the humus. Here the roots store the water whereas the humus sand transition acts as a capillary barrier (Zischak, 1997). Such a vertical transition can be encountered by a simple excavation and sampling of the soil (Figure 6.6). The model does not present a synthetic version of the Tiergarten site, but is rather representative of the present conditions.

In this model some relatively strong gradients are realized. The relative permittivity decreases over the first 0.3 m from 7 to 5 or a vertical gradient of -6.67/m. From profile meter 2 m on an additional horizontal gradient of 0.5/m is implemented. The lower part of the humus layer features a vertical relative permittivity gradient of 10/m down to 0.6 m. Beneath 0.6 m a constant relative permittivity of 7 is assumed. Throughout the model a total of 18 diffractors are distributed. The diffractors are assembled in three groups and aligned to cover a vertical profile. The diffractors are located at depths of 0.1 m, 0.2 m, 0.4 m, 0.5 m, 0.7 m, and 0.8 m. The diffractors resemble metallic objects of quadratic shape with 0.02 m side length. The first group is situated at 1.25 m the second at 2.25 m and the third at 3.25 m. Therefore all three zones of the horizontal gradient, i.e. no gradient, partially affected, and fully affected, are covered as well. Additionally, two datasets were derived. One data set corresponded to a dense measurement interval of 0.005 m increments along the x-axis and one to a more field-realistic interval of 0.02 m. The synthetic radar sections were derived using the FDTD modeling tool implemented in REFLEXW (Sandmeier, 2006), and a zero-offset measurement was simulated.

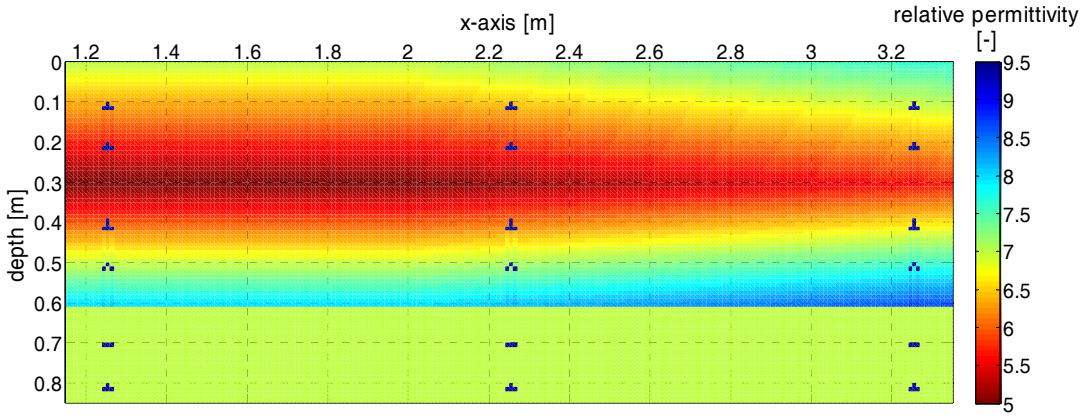

Figure 6.5: Two-dimensional relative permittivity distribution of the initial model and the inserted diffractors.

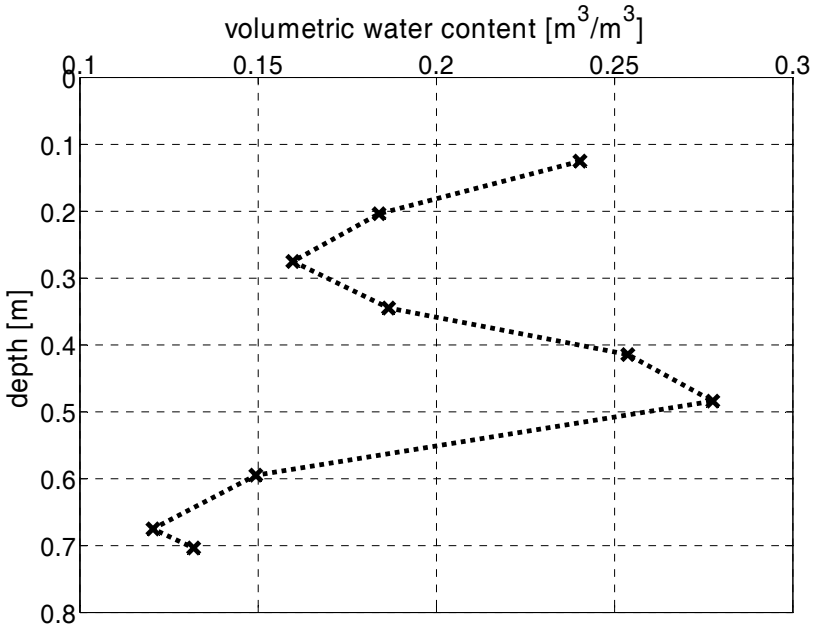

Figure 6.6: Determined vertical volumetric water content distribution from soil samples at the INTERURBAN test site Tiergarten.

The synthetic radar section with the 0.005 m interval is displayed in Figure 6.7. The center frequency of the georadar signal was 800 MHz. The diffraction hyperbolas are clearly visible and the interface at the depth of 0.6 m is also distinguishable. Due to the implemented horizontal gradient beginning at 2.0 m, a distinct shift of the reflection of the interface to later arrival times is noticeable. The low signal intensity at the apexes of lower (later) diffraction hyperbolas is caused by the respective diffractors above, which act as a shielding, preventing a direct passage to the lower located diffractors. The diffracted signal in the normal incident case can be explained by EM wave propagation. Here, the EM wave is diffracted at the diffractor above and can consequently reach lower regions not explainable with simple ray optics. The signals are shifted to later arrival times due to the longer propagation path. Because of the simple assumptions of the FDTD algorithm, e.g. infinitesimal small dipoles

without additional regard for antenna characteristics, good signal intensities are still present for greater offsets. This effect is most visible for the diffractor at 3.25 m. Here the fitted diffraction hyperbola shows less correspondence for later arrival times. The fitted diffraction hyperbola for the diffractor at 1.25 m exhibits good correlation, indicating a weaker effect for gradients solely in vertical direction. This corresponds well with the earlier made observations.

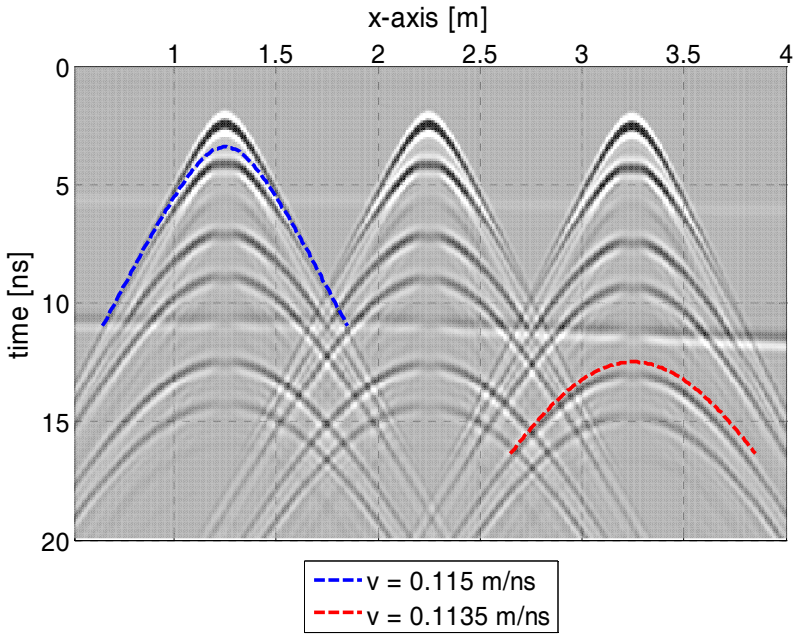

Figure 6.7: Synthetic zero-offset radar section with a measurement interval of 0.005 m. In the presented case, two exemplary diffraction hyperbolas are fitted to the data.

Using the synthetic radar section from Figure 6.7 and fitting diffraction hyperbolas to each diffraction event in the radar section, 18 velocities can be determined. Those integral velocities $\overline{v}_s$ are allocated to the respective diffractor location x_0 and the normal case arrival time t_{x_0}.

$$\overline{v}_s\left(x_0, t_{x_0}\right) = \frac{2}{t}\sqrt{\left(x - x_0\right)^2 + z_0^2} \tag{6.6}$$

Using the determined velocities $\overline{v}_s$ a two dimensional integral velocity distribution can be extrapolated (Figure 6.8). By interpolating the velocities some constraints have to be matched. The most important one is that the interpolated velocities are within the reasonable boundaries for propagation velocities, i.e. the velocities of unsaturated and fully saturated case. A second constraint in this case is that no abrupt changes are allowed to occur. Although an abrupt change of the propagation velocity occurs in the model, evidenced by the reflection caused by the interface, such an interface would normally be used for CMP measurements. In the present case the interface is only considered as an indicator for the quality and accuracy of the determined velocity distribution. An appropriate weighing has to be chosen in horizontal direction to ensure a smooth velocity transition as well. Such weighing can be based on different information and boundary conditions. This can be statistical information from

additional measurements (Tronicke and Holliger, 2005). Otherwise the horizontal resolution of the georadar can be included as a minimum boundary.

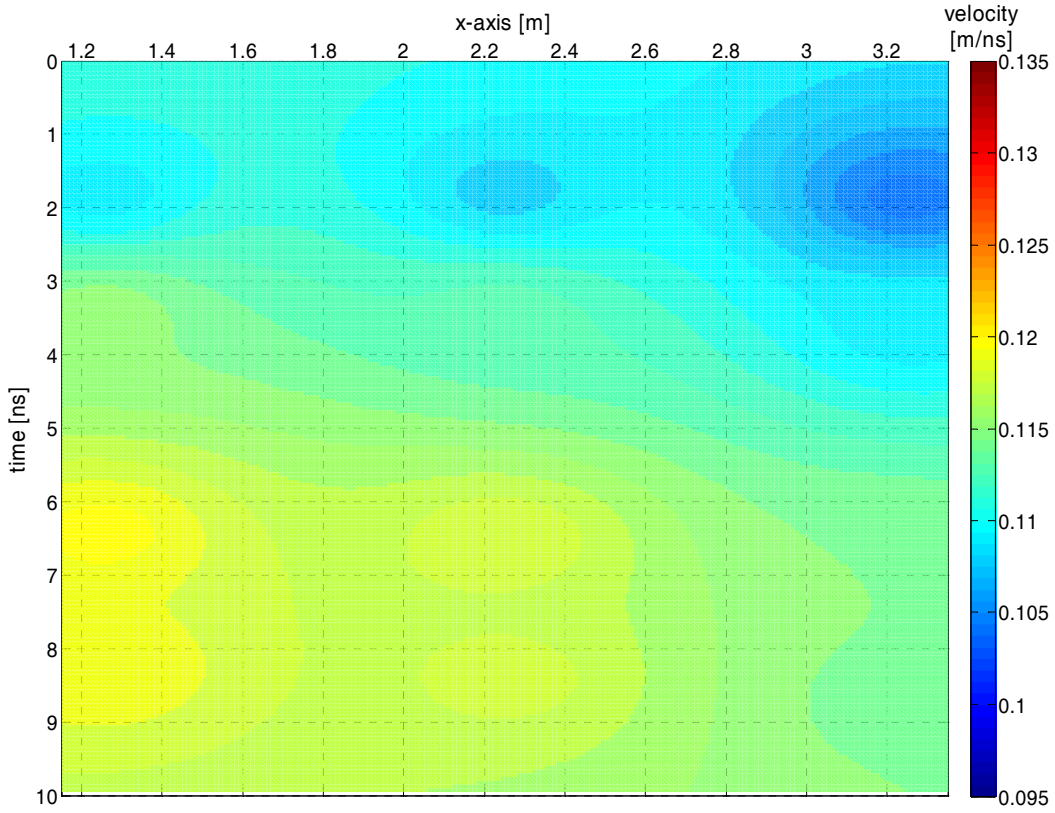

Figure 6.8: Interpolated integral velocity distribution $\bar{v}_s(x_0, t_{x_0})$ for the 0.005 m trace increment dataset, similar to Leucci et al. (2006).

Although an informative velocity distribution of the model is already obtained (e.g. Leucci et al., 2006), an allocation of the respective regions or the corresponding interval velocities is difficult. To transform the radar-section-based velocity distribution $\bar{v}_s(x, t_x)$ to a more graspable interval distribution $v_s(x,z)$, a time depth conversion, or time-to-depth conversion (Sheriff, 1997), has to be performed (Figure 6.9). The time depth conversion in this case can be described by:

$$z_n(x, t_n) = z_{n-1}(x, t_{n-1}) + \bar{v}_s(x, t_n) \cdot (t_n - t_{n-1}) \tag{6.7}$$

Equation (6.7) shows a more straightforward version of the general time depth conversion method:

$$z(x,t) = 2\frac{\frac{1}{n}\sum_{j=1}^{n} \bar{v}_j(x, t_j)}{t} \tag{6.8}$$

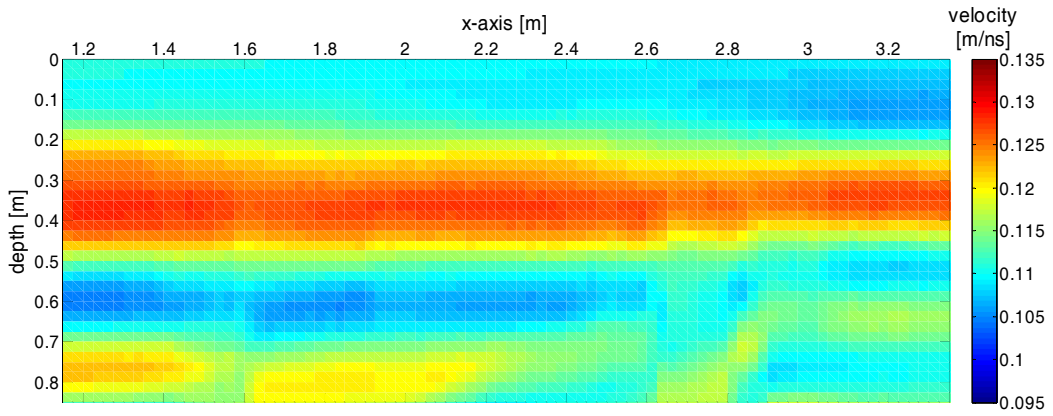

Figure 6.9: Time-depth-converted interval velocities of the velocity distribution in Figure 6.8 for the 0.005 m trace increment dataset.

After application of equation (6.7) to the data and the transformation of the determined velocities to relative permittivities by equation (2.24) or (2.25), a two-dimensional distribution of the relative permittivity of the subsurface is acquired (Figure 6.10). To exclude strong changes of the relative permittivity, an additional smoothing was performed. In the present case a simple restriction was implemented, preventing velocities to reach values beyond the reasonable minimum and maximum values. Since this smoothing was applied over the vertical distribution, stronger variations may occur in horizontal direction.

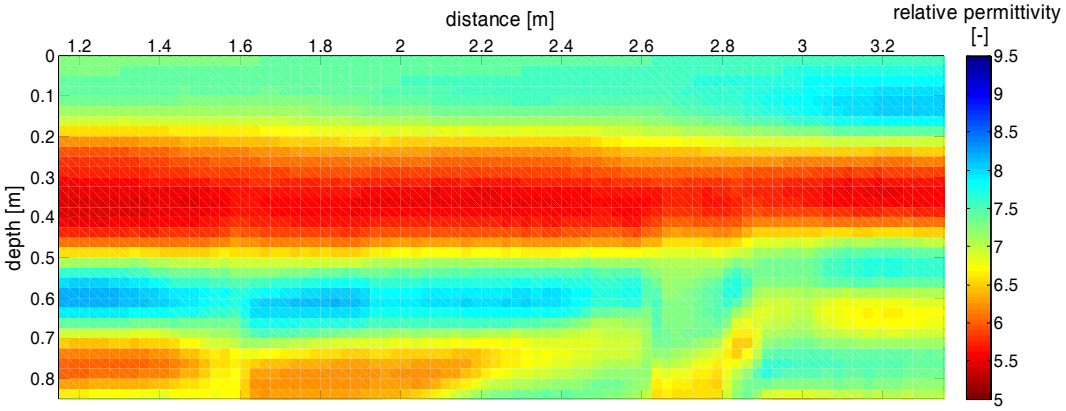

Figure 6.10: Determined relative permittivity distribution after application of time depth conversion for the 0.005 m trace increment dataset.

Looking at the relative permittivity distribution in Figure 6.10, a smoothed image of the initial model (Figure 6.5) is obtained. On the other hand, a few main features of the initial model are reproduced. The result in Figure 6.10 shows the expected vertical profile in the region of $x = 1.25$ m. Here the uppermost 0.35 m indicates a decreasing relative permittivity. The vertical area from 0.35 m to approximately 0.55 m features increasing relative permittivities followed by a decrease in relative permittivity for deeper regions. The horizontal gradient in the uppermost 0.6 m beginning at $x = 2.0$ m is recognizable in Figure 6.10. The constant layer below 0.6 m is not recognizable.

Looking at the absolute differences of the relative permittivities in Figure 6.11 some additional information can be acquired. The uppermost 0.2 m indicates an overestimation of

the relative permittivity by approximately 1 to 1.5. Considering the short propagation paths and taking Figure 6.2 into account, this error appears to be accredited mostly to erroneous time picking. Even using synthetic radar sections without any additional noise applied, the hyperbola fitting has to be performed by the operator. Additionally the shapes of the diffraction hyperbolas do not differ significantly due to the short propagation paths and the consequently short travel times even for big velocity ranges. This overestimation appears to be quite constant over the whole horizontal range which indicates that this effect could be considered in more sophisticated analysis procedures.

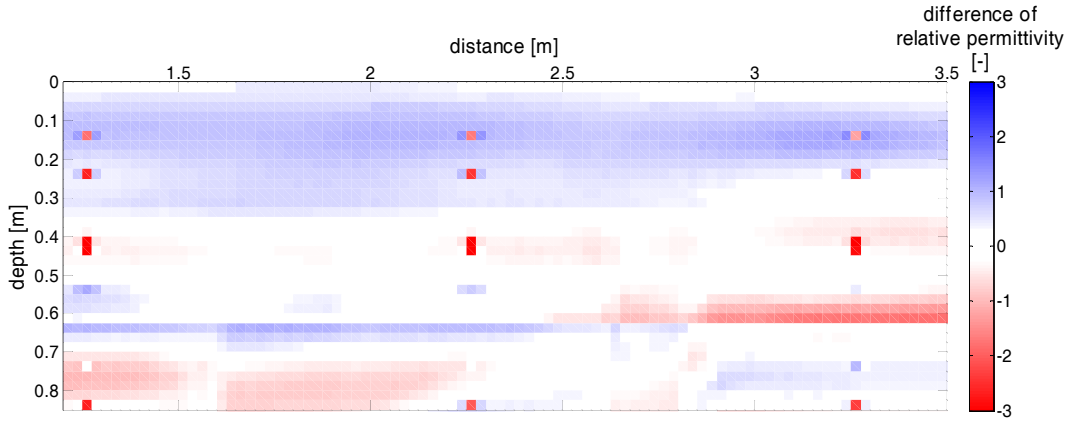

Figure 6.11: Absolute differences of the relative permittivities of the initial model and the determined relative permittivities from the DVA for the 0.005 m trace increment dataset.

Looking at the depth section between 0.2 m and 0.4 m, the correlation between the initial model and the determined relative permittivity distribution is quite good although no diffractors are present in this transition zone. This good agreement is an effect of the aforementioned smoothing of the interval velocities along the vertical axis. In the present case (Figure 6.11) the change of the vertical as well as the horizontal gradient is reproduced.

The following depth section between approximately 0.4 m and 0.5 m presents an almost perfect match between the initial model and the determined relative permittivity distribution. In this case all model assumptions are met. The transition between neighboring data points is smooth with constant gradients. Furthermore the determined relative permittivities are correct for the diffractor group at $x = 3.25$ m. For those diffractors strong horizontal and vertical gradients are encountered, which did not result in great errors. This validates the assumption in chapter 6.1 that the shape of the diffraction hyperbola near the apex is not strongly affected by horizontal and vertical gradients of the relative permittivity.

As expected, the interface at 0.6 m presents a big problem for the interpretation. In the depth section between 0.5 m and 0.7 m strong aberrations between the model and the determined relative permittivity occur. Since the algebraic sign of the error changes for bigger x locations, no constant error can be assumed. This is mainly caused by the constant model relative permittivity below the interface. Generally the depth region is underestimated or overestimated below 0.6 m. This can be interpreted as an indication of the smaller effect of small interval velocity changes on deeper diffractions. Due to the longer propagation path, an increasing insensitivity on small changes arises automatically.

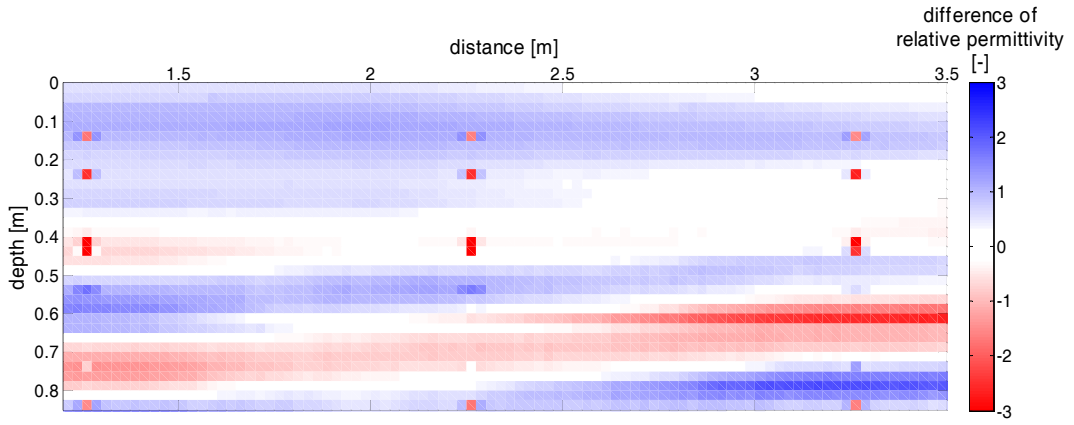

Figure 6.12: Absolute differences of the relative permittivities of the initial model and the determined relative permittivities from the DVA for the 0.02 m trace increment dataset.

A quite similar relative permittivity distribution can be achieved with the 0.02 m measurement interval (Figure 6.12). Generally the errors for all regions are bigger than with the 0.005 m dataset. These errors are located at the same positions as for the 0.005 m dataset. This indicates that the DVA encounters the same problems for both datasets. Depending on the required parameter accuracy, the measurement interval can be changed, but only to a certain degree.

Since the relative permittivity distribution is generally unknown for field measurements, an independent quality check of the derived relative permittivity distribution is required, which is not based on secondary measurements. A two-dimensional migration operation is performed on the synthetic radar section to provide information of the quality of the derived relative permittivity distribution. Applying a migration operation on a radar section rearranges signals in the radar section to its true locations (Sheriff, 1997). This means that the diffraction hyperbolas in the radar section in Figure 6.7 will be focused on their respective origins, i.e. their apexes. By performing the migration and an additional time depth conversion according to equation (6.7), the resulting radar section should feature events only at the actual locations of the 18 diffractors and the interface at 0.6 m depth.

Migration of georadar data was successfully applied for several problems and proved to be a useful tool to identify objects and anomalies in the subsurface (e.g. Bitri and Grandjean, 1998). Various methods of migration are possible such as Kirchhoff migration (e.g. Moran et al., 2000), frequency wavenumber domain (f-k) migration (Stolt, 1978), or even three-dimensional migration (e.g. Grasmueck et al., 2005). In the present case a simple diffraction stack was performed. With the diffraction stack unweighted amplitudes along a hypothetical diffraction hyperbola from equation (6.1) with the velocity $v_s(x,z)$ and the apex $a(x,z)$ are summarized. If an actual signal is recorded along the hypothetical hyperbola, the migration should produce a strong intensity at the apex of the hyperbola. If no signal is recorded along the hyperbola, the migration should produce an intensity of almost zero. The summation is performed over a restricted number of traces to reduce computation time. The effect of the transmission characteristics of the georadar antenna, i.e. energy is transmitted into and received from a narrow angular zone, makes a summation over a wide range unnecessary. The summation width has to be chosen with regard to the encountered detectability of the diffraction hyperbola.

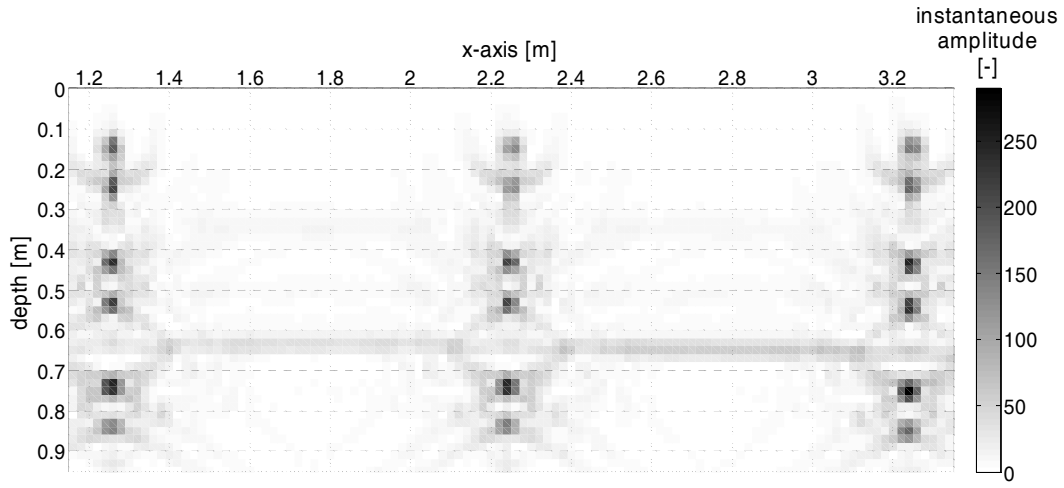

Figure 6.13: Instantaneous amplitudes of the migrated and time depth converted dataset with a measurement interval of 0.005 m and a summation width over 160 traces. The data was additionally processed by applying a gain function solely for better visualization.

Looking at the results of the combined migration and time depth conversion in Figure 6.13 and Figure 6.14, all 18 diffractors and the interface at a depth of 0.6 m can be identified. In order to display the data, two additional processing steps were performed. To enhance the signal intensity of deeper events, a simple geometrical gain function was applied. Here the attenuation of the signal due to geometrical spreading, i.e. distribution of the EM energy on an expanding wave surface, is corrected for. This can be achieved quite easily after the time depth conversion since the geometrical spreading is a distance-dependent effect (see. equation (2.43)). The second additional processing step was the derivation of the instantaneous amplitude (see 3.1.1). By deriving the instantaneous amplitude, the shape of the synthetic georadar signal is better visible.

The diffraction hyperbolas are well refocused. Some diffractors are better reproduced than others, which has various causes. For one, the used velocities for the migration were constant and did not regard the respective propagation paths for each trace. The mean propagation velocities of different traces for one diffraction hyperbola can vary quite strongly if strong gradients are present. This effect could be reduced by narrowing the summation width used for the migration, but would also result in lower signal intensities for the refocused diffractors. Another effect of the erroneous assumption of a constant propagation velocity for the whole diffraction hyperbola can be seen for deeper diffractors. Comparing the area of the instantaneous amplitude for the diffractors at 0.1 m and 0.7 m depth, a blurring of the diffractor is noticeable. Due to the diverging shape of the diffraction hyperbola, more and more points in the immediate vicinity of the diffractor achieve sufficient summed intensities to be recognized. The smoothing ray-like events at the diffractors on the other hand are artifacts of the migration operation.

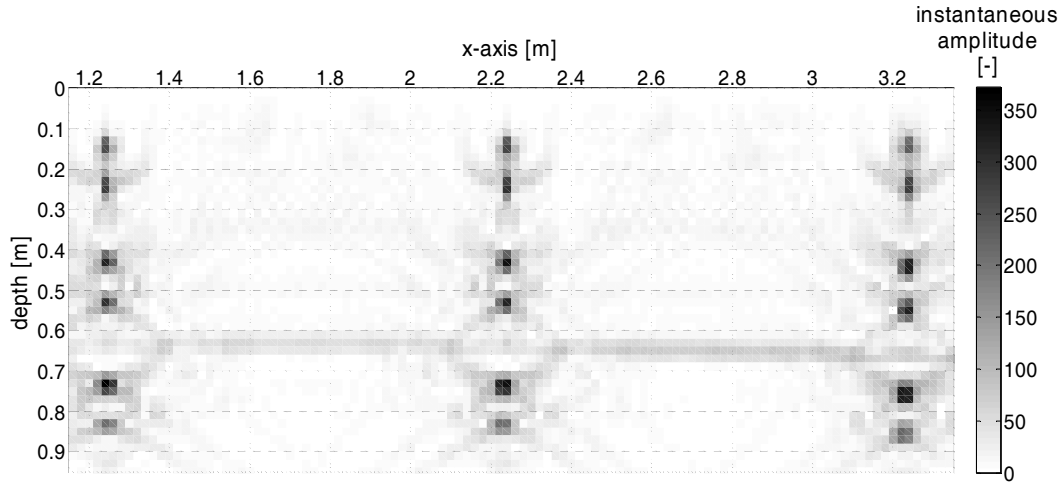

Figure 6.14: Instantaneous amplitudes of the migrated and time depth converted dataset with a measurement interval of 0.02 m and a summation width over 40 traces. The data was additionally processed by applying a gain function solely for comprehensibility reasons.

Looking at the refocused location of the events in the migrated depth section all diffractors are relocated at the correct position. All topsides of the diffractors are within 0.01 m of the initial position with the diffractor at $x = 3.25$ m and $z = 0.7$ m being the sole exception for both datasets (Figure 6.13 and Figure 6.14). Looking at Figure 6.11 and Figure 6.12 this shift is plausible since the strong aberrations in the relative permittivity occur directly above the diffractor. In both cases the location of the interface is sufficiently allocated. The vertical location of the interface is reproduced quite well for low x distances, but an increasing error is noticeable for higher x distances. This is caused by the increasing error of the determined relative permittivity distribution at higher x distances. For the maximum x distance this wrong allocation is approximately 0.03 m or 5% of the actual depth. The horizontal position of the diffractors is reproduced with accuracies higher than the measurement interval of 0.005 m or 0.02 m, respectively.

6.3 Application Example

Evaluating the DVA under controlled circumstances is difficult. To evaluate the DVA under field conditions a test site was installed at the INTERURBAN site Tiergarten (see 4.4). A hole was excavated and several diffractors were buried (Figure 6.15).

- A metal lattice was buried in a depth of 0.41 m and is situated at the interface humus to sand. A metal lattice was chosen to enable water movement through the metal grid minimizing the retention of seepage water. This also minimizes the occurrence of additional relative permittivity gradients caused by the lattice.
- The two air-filled tubes were buried in depths of 0.31 m and 0.32 m. With a diameter of 0.04 m the tubes are in the range of dens or passages of small rodents.
- The five metallic rods (diameter 0.023 m) were located in depths of 0.49 m, 0.39 m, 0.29 m, 0.21 m, and 0.1 m. Contrary to the air-filled tubes and the metal lattice the metallic rods were pushed into the wall of a trench next to the profile to minimize soil disturbance.

With the knowledge of the location of those diffractors an evaluation of the determined relative permittivity distribution can be performed similar to the method described in chapter 6.2.

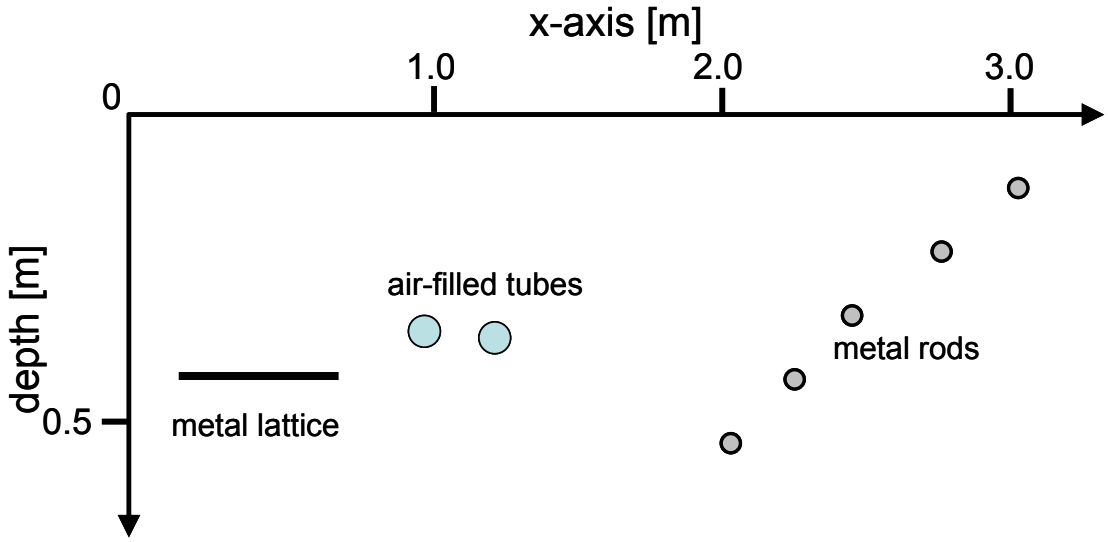

Figure 6.15: Location of the buried objects at the INTERURBAN test site Tiergarten.

In Figure 6.16 a preprocessed data set of a CO measurement at the INTERURBAN test site Tiergarten is displayed. The data was recorded with a 1 GHz georadar antenna, MALÅ GeoScience, Sweden. The 1 GHz antenna has an antenna separation of 0.11 m, which was taken into account. The processing steps included initial time zero correction to ensure that the radar section time $t = 0$ ns is equal to initial time zero. Bandpass filtering was additionally applied to eliminate high frequency noise in the recorded data. Furthermore, a gain function was applied to solely enhance the visibility of diffraction hyperbolas at later recording times. In Figure 6.16 almost every artificial diffractor can be spotted. The only apparently missing object is the deepest metallic rod. Additionally to the artificial objects some distinct diffractions are visible in the radar section. Those are most likely originated by natural diffractors located in the soil. Figure 6.17 shows some natural diffractors encountered during a nearby excavation at the INTERURBAN test site Tiergarten. The excavation was restricted to the humus zone of the soil and had a square base of less than 1 m^2. Although partially of anthropogenic origin, those natural diffractors present objects capable of generating diffraction hyperbolas under specific circumstances. For example tree roots can pose a high relative permittivity contrast during dry periods due to their high water contents.

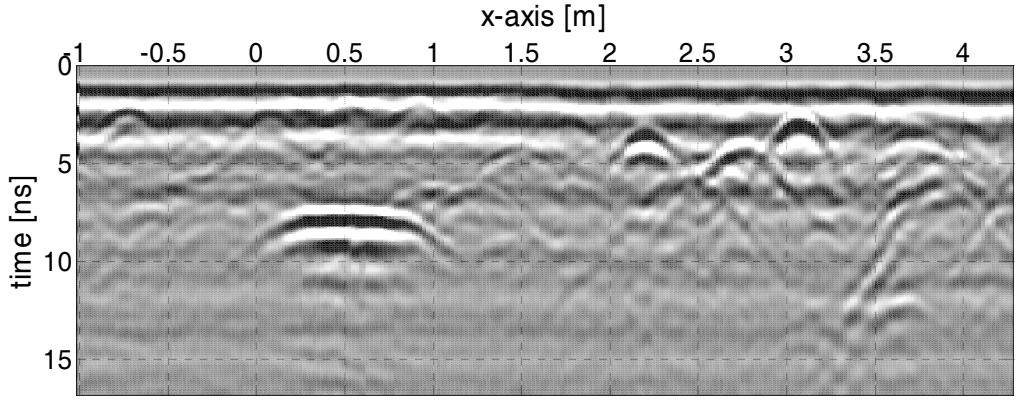

Figure 6.16: Preprocessed radar section along the INTERURBAN test site Tiergarten.

Figure 6.17: Assortment of various potential diffractors excavated at the INTERURBAN test site Tiergarten. The pen is pointing at a Kopecky cylinder with approximately 0.05 m diameter. Both the pen and the Kopecky cylinder are displayed for the purpose of comparison.

Fitting diffraction hyperbolas and deriving a two-dimensional velocity field v(x,t) enables the migration of the preprocessed data. To check the validity of the adapted diffraction hyperbolas a two-dimensional migration using the diffraction stacking is performed (Figure 6.18). To enhance the visibility of deeper events a gain function regarding geometrical spreading was applied. Due to the electrical conductivity in the field, a gain function to correct both the geometrical spreading and the attenuation caused by dielectric losses would be necessary. Those attenuation mechanics are not taken into account and the signal intensities consequently cannot be evaluated. Nevertheless, a good image of the subsurface is created. All eight artificial diffractors are distinguishable, although the deepest metallic rod was not clearly visible in the preprocessed radar section (Figure 6.16). The migration and the time depth conversion changed the shape of the refocused diffraction hyperbolas drastically. The horizontal blurring of the refocused events can be accredited to the migration algorithm. The compression or elongation of the georadar wavelet, e.g. the reflection of the metal lattice, is an effect of the time depth conversion. Since the wavelet is of finite time, the v(x,t) distribution can assign different velocities to the same signal reflected from an object. This results in a deformation of the wavelet after the time depth conversion from the x-t radar section into the x-z radar section.

The vertical location of the metal lattice is approximately 0.42 m and resembles an almost plane reflector after migration. Taking the fact into account that the metal lattice had to be buried, an inaccuracy in the localization of 0.01 m is quite good. The vertical position of the two air filled tubes is a little bit more difficult to determine. Due to the inferior signal intensity, a greater vertical area can be attributed for the arrival of the diffracted wavelet. Depending on the chosen area, a depth of 0.30 m to 0.32 m can be assigned to the first air filled tube. The second air filled tube is slightly deeper and the depth interval of 0.31 m to 0.33 m is a reasonable depth picked. Although the deepest metallic rod was not clearly observable in the unmigrated radar section (Figure 6.16) a depth of approximately 0.50 m can

be assigned. The depth of the following metallic rods can be determined as 0.38 m, 0.28 m, 0.20 m, and 0.10 m, respectively. This implies a vertical allocation accuracy of approximately 0.01 m for all known diffractors. This relative constant allocation error of 0.01 m indicates the problem of the DVA for shallow events. Whereas the location for the deepest diffractor is within a 2% error margin, this margin increases to 10% for the shallowest metallic rod. There are several additional refocused events visible in the migrated radar section. Although their optimal refocusing may be not achieved, their appearance in the data suggests at least a relatively correct velocity distribution.

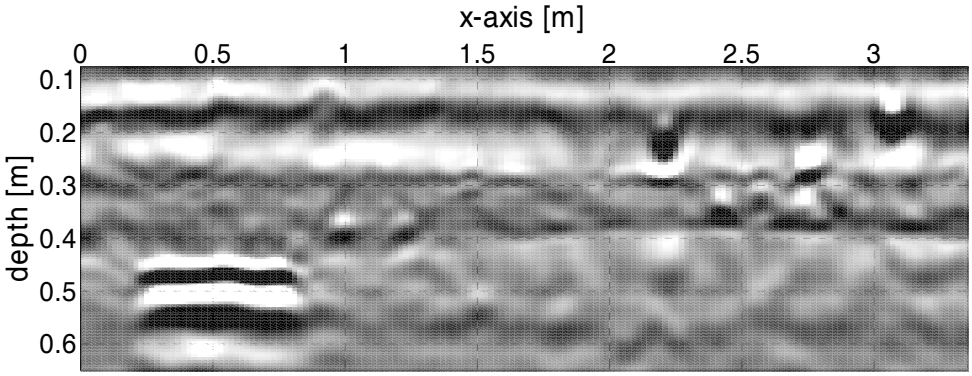

Figure 6.18: Migrated and time depth converted radar section, INTERURBAN test site Tiergarten. Depth axis is enlarged by a factor of 2.

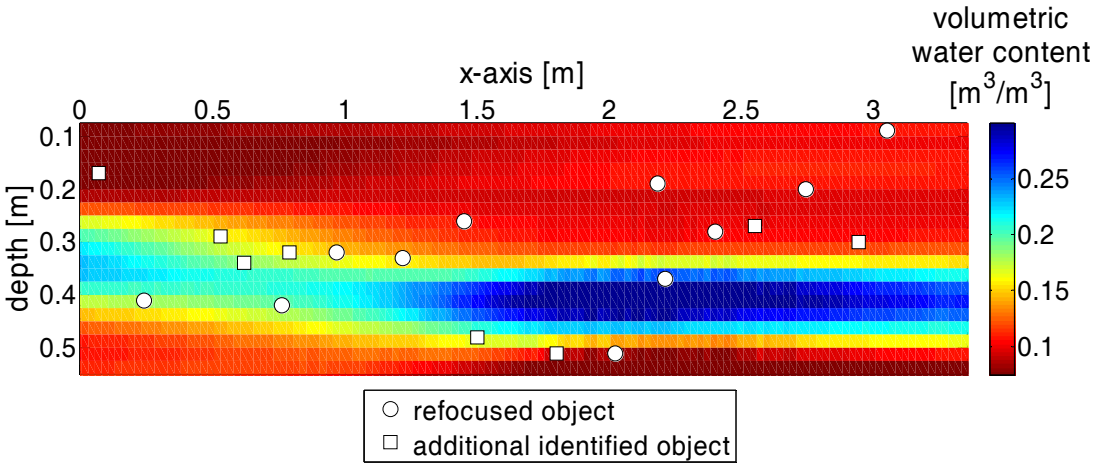

Figure 6.19: Calculated volumetric water content distribution, INTERURBAN test site Tiergarten. The circles indicate the location of actual objects refocused by determining velocities of diffraction events, whereas the squares indicate refocused events invisible before migration. Depth axis is enlarged by a factor of 2.

The determined volumetric water content distribution from DVA is displayed in Figure 6.19. The various diffracting objects are additionally indicated by markers. The circles indicate the diffractors used for the determination of the two-dimensional velocity distribution. The squares indicate the location of refocusing events initially not visible in the radar section. Those events are not necessarily refocused to their optimum, but present an indication of the

validity of the calculated volumetric water content distribution. The soil can be distributed into three main observations:

- The uppermost 0.3 m appears to be relatively dry with low volumetric water contents of below 0.14 m^3/m^3.
- After this dry zone, i.e. low volumetric water content, a steep increase of the volumetric water content is noticeable. Here values of over 0.20 m^3/m^3 are reached before the volumetric water content decreases again in deeper areas. This vertical region of high volumetric water content correlates quite well with the interface humus to sand.
- Additionally a horizontal gradient is visible with lower volumetric water contents for smaller x locations. This transition correlates to observations of Huraß and Schaumann (2006), who noticed a transition of generally water-repellent regions to almost totally wettable soils at the test site Tiergarten.

Although the absolute accuracy of the determined volumetric water contents is expected to be low, valuable information can still be gathered. Even for gradual parameter transitions without significant interfaces horizontal trends as well as the vertical profile can be identified. Depending on the number of detected diffractors this accuracy can increase or decrease. The identification of additional refocusing events presents a promising outlook to further increase the accuracy of the DVA method.

The occurrence of additional refocusing events could enhance the quality of the determined relative permittivity distribution. On the other hand an automatic identification of refocusing events could replace the diffraction hyperbola adaptation by hand. For diffraction hyperbola identification Shihab and Al-Nuaimy (2004) used a pattern recognition algorithm on their radar sections. Here, the used algorithm spots hyperbola events in the radar section. Such an algorithm could be useful, but would still require the adaptation of the velocity determination by hand. Masked diffraction hyperbolas might however be overlooked by the algorithm, since stronger events interfere with the hyperbola shapes.

To utilize the refocusing effect of the migration algorithm a small synthetic experiment is performed. A homogeneous background model is derived with a background relative permittivity of 9. In this background a small diffractor is inserted at the location $x = 1.5$ m at the depth $z = 0.8$ m. The derived synthetic radar section is then migrated with gradual increasing propagation velocities starting from 0.07 m/ns to 0.13 m/ns in 0.002 m/ns intervals. This interval is based on the estimated accuracy of propagation velocity determination performed earlier (6.1). The resulting migrated radar sections are then combined into a three-dimensional data cube. The axis of the cube are the distance x, the time t, and the migration velocity v respectively. The registered intensities I can be plotted as a function $I(x,\mathrm{v},t)$ (Figure 6.20). Using the intensity function the maximum can be determined. In the present case a maximum is localized at $I(x = 1.52\ \mathrm{m},\ \mathrm{v} = 0.102\ \mathrm{m/ns},\ t = 16.75\ \mathrm{ns})$. Since intensities are registered, the shift of the propagation time from 16 ns to 16.75 ns is solely explained by the wavelet shape.

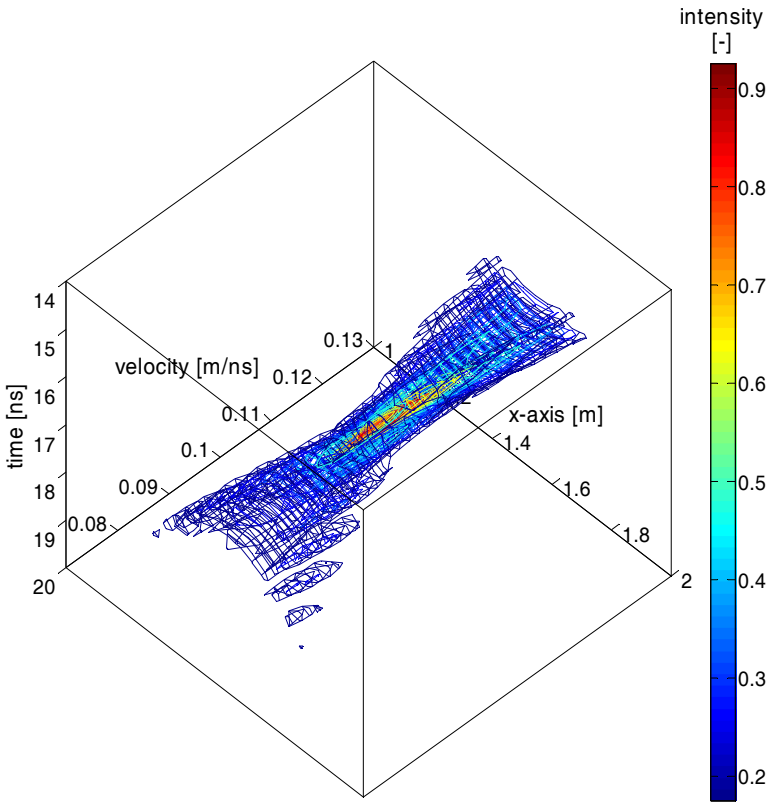

Figure 6.20: Signal intensity distribution in the location-velocity-time space.

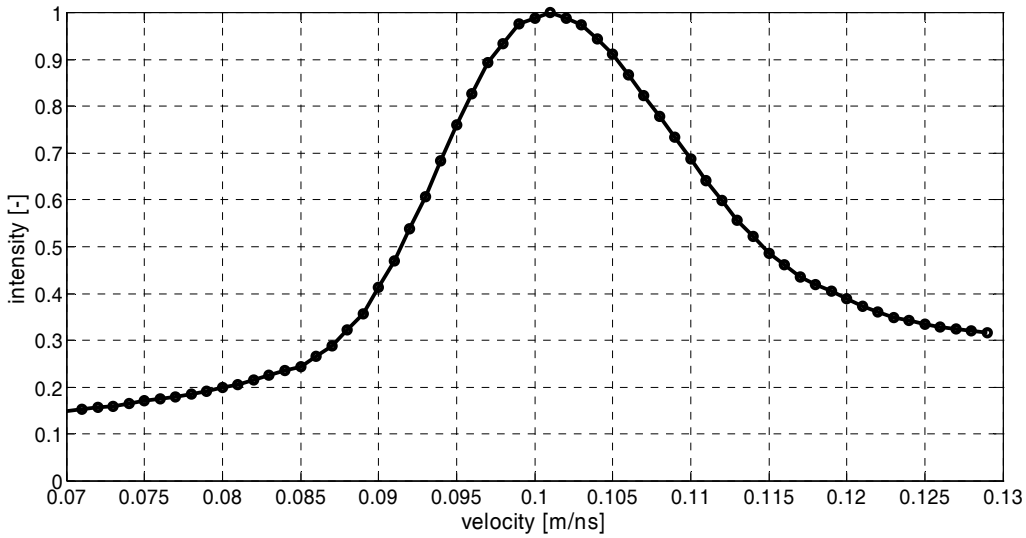

Figure 6.21: Registered intensities along the velocity axis for $t = 16.75$ ns and $x = 1.52$ m.

Due to the refocusing effect of the applied migration, a bow-tie-like shape is recognizable (Figure 6.20). In the present case, the narrowing of the bow tie shape is centered at the correct velocity of 0.10 m/ns but features a broad intensity maximum. To estimate the quality of the focusing, the intensity along the velocity axis at the maximum position $x = 1.52$m and $t = 16.75$ ns is drawn (Figure 6.21). Looking at the intensity distribution in Figure 6.21 the

broad maximum is recognizable. Although relatively steep trailing edges are present accuracy in the range of ±0.01 m/ns appears realistic in this case.

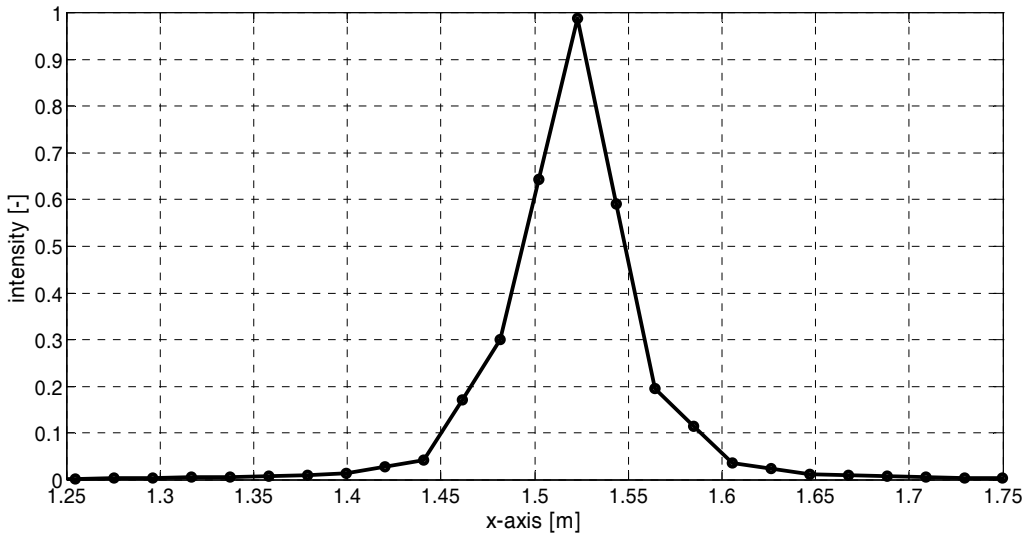

Figure 6.22: Registered intensities along the x-axis for t = 16.75 ns and v = 0.102 m/ns.

The intensity maximum in the x dimension is shifted to 1.52 m (Figure 6.22). This horizontal shift is caused by the used data discretization, which features an allocation accuracy of 0.02 m. The horizontal allocation is reproduced well when taking the uncertainty into account. The signal intensities provide a distinct feature restricting the maximum in the range of ±0.02 m. Since the velocity shows a lesser explicitness in Figure 6.21 perhaps an alternative migration algorithm could provide a better result.

By performing several migrations on the same dataset and plotting each acquired migration result in the location-velocity-time space, refocusing events can be identified. The horizontal and time location can be restricted quite well and a good estimate of the velocity is acquired. Although relatively time-consuming, this procedure could help identify previously unrecognized diffraction events. The velocity interval for the manual diffraction hyperbola adaptation could be restricted, too. The observed focusing and defocusing effect of a distinct diffraction event could be used for automatic target identification and velocity determination. Utilizing a search algorithm could spot the diffraction origin as well as the optimum location, time, and velocity combination.

7 Conclusions

In the course of the presented work the georadar was successfully applied to determine the volumetric water content of soils. The high correlation between the relative permittivity of the soil and its volumetric water content makes the georadar predestined for water content determinations. Due to the integral character of georadar measurements, investigations were previously restricted to areas generally larger than several decimeters. To increase the spatial resolution new methods for georadar interpretations were evaluated. The various introduced methods enabled spatial resolutions of few decimeters. All methods were performed with common georadar systems, and their implementation for georadar investigations to determine the relative permittivity is easy to realize. To emphasize the efficiency of the introduced methods no highly sophisticated interpretation tools were necessary.

With the utilization of parallel transmission measurements good matches of the relative permittivity were achieved. By applying existing models for the electrical behavior of water on measured georadar data, satisfying estimates of the electrical conductivity can be achieved. Both the relative permittivity and the electrical conductivity can be determined with high accuracy, provided that the traversing EM wave is attenuated sufficiently. The assumption of insignificant signal dispersion for small-scale investigations was justified reducing the data processing noticeably. On the other hand, reliable values of the electrical conductivity cannot be acquired for small objects filled with soil. In the investigated case electrical conductivities of less than 0.02 S/m did not provide sufficient signal attenuation. Furthermore, the utilized georadar system featured variations in signal intensities of ± 10% under controlled conditions. Considering the ideal conditions present during the experiment, quantitative evaluations of the signal attenuation appear unrealistic for small-scale field measurements.

The application of parallel transmission measurements on a sector irrigation experiment conducted on a lysimeter revealed feasibility of the parallel transmission measurement. The seepage of the irrigated water was traceable with a vertical resolution of 0.05 m and a temporal resolution of less than a minute. Due to simple control measurements with the georadar a lateral constriction of the irrigated area was possible. The travel time analysis as well as the qualitative evaluation of the signal attenuation resulted in a similar vertical zone classification of the soil inside the lysimeter. The attenuation data shows a more complex behavior than simple electrical conductivity effects. In the presented case attenuation for certain regions remained unaffected albeit an increase of the volumetric water content was registered.

Tomographical transmission measurements were carried out at the same lysimeter to check the potential of georadar to locate short-term volumetric water content changes inside small soil columns. Due to the small dimensions of the lysimeter, common automatic arrival time picking tools cannot be applied. With the proposed assumption of negligible signal dispersion for small scale investigations, arrival times were determined manually with high accuracy. A sensible reduction of transmitter-receiver positions was necessary to accomplish a temporal resolution of approximately 30 min. Ensuring optimal data quality several calibration measurements were performed in the course of data acquisition. The determined volumetric water contents correlate well with simultaneously collected TDR data. The spatial resolution was approximately 0.1 m, but reliable determinations were not possible for quick changes of the volumetric water content during data acquisition.

Travel time analysis of the ground wave measurement is a common georadar method for shallow volumetric water content determination. Due to the integral nature of the ground wave method common sense implies smaller antenna separations for higher spatial

resolutions. Analyzing synthetic data revealed disadvantages of this conclusion since shorter propagation paths increase the error of propagation time determination. Therefore an inversion of the ground wave travel time is proposed to enhance the spatial resolution and simultaneously ensuring high data reliability. Based on simple propagation models a significant improvement of the localization of relative permittivity changes is achieved. The travel time inversion proved to be robust to deal with noisy data sets and an easy threshold criterion was introduced to identify relative permittivity changes with a spatial resolution of approximately 0.1 m. FDTD modeling provided additional verification of the proposed procedure under more realistic conditions. A field experiment showed good correlation between common georadar ground wave measurements and TDR, emphasizing the good applicability and validity of the ground wave method. Global trends were reproduced quite well, but only the additional travel time inversion reproduced the small-scale heterogeneity indicated by TDR.

Commonly applied georadar methods for the determination of the vertical relative permittivity distribution cannot be used for small-scale investigations in soils. Therefore a specialized georadar method was utilized, which was entitled radar based time domain reflectrometry (RB-TDR). 3D FDTD modeling indicated the existence of a guided EM wave when placing a georadar antenna next to a metal rod vertically inserted into the subsurface. Although no antenna characteristics could be simulated with the utilized FDTD code, the guided EM wave showed an EM intensity distribution not circularly symmetric to the centerline of the metal rod.

Using the results from the synthetic modeling, an adapted antenna layout is proposed to ensure optimal data quality. This adapted antenna layout proved validity during a controlled field experiment. The distance of the antenna to the metal rod providing still constant recording characteristics from the guided EM wave was called reach and was determined to be in the range of one wavelength. A more thorough determination of the EM field distribution of the guided EM wave was not possible. In the course of two laboratory experiments the accuracy as well as the reliability of the RB-TDR method was tested. The measurements provided correct relative permittivity values. During a controlled irrigation experiment in the field, water infiltration was traced over a depth of approximately 1 m with temporal resolutions in the range of three minutes. The vertical resolution was 0.02 m, but an averaging over approximately 0.1 m was necessary to ensure reliable data.

With the introduction of the diffraction velocity analysis (DVA) a powerful method to determine the volumetric water content distribution in soils is presented. Due to the general absence of significant reflectors in the uppermost soil, common georadar methods are limited in their applicability. The advantage of the DVA is that it requires the presence of diffracting rather than reflecting events in the radar section. A far better coverage of the investigated region can be achieved since the origins are small objects or edges of small reflectors inside the soil. Based on geometrical assumptions and computations, changes of the shape of diffraction hyperbolas are deduced to changes of the relative permittivity distribution above the diffractor. Consequently a reasonable accurate two-dimensional EM velocity distribution can be derived. This velocity distribution was transformed to a relative permittivity distribution with the application of a time depth conversion.

Synthetic FDTD modeling was performed to check the accuracy of DVA for relative permittivity determination. A field experiment proved good applicability of DVA and revealed additional potential. Depending on the distribution of the diffracting objects, spatial resolutions that are better than 0.3 m are achievable. By performing a 2D migration and utilizing the determined EM velocity distribution, previously undetectable diffractors were discovered. Based on FDTD modeling a procedure is presented to detect previously undetected diffractors and simultaneously determine their location and the relative

permittivity above the diffractor. Implementing this procedure could increase the number of grid points and consequently improve the determined relative permittivity distribution.

All discussed georadar methods increase the applicability of georadar for small-scale dielectric parameter determination of soils. The accuracy can be easily enhanced by application of more sophisticated processing and inversion routines. Due to their high potential, the discussed methods represent a good base for future improvements. All presented methods feature their own advantages and disadvantages. A combined application of more than one of these methods could provide supplementary results. Apart from obvious issues to improve the accuracy of the discussed methods some other problems need to be addressed.

With the prerequisite to analyze the whole data set for RB-TDR, tomographical transmission measurements, and DVA, only parallel transmission measurements and ground wave measurements appear capable of investigating the dynamical processes in the sub-minute range. With exception of DVA all discussed methods have the potential for easy analysis of amplitude information in addition to propagation time analysis. To implement this information several issues require close attention. Without the exact knowledge of the antenna characteristics and the exact emitted and received EM energy, attenuation cannot be determined with the required accuracy. Furthermore, a better understanding of the soil's electrical behavior and its regulating properties will be necessary to deduce a correct mixing model for complex relative permittivity data. Measurements under controlled conditions become increasingly difficult with improved spatial resolution. Due to the high resolution formerly homogeneous objects reveal their heterogeneity, complicating necessary calibration measurements.

8 Bibliography

Arcone, S. A. 1995. Numerical studies of the radiation patterns of resistively loaded dipoles. Journal of Applied Geophysics, 33, 39-52.

Bachmann, C. 1997. Kernstrahlungsverfahren. In Kupfer, K. 1997. Materialfeuchtemessung, Grundlagen- Meßverfahren- Applikationen- Normen. expert verlag.

Bauters, T. W. J., Steenhuis, T. S., DiCarlo, D. A., Nieber, J. L., Dekker, L. W., Ritsema, C. J., Parlange, J.-Y., Haverkamp, R. 2000. Physics of water repellent soils. Journal of Hydrology, 231-232, 233-243.

Becht, A., Appel, E., Dietrich, P. 2006. Analysis of multi-offset GPR data: a case study in a coarse-grained gravel aquifer. Near Surface Geophysics, 4, 227-240.

Binley, A., P. Winship, R. Middleton, M. Pokar, and J. West. 2001. High resolution characterization of vadose zone dynamics using cross-borehole radar. Water Resources Research, 37, 2639-2652.

Bitri, A., Grandjean, G. 1998.Frequency-Wavenumber modelling and migration of 2D GPR data in moderately heterogeneous dispersive media. Geophysical Prospecting, 46, 287-302.

Bohrleber, A. 1992. Quantifizierung von Bodenwasserbewegungen unter kombiniertem Einsatz von Neutronen- und Gamma-Gamma- Sonde. Schriftenreihe Angewandte Geologie, 18.

Bronstein, I. N., Semendjajew, K. A. 1991. Taschenbuch der Mathematik. B.G. Teubner Verlagsgesellschaft Stuttgart-Leipzig, Verlag Harri Deutsch Thun und Frankfurt/Main.

Buttkus, B. 2000. Spectral analysis and filter heory in applied geophysics. Springer-Verlag, Berlin Heidelberg New York.

Daniels, D. 2004. Ground-penetrating radar - 2nd ed. – (Radar, sonar, navigations & avionics. London, United Kingdom, The Institution of Electrical Engineers.

Dannowski, G. and Yaramanci, U. 1999. Estimation of water content and porosity using combined radar and geoelectrical measurements. European Journal of Environmental and Engineering Geophysics, Vol. 4, 71-85.

Demtröder, W., 1995. Experimentalphysik, Band 2: Elektrizität und Optik. Berlin Heidelberg, Germany, Springer-Verlag.

Dines, K. A., Lytle, R. J. 1979. Computerized geophysical tomography. Proc. IEEE, 67, 7, 1065-1073.

Du, S. 1995 Determination of Water in the Subsurface with the Ground Wave of Ground Penetrating Radar, PhD thesis Ludwig-Maximilians-University, Munich, Germany.

Fechner, T., Börner, F. D., Richter, T., Yaramanci, U., Weihnacht, B. 2004. Lithological interpretation of spectral dielectric properties of limestone. Near Surface Geophysics. 150-159.

Fellner-Feldegg, H. 1969. The measurement of dielectrics in the time domain. J. Phs. Chem., 73, 616-623.

Fisher, E., McMechan, G., and Annan, A. P. 1992. Acquisition and processing of wide-aperture ground-penetrating radar data. Geophysics, 57, 495-504.

Fließbach, T. 1997. Elektrodynamik: Lehrbuch zur Theoretischen Physik II. Siegen, Spektrum Akkad. Verlag, 2. Überarbeitete Auflage.

Friedman, S. P. 1997. Statistical mixing model for the apparaent dielectric constant of unsaturated porous media. Soil Sci. Soc. Am. J., 61, 742-745.

Galagedara, L. W., Parkin, G. W., Redman, J. D., von Bertoldi, P., Endres, A. L. 2005a. Field studies of the GPR ground wave method for estimating soil water content during irrigation and drainage. Journal of Hydrology, 301, 182-197.

Galagedara, L. W., Redman, J. D., Parkin, G. W., Annan, A. P., Endres, A. L. 2005b. Numerical modeling of GPR to determine the direct ground wave sampling depth. Vadose Zone Journal, 4, 1096-1106.

Grasmueck, M., Weger, R., Horstmeyer, H. 2005. Full-resolution 3D GPR imaging. Geophysics, Vol. 70, No. 1, K12-K19.

Greaves, R. J., Lesmes, D. P., Lee, J. M., Toksöz, M. N. 1996. Velocity variations and water content estimated from multi-offset, ground-penetrating radar. Geophysics, 61, 683-695.

Gregoire, C., Hollender, F. 2004. Discontinuity characterization by the inversion of the spectral content of ground-penetrating radar (GPR) reflections—Application of the Jonscher model. Geophysics, 69, 1414-1424.

Grote, K., Hubbard, S., Rubin, Y. 2002. GPR monitoring of volumetric water content in soils applied to highway construction and maintenance. Leading Edge of Exploration, 21, 482-485.

Grote, K., Hubbard, S., Rubin, Y. 2003. Field-scale estimation of volumetric water content using ground-penetrating radar ground wave techniques. Water Resources Research, Vol. 39, No. 11, 1321-1335.

Hagrey, S. A. el, Müller, C. 2000. GPR study of pore water content and salinity in sand. Geophysical Prospecting, 48, 63-85.

Hanafy, S. and al Hagrey, S. A. 2006. Ground-penetrating radar tomography for soil-moisture heterogeneity. Geophysics, 71, K9-K18.

Harari, Z. 1996: Ground-penetrating radar (GPR) for imaging stratigraphic features and groundwater in sand dunes. Journal of Applied Geophysics, 36, 43-52.

Helm, A. 1998. Einfluß von Offset und Antennenorientierung auf Reflexionsmerkmale beim Bodenradar. Diploma thesis, Department of Applied Geophysics, Technical University of Berlin, Germany.

Herman, G. T., Kuba, A. 1999. Discrete Tomography: Foundations, Algorithms and Applications. Birkhäuser, Boston, USA.

Hippel, A. von 1988. The dielectric relaxation spectra of water, ice and aqueous solutions, and their interpretation. IEEE Trans. Electr. Insul. 23, 801-816.

Holliger, K., Lampe, B., Meier, U., Lambert, M. 2004. Realistic modelling of surface ground-penetrating radar antenna systems: where do we stand? Near Surface Geophysics, 13-21.

Holliger, K., Maurer, H. 2004. Effects of stochastic heterogeneity on ray-based tomographic inversion of crosshole georadar amplitude data. Journal of Applied Geophysics, 56, 177-193.

Holliger, K., Musil, M., Maurer, H. R. 2001. Ray-based amplitude tomography of crosshole georadar data: a numerical assessment. Journal of Applied Geophysics, 47, 285-298.

Hübner, C. 1999. Entwicklung hochfrequenter Meßverfahren zur Boden- und Schneefeuchtebestimmung. Wissenschaftl. Berichte FZKA 6329, Forschungszentrum Karlsruhe, Karlsruhe, Germany.

Hugenschmidt, J. 2000. Railway track inspection using GPR. Journal of Applied Geophysics, 43, 147–155.

Huisman, J. A., Hubbard, S. S., Redman, J. D., Annan, A. P. 2003. Measuring soil water content with ground penetrating radar : a review. Vadose Zone Journal, 2, 476-491.

Huisman, J. A., Sperl, C., Bouten, W., Verstraten, J. M. 2001. Soil water content measurements at different scales: accuracy of time domain reflectometry and ground-penetrating radar. Journal of Hydrology, 245, 45-58.

Huraß, J., Schaumann, G. E. 2006. Properties of soil organic matter and aqueous extracts of actually water repellent and wettable soil samples. Geoderma, 132, 222-239.

Igel, J. S., Schmalholz, J., Anschütz, H. R., Wilhelm, H., Breh, W., Hötzl, H., Hübner C. 2001. Methods for Determining Soil Moisture with the Ground Penetrating Radar (GPR). Conference Proceedings of the Fourth International Conference on Electromagnetic Wave Interaction with Water and Moist Substances, Weimar, 484-491.

Irving, J. D., Knight, R. J. 2003. Removal of wavelet dispersion from ground-penetrating radar data. Geophysics, 98, 960-970.

Jackson, J. D. 1975. Classical Electrodynamics. Berkeley, Kalifornien, USA, John Wiley & Sons.

Johnson, R. H., Poeter, E. P. 2005. Iterative use of the Bruggeman-Hanai-Sen mixing model to determine water saturations in sand. Geophysics, 70, K33-K38.

Jol, H., M. 1995. Ground penetrating radar antennae frequencies and transmitter powers compared for penetration depth, resolution and reflection continuity. Geophysical Prospecting, 43, 693-709.

Kaatze, U. 1989. Permittivity of water as a function of frequency and temperature. Journal of Chemical Engeneering Data, 34, 371-374.

Kemna, A., Kulessa, B., Vereecken, H., 2002. Imaging and characterisation of subsurface solute transport using electrical resistivity tomography (ERT) and equivalent transport models. Journal of Hydrology, Vol. 267, No. 3-4, 125-146.

Knödel, K., Krummel, H., Lange, G. 1997. Handbuch zur Erkundung des Untergrundes von Deponien und Altlasten: Band 3 Geophysik. Springer-Verlag, Berlin, Germany.

Kruk, J. van der, Slob, E. C. 2004. Reduction of reflections from above surface objects in GPR data. Journal of Applied Geophysics, 55, 271-278.

Kruk, J. van der, Zeeman, J., H., Groenenboom, J. 2002. Multicomponent imaging of different objects with different strike orientations. Proceedings of the Ninth international conference on Ground Penetrating Radar, Santa Barbara, USA, 150-155.

Kruk, J. van der. 2004. Three-dimensional GPR imaging in the horizontal wavenumber domain for different heights of source and receiver antennae. Near Surface Geophysics, 23-29.

Kupfer, K. 1997. Materialfeuchtemessung, Grundlagen- Meßverfahren- Applikationen- Normen. expert verlag.

Lampe, B., Holliger, K., and Green, A. G. 2003. A finite-difference time-domain simulation tool for ground-penetrating radar antennas. Geophysics, 68, 971-987.

Leucci, G., Cataldo, R., De Nunzio, G. 2006. Subsurface water-content identification in a crypt using GPR and comparison with microclimatic conditions. Near Surface Geophysics, 4, 207-213.

Loeffler, O., Bano, M. 2004. Ground Penetrating Radar Measurements in a Controlled Vadose Zone: Influence of the water Content. Vadose Zone Journal, 3, 1082-1092.

Messinger, J. 2004. Effective automatic picking of traveltime data with high precision. Proceedings of the Tenth Conference on Ground Penetrating Radar, 91-94.

Moran, M., L., Greenfield, R., J., Arcone, S., A., Delaney, A., J., 2000. Multidimensional GPR array processing using Kirchhoff migration. Journal of Applied Geophysics, 43, 281-295.

Mosey, S., Knight, R., 2004. Modeling the field-scale relationship between dielectric constant and water content in heterogeneous systems. Water Resources Research, 40, W03510, doi:10.1029/2003WR002589.

Müller, M., Mohnke, O., Schmalholz, J. and Yaramanci, U., 2003. Moisture assessment with small-scale geophysics - The Interurban Project. Near Surface Geophysics, 1, No. 4, 173-182.

Nabighian, M. N., Macnae, J. C. 1991. Time domain electromagnetic prospection methods. In: Investigations in Geophysics No. 3: Electromagnetic methods in Applied Geophysics, Volume 2, Application, Parts A and B. Edited by Nabighian, M. N. Society of Exploration Geophysisicsts.

Nolting, W. 1993. Grundkurs: Theoretische Physik 3 Elektrodynamik. Verlag Zimmermann-Neufang, Ulmen, Germany, 3. Auflage.

Or, D., Wraith, J. M. 1999. Temperature effects on soil bulk dielectric permittivity measured by time domain reflectometry: A physical model. Water Resources Research, Vol. 35, No. 2, 371-383.

Orlando, L. 2003. Semiquantative evaluation of massive rock quality using ground penetrating radar. Journal of Applied Geophysics. 52, 1-9.

Oswald, B., Benedikter, H. R., Bächtold, W., Flühler, H. 2004. A Single-Rod Probe for Time Domain Reflectometry Measurements of the Water Content. Vadose Zone Journal, 3, 1152-1159.

Oswald, B., Doetsch, J., Roth, K. 2006. A new computational technique for processing transmission-line measurements to determine dispersive dielectric properties. Geophysics, 71, K31-K35.

Overmeeren, R. A. van, Sariowan, S. V., Gehrels, J. C. 1997. Ground penetrating radar for determining volumetric soil water content; results of comparative measurements at two test sites. Journal of Hydrology, 197, 316-338.

Pelster, R. 1995. A novel analytical method for the broadband determination of electromagnetic impedances and material parameters. IEEE Transactions on Microwave Theory and Technique, 43, 1494-1501.

Peplinski, N. R., Ulaby, F. T., Dobson, M. C. 1995. Dielectric properties in the 0.3-1.3 GHz range. IEEE Transactions on Geoscience and Remote Sensing, 33, 803-807.

Pütz, T. and Klimsa, K. 1991. Profilbeschreibung und Analyseergebnisse des Standortes Kaldenkirchen – Hülst. Internal Report IRA 6/91, Forschungszentrum Jülich, Germany.

Radzevicius, S. J., Chen, C.-C., Peters, L., Jr., Daniels, J. J. 2003. Near-field dipole radiation dynamics through FDTD modeling. Journal of Applied Geophysics, 52 (2003), 75-91.

Robinson, D. A., Friedman, S. P. 2003. A method for measuring the solid particle permittivity or electrical conductivity of rocks, sediments, and granular materials. J. Geopys. Res., 108(B2), 2076, doi : 10,1029/2001JB000691, 2003-09-10.

Robinson, D. A., Friedman, S. P. 2003. A method for measuring the solid particle permittivity or electrical conductivity of rocks, sediments, and granular materials. J. Geophys. Res., 108(B2), 2076, doi : 10,1029/2001JB000691, 2003-09-10.

Roth, K., Schulin, R., Flühler, H., Attinger, W. 1990. Calibration of Time Domain Reflectometry for water content measurement using composite dielectric approach. Water Resources Research, 26, 2267-2273.

Sandmeier, K. J. 2006. Reflexw 4.0, Windows 9X/NT-program for the processing of seismic, acoustic or electromagnetic reflection, refraction and transmission data. Handbook.

Scheuermann, A., Schlaeger, S., Brauns, J., Hübner, C., Brandelik, A. 2002. Bestimmung von Feuchteprofilen mittels TDR während eines Einstauversuches an einem naturgemäßen Deichmodell. Technisches Messen, 69, 37-42.

Schmalholz, J. 2000. Bestimmung dielektischer Eigenschaften kontaminierter Bodenproben in Abhängigkeit von Feuchte, Frequenz und elektrischer Leitfähigkeit. Diploma thesis, Geophysical Institute, University of Karlsruhe, Karlsruhe, Germany.

Schmalholz, J., Igel, J. S., Anschütz, H. R., Wilhelm, H., Hübner, C. 2001. Inversion of measured dielectric properties of diesel-contaminated sands and modeling of GPR-measurements on contaminated sites. Conference Proceedings of the Fourth International Conference on Electromagnetic Wave Interaction with Water and Moist Substances, Weimar, 477-483.

Schmalholz, J., Müller, M., Yaramanci, U., Kemna, A., Stoffregen, H., 2004a. Small Scale Determination of Volumetric Water Content Distribution in the Uppermost Soil, Proceedings of the Tenth International Conference on Ground Penetrating Radar, p 489-492.

Schmalholz, J., Stoffregen, H., Kemna, A., Yaramanci, U. 2004b. Imaging of Water content Distributions inside a Lysimeter using GPR Tomography. Vadose Zone Journal, 3, 1106-1115.

Schön, J. H. 1996. Pysical properties of rocks; Fundamentals and principles of petrophysics. Pergamon, Leoben, Austria.

Serbin, G., Or, D. 2003. Near-Surface Water Content Measurements Using Horn Antenna Radar: Methodology and Overview. Vadose Zone Journal, 2, 2003.

Shen, L. C., Savre, W. C., Price, J. M., Athavale, K. 1985. Dielectric properties of reservoir rocks at ultra-high frequencies. Geophysics, 50, 692-704.

Sheriff, R., E. 1997. Encyclopedic Dictonary of Exploration Geophysics, Third Edition. Society of Exploration Geophysicists.

Shihab, S., Al-Nuaimy, W. 2004. A comparison of segmentation techniques for target extraction in ground-penetrating radar data. Near Surface Geophysics, 2, 47-55.

Sihvola, A. H., Alanen, E. 1991. Studies of Mixing Formulae in the Complex Plane. IEEE Transactions on Geoscience and Remote Sensing, Vol. 29, No. 4.

Sihvola, A. H., Kong, J. A. 1988. Effective permittivity of dielectric mixtures. IEEE Transactions on Geoscience and Remote Sensing, 26, 420-429.

Sommerfeld, A. 1899. Über die Fortpflanzung elektrodynamischer Wellen längs eines Drahtes. Annalen der Physik und Chemie, Vol. 67, No. 2, 233-290.

Sperl, C. 1999. Erfassung der raum-zeitlichen Variation des Bodenwassergehaltes in einem Agrarökosystem mit dem Ground-Penetrating Radar. Ph.D diss. at the Departement of Soil Sciences, Technical University of Munich, Germany.

Stolt, R., 1978. Migration by Fourier transform. Geophysics, 43, 23-48.

Tabbagh, A. (1986): Applications and advantages of the Slingram electromagnetic method for archaeological prospecting.- Geophysics, 51, 576-584.

Täumer K., Stoffregen, H., Wessolek, G. 2006. Seasonal dynamics of preferential flow in a water repellent soil. Vadose Zone Journal, 5, 405-411.

Thierbach, R. 1974. Electromagnetic reflections in salt deposits. Journal of Geophysics, 40, 633-637.

Topp, G. C., Davis, J. L., Annan, A.P. 1980. Electromagnetic Determination of Soil Water Content: Measurement in Coaxial Transmission Lines. Water Resources Research, 16, 574-582.

Tronicke, J., Holliger, K. 2005. Quantitative integration of hydrogeophysical data: Conditional geostatistical simulation for characterizing heterogeneous alluvial aquifers. Geophysics, 70, H1-H10.

Tronicke, J., Knoll, M. D. 2005. Vertical radar profiling: influence of survey geometry on first-arrival traveltimes and amplitudes. Journal of Applied Geophysics, 57, 179-191.

Tronicke, J., Tweeton, D., R., Dietrich, P., Appel, E. 2001. Improved crosshole radar tomography by using direct reflected arrival times. Journal of Applied Geophysics, 47, 97-105.

Turesson, A. 2006. Water content and porosity estimated from ground-penetrating radar and resistivity. Journal of Applied Geophysics. 58, 99-111.

Ulaby, F. U., Moore, R. K., Adrian, K. F. 1986. Microwave remote sensing: active and passive, vol. III: from theory to applications. Artech House.

Valle, S., Zanzi, L., Rocca, F. 1999. Radar tomography for NDT: comparison of techniques. Journal of Applied Geophysics, 41, 259-269.

Vasco, D. W., Peterson, J. E., Jr., Lee, K. H. 1997. Ground-penetrating radar velocity tomography in heterogeneous and anisotropic media. Geophysics, 62, 1758-1773.

Voss, T. 2006. Untersuchungen zur Erfassungstiefe der Radarwellen für die direkte Bodenwelle. Student research project at the Department of Applied Geophysics, Technical University of Berlin, Germany.

Wensink, W. A. 1993. Dielectric properties of wet soils in the frequency range 1-3000 MHz. Geophysical Prospecting, 41, 671-696.

Witten, A., J., Molyneux, J., E., Nyquist, J., E. 1994. Ground Penetrating Radar Tomography: Algorithms and ase Studies. IEEE Transactions on Geoscience and Remote Sensing, 32, 461-467.

Wollny, K. G. 1999. Die Natur der Bodenwelle und ihr Einsatz zur Feuchtebestimmung. Ph.D diss. at the Faculty of Geosciences, Ludwig-Maximilians University of Munich, Germany.

Yaramanci, U., Hertrich, M. 2006. Magnetic Resonance Sounding. In Kirsch, R. 2006. Groundwater Geophysics – A Tool for Hydrogeology. Springer-Verlag Berlin Heidelberg, Germany.

Young, R. A., Sun, J. 1999. Revealing stratigraphy in ground-penetrating radar data using domain filtering. Geophysics, 64, 435-442.

Zischak, R. 1997. Alternatives Oberflächenabdichtungssytem ´Verstärkte mineralische Abdichtung mit untenliegender Kapillarsperre´. Schriftenreihe Angewandte Geologie Karlsruhe, 47, 1997.

9 List of figures

10 List of tables

Acknowledgements

During my research in Berlin many people contributed directly or indirectly to this work and helped an Allgäuer acclimating to the big city.

Prof. U. Yaramanci who provided good and supportive working conditions during my whole PhD. I am grateful for his help to improve my work in the course of many fruitful discussions. Fortunately he succeeded more than once to push me into directions I was too hesitant to go.

Dr. A. Kemna who always stayed interested since our first encounter and accepted to act as second referee of my PhD-thesis. I found a discussion partner for the evaluation of the various hydrogeophysical techniques and other subjects. Some of these discussions took place in the course of an evening's beer and will be fondly remembered.

Prof. G. Wessolek and all the people in the DFG research group INTERURBAN for their interest and their infinite patience in explaining all their intuitive aberrations to a simple-minded geophysicist.

- In Heiner I found a steady source of pressure to right me back into the global goal of this work, an open-minded listener and discussion partner, and a helping hand in numerous field experiments. But most importantly, in several evenings during our last beer, he trained me to plan a tight time schedule for next-days experiments. And he taught me to accept the fact of being already hopelessly out of schedule during next-days breakfast.
- In Martin I found a permanent fixture to keep the subproject GEO on course. Often he had to be the one to present the results of our subproject on conferences or to keep the student assistants busy and on track. I always enjoyed our friendly headbutting while discussing local bureaucracy or regulations.

I thank all the people at the Department of Applied Geophysics of the Technical University of Berlin for supporting me in so many ways.

- Each member of the MRS-group for carefully listening to my initially abstruse hypothesis and their efforts to prove this thesis right. 15:2 is a convincing end result.
- All the members of the Sachsen-project for being so indulgent to me and for calmly enduring my differing opinions concerning equipment handling and maintenance.
- Manfred, Udo and Uwe for being always open for my ideas to improve the GPR method and their handy craftsmanship to transfer these ideas into reality. All their fun anecdotes and stories, often told way past working hours, will be always fond memories.
- Marco and Thomas for co-founding our weekly GPR-meeting and for all the fruitful, informative and fun discussions.

Next to Dr. A. Kemna and Prof. H. Vereecken a lot of people at the Forschungszentrum Jülich GmbH supported me during my experiments and time in Jülich. Especially John, Arre and Axel, who always shared more then one laugh with me during my stays in Jülich and who never tried to resist in joining me to go for the next round of beer at the various conferences we met.

In Oli I found the patient listener for all my questions and a prefect mate for all the field experiments during the INTERURBAN campaign. More than once we teamed up to defy the worst weather conditions to acquire the next dataset while discussing all the important things in life. The numerous meetings to pass in review the past week's work will be always appreciated.

In Helgard and Yann I struck gold during my former time in Karlsruhe. Thanks to today's technology scientific discussions or encouraging words were only an email or a SKYPE™ post away.

I thank Verena for her fast and thorough help. Thanks to my “second family” for their support and their patience in learning to live with the objective and analytical demeanor of a scientist.

I am very grateful to my parents who always supported me during my studies and this PhD work. Many thanks to my brother for paving so many ways by his example and for indirectly training me to stoically insist on my opinion.

Finally, to Micha for her endless patience and her acceptance for my self-imposed unusual working hours. Life would not be so beautiful without your support and love.